UNIVERSITY OF OKLAHOMA

GRADUATE COLLEGE

CONTROLLED GROWTH AND METROLOGY OF CARBON NANOTUBES ON SUPPORTED Co-Mo CATALYSTS

A DISSERTATION

SUBMITTED TO THE GRADUATE FACULTY

in partial fulfillment of the requirements for the

Degree of

DOCTOR OF PHILOSOPHY

By

VERONICA MAGALI IRURZUN
Norman, Oklahoma
2011

CONTROLLED GROWTH AND METROLOGY OF CARBON NANOTUBES ON SUPPORTED Co-Mo CATALYSTS

A DISSERTATION APPROVED FOR THE
SCHOOL OF CHEMICAL, BIOLOGICAL AND MATERIALS ENGINEERING

BY

Dr. Daniel E. Resasco, Chair

Dr. Lance L. Lobban

Dr. Jeffrey H. Harwell

Dr Robert L. Shambaugh

Dr. Lloyd A. Bumm

ACKNOWLEDGMENTS

Dr. Daniel E. Resasco

Thanks to him for his guidance and for giving me the honor to study under his supervision. Coming to complete a doctoral degree has truly been a great experience and I believe that my work with him has prepared me well to have a successful career. In a personal aspect he has been also a great mentor.

My committee

Thanks to them for their time and guidance. I appreciate their willingness to serve on my graduation committee and for all of their assistance.

My family

Thanks to my parents and brother for their support during my undergraduate and graduate careers. Special thanks to my husband for helping me every day.

Dr. Fabián Buffa

Thanks to him for giving me the opportunity to start doing research while I was still an undergraduate.

Dr. Yongqiang Tan

Thanks to him for all his guidance and instruction. His help in the beginning of my studies definitely helped me get to where I am today. He taught me the day to day in the lab.

Dr. Antonio Monzón

Thanks not only for the interesting discussions during a full semester of his stay in the U.S.A., but also for sponsoring part of my trip to the SOLEIL synchrotron in France.

Tanate and Thai friends

Special thanks to Tanate, Kiu and other Thai friends for their friendship and kindness.

M. Pilar Ruiz

Thanks to her for her invaluable friendship and companionship through everything.

Jimmy Faria Albanese

Thank to him for his contribution of long research conversations and peculiar questions.

Dr. Rolf E. Jentoft

Thank to him for his contribution and suggestions related to many of the topics in this dissertation.

Walter Alvarez

Thanks to him for his guidance and companion during the summer internship at ConocoPhillips.

Uvita and Olive

Thanks to them both for making me smile every day and special thanks to Uvi for making me get out of bed every day no later than 7 am.

SouthWest NanoTechnologies-Ricardo Prada Silvy

Thanks to them for their support and collaboration in each project that I have been involved.

TABLE OF CONTENTS

INTRODUCTION

CHAPTER 1

CHAPTER 2

CHAPTER 3

CHAPTER 4

LIST OF TABLES

LIST OF FIGURES

ABSTRACT

Studies related to selectivity assessment and yield upgrade of different types of Carbon Nanotubes have been conducted in order to determine the optimum supported Co-Mo catalysts design to achieve the desired performance.

Our group has developed and optimized a catalyst highly selective to the production of high (n,m) selectivity Single-Walled Carbon Nanotubes known as CoMoCAT®. In order to make their production more cost effective, different studies were devoted to increasing the carbon yield while keeping the selectivity high (as defined in Appendix A-1). In order to increase the carbon yield, several catalyst formulations have been tried. Catalysts synthesized using the sol-gel method have shown an improvement on the carbon yield while keeping the SWCNT selectivity high. In this work the synthesis of catalysts by using the sol-gel method is shown.

Carbon Nanotubes are widely recognized for being suitable for different applications because of their outstanding properties. Different types of Carbon Nanotubes are desired for different applications. Therefore the synthesis of controlled structure tubes is of high economic interest. Nowadays, the production of controlled structure Multi-Walled Carbon Nanotubes is also desirable not only because they are preferred for some applications over Single-Walled Carbon Nanotubes, but also because of the high cost effectiveness of their production. It is desirable to use all the knowledge gained during the development and optimization of Single-Walled Carbon Nanotubes production to control the structure of catalytically synthesized Multi-Walled Carbon Nanotubes. In this work the transition between CoMoCAT® and highly selective catalysts for the production of Multi-Walled Carbon Nanotubes is shown.

As mentioned before, it is important to produce Carbon Nanotubes not only at a high rate but also with high selectivity. In order to quantify the selectivity, different studies have been conducted using a variety of analytical techniques. The advantages and disadvantages of widely used metrology techniques are analyzed and shown in this work. A new quantitative method to measure the SWCNT selectivity is also presented here.

INTRODUCTION

INTRODUCTION

Although there was evidence of the production of different carbon crystal structures, it was not until 1991 that the carbon nanotubes (CNT) were identified. This year Sumio Ijima [1] (NEC) identified them as a product of the arc discharge method typically used to produce fullerenes. It was found that they were composed of more than one graphene layer. After two years (1993), single layer carbon nanotubes were produced and identified by Ijima [2] and Bethune [3].

The discovery of these crystal structures has revolutionized the science due to their outstanding properties.

i.1- Carbon Materials

Carbon is the first element of Group IV (Si, Ge, Sn, Pb) in the periodic table. This group is characterized by the ability to form chains of atoms with themselves (catenate) and to form covalent compounds having an oxidation number of +4. It has four valence electrons and they hybridize in three different forms: sp, sp^2 and sp^3. Carbon is distinguished from the rest of the group because it is smaller, it has higher electronegativity and it does not have aa accessible d orbital. This element is also distinguished for its ability of forming π-π bonds [4, 5].

There are two carbon allotropes, diamond and graphite. Diamond (Fig. 1(a)) is characterized by the overlapping of the four sp^3 orbitals of neighboring carbons. diamonds possess a cubic form (ZnS-sphalerite, [5]) where the tetrahedral carbons are arranged by covalent bonds. This 3D interconnected structure makes diamond not only an excellent thermal conductor but also a strong solid. It is also known for being an electrical insulator.

Graphite (Fig. 1(b)), on the other hand is formed by the stacking (0.335 nm) of 2D carbon layers formed by the overlapping of three sp^2 orbitals (6 C rings). The C-C bond distance in this case is shorter than in diamond (0.154 nm). The fourth electron is delocalized making graphite a high electrical conductor material (on plane conductivity). While the in-plane bonding of carbon is very strong, the layer to layer interaction is weak, making graphite a good lubricant. There are different types of graphite. Turbostatic (defected graphite with layer to layer spacing larger than 0.335 nm), Kish (single crystals of graphite formed onto molten iron), Highly Oriented Pyrolitic Graphite (HOPG, graphite produced by pyrolysis and annealing at high temperatures) and graphite whiskers (cylindrical and hollow structure with diameters in the micrometer range).

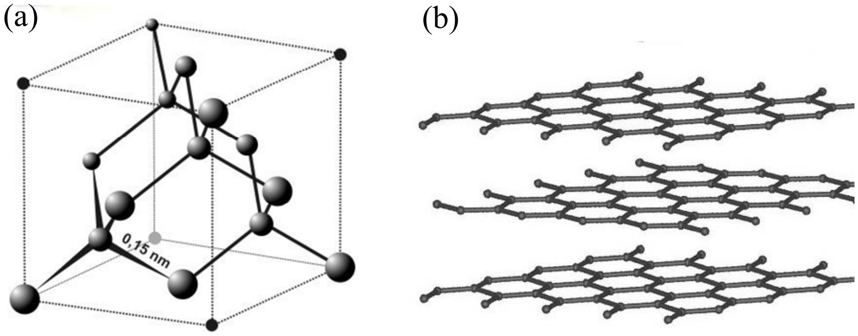

Figure 1: Carbon allotropes: (a) diamond, (b) graphite.

Other carbon forms such as carbon fibers, carbon black, activated carbon, fullerenes and CNT can not be classified either as diamond (100 % sp^3 bonds) or graphite (100 % sp^2 bonds). They have different sp^3 to sp^2 ratios [4].

Carbon fibers (CF) (Fig. 2) [6] are composed of stacked layers of six carbon rings. They can be crystalline, semi-crystalline or amorphous depending on how the layers are stacked. Graphite is crystalline because its layers are always stacked parallel to each other (order).

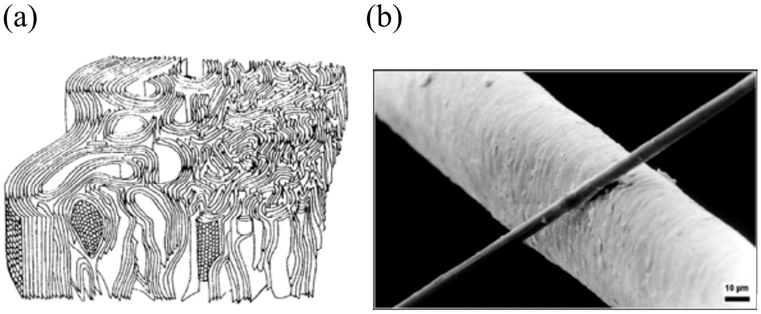

Figure 2: (a) Transversal view of carbon fiber cut, (b) Carbon fiber (top)-human hair (bottom).

Carbon black is a type of amorphous carbon (Fig. 3) found in soot and coal. It has high concentration of dangling bonds. Activated carbon is also a type of amorphous carbon but it is pre-treated to have a very large surface area (500-1500 m^2/g).

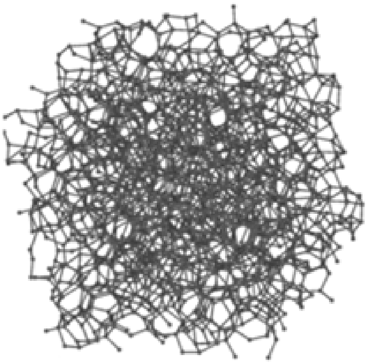

Figure 3: Amorphous carbon.

Fullerenes (Fig. 4) are formed by carbon pentagons, hexagons and heptagons. For example in C_{60}, fullerenes there are 12 pentagons separated by 20 hexagons forming an icosahedral structure. The high curvature causes the presence of sp^3 bonds.

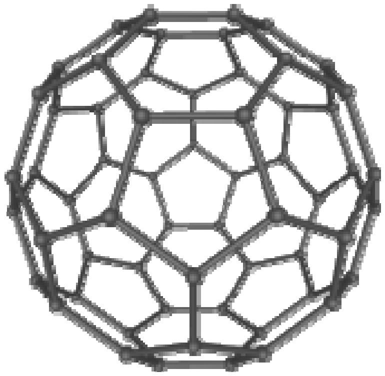

Figure 4: Fullerene C_{60}.

CNT are the carbon nano-structures that have revolutionized technology because they are light, they have high aspect ratio, high mechanical strength and high thermal and electrical conductivity. Their structure, characteristics, production and applications will be described throughout this dissertation.

i.2- Carbon Nanotubes

i.2.1- Production

CNT were primarily produced by Arc discharge (Fig. 5). This method consists of two carbon rods that are used as a cathode and an anode, through which DC current is applied. Carbon is vaporized from the cathode and condensates onto the anode. Multi-Walled Carbon nanotubes (MWCNT) were produced using this method by Ijima in 1991. Later, with the incorporation of catalysts into the anode rod, Single-Walled Carbon Nanotubes (SWCNT) (Bethune et al., 1993 – Ijima and Ichihashi, 1993) were synthesized using this technique.

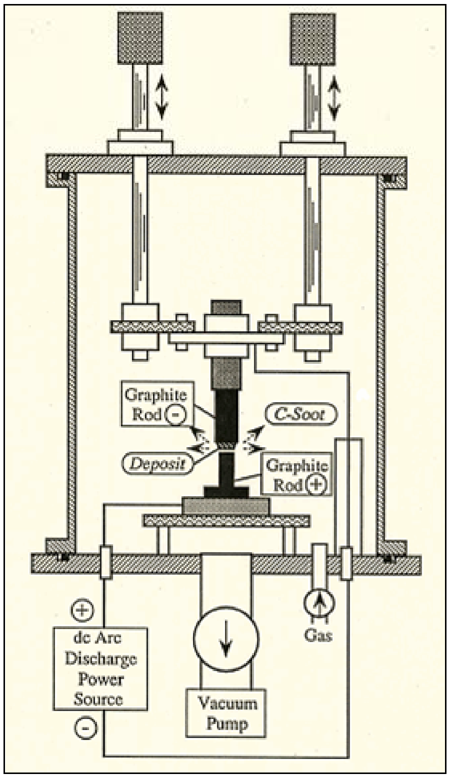

Figure 5: Arc discharge. [7]

Another technique that has been widely used to synthesize CNT is Laser ablation (Fig. 6). In this case a pulsed laser beam hits a target (graphite) kept under vacuum, evaporating the carbon. This is carried by an inert gas and condenses on the surface of a temperature controlled substrate. Even though this technique was primarily used to produce MWCNT, SWCNT (Maiti et al., 1997) have also been synthesized, but in this case the target was enriched with metals such as Co-Ni.

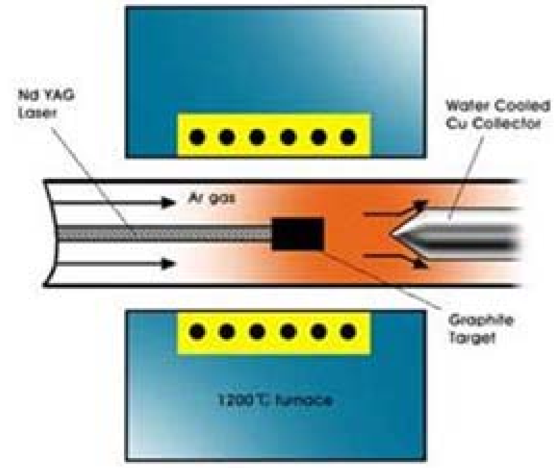

Figure 6: Laser ablation. [8]

Since none of the previously mentioned methods are scalable for industrial production, and the selectivity of CNT obtained is low, the use of a third method has been developed. This method is named Catalytic Chemical Vapor Deposition (CVD, Fig. 7)) [9].

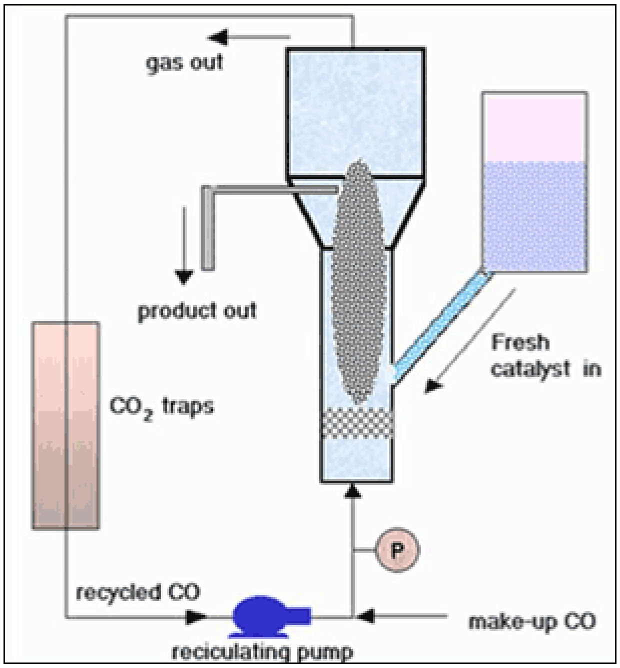

Figure 7: Chemical vapor deposition. CoMoCAT® process.

This method is interesting not only for its cost effectiveness and scalability, but also because the CNT produced have narrow chirality and diameter distribution. This method is based on the decomposition and precipitation of a carbon source (gas) onto a catalyst.

As mentioned before, CNT can be composed of a single wall or multiple walls. Different mechanisms have been proposed in order to explain the formation of CNT by the CVD method. A brief description of growth mechanisms for MWCNT and SWCNT will be presented next.

For the production of MWCNT it has been shown in the literature [10] that Fe, Co and Ni are the most active metals. As mentioned by Deck et al. [10], the catalytic activity depends on the solubility of carbon in the metal cluster (active range: 0.5-1.5 wt %). Baker et al. [11] have proposed two types of growth, tip and root growth. The decomposition of the carbon source on top of the metal particle followed by the diffusion into the particle to the other side, and final deposition leads to the tip growth type (Fig. 8(a)). If the interaction between the metal particle and the surface is strong, then the decomposition of the carbon source is from the sides of the metal cluster and the diffusion is from the bottom to the top (Fig. 8(b)). The physical state of the metal during the growth is still being studied. Tibbets [12] has proposed the vapor-liquid-solid (VLS) mechanism were the metal particle is liquid while the tube is growing. As mentioned by Harris [13], the temperatures used to grow MWCNT (500-700 °C) are not high enough to melt some the most used metals such as Fe (m.p. 1536 °C). Moisala et al. [14] showed that for Fe nanoparticles of 10 nm, the melting point would be approximately 940 °C, therefore not even particles in the nano-scale would be in the liquid phase at the reaction temperatures. Though, as mentioned by Harris [13], the nano-particles have to be in the solid state when MWCNT are grown. It is also important to mention another mechanism proposed where the carbon diffuses around the particle on the surface [15,16,13].

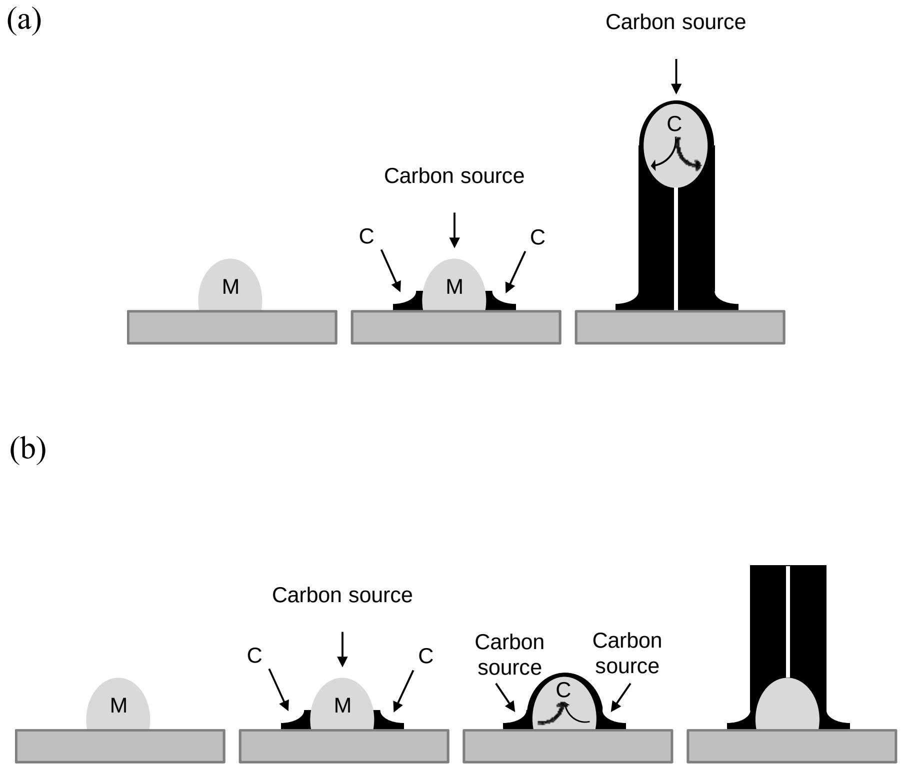

Figure 8: (a) Tip and (b) root growth mechanisms scheme.

It has been mentioned above the different mechanisms proposed for the catalytic growing of MWCNT. In the case of SWCNT, all the parameters related to the catalyst and the reactions have to be controlled since their growth is much more selective than in the case of MWCNT. Reaction temperatures commonly used for SWCNT production are higher than the ones used for MWCNT (900-1200 °C). Carbon sources that are typically used are CO and CH_4 because of their high thermal stability. As mentioned by

Harris [13], other type of carbon sources such as acetylene will tend to pyrolize and produce amorphous carbon instead of SWCNT due to their low thermal stability. He also mentioned than H_2 is used to decrease (cleaning effect) the amount of carbon when these types of sources are used. For the production of SWCNT metals such as Fe, Ni, Co and Mo (also some combinations) are the most used ones. Different research groups have been producing SWCNT. Smalley's group, for example, has produced SWCNT by using different catalysts and conditions [17,18] with HiPco® (High pressure carbon monoxide, [19]) being the most well-known. These types of tubes are produced by the decomposition of carbon monoxide at high pressure while feeding $Fe(CO)_n$ as catalyst at the same time. It is important to mention that this floating type of catalyst was used for the first time to produce CNT by Dresselhaus et al. [20]. Resasco's group [21-29] has also been successful in growing high yield and SWCNT selectivity. In this case the SWCNT were produced by using the well know CoMoCAT® process. Briefly, this process is based on the decomposition of carbon monoxide at high temperature over cobalt-molybdenum supported on silica catalysts.

As mentioned by Harris [13], the VLS mechanism has been widely accepted for the growing of SWCNT. An interesting study done by Bolton et al. [30,31] showed that when iron nanoparticles were saturated with carbon, graphitic caps were formed and lifted at certain temperature forming CNT (Fig. 9). They also mentioned that temperatures below those necessary for cap lifting would lead to encapsulation of the metal cluster while higher temperatures would lead to soot formation.

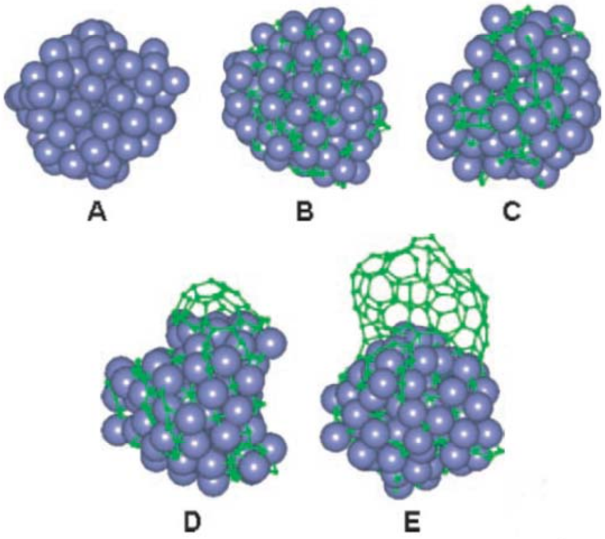

Figure 9: SWCNT nucleation and growth. [30]

As mentioned before, the VLS mechanism is widely accepted for SWCNT. However, there are different theories related to the carbon diffusion and cap formation. While Bolton et al. [30,31] supported the diffusion through the particle, other researchers such as Raty et al. [32] showed that carbon diffuses on the particle surface forming an sp^2 cap (Fig. 10).

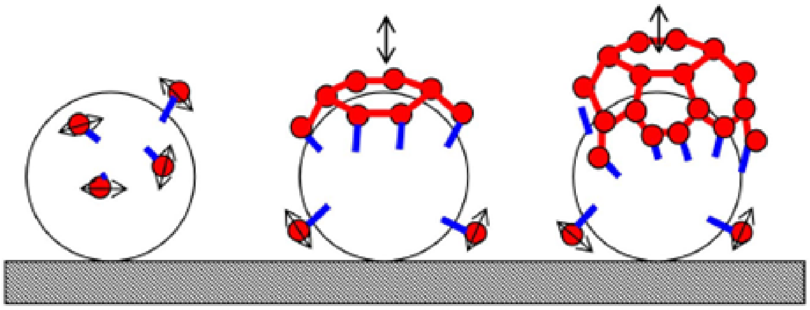

Figure 10: Carbon diffusion on the surface. [32]

Harris [13] mentioned the possibility of having a solid state mechanism instead of VLS during the SWCNT growing. In this case, the mechanism involves the transformation of amorphous carbon [33,34] deposited on the metallic particle to CNT (Fig. 11). This mechanism might explain the formation of CNT from particles where carbon dissolution is limited.

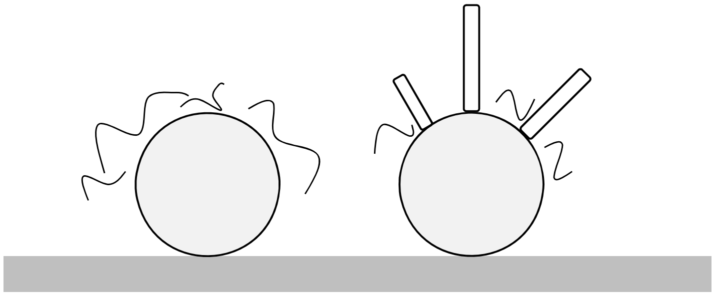

Figure 11: SWCNT solid state growth mechanism. [13]

i.2.2- Structure

CNT can be defined as graphene honeycomb layers rolled into cylinders. The carbon bonds in the graphene layer are similar to those in graphite where three of the carbon valence electrons have sp^2 hybridization and one electron is delocalized. The sp^2 orbitals form strong σ bonds between carbons in each layer while the delocalized electron (2s) forms π bonds between layers. Even though the π bonds weakly (van der Waals forces) hold the layers together, they gave graphite high electrical conductivity due to their overlapping (electron cloud). The strong σ covalent bonds give graphite high in-plane thermal conductivity. The main difference between graphite's structure (many graphene layers with an interspace of 0.335 nm) and the CNT's structure is that in the former, the graphene layers are planar and in the last one they are curved [35]. It is important to mention that even though CNT are mainly formed of sp^2 bonds, their curvature introduces sp^3 bonds. As mentioned before, when more than one concentric graphene layer is founded the CNT are called MWCNT and when there is only one shell they are called SWCNT [36]. MWCNT diameters have values between 10 and 40 nm and SWCNT have diameters around 1 nm. The length in both cases is a thousand times larger than the diameter. It is important to point out that SWCNT tend to assemble in bundles of 10 to 50 single tubes due to van der Waals interactions.

The outstanding properties are directly related to the high aspect ratio (length/diameter) and to the orientation of the carbon rings with respect to the axis. These two characteristics are related to how the graphene sheet is rolled into a cylinder. This folding is directed by a chiral vector Ch (circumference of the CNT) whose components are n and m (both are integer numbers in the direction of the unit vectors a_1 and a_2), and a chiral angle θ [36]. Ch and θ define the chirality and the diameter (d) of the tube.

$Ch = \hat{a}_1.n + \hat{a}_2.m$

$d = \sqrt{3}a_{C\text{-}C}\,(m^2+mn+n^2)^{1/2}/\pi = Ch/\pi$ ($a_{C\text{-}C}$ is the C-C bond length, 1.42Å)

$\theta = \tan^{-1}[\sqrt{3}n/(2m+n)]$

Depending on the chirality, the CNT have different denominations (Fig. 12). They are called zigzag, (n,0), when the chiral angle is 0º, armchair,(n,n) when the chiral angle is 30º and the rest are called chiral tubes because they do not have a superimposable mirror image. [37]. The unit cell for each type of tubes is different in size and it can be seen as a translational cylinder along the tube axis.

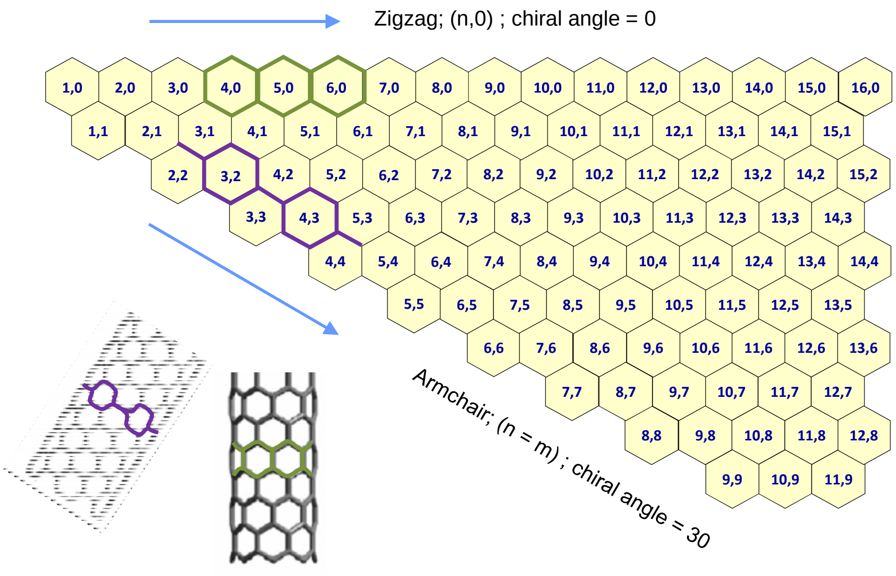

Figure 12: Carbon nanotubes chiral map.

As it was mentioned before, CNT are mostly formed of sp^2 bonds, having some sp^3 bonds too. It is important to mention that sp^3 bonds are not only located on the tips but also in the walls generating defects [13]. Other types of defects are also present in the side of the walls such as elbow connections [38-42], tori, helices, vacancies, adatoms, etc.

i.2.3- Properties

i.2.3.1- Physical

The chirality will determine if the tubes are metallics or semiconductors. If n-m = 3q (where q is an integer) they are metallic as predicted by Dresselhaus et al. [43-45]. Therefore, all the armchair tubes are metallic while only 1/3 of the zigzag and chiral tubes are metallic leaving the rest to the semiconductor classification. It is important to point out that this will make a difference in the electronic behavior of the tubes.

Individual metallic tubes will have a non zero energy value at the Fermi level (there is no band gap between the valence and the conduction band) and the semiconductors will have an energy gap at the Fermi level (Fig 13).

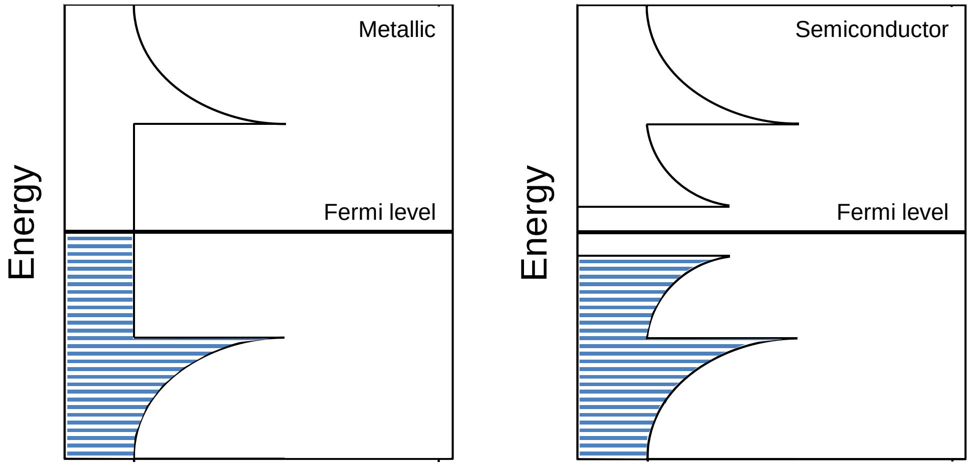

Figure 13: Carbon nanotubes density of states.

Most of the theoretical derivations related to the density of states were done for graphene where the curvature effect was not considered. If this is considered, the position of the Fermi level can be affected. While metallic armchairs remain metallic, zigzag and chiral tubes with small diameter can be transformed to semiconductors [13].

The electrical conductivity of CNT is due to the transport of electrons across the tubes. CNT behave as quantum wires. Metallic tubes show ballistic transportation where the electrons do not suffer resistivity and do not dissipate energy as they travel through the tube. This ballistic behavior allows metallic tubes to conduct large current without getting hot. On the other hand, semiconductor tubes show diffusive conduction [13].

It has been seen in the literature [13,46] that typical values for the Young's modulus and the tensile strength of CNT are 1000 GPa (5 times larger than steel) and 63 GPa (50 times larger than steel), respectively. CNT are stiff and strong while having low density. All these characteristics together make them suitable materials to improve mechanical properties of different matrices. CNT differ from carbon fibers in the fact that they can be exposed to stresses beyond the elastic point and they will return to their original shape if the stress is released. The mechanical properties of CNT are related to their structure and defects. It has been shown in the literature [13] that the stiffness increases with the tube diameter and that the Young's modulus decreases with the amount of defects.

Optically, CNT are also outstanding materials. For example, due to their large penetration depth, thin films would be transparent. The transparency in carbon materials is related to the absorption of visible light. The sp^3 bonds in diamond do not absorb visible light making this material transparent. On the other hand, the π electrons in the sp^2 bonds of soot absorb light in a wide range making them look black. Graphite differs from soot in the high orientation of the graphene layers. This orientation generates higher reflection that makes graphite look lighter than soot. Different characterization techniques based on the optical properties of CNT such as optical absorption, fluorescence and Raman scattering are widely used.

The thermal conductivity of CNT is, as the electrical conductivity, quantized being dominated by acoustic phonons. It has been shown in the literature [47,48] that typical thermal conductivity values are in the order of 2000 W/m/K (Copper: 385

W/m/K). It is important to mention that this value depends on the CNT material, arrangement and experimental temperature.

i.2.3.2- Chemical

Functionalization of CNT is a widely used technique for different applications [49-51]. As mentioned by Harris [13], the reactivity depends on the curvature. Pyramidalization of the sp^2 bonds increases the reactivity. Therefore the tips and small diameter tubes are more reactive. There are two different types of functionalization, covalent (fluorination, carbine addition, sylation etc.) and non-covalent (surfactants, polymers etc.).

i.3- References

[1]- Ijima S., Helical microtubules of graphitic carbon, *Nature*, **1991**, 354, 56.

[2]- Ijima S., Single-shell carbon nanotubes of 1-nm diameter, *Nature*, **1993**, 363, 603.

[3]- Bethune D.S., Kiang C.H., de Vries M.S., Gorman G., Savoy R., Vazquez J., Beyers R., Cobalt-catalysed growth of carbon nanotubes with single-atomic-layer walls, *Nature*, **1993**, 363, 605.

[4]- Sharon M., Sharon M., Carbon nanoforms and applications, Mc Graw Hill, **2010**.

[5]- Rayner-Canhnam J., Overton T., Descriptive inorganic chemistry, 4th ed., Freeman, **2006**.

[6]- Chung D.D.L., Carbon fiber composites, Butterworth-Heinemann, **1994**.

[7]- Ando Y., Iijima S., *Jpn. J. Appl. Phys*., **1993**, 32, L107.

[8]- Daenen M., de Fouw R.D., Hamers B., Janssen P.G.A., Schoteden K., Veld M.A.J., The Wondrous World of Carbon Nanotubes: a review of current carbon nanotube technologies, **2003**, Eindhoven University of Technology.

[9]- Qin L.C., CVD synthesis of carbon nanotubes, *J. Mater. Sci. Lett*., **1997**, 16, 457.

[10]- Deck C.P., Vecchio K., Prediction of carbon nanotube growth success by the analysis of carbon-catalyst binary phase diagrams, *Carbon*, **2006**, 44, 267.

[11]- Baker R.T.K., Harris P/.S., Thomas R.B., Feates F.S., Waite R.J., Nucleation and growth of carbon deposits from the nickel catalyzed decomposition of acetylene, *J. Catal*., **1972**, 26, 51.

[12]- Tibbetts G.G., Why are carbon filaments tubular?, *J. Cryst. Growth*, **1984**, 66, 632.

[13]- Harris P.J.F., Carbon nanotube science-Synthesis, properties and applications, **2009**, Cambridge University press.

[14]- Moisala A., Nasibulin A.G., Kauppinen E.I., The role of metal nanoparticles in the catalytic production of single-walled carbon nanotubes-a review, *J. Phys. Cond. Matter*., **2003**, 15, S3011.

[15]- Baird T., Fryer J.R., Grant B., Carbon formation on iron and nickel foils by hydrocarbon pyrolysis-reactions at 700 °C, *Carbon*, **1974**, 12, 591.

[16]- Oberlin A., Endo M., Koyama T., Filamentous growth of carbon through benzene decomposition, *J. Cryst. Growth*, **1976**, 32, 335.

---

[17]- Hafner J.H., Bronikowski B.R., Azamian B.R., Nikolaev P., Rinzler A.G., Colbert D.T., Smith K.A., Smalley R.E., Catalytic growth of single-wall carbon nanotubes from metal particles, *Chem. Phys. Lett.*, **1998**, 296, 195.

[18]- Dai H.J., Rinzler A.G., Nikolaev P., Thess A., Colbert D.T., Smalley R.E., Single-wall nanotubes produced by metal-catalyzed disproportionation of carbon monoxide, *Chem. Phys. Lett.*, **1996**, 260, 471.

[19]- Bronikowski M.J., Willis P.A., Colbert D.T., Smith K.A., Smalley R.E., Gas-phase production of carbon single-walled nanotubes from carbon monoxide via the HiPco process: A parametric study, *J. Vac. Sci. Technol. A*, **2001**, 19, 4, 1800.

[20]- Cheng H.M., Li F., Su G., Pan H.Y., He L.L., Sun X., Dresselhaus M.S., Large-scale and low-cost synthesis of single-walled carbon nanotubes by the catalytic pyrolysis of hydrocarbons, *Appl. Phys. Lett.*, **1998**, 72, 3282.

[21]- Resasco D.E., Kitiyanan B., Harwell J.H., Alvarez W., Method of producing carbon nanotubes, U.S. Patent No. 6333016, **2001**.

[22]- Alvarez W.E., Pompeo F., Herrera J.E., Balzano L., Resasco D.E., Characterization of single-walled carbon nanotubes (SWCNTs) produced by CO disproportionation on Co-Mo catalysts, *Chem. Mater.*, **2002**, 14, 4, 1853.

[23]- Resasco D.E., Alvarez W.E., Pompeo F., Balzano L., Herrera J.E., Kitiyanan B., Borgna A., A scalable process for production of single-walled carbon nanotubes (SWCNT) by catalytic disproportionation of CO on a solid catalyst, *J. Nanopart. Res.*, **2002**, 4,1-2, 131.

[24]- Resasco D.E., Herrera J.E., Balzano L., Decomposition of carbon-containing compounds on solid catalysts for single-walled nanotubes production, *J. Nanosci. Nanotechol.*, **2004**, 4, 4, 398.

[25]- Herrera J.E., Resasco D.E., In situ TPO/Raman to characterize single-walled carbon nanotubes, *Chem. Phys. Lett.*, **2003**, 376,3-4, 302.

[26]- Herrera J.E., Balzano L., Pompeo F., Resasco D.E., Raman characterization of single-walled nanotubes of various diameters obtained by catalytic disproportionation of CO, *J. Nanosci. Nanotechol.*, **2003**, 3, 1.

[27]- Alvarez W.E., Pompeo F., Herrera J.E., Balzano L., Resasco D.E., Characterization of single-walled carbon nanotubes (SWNTs) produced by CO disproportionation on Co-Mo catalysts, *Chem. Mater.*, **2002**, 14,1853.

[28]- Alvarez W., Kitiyanan B., Borgna A., Resasco D.E., Synergism of Co and Mo in the catalytic production of single-wall carbon nanotubes by decomposition of CO, *Carbon*, **2001**, 39, 547.

---

[29]- Monzon A., Lolli G., Cosma S., Mohamed S.B., Resasco D.E., Kinetic Modeling of the SWNT Growth by CO Disproportionation on CoMo Catalysts, *J. Nanosci. Nanotechol.*, **2008**, 8, 6141.

[30]- Bolton K., Ding F., Rosén A., Atomistic simulations of catalyzed carbon nanotube growth, *J. Nanosci. Nanotechol.*, **2006**, 6, 1211.

[31]- Bolton K., Ding F., Rosén A, Nucleation and growth of single-walled carbon nanotubes: a molecular dynamics study, *J. Phys. Chem. B*, **2004**, 108, 17369.

[32]- Raty J.Y., Gygi F., Galli G., Growth of carbon nanotubes on metal nanoparticles: a microscopic mechanism from ab initio molecular dynamics simulations, *Phys. Rev. Lett.*, **2005**, 95, 096103.

[33]- Gorbunov A., Jost O., Pompe W., Graff A., Solid-liquid-solid growth mechanism of single-wall carbon nanotubes, *Carbon*, **2002**, 40, 113.

[34]- Sen R., Suzuki S., Kataura H., Achiva Y., Growth of single-walled carbon nanotubes from the condensed phase, *Chem. Phys. Lett.*, **2001**, 349, 383.

[35]- Resasco D.E., Herrera J.E. Encyclopedia of Nanoscience and Nanotechnology **2003**, 1, 23.

[36]- Guo P., Nikolaev A., Thess D.T., Colbert R.E., Catalytic growth of single-walled nanotubes by laser ablation, *Chem. Phys. Lett.*, **1995**, 243, 4954.

[37]- Resasco D.E. Carbon nanotubes and related structures. Book chapter, in press.

[38]- Chernozatonskii L.A., Carbon nanotube elbow connections and tori, *Phys. Lett. A*, **1992**, 170, 37.

[39]- Dunlap B.I., Relating carbon tubules, *Phys. Rev. B*, **1994**, 49, 5643.

[40]- Fonseca A., Hernadi K., Nagy J.B., Lambin Ph., Lucas A.A., Model structure of perfectly graphitizable coiled carbon nanotubes, *Carbon*, **1995**, 33, 1759.

[41]- Lambin P., Fonseca J.P., Vigneron J.P., Nagy J.B., Lucas A.A., Structural and electronic properties of bent carbon nanotubes, *Chem. Phys. Lett.*,**1995**, 245, 85.

[42]- Chico L., Crespi V.H., Benedict L.X., Louie S.G., Cohen M.L., Pure carbon nanoscale devices: nanotube heterojunctions, *Phys. Rev. Lett.*, **1996**, 76, 971.

[43]- Dresselhaus M.S., Dresselhaus G., Saito R., Physics of carbon nanotubes, *Carbon*, **1995**, 33, 883.

[44]- Dresselahus M.S., Dresselhaus G., Eklund P.C., Science of fullerenes and carbon nanotubes, Academic Press, San Diego, **1996**.

[45]- Saito R., Fujita M., Dresselhaus G., et al., Electronic structure of chiral grapheme tubules, *Appl. Phys. Lett.*, **1992**, 60, 2204.

[46]- http://www.pa.msu.edu/cmp/csc/ntproperties/ .

[47]- Hone J., Whitney M., Piskoti C., Zettl A., Thermal conductivity of single-walled carbon nanotubes, *Phys. Rev. B*, **1999**, 59, R2514.

[48]- Hone J., Carbon Nanotubes: Thermal Properties, Dekker Encyclopedia of Nanoscience and Nanotechnology, **2004**.

[49]- Peng-Cheng Ma, Naveed A. Siddiqui, Gad Marom and Jang-Kyo Kim, Dispersion and functionalization of carbon nanotubes for polymer-based nanocomposites: A review, *Composites: Part A*, **2010**, 41, 1345.

[50]- Hirsch A., Functionalization of Single-Walled Carbon Nanotubes, *Angew. Chem. Int. Ed.*, **2002**, 41, 11.

[51]- Tasis D., Tagmatarchis N., Bianco A., Prato M, Chemistry of Carbon Nanotubes, *Chem. Rev.*, **2006**, 106, 1105.

CHAPTER 1

Acknowledgments:
Y. Tan, SouthWest Nanotechnologies
R. Prada Silvy, SouthWest Nanotechnologies
J. Brown III, The University of Oklahoma.

CHAPTER 1

1.1- Growth and characterization of Carbon Nanotubes

The CNT presented in this work have been produced by CVD [1]. As mentioned before, this method is interesting not only for its cost effectiveness and scalability, but also because the CNT produced have a narrow chirality and diameter distribution.

In this chapter, the selectivity and carbon yield of CNT produced using different catalysts are shown. These catalysts are composed of different metals supported on either aluminum or silicon materials. In particular, the metals used are cobalt and molybdenum. The CNT have been synthesized by using different carbon sources.

The CNT have been characterized by using different analytical techniques, such as optical absorption, Raman scattering, electron microscopy and thermal analysis. A brief description of these techniques is given below.

Characterization techniques

Infrared and UV-Vis spectroscopy

In the infrared (IR) range, Raman scattering is used to obtain information about the structure and properties of molecules from their vibrational transitions. This technique differs from IR absorption because it involves only one photon while Raman scattering involves two photons. The photon generated in IR hits a molecule and when they are in resonance, disappears and the molecule gains the photon's energy. The molecules that present active modes in IR have to have dipole moments. On the other hand, by using Raman scattering, polarizable molecules interact with a photon inducing a dipole moment, then this induced dipole molecule emits a second photon. The difference in energy between the first and the second photon is the Raman shift. Figure 14 shows a scheme of both vibrational techniques. It can be seen that while for IR absorption there is only one step (photon) to reach the excited energy level, for Raman scattering there are two steps (photons) to reach the excited energy level. As it can be seen also in Fig. 14, the energy levels that are reached by using Raman scattering are much higher that the ones that are reached by using IR absorption. This would open the possibility that the photon energy approaches the transition energy to an excited electronic state. When these phenomena happen, Raman scattering becomes resonance Raman scattering, where the scattering is dominated by the resonant electronic states [2]. When the resonance is strong, the non-resonant energy exchange is not important.

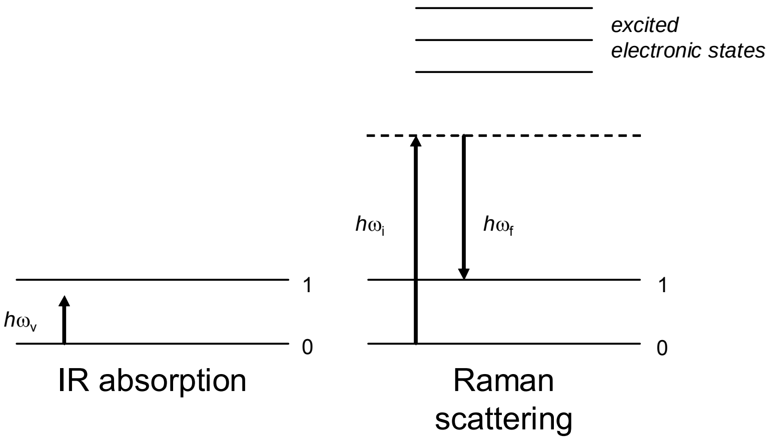

Figure 14: Energy level scheme for IR and Raman scattering.

UV-Vis absorption is based on the IR absorption explained above, but in this case the wavelength range is between 200-900 nm.

These techniques are used for the characterization of CNT. Typical spectra for SWCNT are shown below.

Figure 15 shows the typical vibration modes (Raman scattering) used for the characterization of CNT. The radial breathing mode (RBM) is related to the radial vibration of the CNT and the frequency varies inversely with the diameter. The D band is related to disordered carbon and defects. The G band is related to ordered or graphitic carbon and it is split in two modes, G^+ and G^-. While the frequency of G^- depends on the diameter, the frequency of G^+ does not [3]. The G' band is the second order harmonic of the D mode.

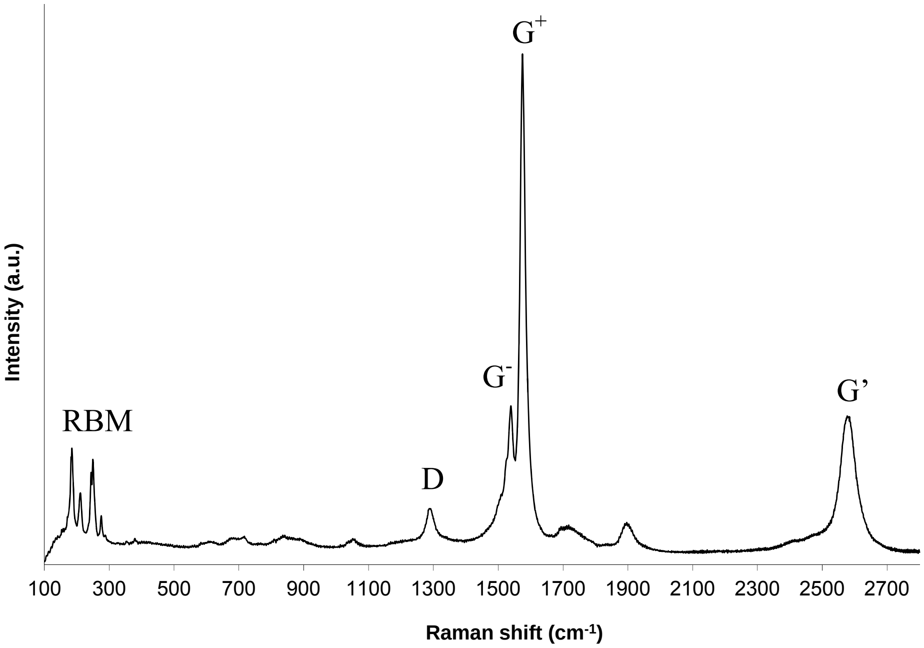

Figure 15: SWCNT typical Raman scattering spectrum.

Figure 16 shows the typical optical absorption (OA) spectrum of a SWCNT suspension. This spectrum is composed of a non-resonant background related to all the suspended species and a resonant zone related to the optical transition of electrons in SWCNT. The frequency is related to the chirality of the tubes [4].

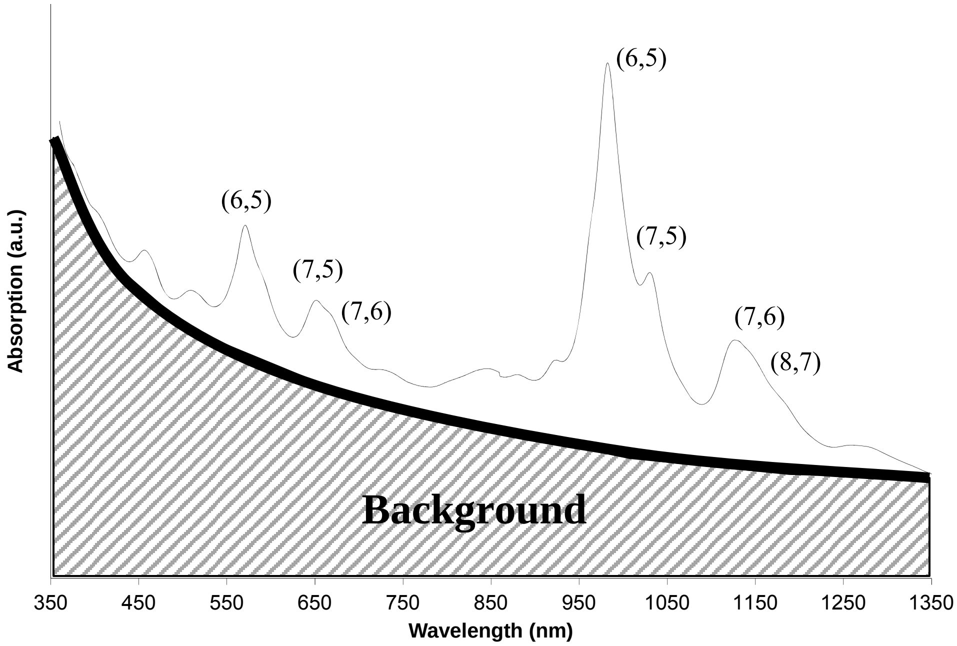

Figure 16: SWCNT typical optical absorption spectrum.

Temperature programmed oxidation (TPO)

This technique involves the oxidation of carbon with controlled amounts of O_2 to produce carbon dioxide that is monitored by using a detector (flame ionization detector or thermal conductivity detector) while the temperature increases.

Electron microscopy

Scanning and transmission electron microscopy (SEM-TEM) are techniques that can be used to determine the shape and size of CNT. When a sample is intersected by a primary electron beam, the electrons behave in different ways such as diffracted, transmitted and backscattered. From each type of electron, different information can be collected. Transmitted and diffracted electrons are used to generate images by transmission electron microscopy. Scanning electron microcopy images are obtained by detecting secondary and backscattered electrons.

As mentioned before, in this chapter are shown the selectivity and carbon yield of CNT produced by using catalysts supported on different materials, with different precursors and different carbon sources. The first case presented is related to SWCNT produced by using Co-Mo (1:3) supported on silica and carbon monoxide as the carbon source. The second case analyzed is related to MWCNT produced by using Co-Mo (1:3-3:1) supported on aluminum or silicon materials and different carbon sources (carbon monoxide and ethylene). Different analytical techniques, such as OA, Raman scattering, SEM-TEM and thermal analysis have been used for characterization.

1.1.1- Single Wall Carbon Nanotubes - Co-Mo (1:3) - silica - carbon monoxide as carbon source.

As it has been published previously by our group [5-9], the bimetallic Co-Mo catalysts (CoMoCAT®) supported on high surface area silica are highly selective towards SWCNT. However, the carbon yield obtained with these catalysts is in the 2-4 wt % range. Seeking catalysts with a more open structure to increase the carbon yield, different techniques have been used to develop new materials. It is known that the sol-gel method has been extensively used in the preparation of supported metal catalysts, since it typically results in highly homogenous materials with a high degree of metal dispersion [10-12]. For example, Pd/SiO_2 catalysts for methane combustion prepared by the sol-gel method have not only exhibited higher surface area, narrower pore size distribution, and higher support thermal stability, but also higher resistance to metal particle sintering, with consequential lower deactivation [13]. Particularly relevant to the current work, this method has also been used to obtain active phases of Ni-Mo and

Co-Mo [14] bimetallic catalysts supported on silica for the oxidative dehydrogenation of alkanes. It has been observed that catalysts prepared by the sol-gel method can stabilize the bimetallic active phases much more efficiently than those prepared by other methods. Therefore, sol-gel appears as a suitable method to produce Co-Mo/SiO_2 catalysts for the synthesis of SWCNT.

In order to obtain metal catalysts supported on high-surface area silica by the sol-gel method, the polymerization of an alkoxy-silane such as tetraethoxysilane (TEOS), also known as tetraethyl orthosilicate, is carried out in the presence of the appropriate metal precursors [15]. When exposed to water, the alkoxy-silane hydrolyses and, at different pH values, forms different monomeric species [16]. These species range from $[Si(OH)_3(OH_2)]^+$ at pH=0 to $[SiO_2(OH)_2]^{2-}$ at pH=14. Depending on the conditions, these species can condense and form oligomers at a different rate and with different configurations. To accelerate the polymerization, a change in pH can be brought about by the addition of a base, which causes a rapid hydrolysis followed by polymerization. Simultaneously with this polymerization process, the metal ions (e.g. Co and Mo) precipitate, thus forming a homogenous and well dispersed mixture.

Previous studies [17,18] have shown that the final structure of the silica produced by sol-gel methods can be modified by varying preparation parameters such as type of alkoxide, presence of a catalyst (acidic or basic), water content, type of solvent and process temperature. For example, it has been shown that the silica particle size increases with increasing concentration of alkoxide or ammonia as well as with increasing alcohol's chain of the solvent [18]. By contrast, the particle size decreases when water concentration or process temperature increases [17]. When the sol-gel method is used for the synthesis of supported metal catalysts, additional parameters related to the chemistry of the metal precursors such as the solubility, acidity and reactivity are also important.

In this case, the effect of varying the ratio of the added ammonium hydroxide concentration has been studied, while keeping the other parameters constant. The concentration of ammonium hydroxide has an important effect on the rate of polymerization [19] and consequently, we expect that it will affect significantly the resulting morphology. In addition, a sol-gel catalyst prepared using a burnable sacrificial template which, after calcination results in an open micro-scale structure, was also studied. This approach, known as sol-gel nano-coating and extensively employed by previous researchers to prepare structured materials [20], gives us the opportunity to investigate the influence of the micro-structure, while keeping the composition unchanged.

1.1.1.1- Sol-gel method

1.1.1.1.2- Experimental

Four different powder catalysts and a micro-scale structured catalyst were prepared by the sol-gel method. A constant total metal loading of 9 wt % of Co-Mo on SiO_2 (Co/Mo molar ratio of 1:3) was kept in all preparations. For the preparation of the powder catalysts, a solution of $Co(NO_3)_2 \cdot 6H_2O$ (Sigma Aldrich) in isopropanol was combined with an aqueous solution of $MoCl_5$ (Sigma Aldrich), then mixtures of tetraethyl orthosilicate (TEOS) and ammonium hydroxide (28 wt %) were added in different ratios. The corresponding samples are designated as AT(1/6), AT(2/6), AT(4/6) and AT(6/6), in which the numbers in parenthesis indicate the volume ratio of ammonium hydroxide to TEOS. The four solutions were left to gel at room temperature for 20 h. The resulting colors of the gels were different for all samples, going from a dark orange to a light violet as the ammonia concentration increased. The gels were filtered and subsequently dried in air at 200 ºC for 30 min, and further calcined at 650 °C for 150 min.

To study the effect of incorporating a micro-scale structure in the sol-gel catalyst, a microporous tubular-shaped supported catalyst has been prepared by using a sol-gel preparation method and a tubular template. The tubular template used was a carbon fiber (cloth 3K) with diameter of 5-10 μm and cut in small pieces of about 5 mm long, purchased from Fiberlay, Inc. In this case, the metal precursor solutions and the TEOS were mixed together with the carbon fiber template before adding the ammonium hydroxide. The solution was left to gel at room temperature for 20 h, then filtered, subsequently dried at 200 ºC for 30 min, and finally calcined at 650 °C for 150 min. It is important to mention that the sacrificial template was burned during the calcination process, which resulted in an open tubular micro-structure.

The catalyst samples were previously reduced at 500 ºC for 30 min under H_2 (125 sccm) in a ½ inch quartz reactor placed in a vertical furnace. After reduction, H_2 was switched to He (125 sccm) to reach the reaction temperature (750 ºC). Later, the carbon source (CO, 250 sccm) was flowed over the reduced catalyst for 30 min, while keeping the temperature at 750 ºC. The system was finally cooled down under He flow.

SWCNT suspensions for OA were prepared by ultra-sonicating (Horn Sonic Dismembrator, Model 500, Fisher scientific) the SWCNT/catalyst product in sodium cholate (20 %w/v in deionized water (DI)-Sigma Aldrich) for 60 min at 7 mW power. The suspension was then centrifuged (Dupont Sorvall SS-3) for 30 min at 15,000 rpm to separate the nanotubes embedded catalyst from the suspendable nanotubes. The supernatant liquid phase, which contains the nanotube suspended in surfactant, was collected for analysis in a Shimadzu UV-2101PC and a Bruker Equinox 55 FTNIR spectrophotometers.

SEM in a JEOL JSM-880 and TEM in a JEOL 2000-FX Intermediate Voltage were conducted to visualize the morphology of the as-produced samples. The suspensions for TEM analysis were prepared by suspending the SWCNT/catalyst product by mild sonication in isopropanol.

Thermo Gravimetric Analysis (TGA) was conducted in a TGAQ500 (TA instruments Inc.) under an air flow at 200 ºC for 15 min and then it was heated up at a rate of 5 ºC/min to 750 ºC. Before each TGA measurement, the SWCNT/catalyst product was first heated in air to 300 ºC in an oven for 3 h to eliminate any amorphous carbon by oxidation. Then, the product was stirred for several hours in aqueous solution of NH_4HF_2 (Sigma Aldrich) to dissolve the silica support, filtered and washed with DI water. Finally, it was treated with 35 % HCl solution to dissolve the metal particles, further washed with DI water, filtered and dried under vacuum for 2 days.

TPO of the SWCNT/catalyst product material using 80 sccm of 5% O_2 in He has been done to characterize the carbon species present in the samples.

1.1.1.1.2- Results

1.1.1.1.2.1- Optical absorption

The OA spectra for the nanotubes obtained on the different sol-gel powder catalysts and on the microscale structured catalyst are shown in Figures 17(a) and (b), respectively.

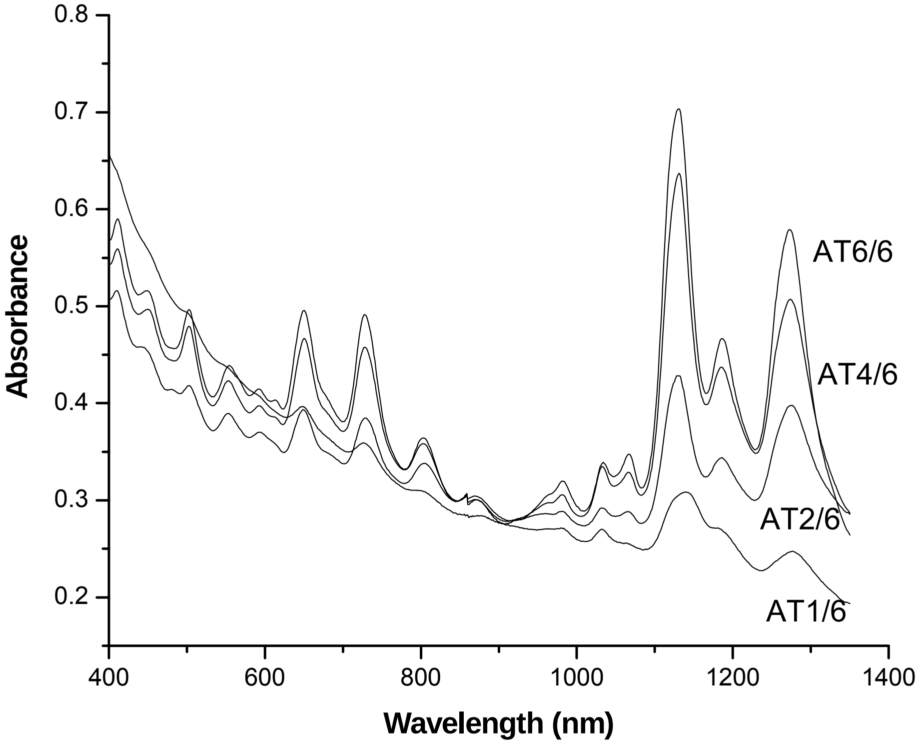

Figure 17(a): OA spectra of SWCNT grown onto four Co-Mo/SiO_2 powder catalysts with NH_4OH/TEOS ratios from1/6 to 6/6.

While the spectra of the products obtained on the powder catalysts show significant differences in absolute intensity from one catalyst to another, the relative intensities do not seem to vary significantly. By contrast, a broader distribution of SWCNT species is apparent on the product obtained over the microscale structured catalyst, with high intensity in the region corresponding to small diameter semiconducting tubes.

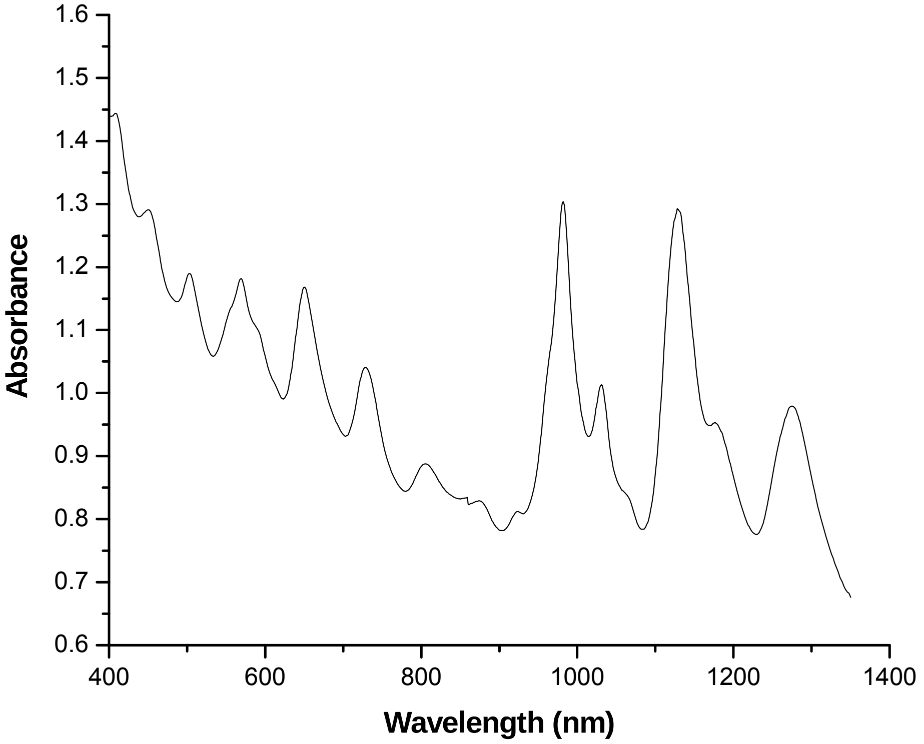

Figure 17(b): OA spectra of SWCNT grown onto a Co-Mo/SiO_2 micro-structured catalyst with an NH_4OH/TEOS ratio of 2/6.

In order to quantify these variations, an analysis of the different (n,m) species in each sample has been conducted. Table 1 shows the wavelength of the bands observed in the OA analysis together with (n,m) assignments for nanotubes that absorb near the observed wavelengths.

Considering simultaneously the positions of both E_{11} and E_{22} transitions, we can accurately determine the (n,m) species in the product of the various catalysts. Accordingly, the stronger bands seen in Figure 17(a) for the powder catalysts can be assigned to the species (7,6) and (8,7). Lower concentrations of (6,5), (7,5), and (8,6) are also observed. Much weaker bands are consistent with the presence of (8,4), (12,1), (9,2), and (9,4) species. In contrast to the typical Co-Mo/SiO_2 catalyst prepared by impregnation and used in our standard CoMoCAT® process, which yields to a product highly enriched in (6,5), the powder catalysts prepared by the sol-gel method result in a broader distribution of chiralities.

Table 1:(n,m) assignments using observed optical absorption and Raman bands of the SWCNT grown onto Co-Mo/SiO_2 powder catalysts.

Wavelength (nm) of observed optical absorption bands, E_{11}	Wavelength (nm) of observed optical absorption bands, E_{22}	(n,m) with E_{11} and E_{22} matching observed wavelengths	d (nm)
410		*(5,5)*	0.688
981	553	**(6,5)**	0.757
450		*(6,6)*	0.825
1033	649	**(7,5)**	0.829
1131	649	**(7,6)**	0.895
502		*(7,7)*	0.963
1131	594	*(8,4)*	0.84
1186	726	**(8,6)**	0.966
1271	726	**(8,7)**	1.032
553		*(8,8)*	1.1
1131	553	*(9,2)*	0.806
1066	726	*(9,4)*	0.916
1186	803	*(12,1)*	0.995

Figure 18(a) summarizes the distribution of the main chiralities for the different samples. It can be observed that as the NH_4OH/TEOS ratio increases from 2/6 to 6/6 the average tube diameters decreases. However, when the NH_4OH/TEOS ratio is the lowest (1/6), the synthesis of small diameter tubes is also favored. Figure 18(b) shows the intensity ratio between (8,7) and (7,6) species. It can be seen that the sample AT(2/6) has the maximum (8,7)/(7,6) ratio.

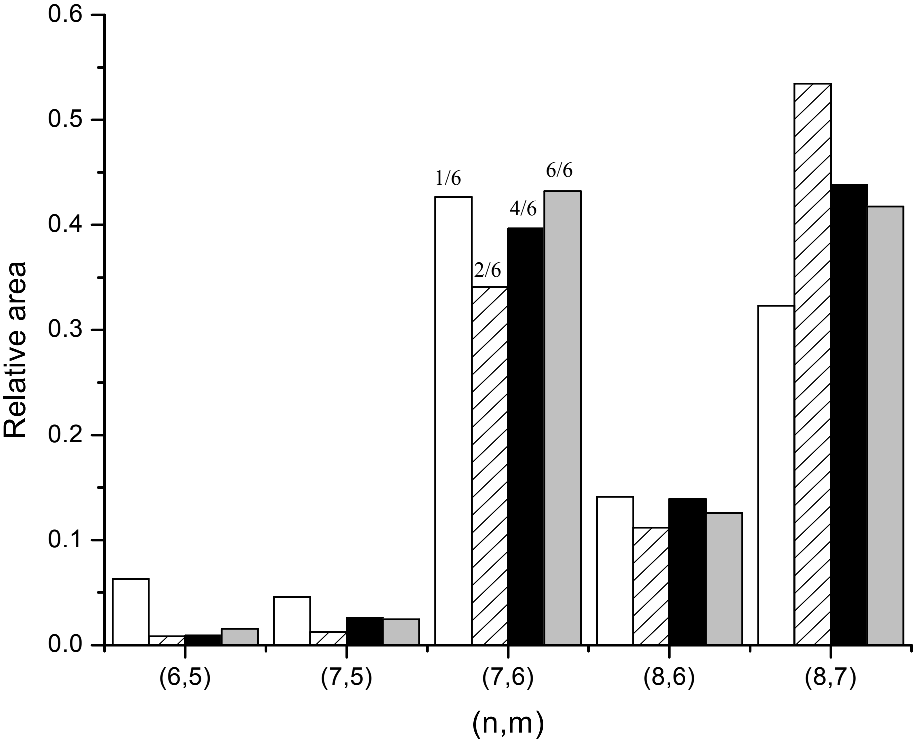

Figure 18(a): (n,m) distribution of SWCNT grown onto four Co-Mo/SiO_2 powder catalysts with NH_4OH/TEOS ratios from1/6 to 6/6.

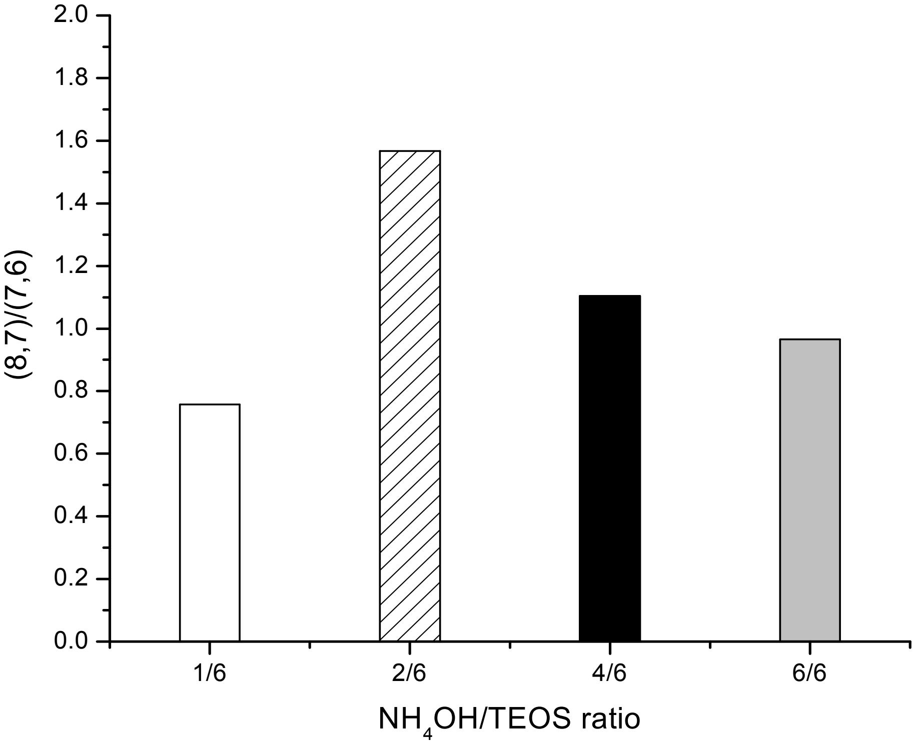

Figure 18(b): Ratio of the two observed main SWCNT chiralities (8,7) and (7,6) grown onto four Co-Mo/SiO_2 powder catalysts with NH_4OH/TEOS ratios from 1/6 to 6/6.

Figure 18(c) shows the distribution of the different (n,m) SWCNT types obtained onto the microscale structured catalyst. As mentioned above, a significant amount of SWCNT of smaller diameter, for example (6,5), is obtained, which is not seen on the powder catalysts. The fraction of carbon nanotubes that remains in suspension after centrifugation has been calculated, and in all cases; it falls in the range of 30-60%.

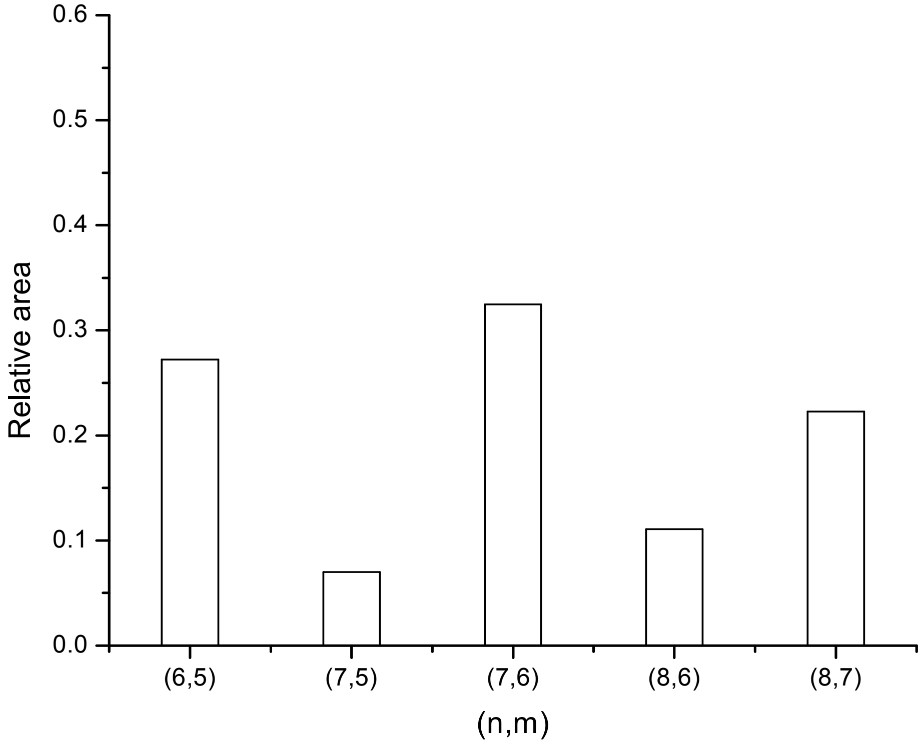

Figure 18(c): (n,m) distribution of SWCNT grown onto a Co-Mo/SiO_2 micro-structured catalyst with an NH_4OH/TEOS ratio of 2/6.

1.1.1.1.2.2- Raman scattering

Figures 19(a) and (b) show the Raman spectra of the SWCNT/catalyst product produced on the sol-gel powder, AT(1/6) to AT(6/6), and on the microscale structured catalysts, respectively. In these measurements, the samples were studied as produced, that is, with the catalyst still embedded in the SWCNT product.

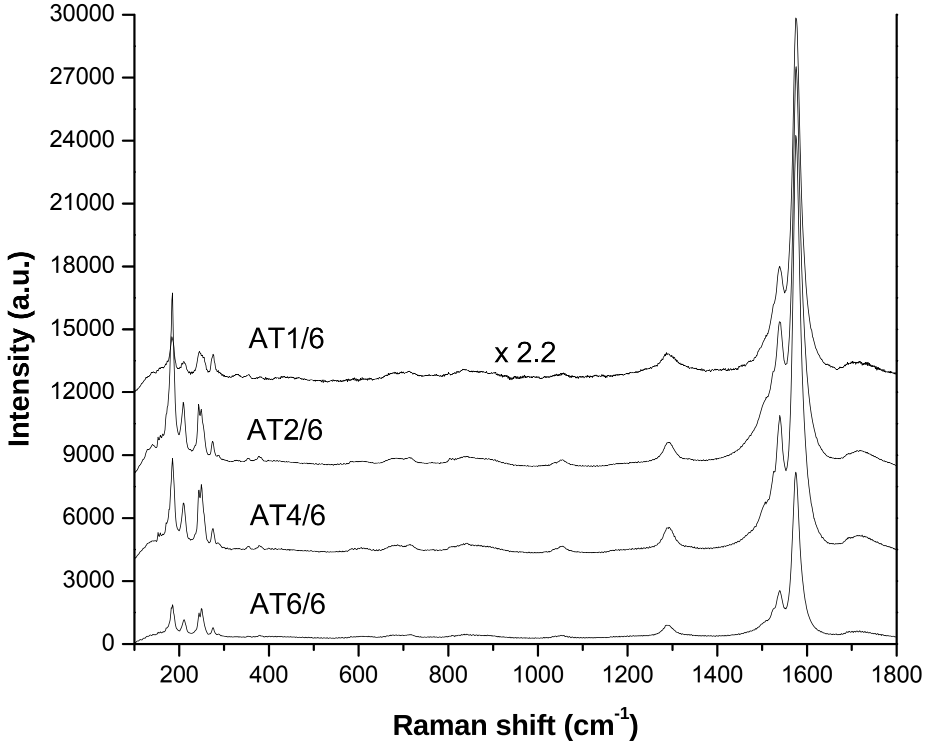

Figure 19(a): Raman spectra of SWCNT grown onto four Co-Mo/SiO_2 powder catalysts with NH_4OH/TEOS ratios from1/6 to 6/6.

As described in previous publications [21], the Raman spectral region below 300 cm^{-1} is related to the RBM, the region between 1250 and 1450 cm^{-1} (D band) is ascribed to disordered carbon and structural defects of the tubes, and the strong band between 1540 and 1600 cm^{-1} (G band) is related to the graphene optical mode and is due to carbon atoms vibrations tangentially to the walls.

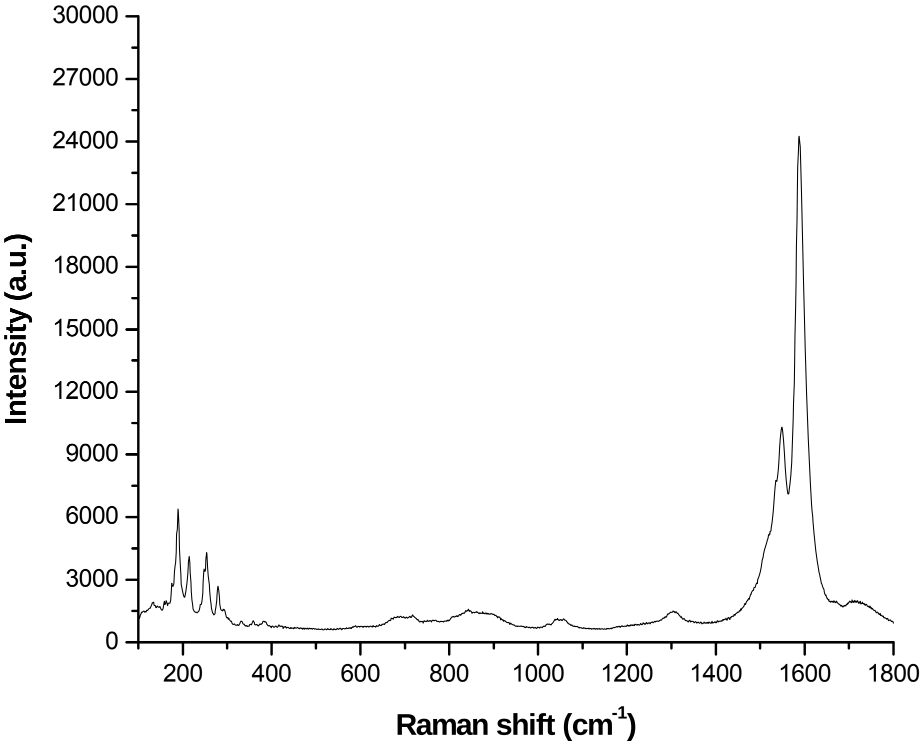

Figure 19(b): Raman spectrum of SWCNT grown onto Co-Mo/SiO_2 micro-structured catalyst with an NH_4OH/TEOS ratio of 2/6.

The intensity ratios between the G and the D bands [6,22] have been typically used as nanotube selectivity indicators. The calculated G/D ratios are shown in Fig. 20. In the sol-gel powder catalyst series, maxima in G/D values and carbon yields are obtained for the AT(2/6) sample. Increasing or decreasing the NH_4OH/TEOS ratio away from this optimum value results in losses for both the G/D ratio and carbon yield. In the case of the sol-gel microscale structured catalyst, the G/D value is as high as that of the best product, AT(2/6), from the powder catalyst series, but the carbon yield is much higher (24%). As anticipated, the open structure of the sol-gel microscale structured catalyst resulted in an enhanced SWCNT yield.

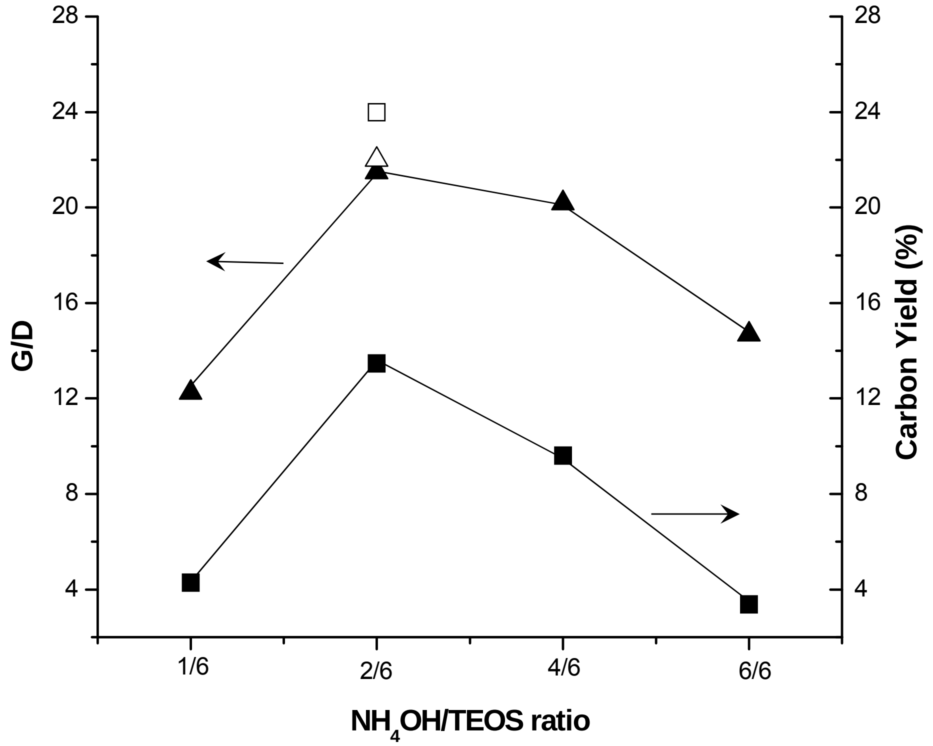

Figure 20: G/D ratios and carbon yields (%) of SWCNT grown onto four Co-Mo/SiO_2 powder catalysts with ammonia ratios from 1/6 to 6/6 (G/D ratios (▲) and carbon yield (%) (■)). G/D ratio and carbon yield (%) of SWCNT grow onto a micro-structured catalyst with an NH_4OH /TEOS ratio of 2/6 (G/D ratio (Δ) and carbon yield (%) (□)).

1.1.1.1.2.3- Electron microscopy

The TEM images in Figs. 21(a) to (c) confirm that the samples with NH_4OH/TEOS ratios from 2/6 to 6/6 display high selectivity towards SWCNT, as anticipated from the SWCNT selectivity showed by the Raman spectra. The TEM images also shown that the particle sizes of both the silica support and the Co-Mo moieties increase as the NH_4OH/TEOS ratio increases from 2/6 to 6/6.

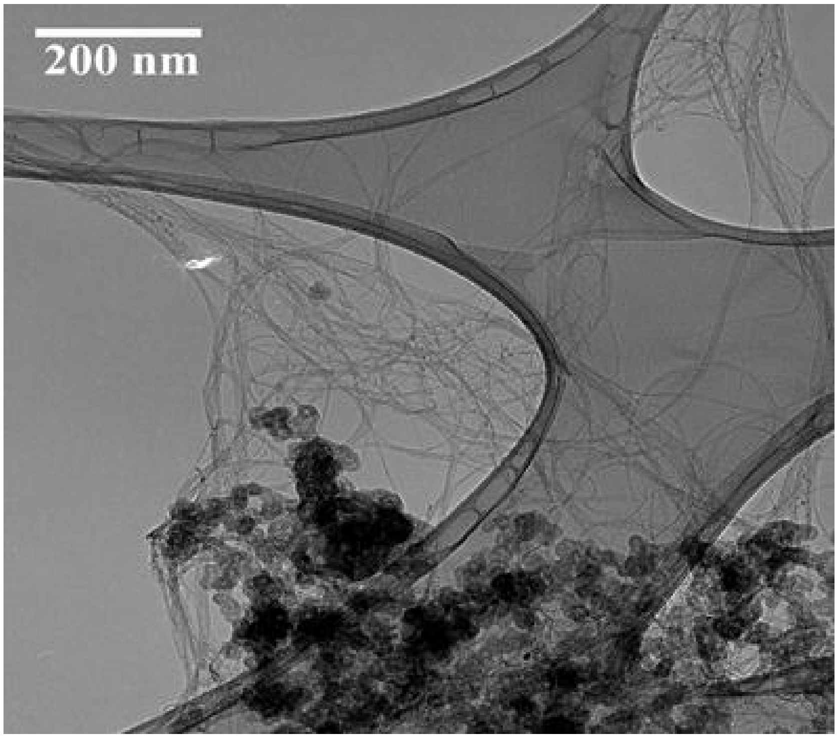

Figure 21(a): TEM image of SWCNT grown onto Co-Mo/SiO_2 powder catalyst with NH_4OH /TEOS ratio of 2/6.

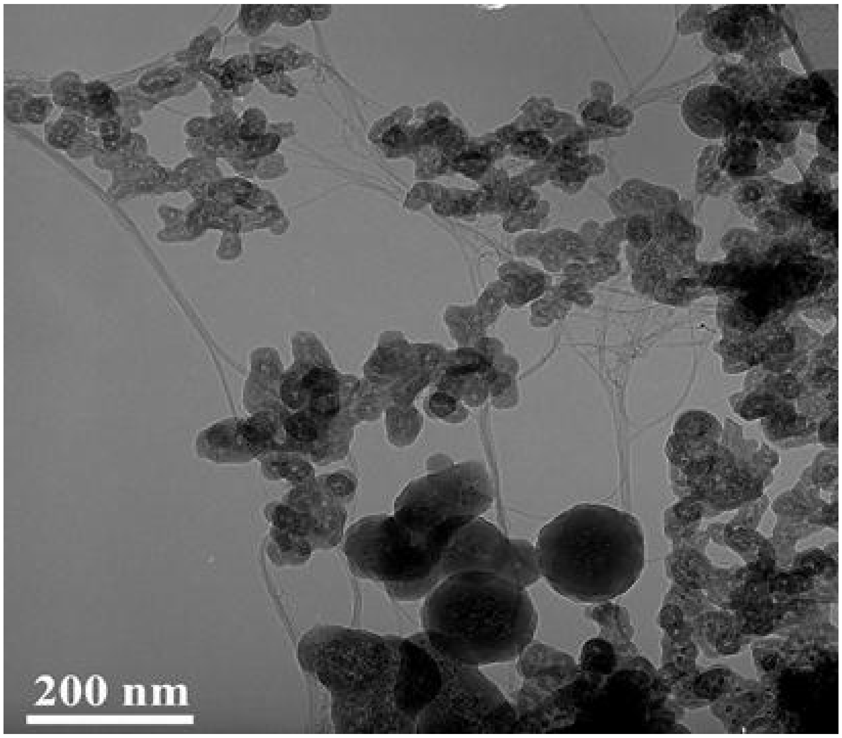

Figure 21(b): TEM image of SWCNT grown onto Co-Mo/SiO_2 powder catalyst with NH_4OH /TEOS ratio of 4/6.

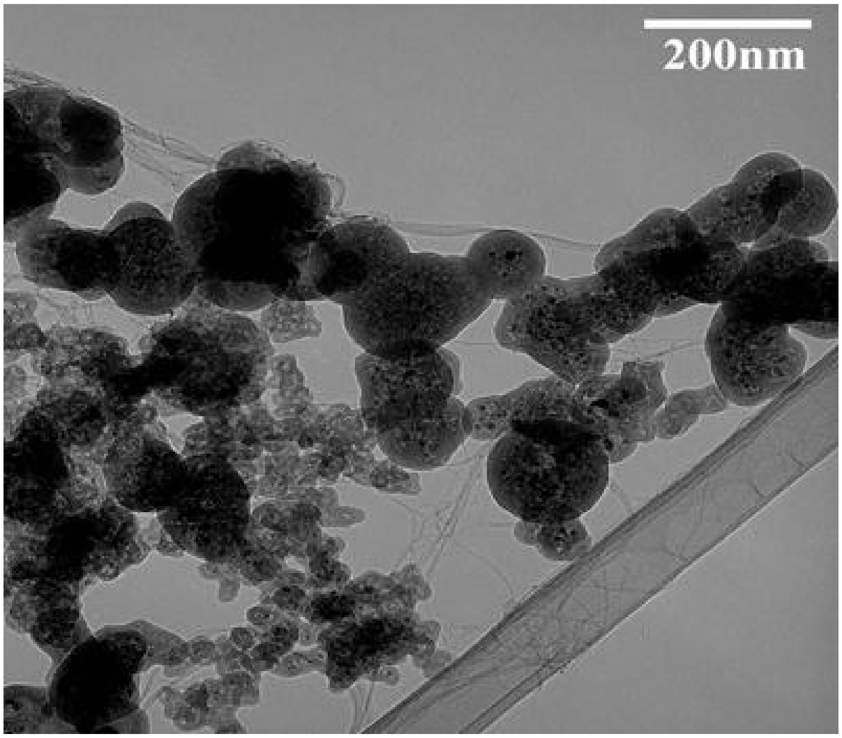

Figure 21(c): TEM image of SWCNT grown onto Co-Mo/SiO_2 powder catalyst with NH_4OH /TEOS ratio of 6/6.

Figure 22 shows an SEM image of SWCNT grown onto the microscale structured catalyst. It can be seen that the catalyst tubular shape is kept after reaction and that the nanotubes have free space to grow with much less hindrance than on the more compact structure present in the powder catalysts. As a result, the carbon yield is much higher on this open-structure catalyst than on the other catalysts.

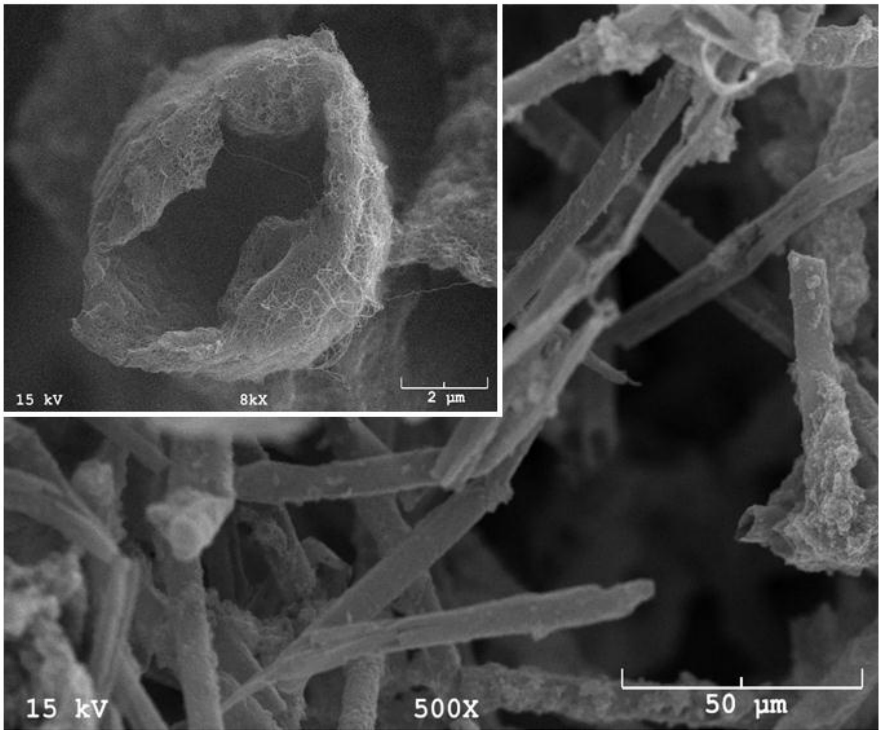

Figure 22: SEM image of the SWCNT grown onto Co-Mo/SiO_2 micro-structured catalyst with NH_4OH /TEOS ratio of 2/6.

1.1.1.1.2.4- Temperature programmed oxidation

TPO profiles of the nanotube product obtained over two catalysts with the same NH_4OH/TEOS ratio of 2/6, but prepared by either impregnation or the sol-gel method, are compared in Fig. 23(a). It must be noted that the TPOs are obtained on the as-produced nanotube product; that is, the sample still contains the Co-Mo/SiO_2 catalyst, which certainly may participate in the oxidation process. It is obvious that the oxidation temperatures for the samples prepared by using the sol-gel method with or without template appear at significantly higher temperatures than those on the impregnated catalyst.

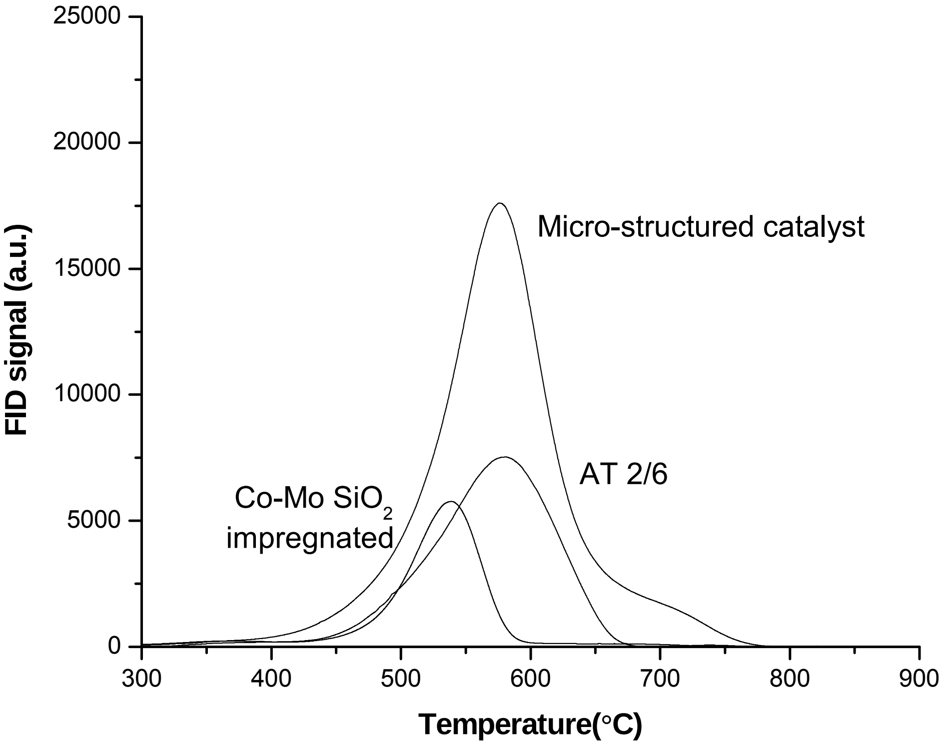

Figure 23(a): TPO profiles of SWCNT grown onto a Co-Mo/SiO$_2$ impregnated catalyst, onto a sol-gel powder catalyst and onto a micro-structured catalyst.

As discussed before [23], differences in oxidation temperature could indicate the presence of other forms of carbon, such as MWCNT or carbon fibers [24]. However, in this case detailed characterization results of the different products by other techniques do not support this explanation. That is, while the AT(2/6) and the microstructured samples have the highest oxidation temperatures, they show the highest selectivity toward SWCNT. Another possibility for the TPO shifts would be differences in the nanotube diameter. That is, the smaller diameter nanotubes are oxidized at lower temperatures. However, as shown above, while the sol gel catalysts do result in slightly larger diameter than the standard impregnated catalyst (i.e., standard CoMoCAT®), these differences are not so substantial to explain the large shifts in TPO. It is important to keep in mind that the position of the TPO peaks is greatly affected by the state of aggregation of the nanotubes and the morphology of the catalyst itself. The catalyst morphology and pore structure may affect the fraction of metal surface exposed, the insulating properties of the silica support, and the state of aggregation of the final product, which may affect the kinetics of the oxidation process. At the same time, external heat and mass transfer effects may play a role, and they can vary from one type of support to the other.

To further analyze these effects, two additional experiments were conducted. First, the heating ramp during the TPO analysis was varied. As shown in Fig. 23(b), when the TPO was conducted at a heating rate of 5 °C/min instead of the standard 10 °C/min, a slight shift to lower temperatures was observed. This shift might indicate a small effect of heat transfer limitations; however, the shift is much smaller than the significant differences observed among the various catalysts. Similarly, the second additional experiment, in which the powder catalyst (AT2/6) was physically diluted with silica (50-50%), did not show any significant effect. As shown in Fig. 23(b), diluting the catalyst in half essentially resulted in a peak of 50% lower intensity, without any significant shift in position. These experiments demonstrate that external heat and mass transfer effects have little influence, and therefore the differences observed in TPO should be related to the internal structure of each individual catalyst particle.

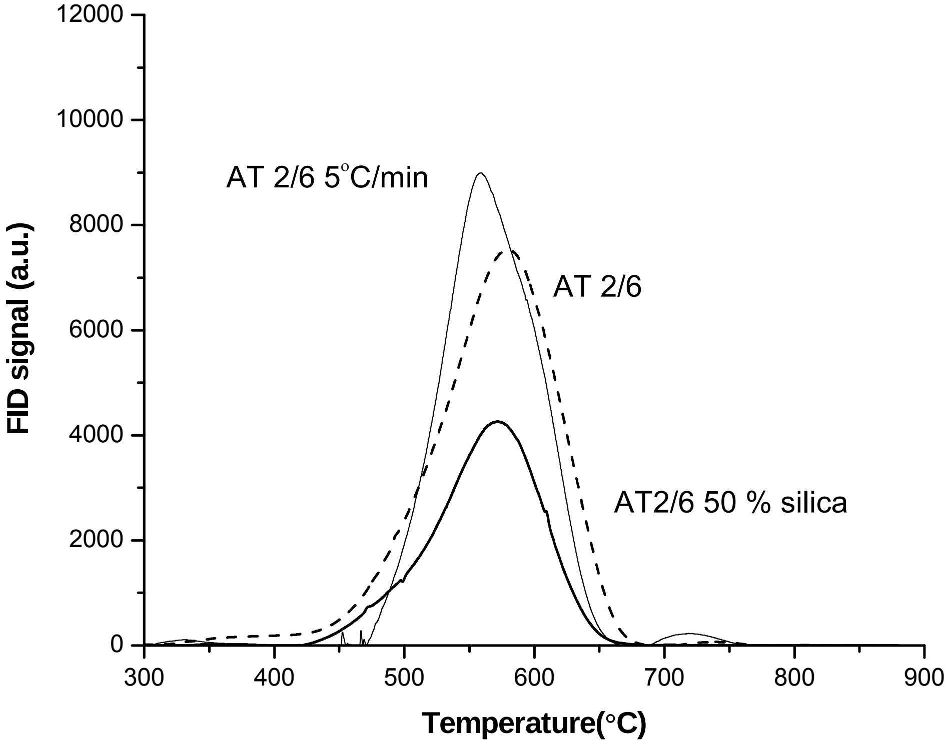

Figure 23(b): TPO profiles of SWCNT grown onto a Co-Mo/SiO_2 sol-gel powder catalyst oxidized at 5 °C/min, 10 °C/min and a 50%-50% SWCNT-silica mixture.

1.1.1.2 Impregnation

As a comparison, the selectivity and carbon yield of SWCNT obtained by using the sol-gel catalyst, was compared with the corresponding one synthesized by using the CoMoCAT® process.

1.1.1.2.1- Experimental

The CoMoCAT® catalyst preparation has been explained in previous publication [5-9,21,24,26,36]. Briefly, $Co(NO_3)_2 \cdot 6H_2O$ and $(NH_4)_6Mo_7O_{24} \cdot 4H_2O$ (Sigma Aldrich) were impregnated by incipient wetness impregnation (IWI) onto a high-surface area silica (HiSil 210, S.A. 150 m^2/g P.V. 1.1 ml/g), with a total metal loading of 2 wt % and a Co-

Mo molar ratio of 1/3. The wet powder was then dried at 110 °C for 12 hours and finally calcined at 500 °C for 3 h.

The catalyst samples were previously reduced at 500 ºC for 30 min under H_2 in a quartz reactor placed in a vertical furnace. After reduction, H_2 was switched to He to reach the reaction temperature (750 ºC). Later, the carbon source (CO) was flowed over the reduced catalyst for a certain amount of time, while keeping the temperature at 750 ºC. The system was finally cooled down under He flow.

1.1.1.2.2- Results

Our group has previously published several papers related to the selectivity and carbon yield of SWCNT produced by the CoMoCAT® process [5-9,21,24,24,36]. As mentioned by Tan et al. [25], the typical absorption spectrum for the CoMoCAT® SWCNT shows high SWCNT and (n,m) selectivity as it can be seen in Fig. 24.

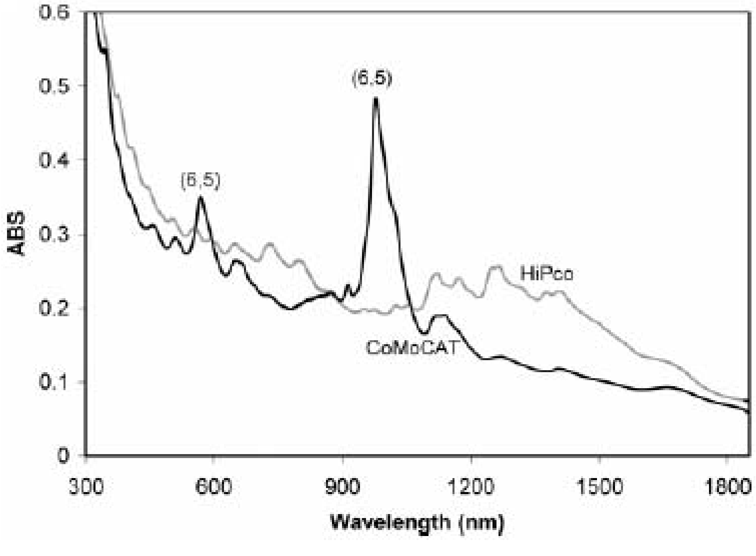

Figure 24: OA spectrum of SWCNT produced by CO disproportionation on CoMoCAT®. [25]

Raman scattering has also been used to characterize the SWCNT selectivity of this product. Monzon et al. [26] have shown that the G/D ratios for this SWCNT type is very high, meaning high SWCNT selectivity as it can be seen in Fig. 25.

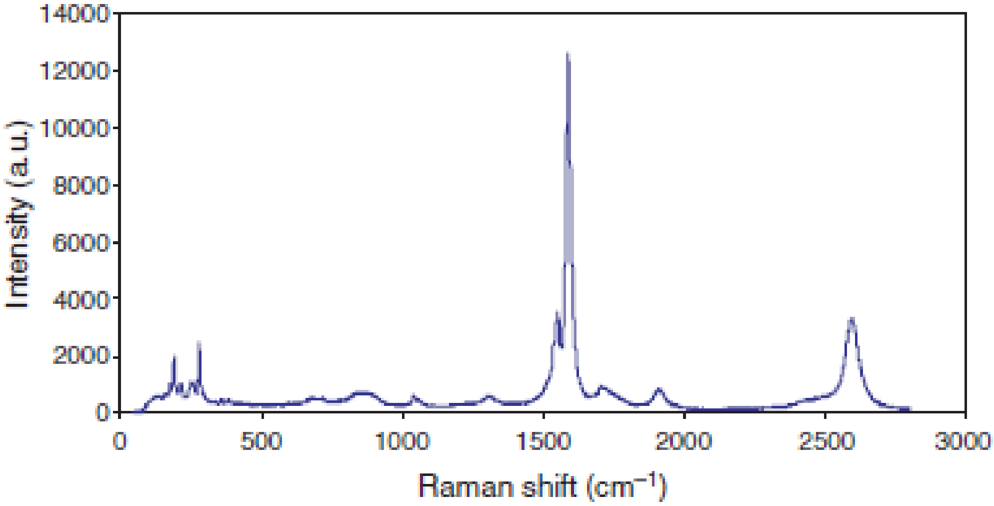

Figure 25: Raman scattering spectrum of SWCNT produced by CO disproportionation on CoMoCAT®. [26]

The typical carbon yield obtained with this material can vary between 2-4 % depending on the reaction conditions.

Figures 26(a) and (b) show SEM and TEM images of this material. It can be seen that the SWCNT selectivity, as inferred by the previous analytical techniques, is very high.

Figure 27 shows an Atomic Force Microscopy (AFM) image of this SWCNT material confirming the narrow distribution in diameter.

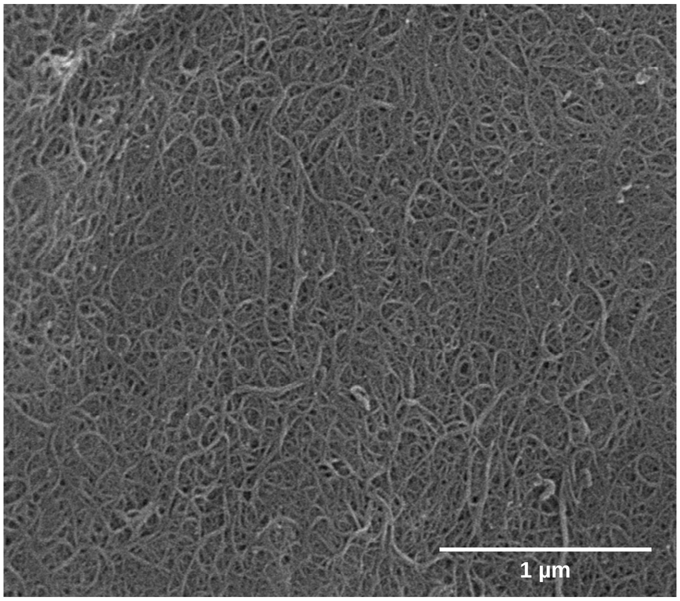

Figure 26(a): SEM image of SWCNT produced by CO disproportionation on CoMoCAT®. Courtesy of SouthWest NanoTechnologies.

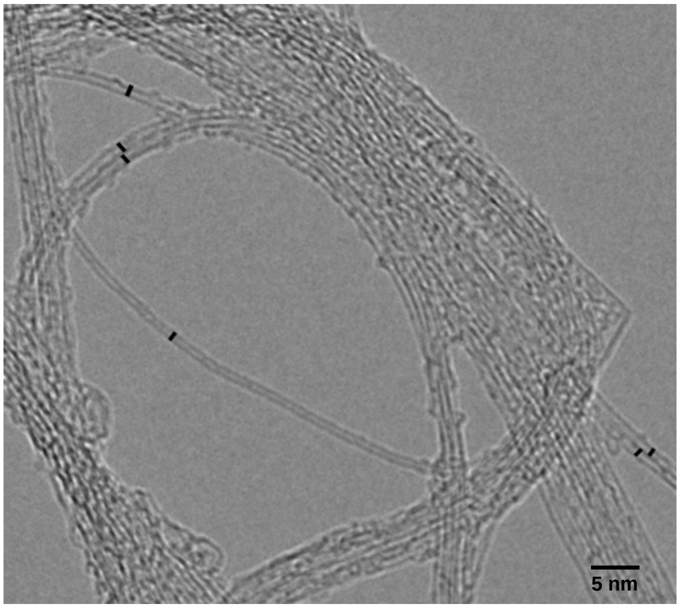

Figure 26(b): TEM image of SWCNT produced by CO disproportionation on CoMoCAT®. Courtesy of SouthWest NanoTechnologies.

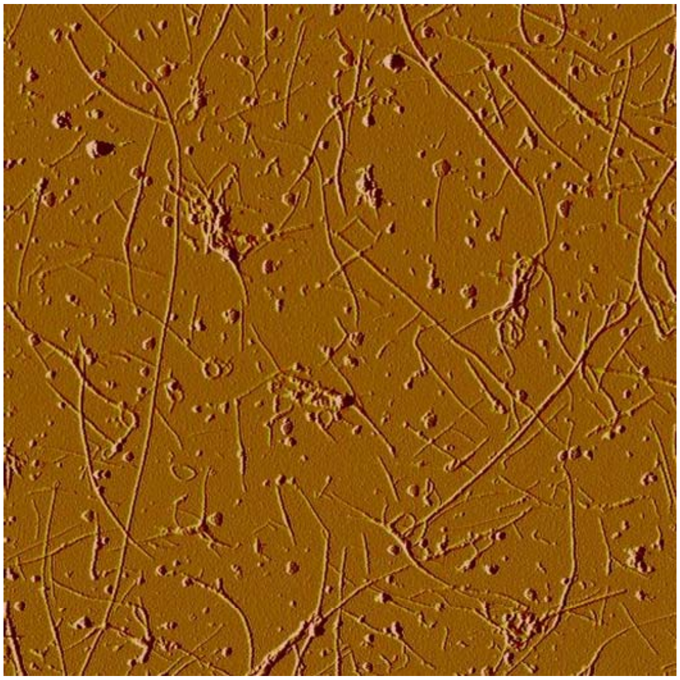

Figure 27: AFM image of SWCNT produced by CO disproportionation on CoMoCAT®. 5x5 um. Courtesy of SouthWest NanoTechnologies.

1.1.2- Multi Wall Carbon Nanotubes - Co-Mo (1:3) - silica/alumina - carbon monoxide or ethylene as carbon sources.

The aiming of producing MWCNT is not only that they are less expensive than SWCNT, but also the fact that they are more suitable than SWCNT for certain applications. Among all the uses, MWCNT have been primarily recognized as an electrically conducting component used in composites [27,28]. MWCNT can be also used as scanning probes on microscope tips for scanning tunneling microscope (STM) and AFM due to their ability to conduct. Another application for aligned MWCNT is as biosensors [27,29]. As field emission sources, MWCNT can be used for flat panel displays, lamps, and X-ray and microwave generators [27].

Gojny et al. [30] have shown that dispersability and mechanical reinforcement properties are compromised. They have shown that, while the mechanical reinforcement properties are better when the number of walls is smaller, the dispersability on the other hand is worse.

Since for different applications, MWCNT with different structural properties are required, it is desirable to control their morphology. Even though previous studies related to the catalytic parameters that affect the MWCNT structure have been done [31], controlled morphology studies are still needed.

$Co/\gamma\text{-}Al_2O_3$ and $Co\text{-}Mo/\gamma\text{-}Al_2O_3$ [32-35] catalysts have been widely studied since they are the most important catalysts used for the hydrodesulfuration of petroleum in the refinery industry. In this case, these catalysts are used to produce CNT. In this work, not only the activity toward CNT is studied [5-9,21,24,25,36], but also the metal-support interaction using different alumina supports. It has been shown in previous publications that the metals can either diffuse into the support matrix or be buried when the catalyst is synthesized. This phenomenon affects the CNT selectivity and carbon yield [36].

Our group has a vast experience on producing SWCNT by using catalysts composed of cobalt and an excess of molybdenum supported on high surface area silica. In order to produce MWCNT, it will be ideal to use all this knowledge to be able to control their structure. For this reason, different variations have been tried starting from the regular catalysts formulation but changing the carbon source and the support to finally arrive to a new formulation that shows high activity and selectivity to MWCNT as it will be shown in the next section.

This section shows the transition between the regular catalyst formulation and typical reaction conditions to an optimized formulation and reaction conditions.

1.1.2.1- Co-Mo (1:3) - silica - ethylene as carbon source.

As mentioned before, these catalysts and reaction conditions are a transition between the original formulation to obtain high SWCNT selectivity and the desirable formulation to obtain high MWCNT selectivity with controlled structure.

Keeping the cobalt to molybdenum molar ratio constant and equal to 1:3 and silica as support, the first experiment consisted on changing the carbon source from carbon monoxide to ethylene. The second set of experiments was done by changing the silica support by commercial alumina while keeping the rest of the parameters constant.

1.1.2.1.1- Experimental

For the first set of experiments two different catalysts were prepared using cobalt and molybdenum as precursors. One of the samples was prepared by IWI onto a high-surface area silica (HiSil 210, S.A. 150 m^2/g P.V. 1.1 ml/g), with a total metal loading of 2 wt % and a Co-Mo molar ratio of 1/3, as it was explained in section 1.1.1.2.1. The second sample was prepared by the sol-gel method as it was explained in section 1.1.1.1.2.

For the second set of experiments, two other catalysts were prepared using cobalt and molybdenum as precursors. One of the sample was prepared by incipient wetness impregnation (IWI) onto γ-alumina (aluminum oxide, gamma phase, 255 m^2/g, 1.14 ml/g), with a total metal loading of 2 wt % and a Co-Mo molar ratio of 1/3 as it was explained in section 1.1.1.2.1. The second sample was prepared by the sol-gel method.

In order to grow CNT, both samples were reduced under H_2 at 500 °C for 30 min, then the temperature was raised to 700 °C under N_2 and a 30 % C_2H_4/N_2 mixture was fed for 20 min. The reactor was finally cool down under N_2 to room temperature.

1.1.2.1.2- Results

SEM was used to visualize the reaction products. Figures 28(a) and (b) correspond to the product obtained by using Co-Mo (1:3) supported on silica and using ethylene as carbon source. As it can be seen, none of the catalysts was highly active and selective towards MWCNT. In the particular case of the sample prepared by the sol-gel method, it can be seen that mostly amorphous carbon was formed.

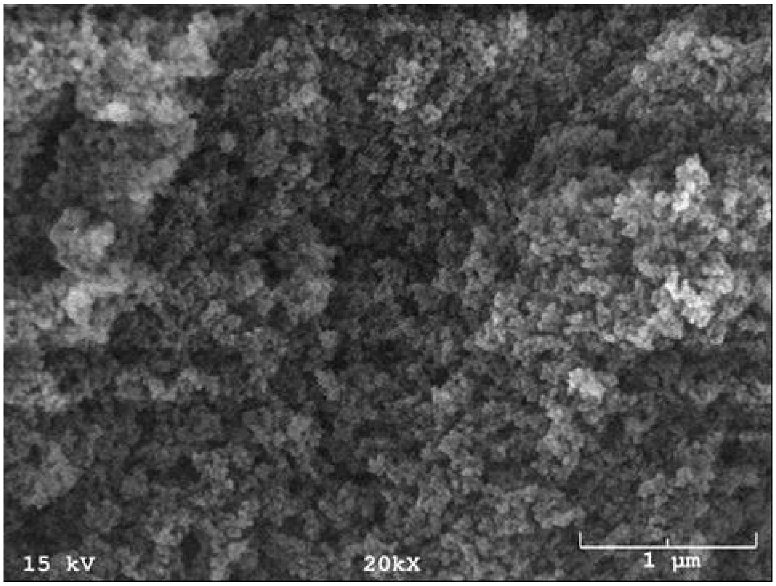

Figure 28(a): SEM images of the as-produced CNT growth onto bimetallic (Co-Mo 1:3) catalysts. Co-Mo/SiO_2. Impregnation. Carbon source to synthesize the CNT: ethylene.

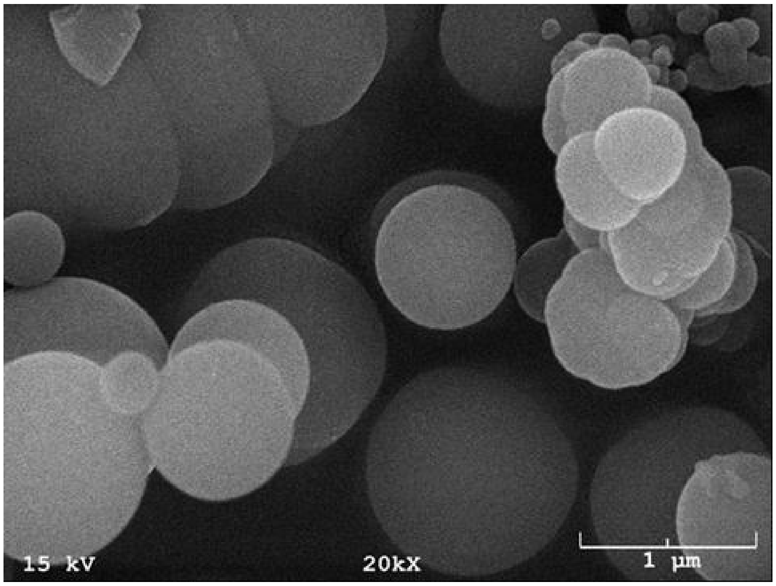

Figure 28(b): SEM images of the as-produced CNT growth onto bimetallic (Co-Mo 1:3) catalysts. Co-Mo/SiO_2. Sol-gel. Carbon source to synthesize the CNT: ethylene.

Raman scattering was also conducted and it is worth mentioning that in both cases the spectra showed highly disordered carbon structures.

It is also important to explain that when these catalysts formulation was used, the minimum reaction temperature to have activity was 700 ° C.

As with the previous formulation, SEM was used to visualize the reaction products obtained by using Co-Mo (1:3) supported on alumina and using ethylene as carbon source. Figures 29(a) and (b) show that the activity was very low. However, by using Raman scattering, these catalysts showed more selectivity towards MWCNT that in the previous ones. Therefore, the alumina support seems to be making the catalysts more selective towards the desirable carbon product. For this reason in the next section different aluminum materials used as supports will be studied and compared. In order to increase the yield, the Co-Mo ratio will be also modified from 1:3 to 3:1.

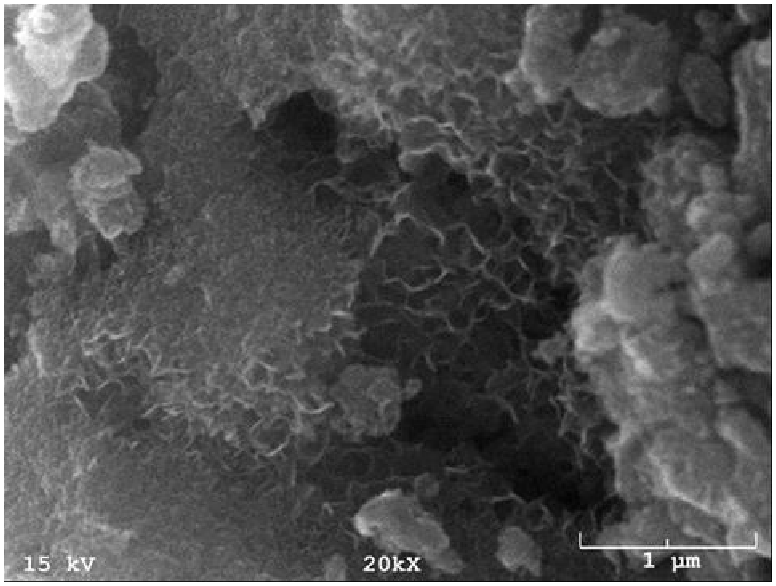

Figure 29(a): SEM images of the as-produced CNT growth onto bimetallic (Co-Mo 1:3) catalysts. Co-Mo/γ-Al_2O_3. Impregnation. Carbon source to synthesize the CNT: ethylene.

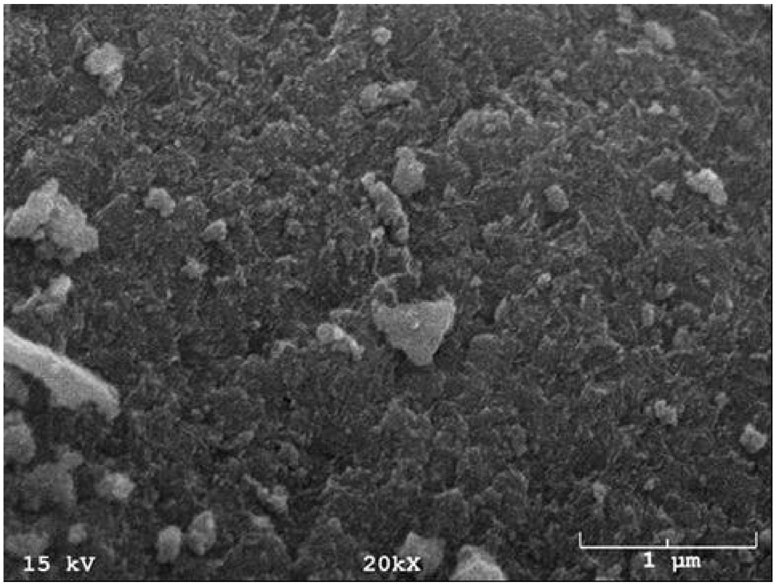

Figure 29(b): SEM images of the as-produced CNT growth onto bimetallic (Co-Mo 1:3) catalysts. Co-Mo/γ-Al_2O_3. Sol-gel. Carbon source to synthesize the CNT: ethylene.

1.1.3- Multi Wall Carbon Nanotubes - Co-Mo (3:1) - alumina/silica - carbon monoxide or ethylene as carbon sources.

As it was mentioned before, in this section studies related to catalysts composed of Co-Mo with an excess of cobalt are shown. The supports used were mostly aluminum materials [37-39] and the carbon source was ethylene. As a comparison, the same formulation supported on silica and/or using carbon monoxide as carbon source are included.

1.1.3.1- Experimental

Two bimetallic catalysts (cobalt-molybdenum, 3:1 molar ratio) were prepared with 2 wt % of metal loading on different alumina supports by IWI. Another two samples, in this case monometallic (cobalt), with the same cobalt loading as the bimetallic samples were prepared for comparison. The metal precursors used were $Co(NO_3)_2 \cdot 6H_2O$ and $(NH_4)_6Mo_7O_{24} \cdot 4H_2O$ (Sigma Aldrich), and the supports were γ-Al_2O_3 (Sigma Aldrich) and $Al(OH)_3$ (gibbsite, Spectrum). The catalysts were named $Co\text{-}Mo_{\gamma\text{-}Al_2O_3}$, $Co\text{-}Mo_{Al(OH)_3}$, $Co_{\gamma\text{-}Al_2O_3}$ and $Co_{Al(OH)_3}$. All the samples were dried for 8 h at 130 °C and then calcined at 450 °C for 3 h under air. A series of monometallic cobalt catalysts varying the metal loading supported on either $Al(OH)_3$ or γ-Al_2O_3 was also synthesized.

As a comparison, both monometallic and bimetallic catalysts were prepared using SiO_2 (Hisil 210, PPG) as support. They were named $Co\text{-}Mo_{SiO_2}$ and Co_{SiO_2}. To further study the metal-support interaction when silica is used as support, two different samples in which the precursors were impregnated (IWI) simultaneously (Co-$Mo_{1:3\text{-}SiO_2\ SIM}$) or sequentially (Co-$Mo_{1:3\text{-}SiO_2\ SEQ}$) with a molar ratio of 1:3 were synthesized.

The bimetallic catalysts were placed in a vertical quartz reactor and pre-reduced under H_2 at 500 °C for 30 min. Once the reaction temperature was reached (700 °C) under He, the carbon source was fed (ethylene or carbon monoxide) for 20 min. The final product (as-produced CNT) was cooled down under He/N_2 to room temperature.

SEM, TEM and TPO with the same characteristics and experimental conditions described before were used to characterize the products obtained.

1.1.3.2- Results

1.1.3.2.1- Scanning electron microscopy

As it was mentioned before, the bimetallic catalysts were used to grow CNT by using different carbon sources. Figures 30(a) to (c) shows the SEM images of the as-produced CNT samples synthesized by using ethylene as carbon source. It can be seen that both the CNT selectivity and carbon yield differ for the different catalysts.

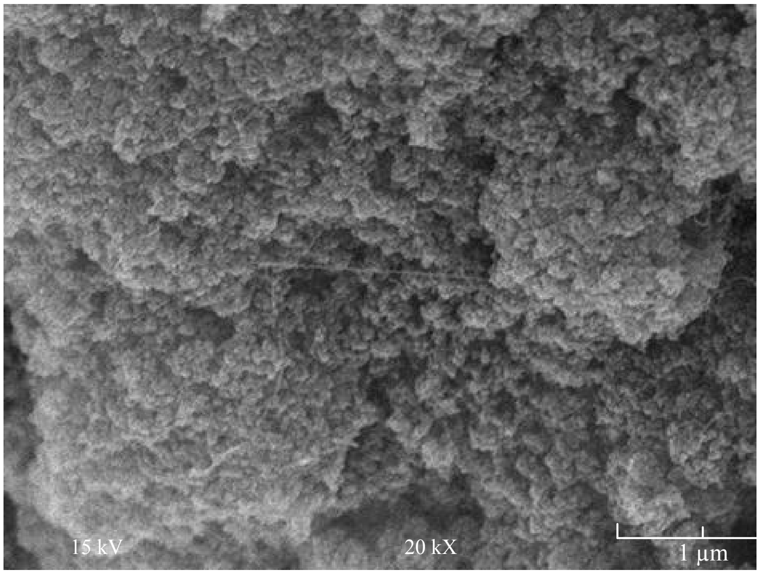

Figure 30(a): SEM images of the as-produced CNT growth onto bimetallic (Co-Mo 3:1) catalysts. Co-Mo_{SiO_2}. Carbon source to synthesize the CNT: ethylene.

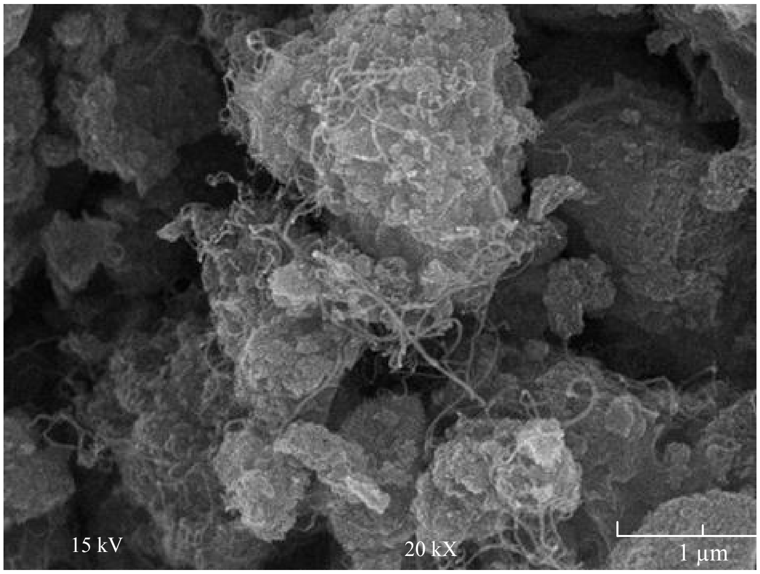

Figure 30(b): SEM images of the as-produced CNT growth onto bimetallic (Co-Mo 3:1) catalysts. Co-$Mo_{\gamma\text{-}Al_2O_3}$. Carbon source to synthesize the CNT: ethylene.

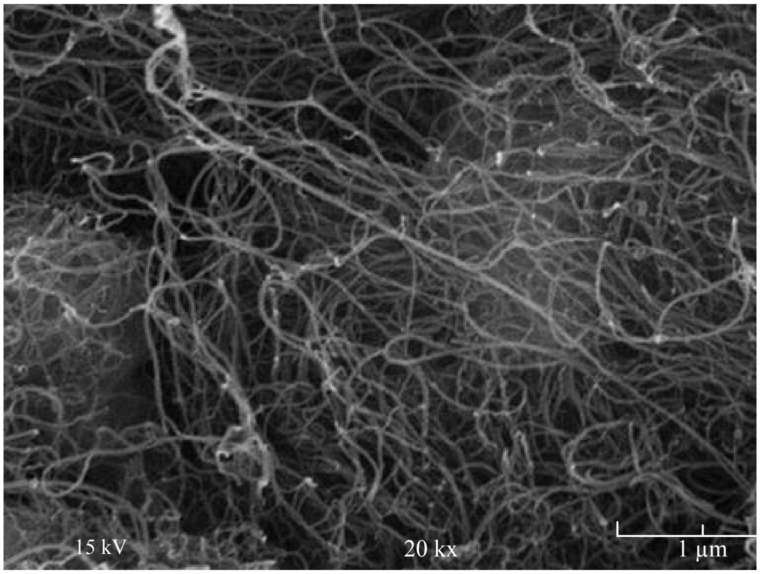

Figure 30(c): SEM images of the as-produced CNT growth onto bimetallic (Co-Mo 3:1) catalysts. Co-Mo$_{Al(OH)_3}$. Carbon source to synthesize the CNT: ethylene.

Figures 31(a) to (c) show the SEM images of the as-produced CNT samples synthesized by using carbon monoxide as carbon source. In both cases, either using ethylene or carbon monoxide, it can be seen that when cobalt and molybdenum are supported on $Al(OH)_3$, the carbon yield [40] seems to be the highest. It is important to mention that these SEM images are used to visualize the samples and not to measure the CNT selectivity and carbon yield.

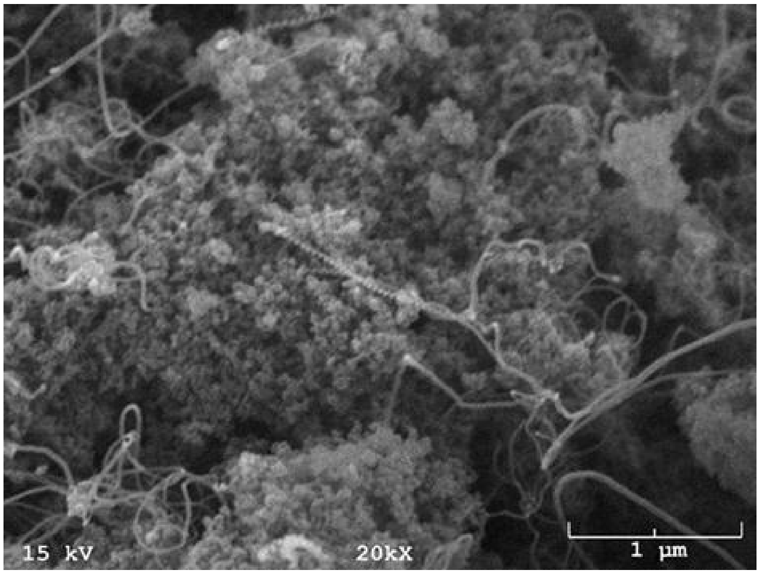

Figure 31(a): SEM images of the as-produced CNT growth onto bimetallic (Co-Mo 3:1) catalysts. Co-Mo$_{SiO_2}$. Carbon source to synthesize the CNT: carbon monoxide.

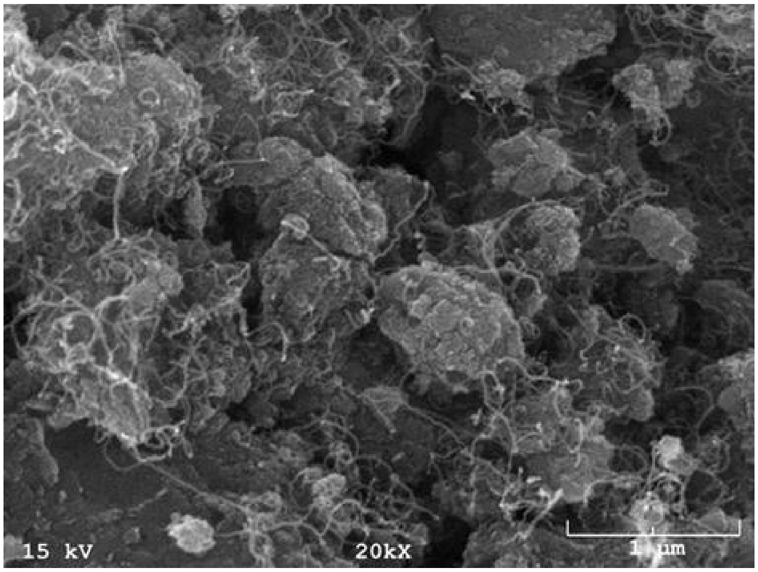

Figure 31(b): SEM images of the as-produced CNT growth onto bimetallic (Co-Mo 3:1) catalysts. Co-Mo$_{\gamma\text{-}Al_2O_3}$. Carbon source to synthesize the CNT: carbon monoxide.

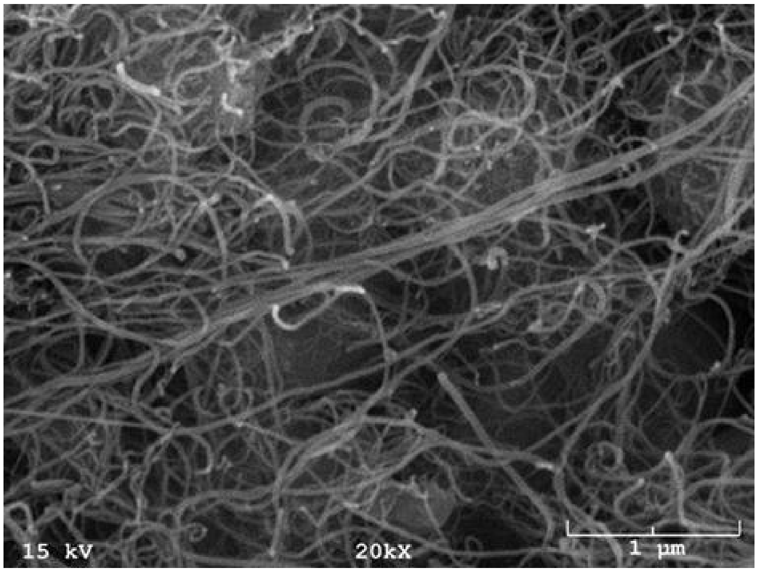

Figure 31(c): SEM images of the as-produced CNT growth onto bimetallic (Co-Mo 3:1) catalysts. Co-Mo$_{Al(OH)_3}$. Carbon source to synthesize the CNT: carbon monoxide.

1.1.3.2.2- Transmission electron microscopy

Figures 32(a) to (c) and 33(a) to (c) show TEM images obtained from the as-produced CNT grown onto the bimetallic catalysts using ethylene or carbon monoxide as carbon sources, respectively. It can be seen that the overall CNT selectivity and carbon yield were always the best when the support used was $Al(OH)_3$. The images corresponding to the CNT grown onto the catalyst conformed of Co-Mo on, either γ-Al_2O_3 or SiO_2, shown that most of the as-produced material is catalyst and that the CNT seem to be thin and defective. It is also important to mention that the Fig. 33(a), corresponding to CNT grown onto Co-Mo/SiO_2 by using carbon monoxide as carbon source, seems to show that the CNT selectivity and carbon yield similar to the ones obtained when the CNT were grown onto Co-Mo/$Al(OH)_3$. However, as it has been seen doing TPO analysis, the yield is the lowest (Figs. 34(a) and (b)).

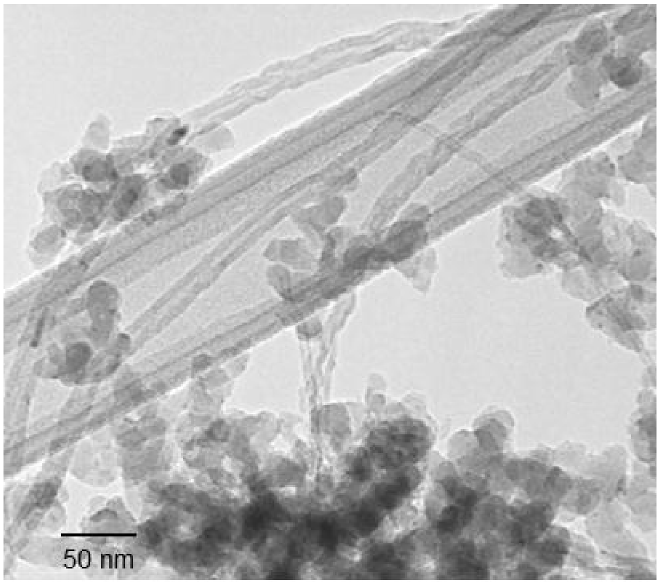

Figure 32(a): TEM images of the as-produced CNT growth onto bimetallic (Co-Mo 3:1) catalysts. Co-Mo$_{SiO_2}$. Carbon source to synthesize the CNT: ethylene.

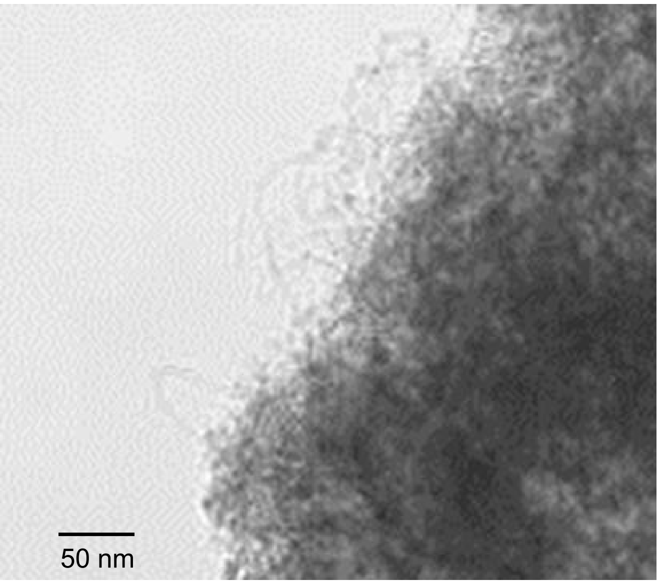

Figure 32(b): TEM images of the as-produced CNT growth onto bimetallic (Co-Mo 3:1) catalysts. Co-Mo$_{\gamma\text{-}Al2O3}$. Carbon source to synthesize the CNT: ethylene.

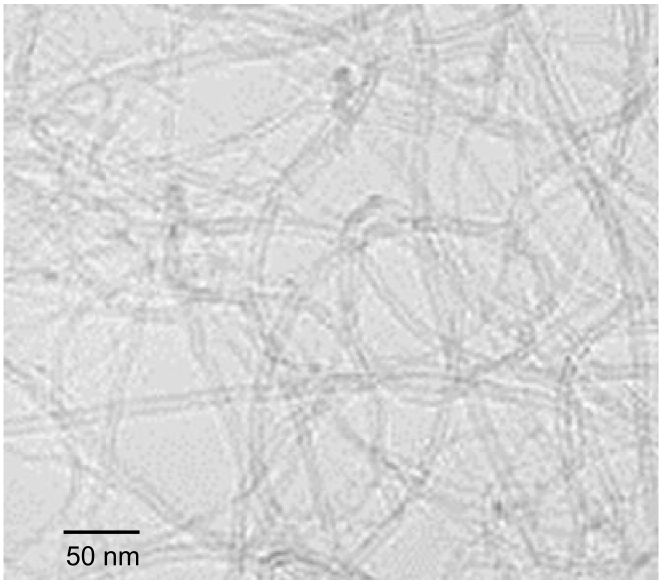

Figure 32(c): TEM images of the as-produced CNT growth onto bimetallic (Co-Mo 3:1) catalysts. Co-Mo$_{Al(OH)3}$. Carbon source to synthesize the CNT: ethylene.

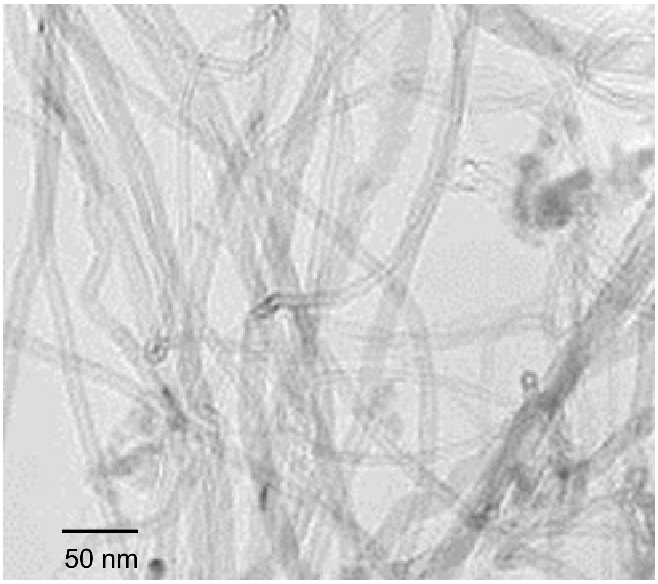

Figure 33(a): TEM images of the as-produced CNT growth onto bimetallic (Co-Mo 3:1) catalysts. Co-Mo$_{SiO2}$. Carbon source to synthesize the CNT: carbon monoxide.

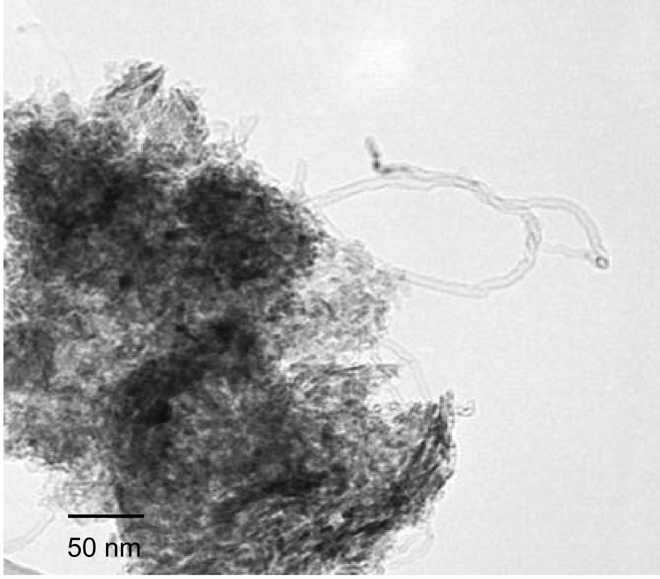

Figure 33(b): TEM images of the as-produced CNT growth onto bimetallic (Co-Mo 3:1) catalysts. Co-$Mo_{\gamma\text{-}Al2O3}$. Carbon source to synthesize the CNT: carbon monoxide.

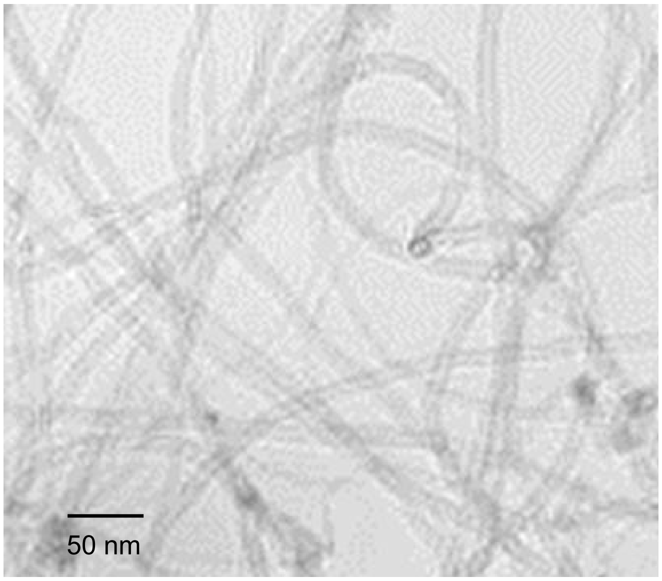

Figure 33(c): TEM images of the as-produced CNT growth onto bimetallic (Co-Mo 3:1) catalysts. Co-$Mo_{Al(OH)3}$. Carbon source to synthesize the CNT: carbon monoxide.

1.1.3.2.3- Temperature programmed oxidation

Figures 34(a) and (b) show the TPO profiles of the as-produced CNT grown by decomposition of different carbon sources (ethylene or carbon monoxide) onto the bimetallic catalysts. As an overall impression it can be seen that when the carbon source used was ethylene (Fig 34(a)), the oxidation temperatures were lower and the carbon content is slightly higher than in the case were carbon monoxide was used. Comparing the carbon yields when the different supports are used, it can be seen that it decreases in this way Al(OH)$_3$>γ-Al$_2$O$_3$> SiO$_2$.

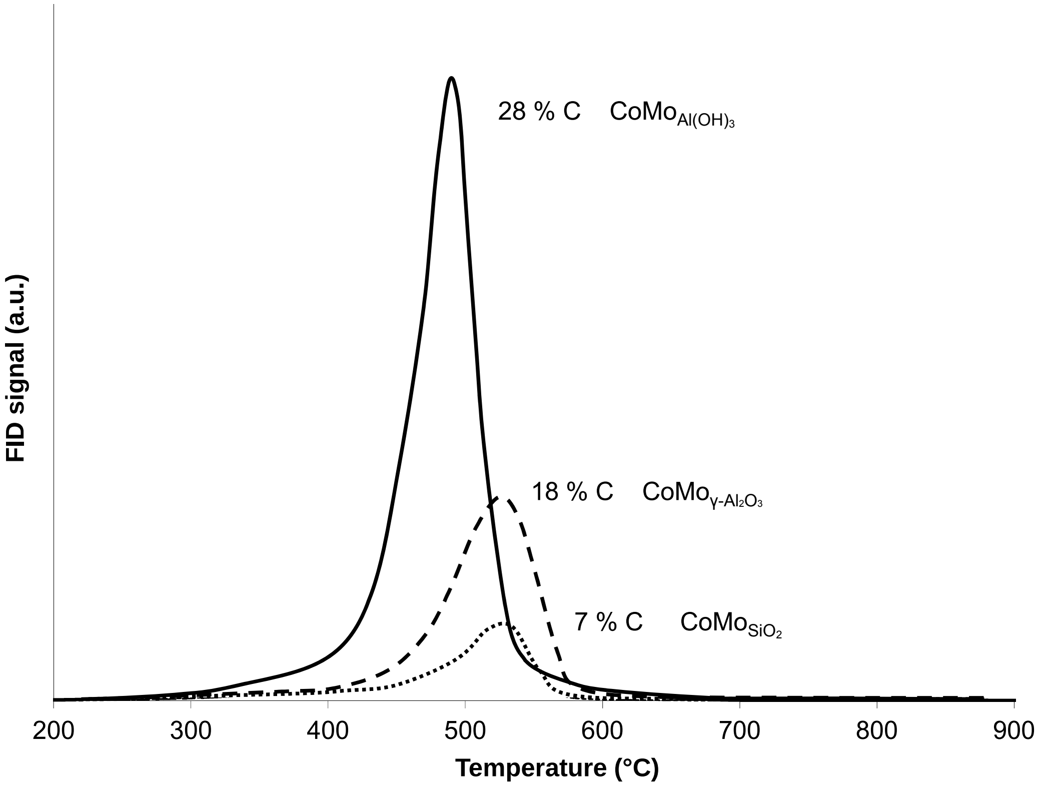

Figure 34(a): TPO profiles of the CNT grown onto bimetallic (Co-Mo 3:1) catalysts. Carbon source to synthesize the CNT: ethylene.

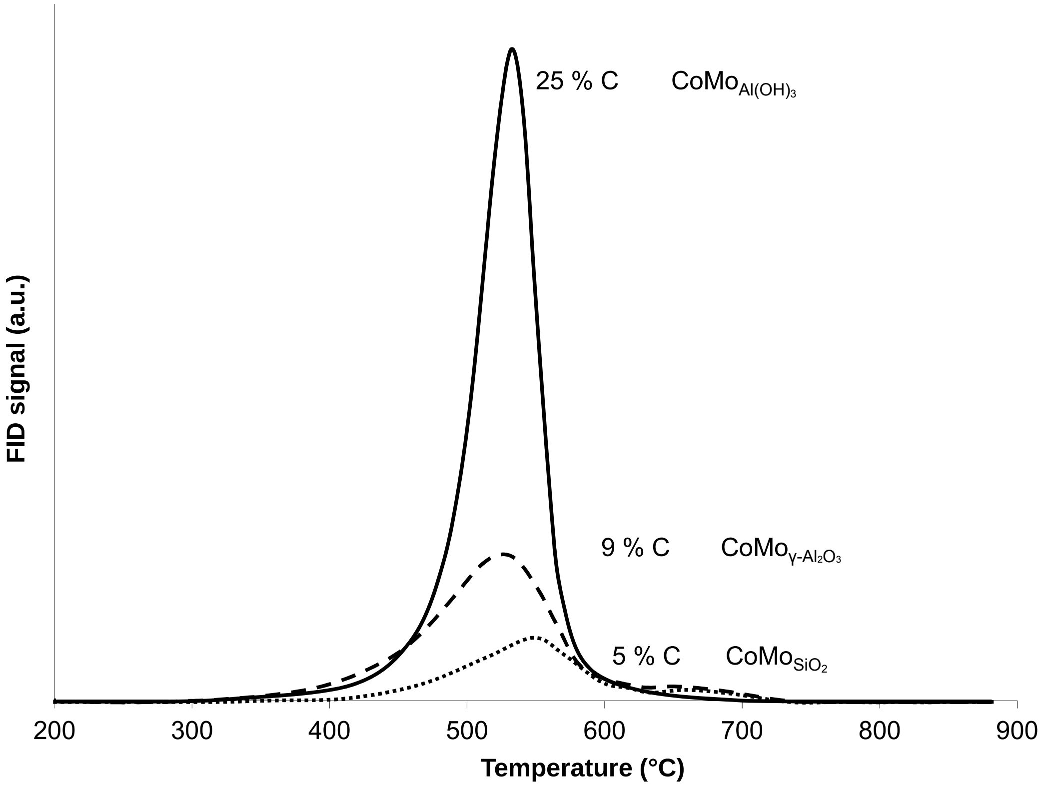

Figure 34(b): TPO profiles of the CNT grown onto the bimetallic (Co-Mo 3:1) catalysts. Carbon source to synthesize the CNT: carbon monoxide.

1.1.3.2.4- CNT diameter distribution of as-produced samples

TEM has been used to obtain the external diameter distribution of CNT grown by feeding different carbon sources onto the same catalyst. It is important to mention that these results were obtained from the bimetallic catalysts prepared using $Al(OH)_3$ as support because they had the highest carbon yield allowing to have a better statistical result.

Figure 35(a) shows the distribution when ethylene was used as carbon source and Fig. 35(b) shows the distribution when carbon monoxide was used as carbon source. If the distributions are compared, it can be seen that with ethylene the average diameter is around 11 nm, while in the case of carbon monoxide, two different sizes are seem to be formed, 7 nm and 11 nm.

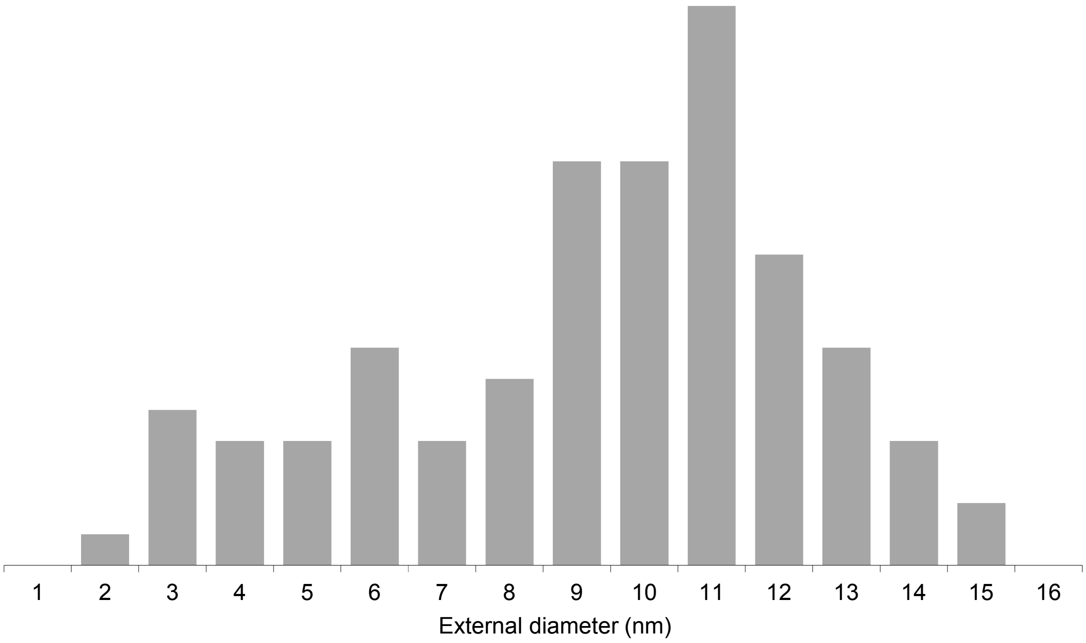

Figure 35(a): External diameter distribution of the as-produced CNT growth onto Co-Mo$_{Al(OH)_3}$ by using ethylene as carbon source.

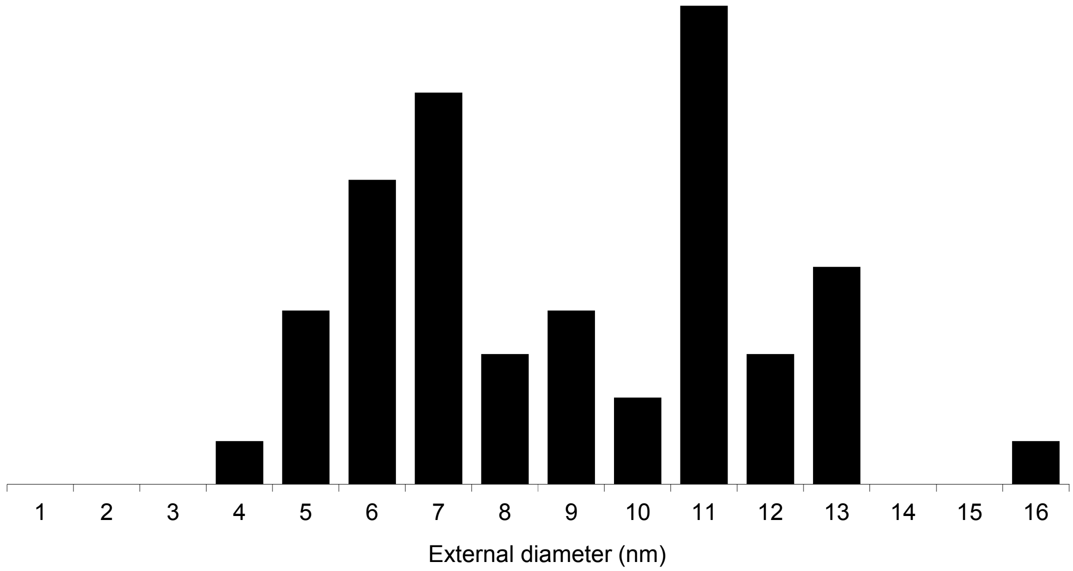

Figure 35(b): External diameter distribution of the as-produced CNT growth onto Co-Mo$_{Al(OH)3}$ by using carbon monoxide as carbon source.

As it was mentioned before, while the CNT's external diameter seems to have uniform distribution when using ethylene as carbon source, it shows dual distribution when carbon monoxide was used as carbon source. This is in agreement with the results obtained from the "same spot-TEM" analysis shown in chapter 2. Carbon monoxide might be reducing the cobalt and, thus, a distribution of cobalt cluster sizes might be forming leading to a wider distribution of CNT diameters. On the other hand, ethylene did not show any reducing effects leading to more uniform metal cluster sizes. Though, a more uniform CNT distribution is expected.

1.2- Conclusions

It was shown that the sol-gel preparation method has versatility to change the selectivity and carbon yield of the SWCNT produced. Different ammonia concentrations in the preparation of the sol-gel samples lead to catalysts with a variety of performances. It has been seen that extremes of ammonia concentration are detrimental to the selectivity and carbon yield of the SWCNT synthesized.

It has also been shown that the production of MWCNT by tailoring Co-Mo supported catalysts that were primarily selective towards SWCNT was successful. MWCNT with controlled structure and yield have been produced by adjusting the metal-support and gas-support interactions. It has been seen that bimetallic Co-Mo catalysts with excess cobalt supported on aluminum hydroxide had the best performance.

1.3- References

[1]- Qin L.C., CVD synthesis of carbon nanotubes, *J. Mater. Sci. Lett.*, **1997**, 16, 457.

[2]- Lewis I.R., Edwards H.G.M., Handbook of Raman Spectroscopy, Marcel Dekker, **2001**.

[3]- Dresselhaus M.S., Dresselhaus G., Saito R., Jorio A., Raman Spectroscopy of carbon nanotubes, *Phys. Rep.*, **2005**, 409, 47.

[4]- Kataura H., Kumazawaa Y., Maniwaa Y., Umezub I., Suzuki S., Ohtsuka Y., Achiba Y., Optical properties of single-wall carbon nanotubes, *Synthetic Metals*, **1999**, 103, 2555.

[5]- Resasco D.E., Kitiyanan B., Harwell J.H., Alvarez W., Method of producing carbon nanotubes, U.S. Patent No. 6333016, **2001**.

[6]- Alvarez W.E., Pompeo F., Herrera J.E., Balzano L., Resasco D.E., Characterization of single-walled carbon nanotubes (SWCNTs) produced by CO disproportionation on Co-Mo catalysts, *Chem. Mater.*, **2002**, 14, 4, 1853.

[7]- Resasco D.E., Alvarez W.E., Pompeo F., Balzano L., Herrera J.E., Kitiyanan B., Borgna A., A scalable process for production of single-walled carbon nanotubes (SWCNT) by catalytic disproportionation of CO on a solid catalyst, *J. Nanopart. Res.*, **2002**, 4,1-2, 131.

[8]- Resasco D.E., Herrera J.E., Balzano L., Decomposition of carbon-containing compounds on solid catalysts for single-walled nanotubes production, *J. Nanosci. Nanotechol.*, **2004**, 4, 4, 398.

[9]- Herrera J.E., Resasco D.E., In situ TPO/Raman to characterize single-walled carbon nanotubes, *Chem. Phys. Lett.*, **2003**, 376,3-4, 302.

[10]- Meille V., Review on methods to deposit catalysts on structured surfaces, *Appl. Catal. A*, **2006**, 315, 1.

[11]- Samanta S., Laha S.C., Mal N.K., Bhaumik K., Co(III)-containing mesoporous silica as an efficient catalyst in selective dihydroxilation of cyclohexene, *J. Mol. Catal. A*, **2004**, 222, 235.

[12]- Delgado M.R., Arean C.O., Surface characterization of gallia-silica prepared by a sol-gel method, *J. Mater. Sci. Lett*, **2003**, 22, 783.

[13]- Pecchi G., Reyes P., Concha I., Fierro J.L.G., Methane combustión on Pd/SiO_2 sol gel catalysts, *J. Catal.*, **1998**, 179, 309.

[14]- Maione A., Devillers M., Solid solutions of Ni and Co molybdates in silica dispersed and bulk catalysts prepared by sol-gel and citrate methods, *J. Sol. State Chem.*, **2004**, 177, 2339.

[15]- Klein L.C., Sol-gel processing of silicates, *Ann. Rev. Mater. Sci.*, **1985**, 15, 227.

[16]- Henry M., Jolivet J.P., Livage J., Aqueous chemistry of metal cations: hydrolysis, condensation and complexation, *Struct. Bond.*, **1992**, 77, 153.

[17]- Rahman I.A., Vejayakumaran P., Sipaut C.S., Isamil J., Abu Bakar M., Adnan R., Chee C.K., An optimized sol-gel synthesis of stable primary equivalent silica particles, *Colloid Surface A*, **2007**, 294, 102.

[18]- Mine E., Nagao D., Kobayashi Y., Konno M., Solvent Effects on Particle Formation in Hydrolysis of Tetraethyl Orthosilicate, *J. Sol-Gel Sci Techn.*, **2005**, 35, 197.

[19]- Brinker C.J., Sherer G.W., Sol-Gel science: The physics and chemistry of sol-gel processing, Academic press, **1989**.

[20]- Caruso R.A., Antonietti M., Sol-gel nanocoating: an approach to the preparation of structured materials, *Chem. Mater.*, **2001**, 13, 3272.

[21]- Herrera J.E., Balzano L., Pompeo F., Resasco D.E., Raman characterization of single-walled nanotubes of various diameters obtained by catalytic disproportionation of CO, *J. Nanosci. Nanotechol.*, **2003**, 3, 1.

[22]- Reich S., Thomsen C., Maultzsch J., Carbon Nanotubes: Basic concepts and physical properties, Wiley-VCH, **2004**.

[23]- Pawelec B., Halachev T., Olivas A., Zepeda T.A., Impact of preparation method and support modification on the activity of mesoporous hydrotreating CoMo catalysts, *Appl. Catal. A*, **2008**, 30.

[24]- Alvarez W., Kitiyanan B., Borgna A., Resasco D.E., Synergism of Co and Mo in the catalytic production of single-wall carbon nanotubes by decomposition of CO, *Carbon*, **2001**, 39, 547.

[25]- Tan Y., Resasco D.E., Dispersion of Single-Walled Carbon Nanotubes of Narrow Diameter Distribution**,** *J. Phys. Chem. B*, **2005,** 109, 14454.

[26]- Monzon A., Lolli G., Cosma S., Mohamed S.B., Resasco D.E., Kinetic Modeling of the SWNT Growth by CO Disproportionation on CoMo Catalysts, *J. Nanosci. Nanotechol.*, **2008**, 8, 6141.

[27]- Paradise M., Goswami T., Carbon nanotubes-production and industrial applications, *Mater. Design.*, **2007**, 28, 1477.

[28]- Baughman R.H., Zakhidov A.A., de Heer W.A., Carbon nanotubes-the reoute toward applications, *Science*, **2002**, 297, 787.

[29]- Merkoçi A., Pumera M., Llopis X., Pérez B., del Valle M., Alegret S., New materials for electrochemical sensing VI: carbona nanotubes, *Trac-Trend Anal. Chem.***, 2005**, 24, 826.

[30]- Gojny F.H., Wichmann M.H.G., Fiedler B., Schulte K., Influence of different carbon nanotubes on the mechanical properties of epoxy matrix composites-a comparative study, *Compos. Sci. Technol.*, **2005**, 65, 2300.

[31]- Ciambelli P., Sannino D., Sarno M., Leone C., Lafont U., Effects of alumina phases and process parameters on the multiwalled carbon nanotubes growth, *Diam. Relat. Mater.*, **2007**, 16, 1144.

[32]- Arnoldy P., Moulijn J.A., Temperature-programmed reduction of CoO/Al_2O_3 catalysts, *J. Catal.*, **1985**, 93, 38.

[33]- Finocchio E., Montanari T., Resini C., Busca G., Spectroscopic characterization of cobalt-containing solid catalysts, *J. Mol. Catal. A-Chem.*, **2003**, 204, 535.

[34]- Lojacono M., Verbeek J.L., Schuit G.C.A., Magnetic and spectroscopic investigations on cobalt-alumina and cobalt-molybdenum-alumina, *J. Catal.*, **1973**, 29, 463.

[35]- Wivel C., Clausen B.S., Candia R., Morup S., Topsoe H., Mössbauer emission studies of calcined $Co-Mo/Al_2O_3$ catalysts: catalytic significance of Co precursors, *J. Catal.*, **1984**, 87, 497.

[36]- Irurzun V.M., Tan Y., Resasco D.E., Sol-gel synthesis and characterization of Co-Mo/silica catalysts for single-walled carbón nanotube production, *Chem. Mater.*, **2009**, 21, 2238.

[37]- Djonev B., Tsyntarski B., Klissursky D., Hadjiiivanov K., IR spectroscopic study of NO_x adsorption and NO_x-O_2 coadsorption on Co^{+2}/SiO2 catalysts, *J. Chem. Soc., Faraday Trans.*, **1997**, 93, 4055.

[38]- Grange P., Catalytic hydrodesulfurization, *Catal. Rev.- Sci. Eng.*, **1980**, 21, 135.

[39]- Silvy R. P., Pirlot C., Culot B., Catalyst system for a multi-walled carbon nanotube production process, U.S. 0206125 A1, **2008**.

[40]- Kathyayini H., Willems I., Fonseca A., Nagy J.B., Nagaraju N., Catalytic materials based on aluminum hydroxide for the large production of bundles of multi-walled (MWNT) carbon nanotubes, *Catal. Commun.*, **2006**, 7, 140.

CHAPTER 2

Acknowledgments:
R. Jentolft, The University of Oklahoma
Y. Tan, SouthWest Nanotechnologies
M. Shen, The University of Oklahoma
M. Pilar Ruiz, The University of Oklahoma
R. Prada Silvy, SouthWest Nanotechnologies

CHAPTER 2

2.1- Characterization of catalysts selective towards CNT

Our group has developed the well-known CoMoCAT® catalyst to produce SWCNT. This catalyst is prepared by incipient wetness impregnation (IWI) of a silica support with an aqueous solution of the cobalt (Co) and molybdenum (Mo) precursors. Then, it is dried at 110 °C for 12 h and calcined at 500 °C for 3 h. The catalyst is then reduced under H_2, heated up to the reaction temperature (700 °C – 900 °C) under He and then the carbon source (e.g. carbon monoxide, CO) is introduced. It has been proved by different characterization techniques (EXAFS, Raman scattering, XANES, etc.) that the interaction between molybdenum and cobalt is essential to grow SWCNT. Molybdenum stabilizes cobalt forming a $CoMoO_4$ phases on Mo oxide species, during the calcination process. In the pre-reduction process under H_2, molybdenum is reduced from Mo^{VI} to Mo^{IV} and only when the CO is in contact with the oxide, the molybdenum is reduced to Mo^{II}, forming molybdenum carbide and the cobalt is reduced to metallic cobalt and segregated to the surface. The CO decomposes (Boudouard reaction) on the metallic cobalt surface and diffuses into the particle, creating a difference in the carbon concentration between the surface and the center of the particle, which would be the driving force for the SWCNT growth. The migration and agglomeration on clusters of metallic cobalt on the surface is called the nucleation. There is a certain cluster size and carbon concentration needed to start the SWCNT growth (this is called the embryo) [1-3].

The catalysts have been characterized by using different analytical techniques, such as OA, Raman scattering, SEM-TEM and thermal analysis. A brief description of these techniques is given below.

Characterization techniques

Temperature programmed reduction (TPR)

This technique involves the reduction of oxide species with controlled amounts of H_2. The H_2 consumption is detected by a thermal conductivity detector (TCD) while the temperature increases. An scheme of the experiment set up is shown in Fig. 36.

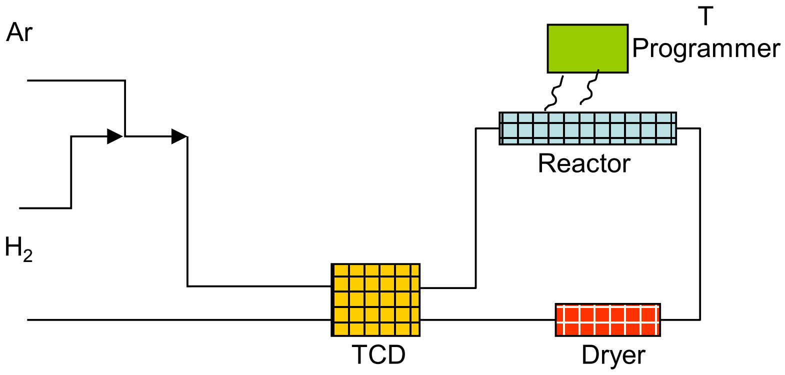

Figure 36: Temperature programmed reduction set up.

X-ray diffraction (XRD)

The electronic cloud surrounding an atom is modify when X-rays (wavelength comparable with inter atomic distances) are incident, leading to the scattering of waves with the same frequency (Fig. 37(a)).

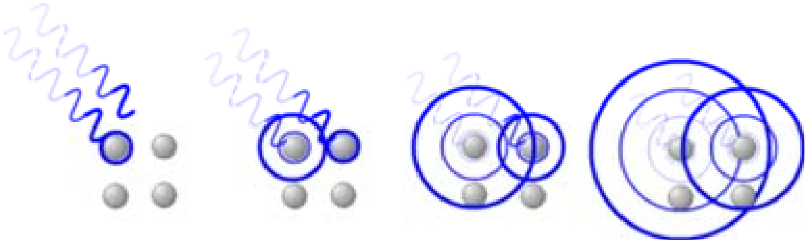

Figure 37(a): Incident X-ray and scattered waves on atoms lattices.

The scattered waves can interfere constructively or destructively as it is shown in Fig 37(b).

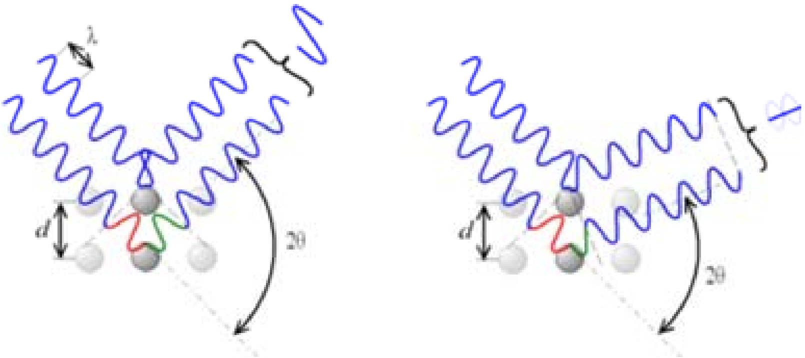

Figure 37(b): Phase shift scheme showing constructive and destructive interferences.

The interference is constructive when the phase shift is a multiple of 2π as established by the Bragg's law shown below. This constructive interference gives a diffraction pattern.

$$\mathbf{n\lambda=2d\sin\theta} \qquad \text{(Bragg's law)}$$

Being, n an integer, λ the wavelength of incident X-ray wave, d the spacing between the planes in the atomic lattice, and θ the angle between the incident X-ray and the scattering planes. Figure 38 shows, as an example, an X-ray diffraction pattern of a spent CoMoCAT® catalyst sample. Monzon et al. [4] published this pattern and identified each phase present in the analyzed sample.

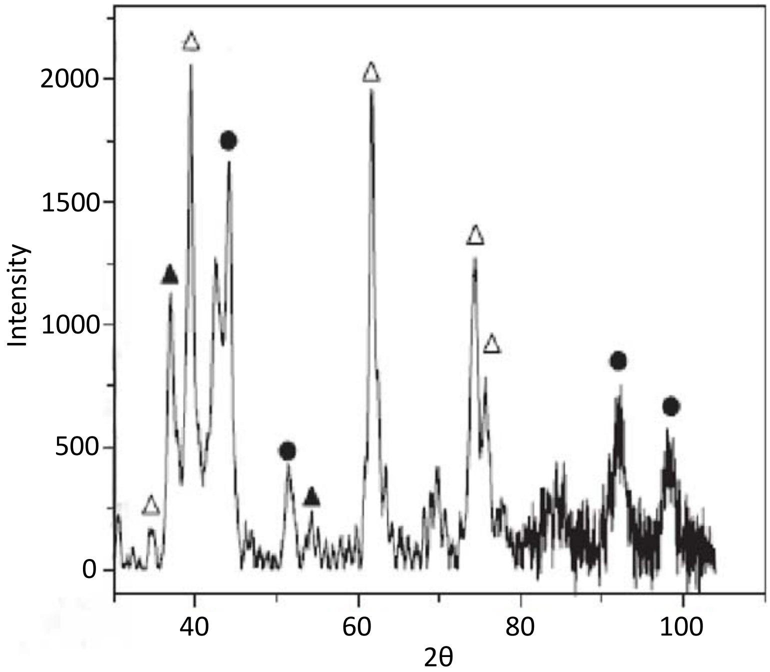

Figure 38: X-ray diffraction pattern of spent CoMoCAT® catalyst, [4].

Electron microscopy (same spot)

Electron microscopy techniques have been described in Chapter 1, section 1.1. In this particular case, a particular experiment using transmission electron microscopy is described. This methodology was developed by a member of our group, L. Zhang.

This technique is useful to study the evolution of a catalyst structure following the same nanometric particle after different treatments at high temperatures. Figure 39(a) is an scheme of the methodology.

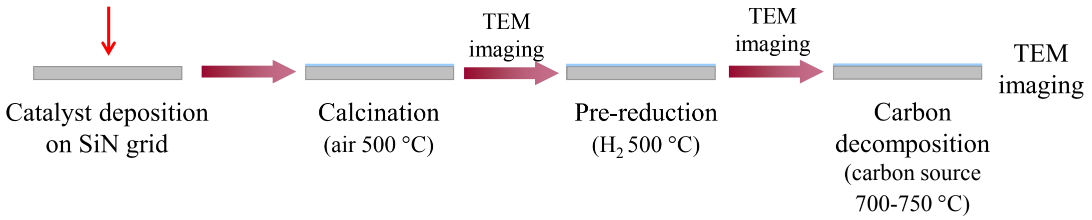

Figure 39(a): Methodology scheme for same spot TEM technique.

First, the catalyst is deposited onto a grid conformed by holes arranged as in a matrix (Fig. 39(b)). In this way if the grid is always aligned in the same way, the same hole can be checked up after each step. After the catalyst deposition, the sample is calcined and a first set of images are taken. Then, the grid is introduced in a reactor and pre-reduced under hydrogen. Once the sample is cooled down, a second set of images is taken. Finally, the grid is set again in the reactor and once the reaction temperature is reached under helium, the carbon source is fed for 1 minute. Then the system is cooled down and the last set of images is taken.

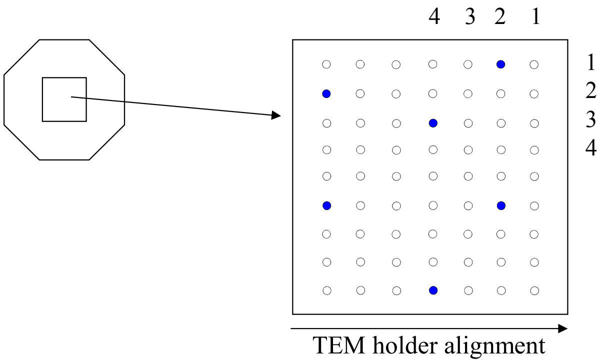

Figure 39(b): Silicon carbide grid used for same spot TEM technique.

Figure 39(c) shows an example done by L. Zhang. The same catalyst particle has been followed and imaged after calcination, reduction and reaction.

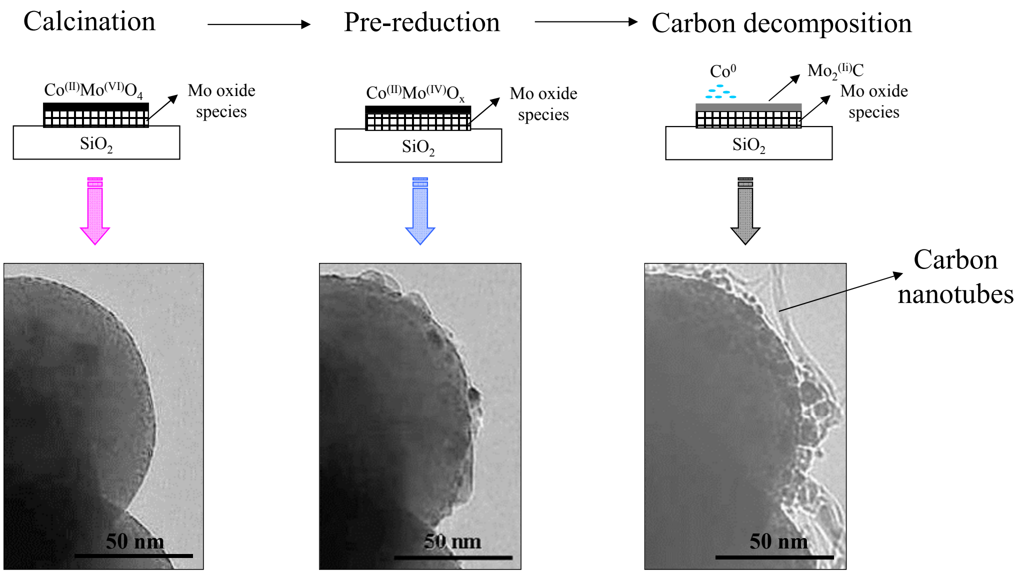

Figure 39(c): Same spot TEM technique applied to a selective catalyst toward SWCNT. Courtesy of L. Zhang.

UV-Vis diffuse reflectance spectroscopy (UV-Vis DRS)

When the UV-Vis light interacts with the sample, it can be reflected or transmitted. The reflected or scattered light is finally collected by a spherical mirror, as shown in Fig. 40, and the light is analyzed by a detector.

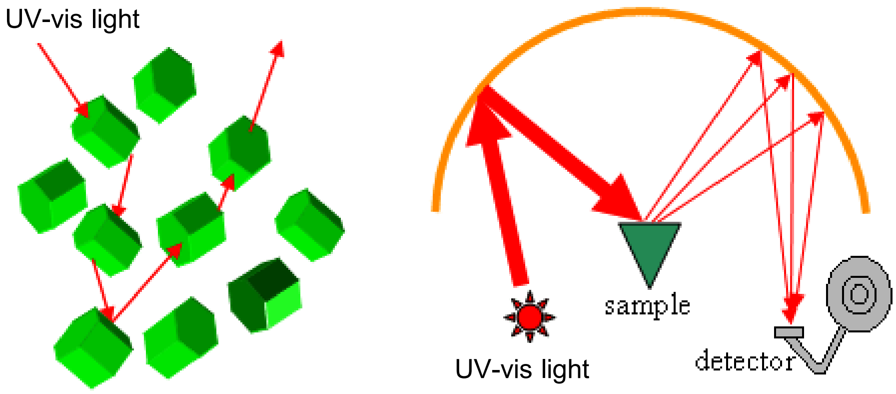

Figure 40: UV-Vis Diffuse reflectance spectroscopy scheme.

X-ray photoelectron spectroscopy (XPS)

XPS is a quantitative technique that measures the composition and chemical-electronic state of the elements on the surface of a sample. An incident beam of X-rays in the sample excites the electrons and make them escape. These electrons are then collected by an analyzer and their kinetic energy is measured. This technique requires ultra-high vacuum conditions. Figure 41 shows an scheme of the XPS set up.

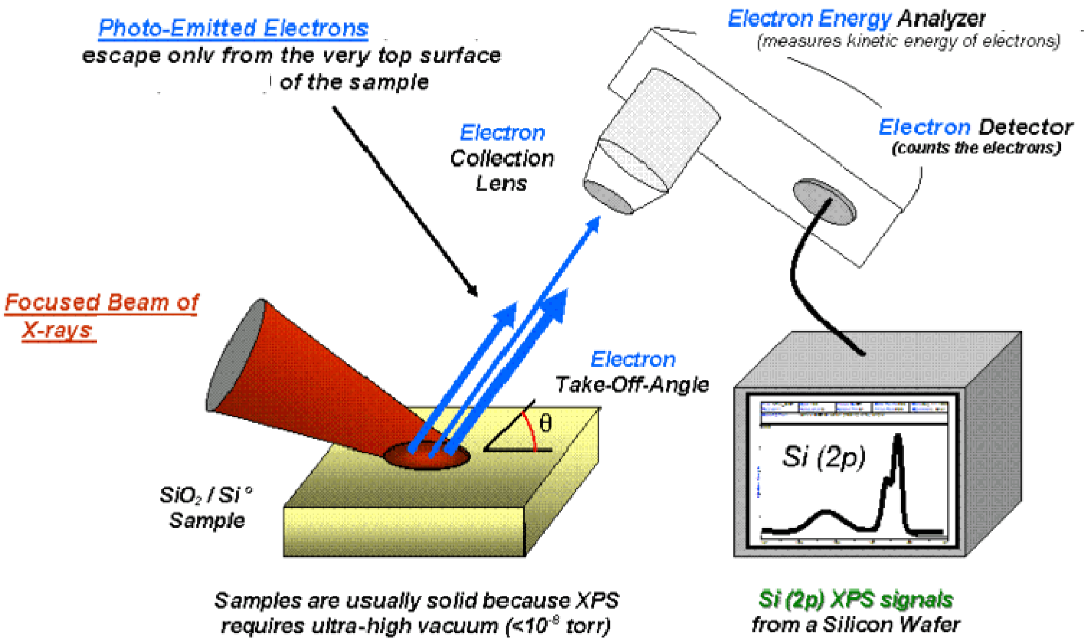

Figure 41: X-ray photoelectron spectroscopy set up.

Other techniques such as Raman scattering were used to characterize catalyst that are shown in this chapter. These techniques have been already explained in chapter 1, section 1.1.

2.1.1- Co-Mo (1:3) - silica

2.1.1.1- Sol gel

The experimental part related to this catalyst has been presented in Chapter 1, section 1.1.1.1.2. The characterization using different analytical techniques is shown below.

The calcined catalysts were characterized by TPR. The samples were placed in a vertical quartz reactor and heated to 750 ºC under He. After they were cooled down, the reduction of the oxide species under 20 sccm of a 5 % H_2/Ar was measured.

Raman spectroscopy characterization of the catalyst samples was conducted in a Jovin Yvon-Horiba Lab Raman equipped with a CCD detector and with a laser excitation of 633 nm (He–Ne laser). The collection time was 60 s. and several spectra from different spots were averaged for each sample. X-Ray Diffraction (XRD) characterization was conducted in Bruker AXS Discovery G8, equipped with a GADDS detector. The diffraction patterns were obtained for the catalysts pre-heated in He at 750C. The micro-scale structured catalyst was characterized by SEM in a JSM-880 SEM microscope.

2.1.1.1.1- Raman scattering

Figure 42 shows the Raman spectra for the sol-gel calcined powder catalyst samples. For comparison, the spectrum of a pure silica sample (calcined TEOS) is included. Without the presence of Co or Mo, the pure silica sample exhibits main bands at 431, 495, 606, and 713 cm^{-1}. As discussed in the literature [5-8], the peak at 431 cm^{-1} is related to the bending of Si-O-Si bonds, the peaks at 495 cm^{-1} and 606 cm^{-1} are related to the vibration of four and three-membered silica rings, and the peak at 713 cm^{-1} is related to the symmetric stretching of the Si-O-Si bonds. Secondary bands are also observed at 820 cm^{-1} and are related to the symmetric stretching of the Si-O-Si bonds, the band at 978 cm^{-1} to the Si-OH stretching, and the band at 1076 cm^{-1} to the asymmetric stretching of the Si-O-Si bonds. On the other hand, the calcined Co-Mo/SiO_2 catalysts, in addition to the bands due to SiO_2, exhibit main peaks between 900 and 1000 cm^{-1}, which vary in intensity among the samples in the series. These bands are due to the Mo-O-Co stretching in α- and β-$CoMoO_4$ species [9-11] with some contribution from bands corresponding to Mo oxides [12], which are also present on the sample since Mo is in excess (i.e., Co/Mo 1/3).

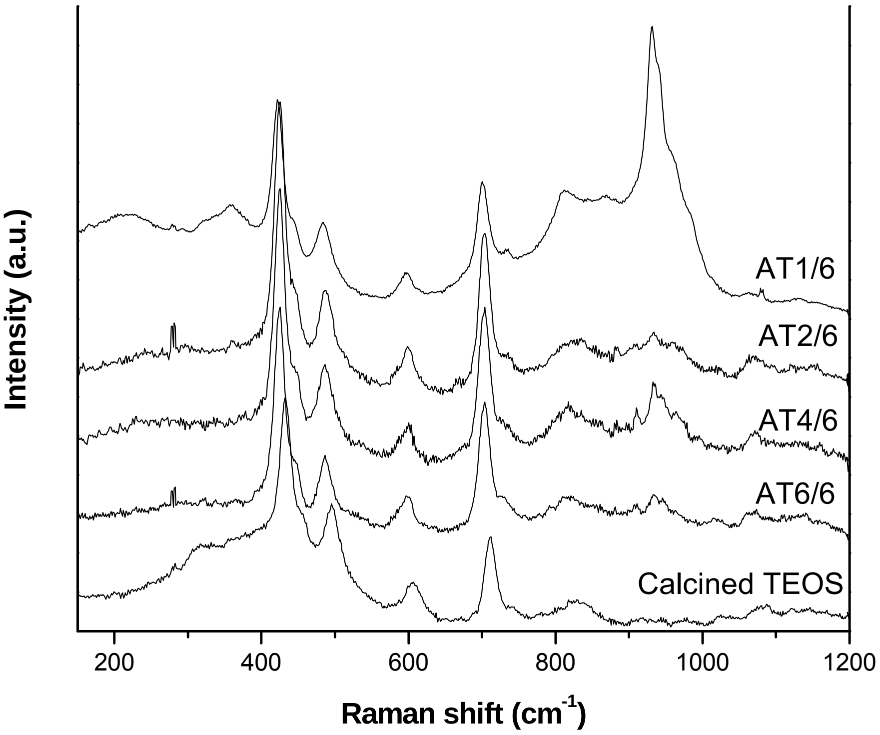

Figure 427: Raman spectra of four Co-Mo/SiO_2 powder calcined catalysts with NH_4OH/TEOS ratios from 1/6 to 6/6 compared with the spectra of pure calcined TEOS.

The intensity of these bands provides a semi-quantitative measurement of the presence of $CoMoO_4$ and Mo oxide crystallites. Specifically, while the intensity of these bands is very low and about the same for all the samples with an NH_4OH/TEOS ratio between 2/6 and 6/6, they are prominent for the sample with a ratio of 1/6, indicating the presence of larger crystals in this sample.

2.1.1.1.2- Temperature programmed reduction

The TPR profiles for three of the powder catalyst samples are summarized in Figure 43(a). It can be seen that for the sample with the lowest NH_4OH/TEOS ratio, AT(1/6), the H_2 consumption was significantly larger than those of the other catalysts. The rate of hydrogen consumption decreases after about 800 °C, about equally for the three catalysts. By contrast, for the other two, the hydrogen uptake is practically the same, while the maximum reduction peaks slightly shift to higher temperatures as the NH_4OH/TEOS ratio increases from AT(4/6) to AT(6/6). Figure 43(b) shows the TPR profile of the AT(2/6) sample which reduces at lower temperatures than the other samples in the series, but has about the same H_2 consumption as the samples with NH_4OH/TEOS ratios of 4/6 and 6/6. The differences in reducibility could be due to one of the following characteristics: (a) different degree of oxide crystallinity; (b) different CoMoOx compositions, or (c) different gas accessibility. A higher degree of crystallinity in the AT(6/6) sample, which would require a higher reduction temperature, should have been detected by Raman or XRD. In fact, sample AT(1/6) does show intense Raman bands confirming the presence of large Co molybdate crystals, but yet, the reduction does not shift to higher temperatures. Likewise, differences in composition as the NH_4OH/TEOS ratio increases could also cause an increment in reduction temperature if the clusters were more enriched in Mo.

However, if this was the case, these oxides should have shown different Raman shifts for the different catalysts, but there were no differences.

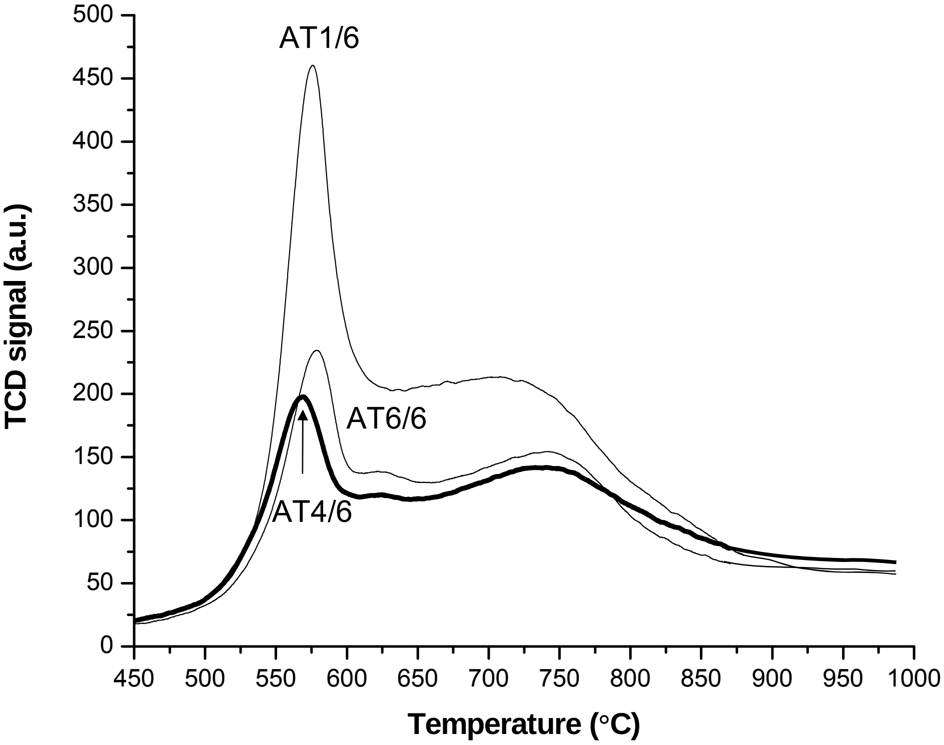

Figure 43(a): TPR profiles of three Co-Mo/SiO_2 calcined powders with NH_4OH/TEOS ratios from1/6 to 6/6. The samples were previously pre-heated under He to 750 °C.

Therefore, we ascribe the increase in reduction temperature with increasing NH_4OH/TEOS ratio to lower accessibility, as Co and Mo species remain partially encapsulated by the silica support. Occlusion of cobalt has been extensively studied on MCM-41 structures [13-21].

The TPR profile for the open microstructure sample is included in Fig. 43(b) as a comparison. It can be seen that the profile differs from the powder catalyst, and this difference may be related to the differences in structure, for example, gas accessibility. For comparison, Fig. 43(c) shows the TPR for the monometallic catalysts, Co/SiO_2 and

Mo/SiO_2, prepared by the sol-gel method and the Co/SiO_2 and Mo/SiO_2 prepared by impregnation. It can be seen that Co reduces at higher temperatures on the sol-gel catalyst than the impregnated catalysts. As discussed above, this difference is due to the lower accessibility of Co on the samples prepared by sol-gel.

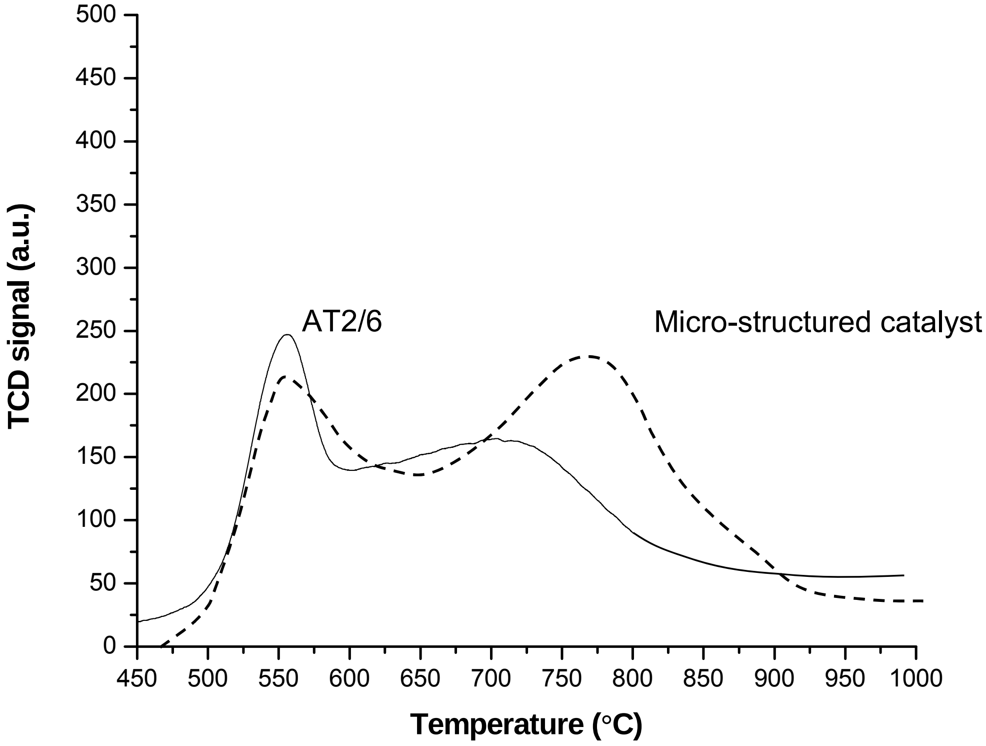

Figure 43(b): TPR profile of a $Co-Mo/SiO_2$ calcined powders with $NH_4OH/TEOS$ ratios of 2/6 and TPR profile of the micro-structured catalyst. The samples were previously pre-heated under He to 750 °C.

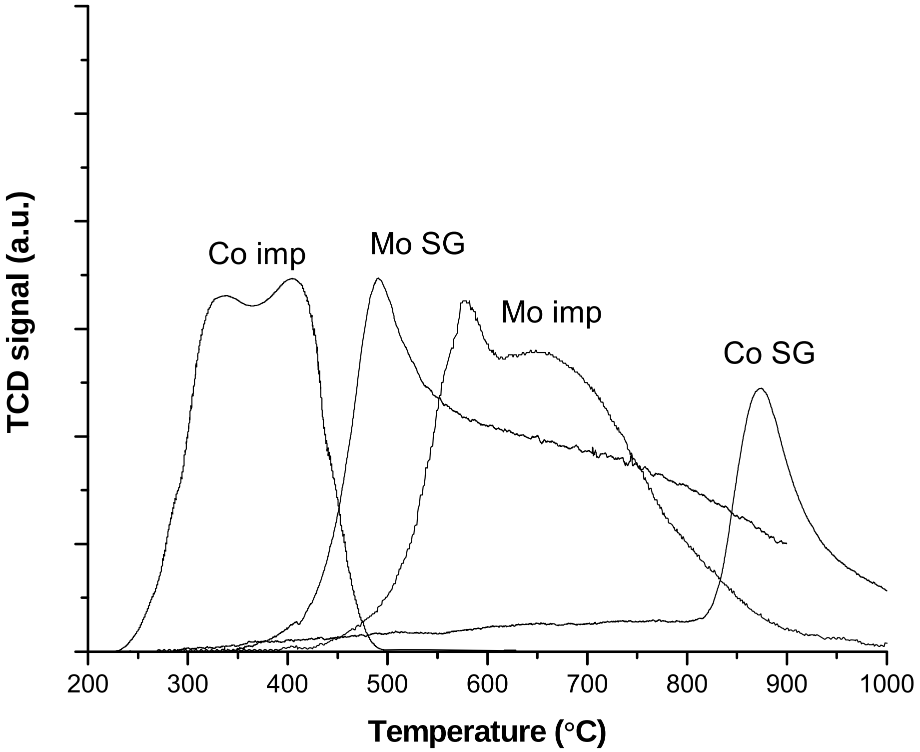

Figure 43(c): TPR profiles of monometallic Co/SiO_2 and Mo/SiO_2 calcined powder catalysts prepared by impregnation (imp) or using the sol gel method (SG). The samples were calcined and pre-heated under He to 750 °C before the TPR analysis was conducted.

2.1.1.1.2- X-ray diffraction

Figure 44 shows the diffractograms for the four powder catalysts obtained after heating under He at 750 °C. Two sharp diffraction peaks are observed at 21° and 23°, and they can be ascribed to cristoballite-like and tridymite-like crystalline silica phases. It can be seen that increasing the NH_4OH/TEOS ratio from 1/6 to 6/6, the silica particles not only become larger but also more crystalline. These differences have not been seen in Raman because this is a shorter range analysis than XRD. The lack of crystallinity exhibited by the AT(1/6) can be due to the low extent of silica polymerization in the sample prepared with low ammonium content.

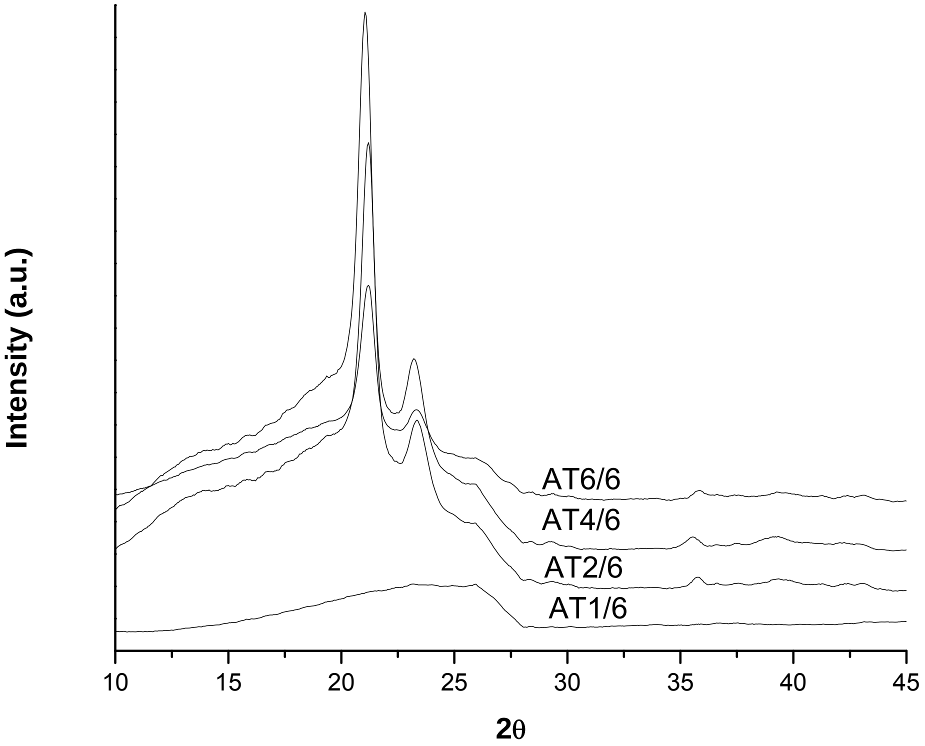

Figure 44: XRD diffractograms of four Co-Mo/SiO$_2$ calcined powder catalysts with NH$_4$OH/TEOS ratios from 1/6 to 6/6. The samples were previously pre-heated under He to 750 °C.

2.1.1.1.3- Transmission electron microscopy

As it was mention in Chapter 1, section 1.1.1.1.2, a sol-gel microscale structured catalyst has been also used to produce CNT. As illustrated schematically in Fig. 45(a) and (b), the carbonaceous tubular template can be burnt away during calcination, leaving a tubular SiO$_2$ shell that preserves the shape of the sacrificial template, as shown in previous studies [22,23]. The characterization of this calcined sample is shown below.

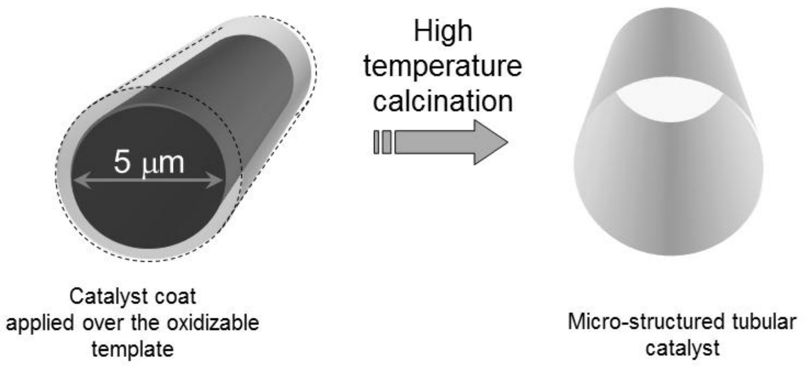

Figure 45(a): Schematic description of the micro-structured catalyst preparation.

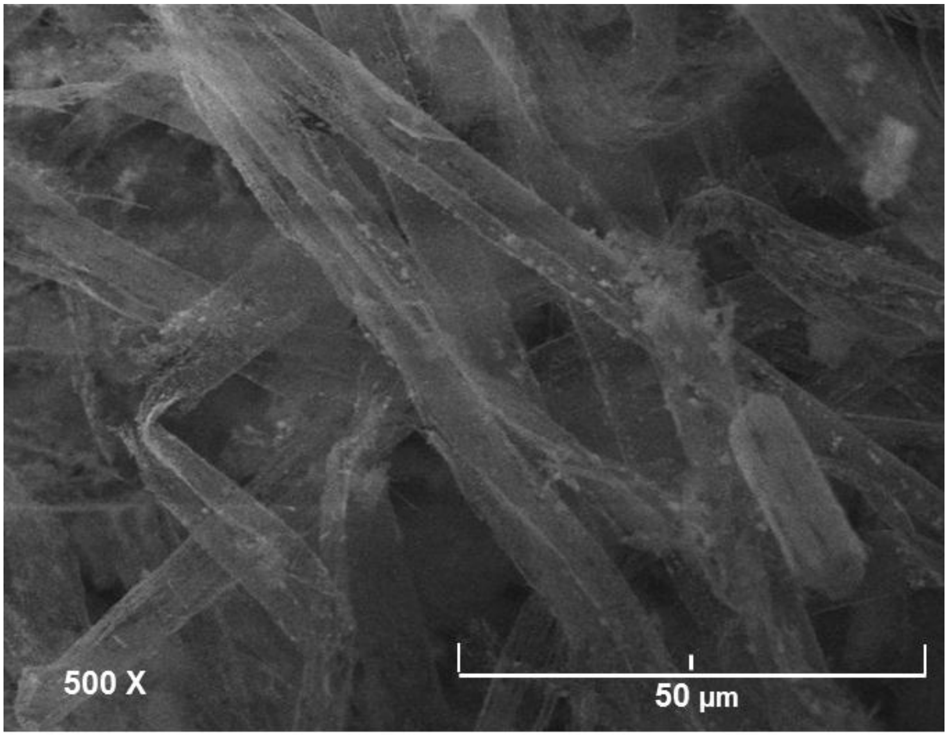

Figure 45(b): SEM image of the micro-structured Co-Mo/SiO_2 catalyst after calcination.

Figures 46(a) and (b) show in detail the morphology of the two samples that produce the lowest nanotube yields, AT(1/6) and AT(6/6). It can be seen that while in the latter, a large fraction of the Co-Mo particles are surrounded by a silica layer, in the former, the metal particles remain exposed to the gas phase. However, in agreement with the Raman results, the size of these exposed Co-Mo crystallites is comparatively large (~10 nm). Previous investigations [24] have demonstrated that by increasing the concentration of the hydrolysis catalyst (NH_4OH, in this case) the average size of the silica particle tends to increase. A rapid increase due to a high concentration of NH_4OH in the case of sample AT(6/6) may result in encapsulation of the Co-Mo species, as observed. On the other hand, when the NH_4OH concentration is too low, that is, AT(1/6), the extent of polymerization is low and consequently there are not enough silica particles to keep Co-Mo species separate, so they agglomerate during synthesis and produce large crystallites, as clearly seen by TEM and Raman. From the analysis of the carbon yields and Raman G/D ratios shown in Chapter 1, section 1.1.1.1.2.2, Fig. 20, it is obvious that both extremes are detrimental for nanotube carbon yield, as well as the SWCNT selectivity. First, if the active species are trapped by the support, one can obviously expect a low carbon yield. Second, large Co-Mo crystallites also have a low fraction of Co exposed to the gas phase, which causes both low carbon yield and SWCNT selectivity, as previously shown [25-29]. Therefore, in the AT(2/6) sample the concentration of NH_4OH seems to be optimum, not resulting in large Co-Mo crystallites, which are nonselective and are formed when the extent of silica polymerization is low, nor forming silica-encapsulated Co-Mo moietes, which have low catalytic activity and are formed when the silica polymerization is fast.

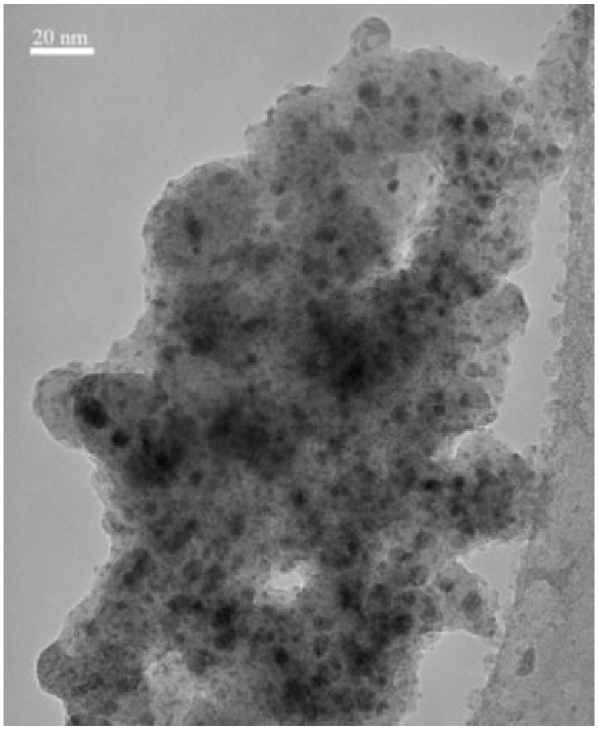

Figure 46(a): TEM image of SWCNT grown onto Co-Mo/SiO_2 powder catalyst with NH_4OH/TEOS ratio of 1/6.

Figure 46(b): TEM image of SWCNT grown onto Co-Mo/SiO_2 powder catalyst with NH_4OH/TEOS ratio of 6/6.

2.1.1.2- Impregnation

As it was mentioned before, our group has developed the CoMoCAT® catalyst that produces tubes with high SWCNT selectivity. Several publications [1-3,10,25-29] have shown this. In order to compared the previous Co-Mo (1:3) supported on silica and prepared by the sol-gel method with the impregnated case, a brief review of the results shown in our group publications related to the CoMoCAT® catalyst is shown next.

Herrera et. al [28] have compared the Raman scattering spectra of calcined cobalt molybdenum catalysts with a molar ratio of 1 to 3 impregnated on silica with commercial molybdenum, cobalt and cobalt molybdate oxides. It can be seen in Fig. 47 that when the calcined catalysts was compared with commercial MoO_3 and $CoMoO_4$, the spectrum was similar to the last one. Therefore they have concluded that cobalt and molybdenum are forming cobalt molybdate oxides when the catalysts are calcined.

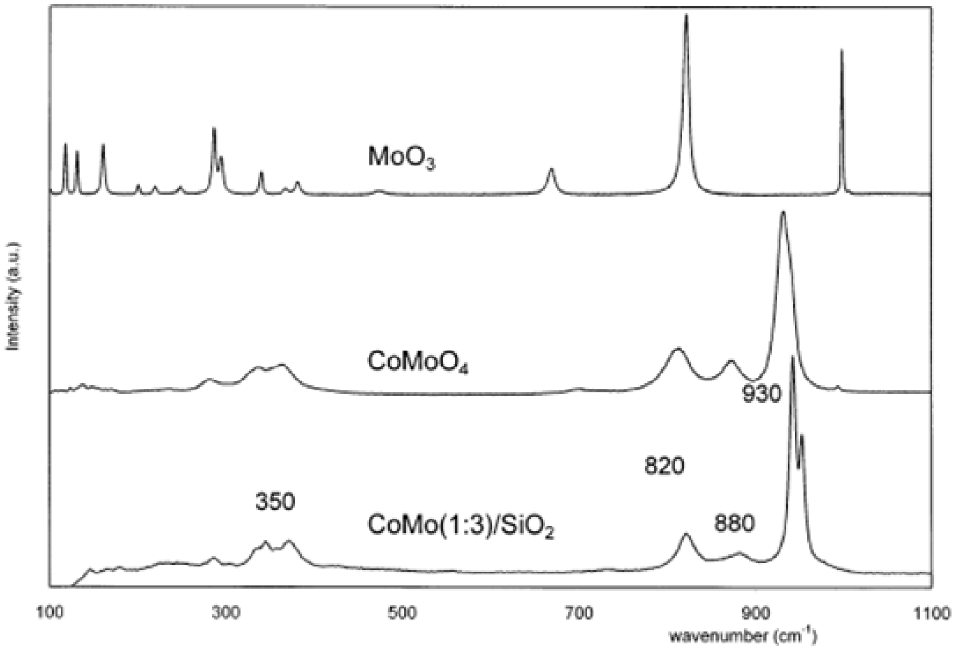

Figure 47: Raman scattering spectra Co-Mo/SiO_2 (1:3). Impregnation. [28]

In a different publication, Herrera et al. [2] have also compared the calcined catalysts spectrum with the one corresponding to Co_3O_4 showing that cobalt is not forming cobalt oxides. In this same publication Herrera et al. [2] also studied the oxide species in the calcined catalysts by conducting TPR. They have compared monometallic cobalt and molybdenum catalysts with the bimetallic one and the results are shown in Fig. 48. It can be observed that most of the cobalt in the bimetallic catalyst is interacting with molybdenum and not forming cobalt oxides.

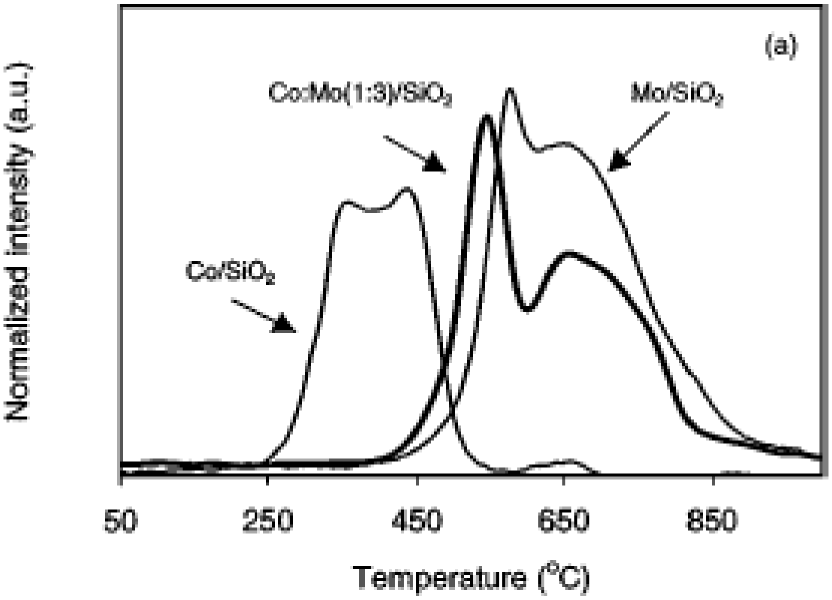

Figure 48: TPR profiles Co-Mo/SiO_2 (1:3). Impregnation. [2]

Figure 49 shows a typical TEM image of the CoMoCAT® catalyst. It can be seen that the size of the catalysts particles is between 10-50 nm. The magnification of this image does not allow differentiating the active metallic nanoparticles from the silica support.

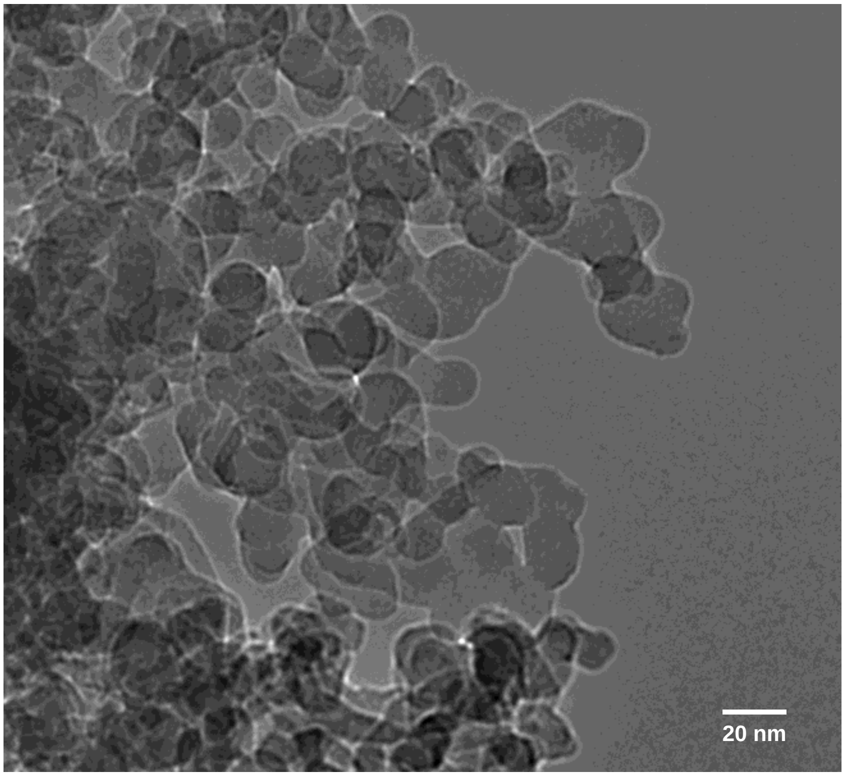

Figure 49: TEM image of Co-Mo/SiO_2 (1:3). Impregnation. Courtesy of SouthWest NanoTechnologies.

In this section the characterization of different cobalt molybdenum catalysts with 1 to 3 molar ratio, supported on silica and prepared either by the sol-gel method or impregnation was shown. As mentioned before, seeking for controlling the production of high MWCNT selectivity products, the original catalysts formulation was changed until the desirable formulation was achieved. The so called transition catalyst formulations were not characterized since the synthesized products were not MWCNT. Therefore, the characterization of cobalt molybdenum catalysts with molar ratio of 3 to 1, supported on silica or aluminum and prepared by impregnation, are shown next.

2.1.2- Co-Mo (3:1) – alumina/silica

The experimental part related to these catalysts (Co-Mo (3:1) – alumina/silica) has been presented in Chapter 1, section 1.1.3.1. Different techniques were used to characterize the calcined catalysts. UV-Vis DRS was conducted in a Shimadzu UV 2450 equipped with a dual beam spectrophotometer. The calcined solid samples were also analyzed by using XPS. The spectra were recorded on a Physical Electronics PHI 5800 ESCA system, equipped with an AlKα X-ray anode operated at 350 W and 15 kV. The base pressure of the main chamber was kept at about 1.0×10^{-8} Torr. TPR was also used to characterize the calcined samples. The powdery samples were reduced under 20 sccm of a 5 % H_2/Ar with a temperature ramp of 10 °C/min. TEM was used to follow up the morphology of the monometallic Co/SiO_2 catalysts at the different stages (fresh, oxidized and reduced).

2.1.2.1- Results

2.1.2.1.1- UV-visible diffuse reflectance spectroscopy

Figure 50(a) shows that the absorption of light in the UV-Vis range of the bimetallic samples Co-$Mo_{\gamma\text{-}Al_2O_3}$ and Co-$Mo_{Al(OH)_3}$ is different from each other. Co-$Mo_{Al(OH)_3}$ presents two main absorption zones between 350-500 nm and 650-800 nm, while Co-$Mo_{\gamma\text{-}Al_2O_3}$ presents only one absorption zone between 500 and 700 nm. As a comparison, the UV-Vis DRS spectra of three standards, Co_3O_4, $CoAl_2O_4$ and $CoMoO_4$, were done and are shown in Fig. 50(b). It can be seen that the spectrum of Co-Mo $_{Al(OH)_3}$ looks similar to the Co_3O_4 one. On the other hand, when cobalt and molybdenum are supported on γ-Al_2O_3, the spectrum looks more similar to $CoAl_2O_4$ or $CoMoO_4$.

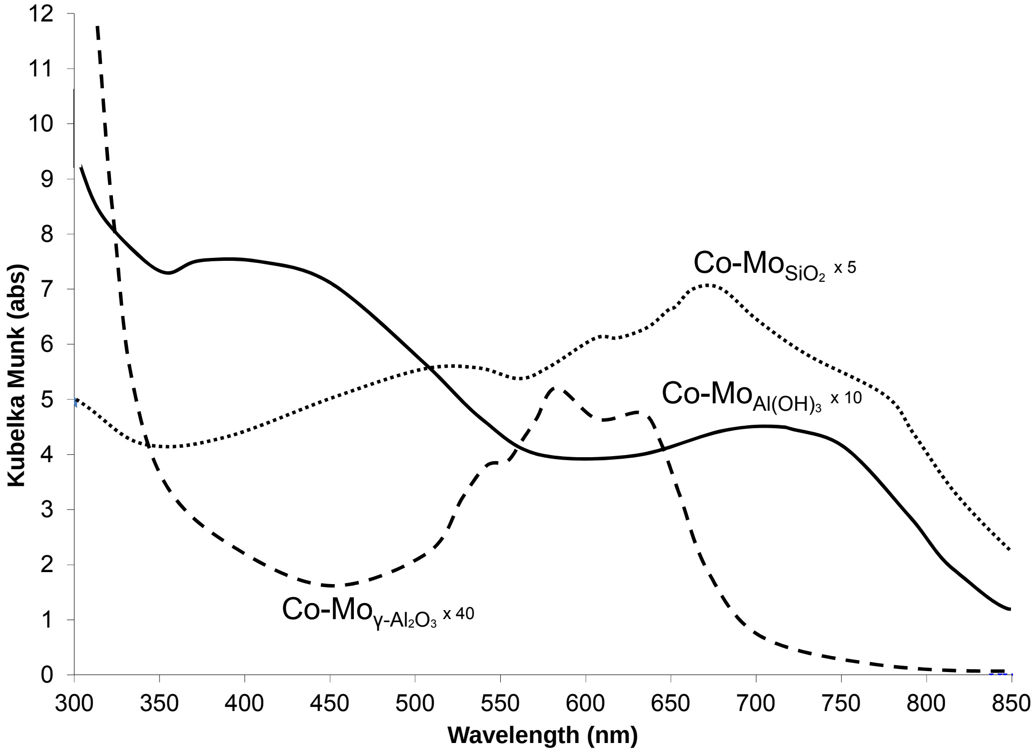

Figure 50(a): UV-Vis Diffuse Reflectance Spectroscopy. Bimetallic (Co-Mo 3:1) catalysts on different supports.

The spectrum of Co-Mo$_{SiO_2}$ was also included in Fig. 50(a) as a comparison. In previous publications, our group has shown that when cobalt and molybdenum are simultaneously impregnated on silica, cobalt can be either as cobalt oxide species or as cobalt molybdate oxide species.

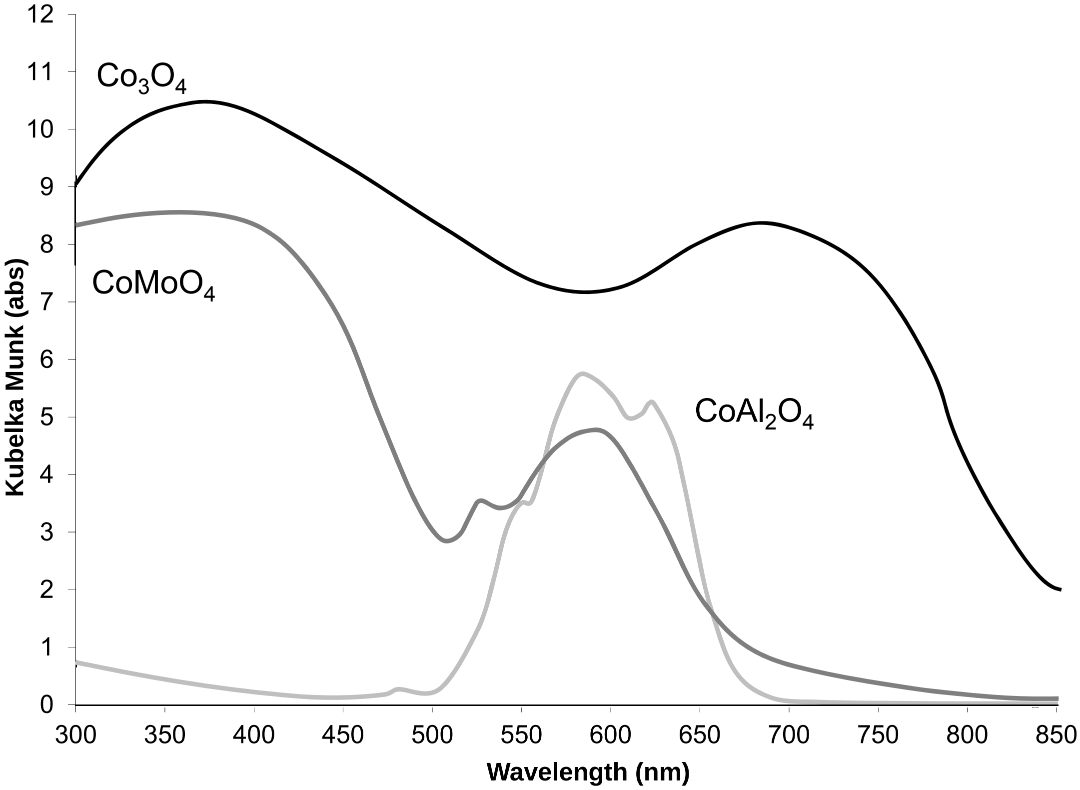

Figure 50(b): UV-Vis Diffuse Reflectance Spectroscopy. Standard samples.

Figure 50(c) shows the UV-Vis DRS of the monometallic catalysts. It can be seen that for the alumina supported cobalt, the spectra look similar to the correspondent to the bimetallic case. On the other hand, when cobalt is supported on silica, there is a change on the absorption zone with respect to the bimetallic sample. It seems that when molybdenum is added there is a shift to lower wavelength numbers compared with the monometallic catalyst.

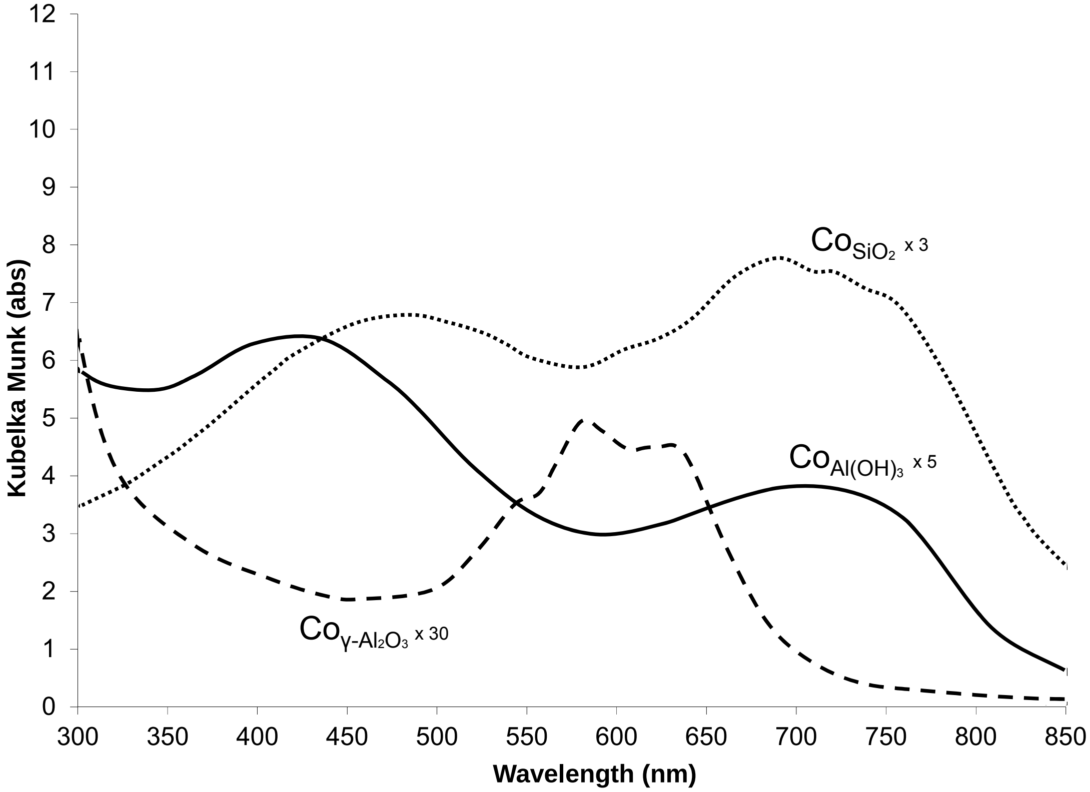

Figure 50(c): UV-Vis Diffuse Reflectance Spectroscopy. Monometallic (Co) catalysts on different supports.

The effect of the molybdenum addition on silica supported catalysts was also studied and it is shown in Fig. 50(d). The absorbance spectra of the Co-Mo_{SiO_2} seem to differ when different molar ratios of the precursors are simultaneously impregnated. The lower the cobalt content the more similar the spectrum is to the $CoMoO_4$ standard showed in Fig. 50(b). When the spectra of the catalysts prepared by using the same precursor's molar ratio but different impregnation sequence (simultaneous or sequential) are compared, it can be seen that the spectrum is more similar to the correspondent to the Co_3O_4 standard when the catalyst is prepared by sequential impregnation.

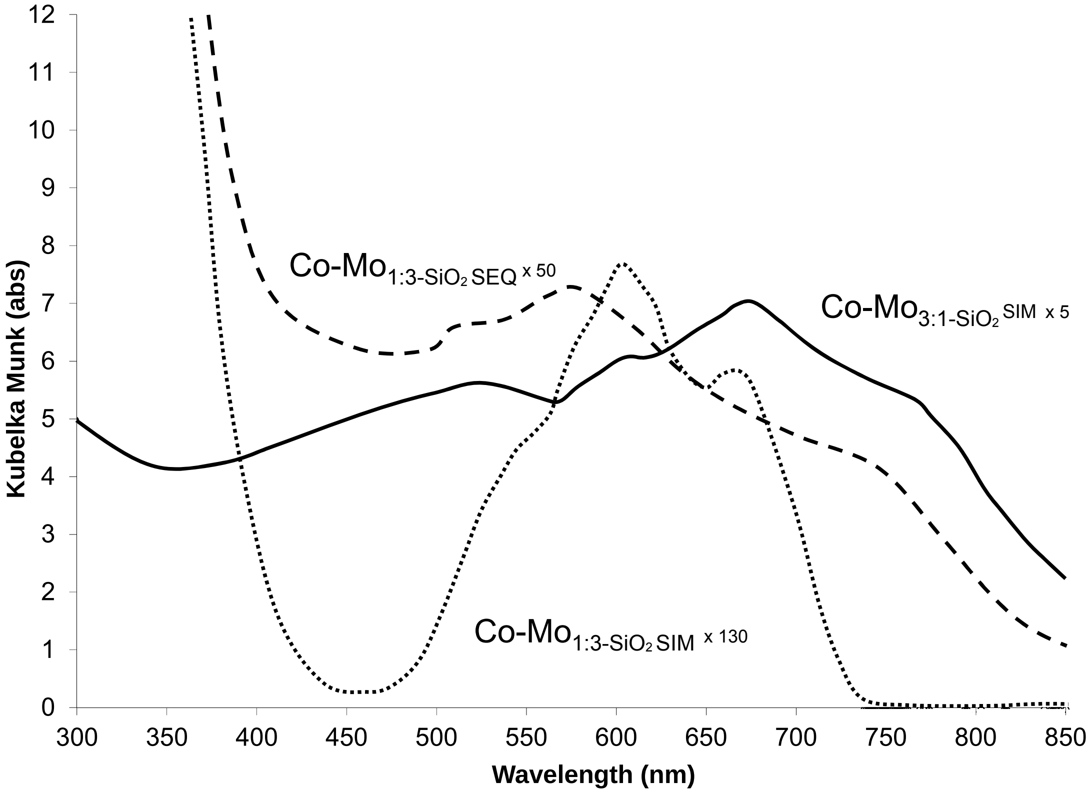

Figure 50(d): UV-Vis Diffuse Reflectance Spectroscopy. Bimetallic (Co-Mo 3:1 1:3) catalysts supported on silica. SEQ: sequential Co-Mo impregnation, SIM: simultaneous Co-Mo impregnation.

Figures 51(a) and (b) show the results obtained from the metal loading catalyst series. When cobalt is impregnated on γ-Al_2O_3, as it can be seen in Fig. 51(a), the reduction profiles are different depending on the metal loading. On the other hand (Fig. 51(b)), when cobalt is impregnated on $Al(OH)_3$, the reduction profiles do not seem to depend on the metal loading.

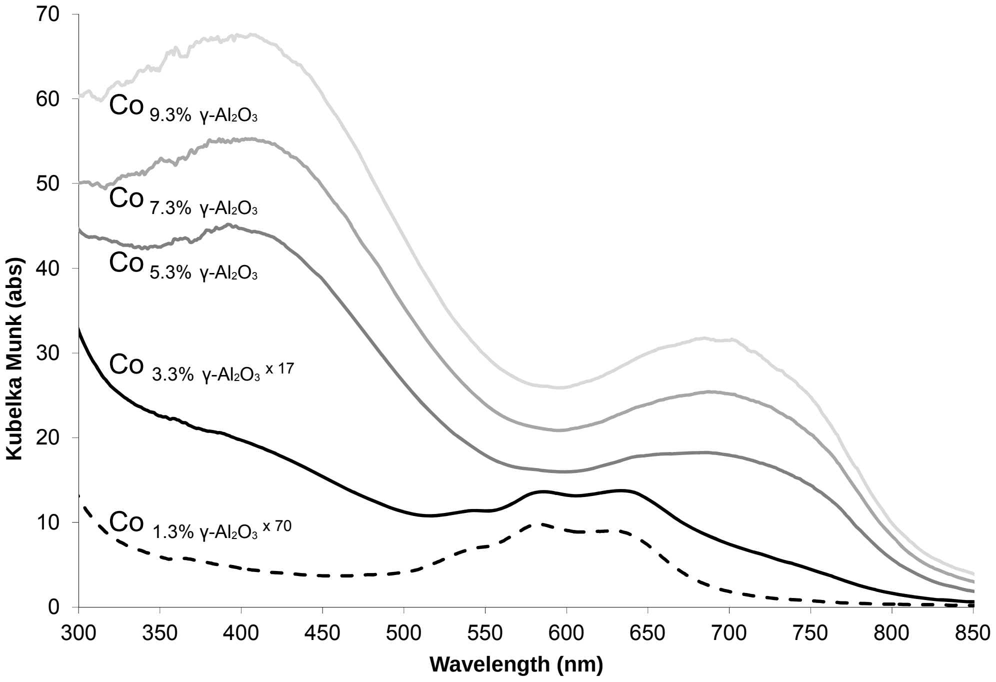

Figure 51(a): UV-Vis Diffuse Reflectance Spectroscopy. Monometallic (Co) catalysts supported on γ-Al_2O_3 with different cobalt loadings.

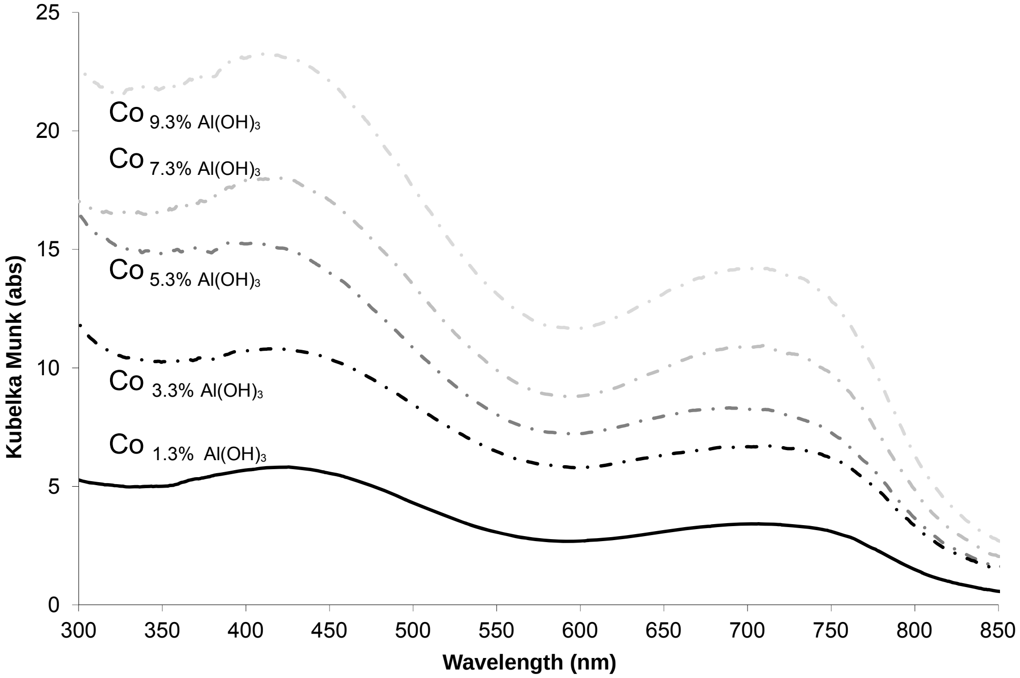

Figure 51(b): UV-Vis Diffuse Reflectance Spectroscopy. Monometallic (Co) catalysts supported on $Al(OH)_3$ with different cobalt loadings.

As it was mentioned before, the oxide species formed on the monometallic and bimetallic catalysts depend on the support used. It has been shown that, while cobalt preferentially forms cobalt aluminates when supported on γ-Al_2O_3, it forms cobalt oxides when supported on $Al(OH)_3$. It has been also seen that while cobalt, despite the metal loading, always forms cobalt oxide species such as Co_3O_4 when supported on $Al(OH)_3$, it does not form them when the metal loading is low and is supported on γ-Al_2O_3. Besides, the addition of molybdenum did not show any effect on the oxide species formed when the supports used were either $Al(OH)_3$ or γ-Al_2O_3. Therefore, the addition of molybdenum does not seem to modify the structure of the catalysts, showing that cobalt is not forming cobalt molybdate species when is supported on alumina.

Monometallic and bimetallic catalysts supported on silica showed a different behavior than the ones supported on aluminum materials. The absorbance spectra were different showing in this case that the addition of molybdenum modified the oxide species formed. Therefore, the addition of molybdenum when silica is used as support seems to favor the formation of cobalt molybdate species as it can be seen in Fig. 50(a). When Co-Mo_{SiO_2} with molar ratios of 3:1 and 1:3 (simultaneously impregnated) are compared, it can be seen that the higher the molybdenum content, the more likely to form $CoMoO_4$ the catalyst is. On the other hand, when the simultaneously impregnated Co-Mo_{SiO_2} with a molar ratio 1:3 is compared with the sequentially impregnated Co-Mo_{SiO_2}, 1:3, it can be seen that there is more cobalt dissociated and forming Co_3O_4 when the precursors are sequentially impregnated.

2.1.2.1.2- X-ray photoelectron spectroscopy

Figures 52(a) and (b) show the Co 2p XPS regions obtained for the bimetallic and monometallic catalysts. It was found that the shape of the Co 2p XPS peaks depends greatly on the type of support used. The Co 2p XPS signal acquired from either $Co_{Al(OH)_3}$ or $Co\text{-}Mo_{Al(OH)_3}$ shows much weaker peaks (shake-up peaks) at binding energies between 785 and 787 eV than the signal acquired from the monometallic and bimetallic catalysts supported either onto γ -Al_2O_3 or SiO_2.

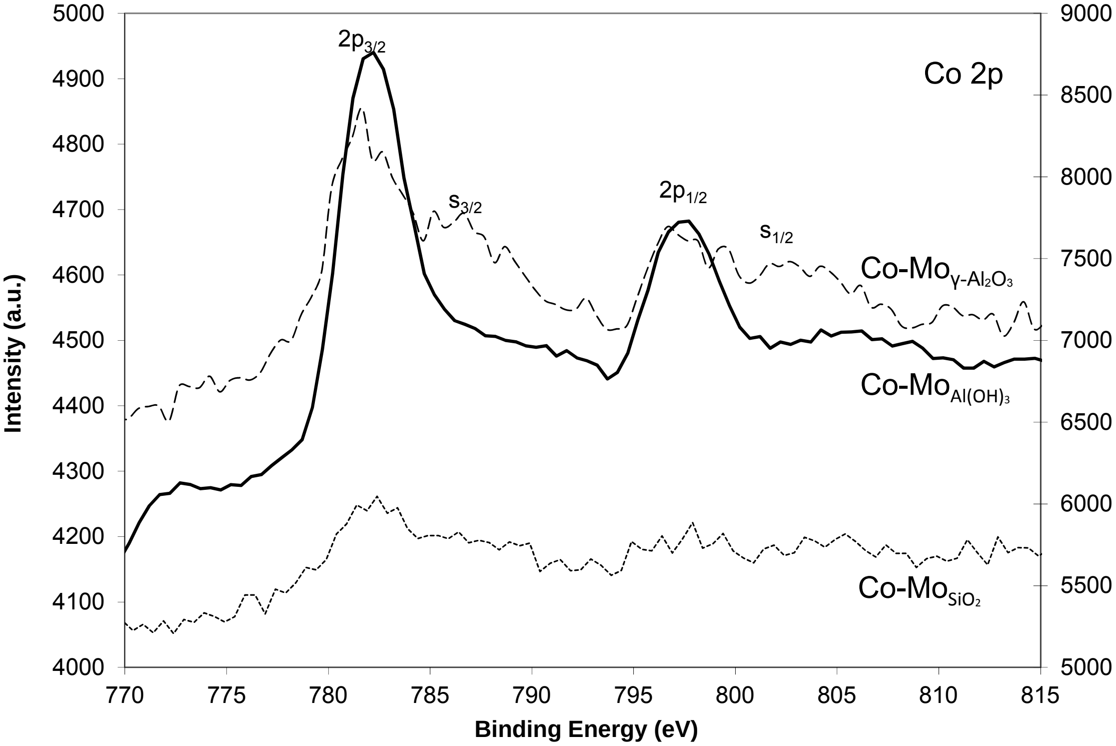

Figure 52(a): X-ray Photoelectron Spectroscopy. Bimetallic (Co-Mo 3:1) catalysts on different supports. Cobalt 2p.

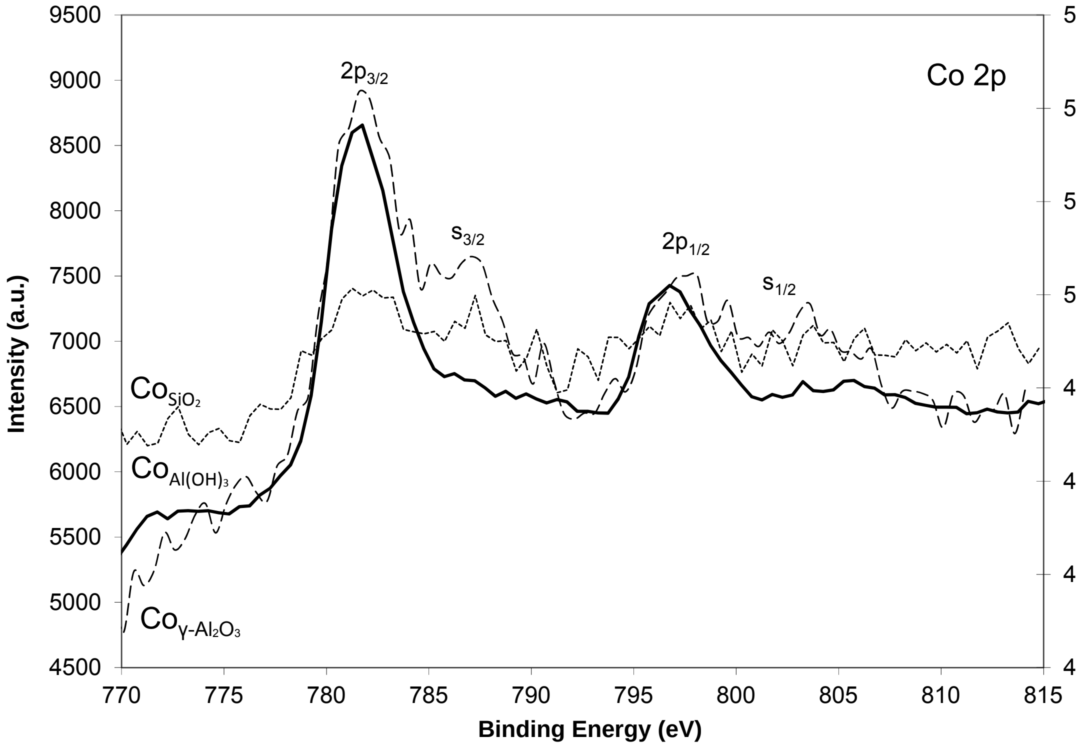

Figure 52(b): X-ray Photoelectron Spectroscopy. Monometallic (Co) catalysts on different supports. Cobalt 2p.

As a comparison, different cobalt standards have been analyzed by using XPS and the spectra are shown in Fig. 52(c). It can be seen that while Co^{3+} (octahedral, Hexaamminecobalt (III) chloride) species exhibit very weak Co 2p shake-up peak, Co^{2+} species (tetrahedral, cobalt (II) chloride ultra dry) show shake-up peaks with high intensities. $CoAlO_4$, $CoMoO_4$ and Co_3O_4 spectra are also shown in Fig. 52(c).

The 2p shake-up peaks mentioned before are due to the excitation of 3d electrons into an unoccupied orbital. It is important to mention that these types of peaks are only observed in atoms containing unpaired number of d-electrons. Therefore, as it has been shown in previous studies [28,30-32], the relative intensity of the Co 2p shake-up peaks can be well correlated with the identities of the Co species. The values presented in Table 2 show that the relative intensity differs when using different supports ($Al(OH)_3 < \gamma\text{-}Al_2O_3 < SiO_2$).

The spectrum of Co_3O_4 is similar to the correspondent to Co^{+3}. It is known that both Co^{+2} and Co^{+3} ions are present in Co_3O_4, but since the Co^{3+}/Co^{+2} molar ratio is 2, the shake-up peak intensity is governed by the Co^{3+}. Hence, the Co species supported onto $Al(OH)_3$ can be mostly ascribed to Co^{3+} species, while the Co species supported by $\gamma\text{-}Al_2O_3$ should be mostly Co^{+2} species. This result is in well accordance with the UV-Vis DRS and TPR results discussed below. It is worth noticing that the addition of Mo does not change this comparison in any significant way.

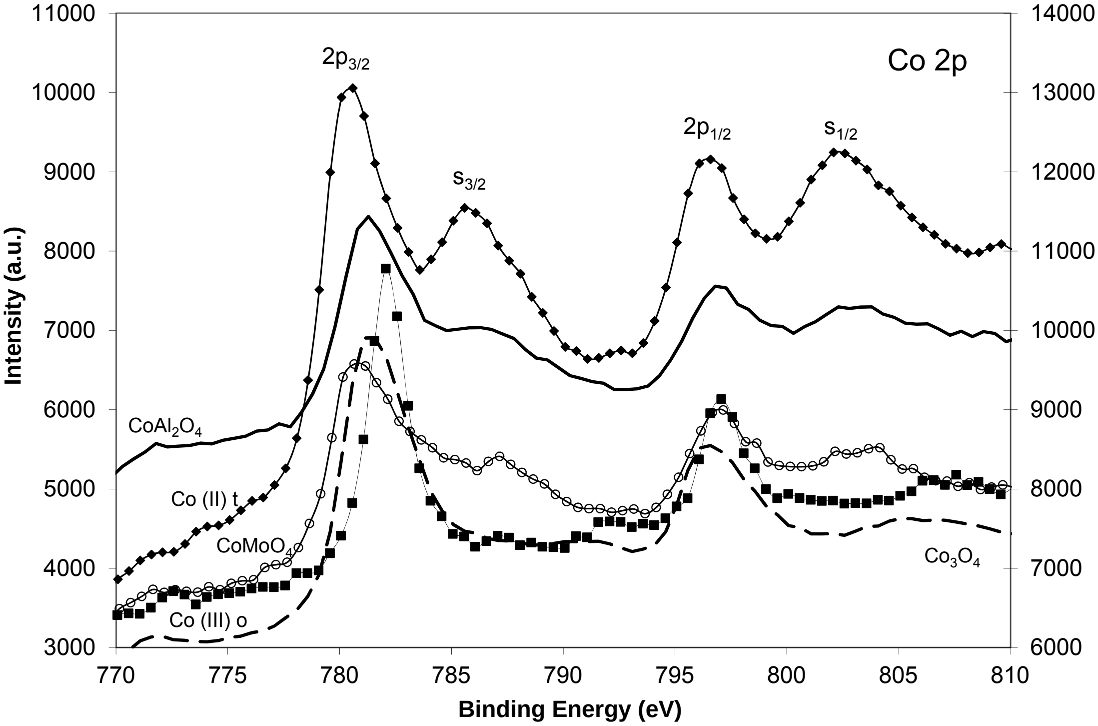

Figure 52(c): X-ray Photoelectron Spectroscopy. Cobalt standards. Cobalt 2p.

Table 2:Relative intensity of the Co 2p shake-up peaks.

Catalyst	**Co $2p_{3/2}$ B.E.**	**Co $2p_{3/2}$ Satellite B.E.**	**Intensity Ratio**
Co_{SiO_2}	781.48 eV	786.72 eV	0.59
$Co_{\gamma\text{-}Al_2O_3}$	781.46 eV	786.71 eV	0.48
$Co_{Al(OH)_3}$	780.31 eV	786.07 eV	0.18

2.1.2.1.3- Temperature programmed reduction

TPR profiles of the bimetallic catalysts are shown in Fig. 53(a). Co-Mo supported on $Al(OH)_3$ shows reduction peaks at low temperatures between 300 and 450 °C, at mid temperatures between 450 and 650 °C, and at high temperatures above 650 °C. On the other hand, when γ-Al_2O_3 is used as support for Co-Mo, while species reducing at high temperatures are still observed, there are none reducible species observed at low temperatures. It has also been included in Fig. 53(a) Co-Mo supported on SiO_2. It can be seen that in this case the TPR profile is governed by peaks at temperatures higher than 450 °C.

Monometallic catalysts have been also studied by using TPR and the results are shown in Fig. 53(b). It can be seen that while cobalt is not forming low temperature reduction species when supported on γ-Al_2O_3, it is when supported on $Al(OH)_3$ or SiO_2.

Figures 54(a) and (b) show a study of a metal loading series were cobalt was either supported on γ-Al_2O_3 or $Al(OH)_3$,respectively. It can be seen that while cobalt was always forming low temperature reduction species, despite the metal loading, when supported in $Al(OH)_3$, it was not when supported on γ-Al_2O_3 at low metal loadings.

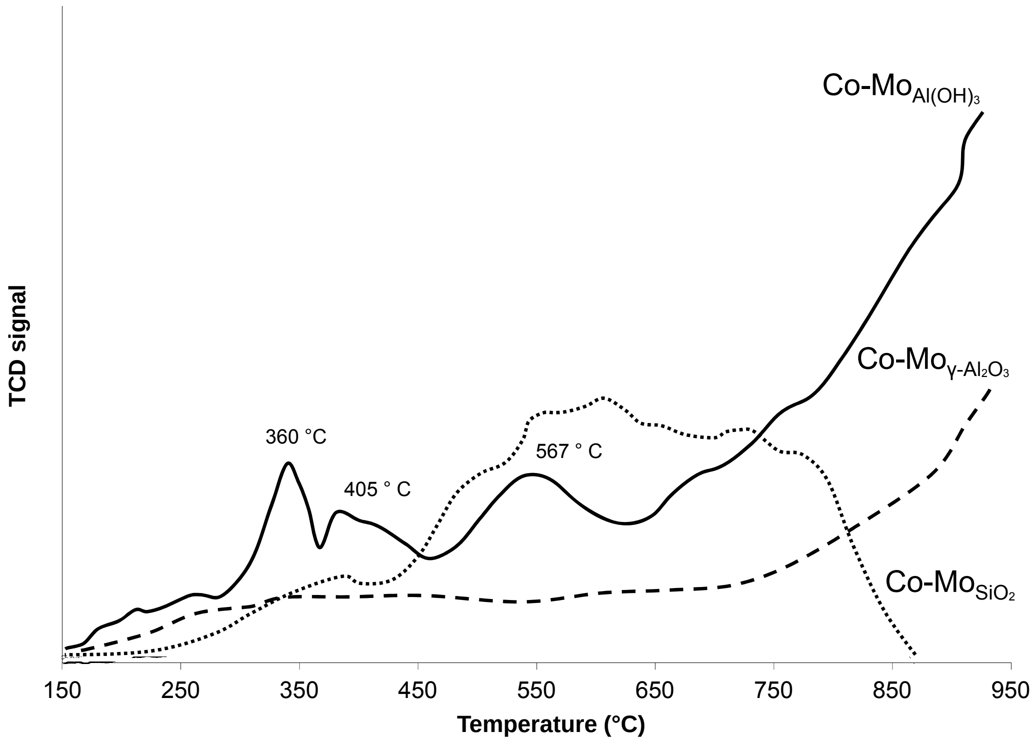

Figure 53(a): TPR profiles of the bimetallic (Co-Mo 3:1) catalysts.

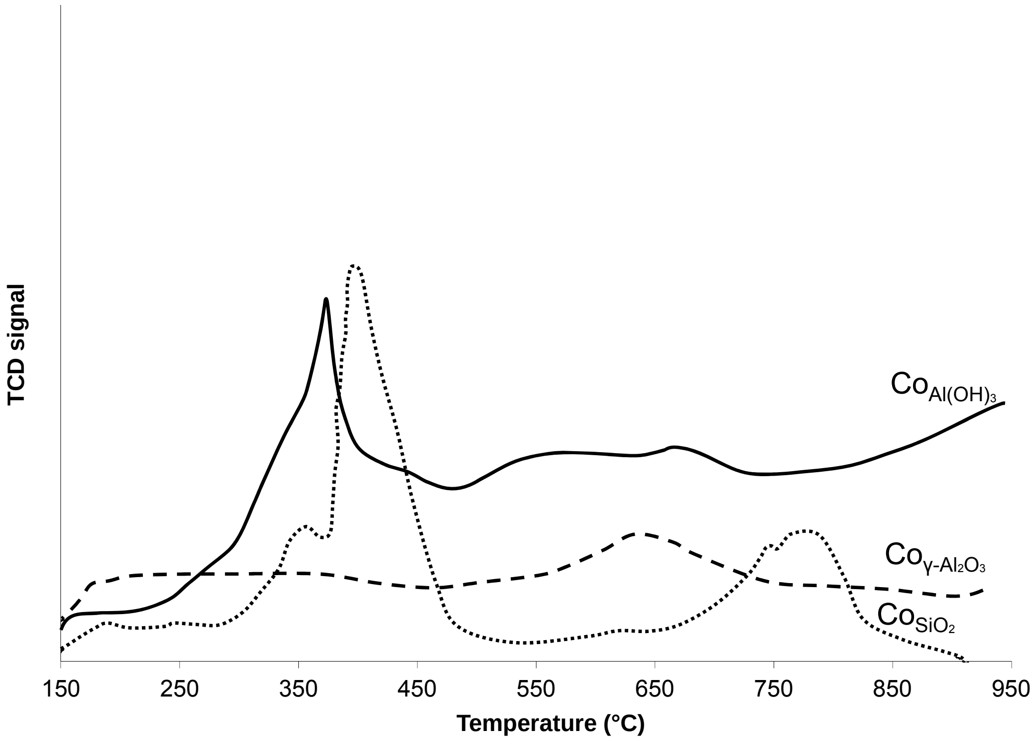

Figure 53(b): TPR profiles of the monometallic (Co) catalysts.

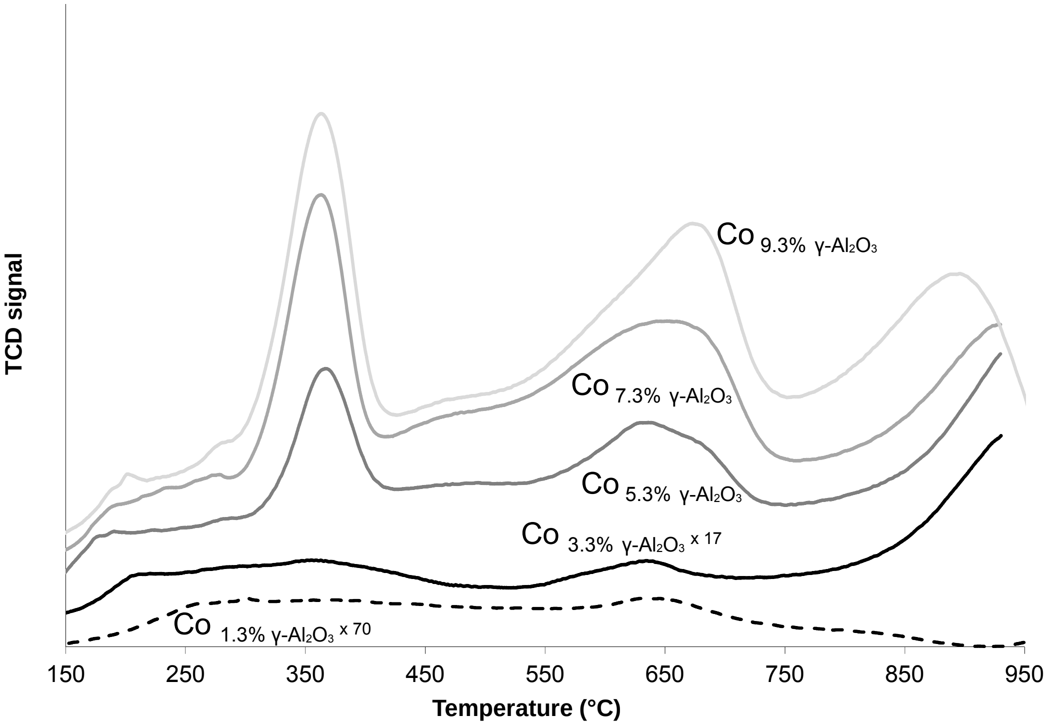

Figure 54(a): TPR profiles of monometallic (Co) catalysts supported on γ-Al_2O_3 with different cobalt loadings.

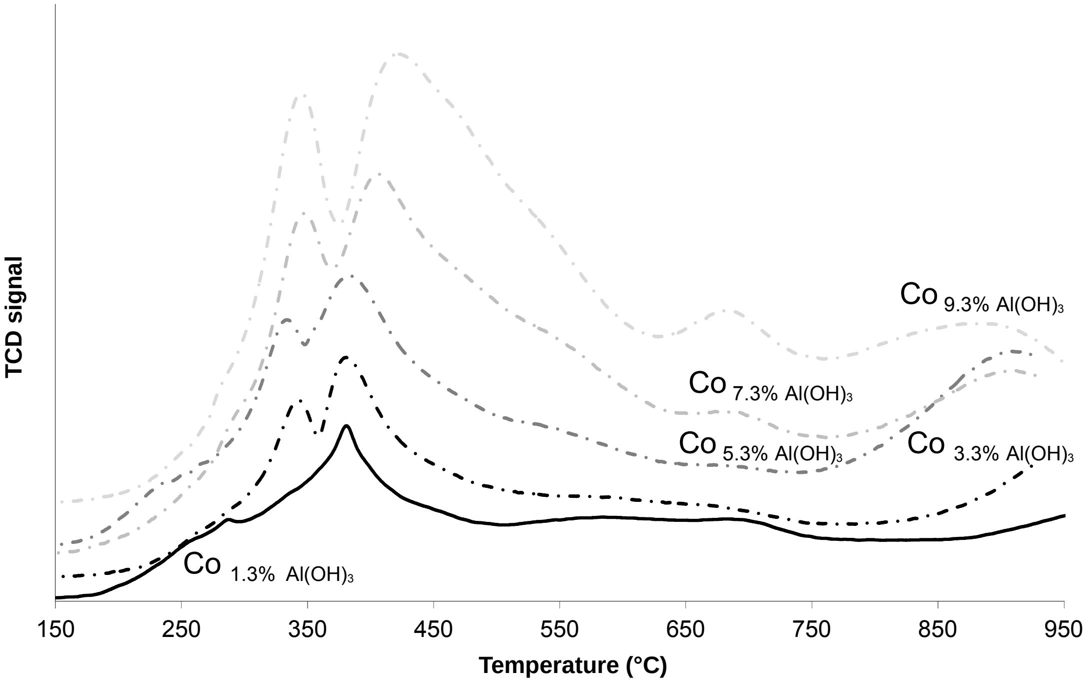

Figure 54(b): TPR profiles of monometallic (Co) catalysts supported on $Al(OH)_3$ with different cobalt loadings.

The reduction profiles for the monometallic and bimetallic catalysts show species reducing at different temperatures. It has been seen in the literature [33-37] that the species that reduce at low temperatures are cobalt oxides (Co^{+3} to Co^0, 300°C - 450°C). The ones that reduce at mid temperatures (450°C - 650°C) are related to cobalt-molybdenum oxides and molybdenum oxides, and the ones that reduce at the highest temperatures are cobalt aluminate species. As it was mentioned previously, monometallic and bimetallic catalysts do not show low temperature reduction species when the support used was γ-Al_2O_3. Therefore, in agreement with the UV-Vis DRS and XPS results, cobalt is preferentially forming aluminates when supported on γ-Al_2O_3.

When cobalt and molybdenum are supported on SiO_2, cobalt can be present as Co_3O_4 or $CoMoO_4$. It was shown before that cobalt forms oxides species that reduce at low temperatures and also species that reduce at high temperatures. The latter ones can be assigned to cobalt silicate species as it was seen in the literature. Therefore, in the bimetallic case, the species reducing at temperatures between 450 and 650 °C can be ascribed to cobalt molybdate oxides and molybdenum oxides.

Figures 54(a) and (b) show the results obtained from the metal loading catalyst series. When cobalt is impregnated on γ-Al_2O_3, as it can be seen in Fig. 54(a), the reduction profiles are different depending on the metal loading. On the other hand (Fig. 54(b)), when cobalt is impregnated on $Al(OH)_3$, the reduction profiles do not seem to depend on the metal loading.

The surface area of both supports has been measured resulting in 4 m^2/g for the $Al(OH)_3$ and 250 m^2/g for the γ-Al_2O_3. This difference in surface area would control the diffusion of cobalt into the matrix leading to less cobalt aluminate formation.

2.1.2.1.4- Same spot-Transmission electron microscopy

The effects of feeding different carbon sources on the catalyst performance have been studied by comparing the catalyst structure of cobalt supported on SiO_2 using TEM. Figure 55 shows how the structure of the cobalt clusters changes after the different reactions steps.

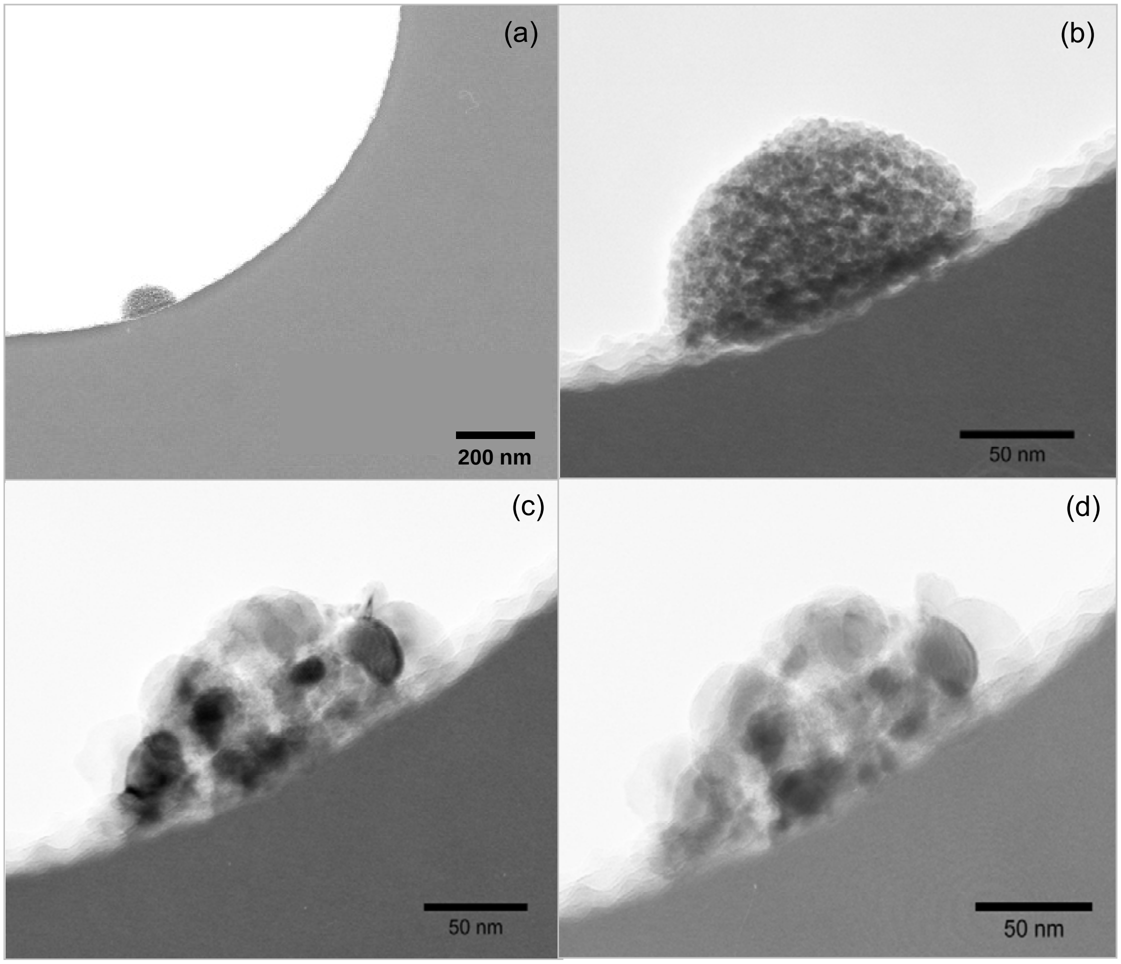

Figure 55: TEM-Same Spot. Catalyst: Co_{SiO_2} - Carbon source: ethylene. (a) TEM grid hole. (b) Calcined in air. (c) Reduced in hydrogen. (d) Ethylene for 1 minute.

After calcination, it can be seen that the cobalt (dark spots) is highly dispersed on the SiO_2 support. After reduction under H_2, it can be observed that the cobalt clusters have increased in size. Finally, after feeding ethylene for 1 minute, it can be seen that there is no change in cluster size compared with the reduced stage.

On the other hand, when carbon monoxide was used as carbon source, the metal cluster size increased after feeding it for 1 minute (Fig. 56).

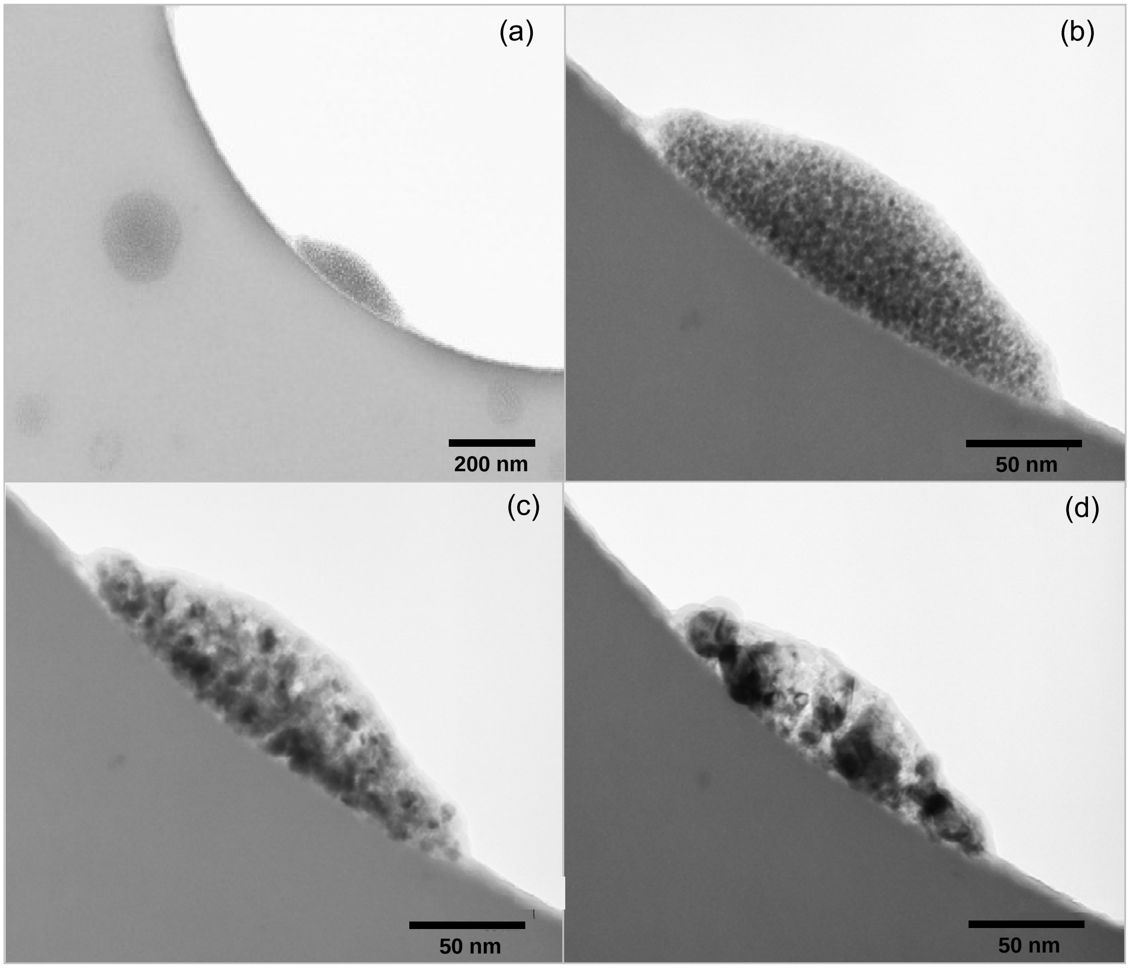

Figure 56: TEM-Same Spot. Catalyst: Co_{SiO_2}- Carbon source: carbon monoxide. (a) TEM grid hole. (b) Calcined in air. (c) Reduced in hydrogen. (d) Carbon monoxide for 1 minute.

Therefore, the type of feeding gas affects the catalysts performance. Carbon monoxide seems to reduce even further the cobalt, leading to the presence of some larger metal clusters. The sintering might lead to a decrease in carbon yield. It is also important to mention that the reactivity of the ethylene is higher than the carbon monoxide one, leading to larger carbon yield.

Figure 57 show an electron dispersion spectroscopy (EDS) spectrum obtained from one of these samples in order to probe that the dark spots are cobalt and not the support.

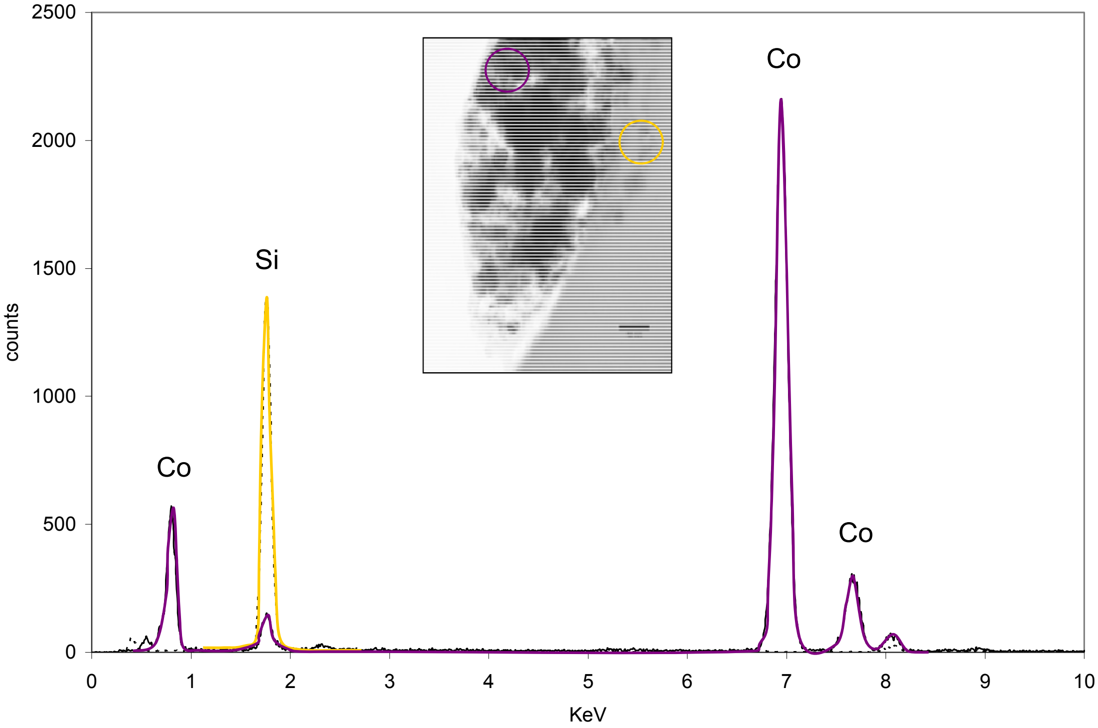

Figure 57: EDS spectrum of samples analyzed by same spot TEM.

2.2- Conclusions

It has been shown in this chapter that the variety of SWCNT selectivity and carbon yield shown in chapter 1 was due to the versatility of the sol-gel preparation method. By using this technique the morphology of Co-Mo catalysts used in the synthesis of SWCNT can be modified. In turn, these changes in morphology result in reproducible changes in SWCNT selectivity and carbon yield. By increasing the ammonia concentration in the sol-gel step, the silica particle size increases as the rates of hydrolysis and polymerization of TEOS are accelerated. Therefore, when the NH_4OH/TEOS ratio is high a large fraction of Co-Mo species remains encapsulated under the silica. By contrast, at low NH_4OH/TEOS ratios, the rate of silica polymerization is low, which results in an enhanced agglomeration of Co and Mo species. Both extremes are detrimental for SWCNT production. An optimum preparation is found at intermediate NH_4OH/TEOS ratios.

In chapter 1 it was also shown that MWCNT with different structures and yields are obtained while using different metal molar ratios, supports and carbon sources. It has been seen that Co-Mo catalysts with excesses of cobalt supported on aluminum hydroxide, and where ethylene was the carbon source, had the best performance. In this case the active phase, cobalt, was forming oxidic species that would reduce at low temperatures. On the other hand, when using gamma alumina, it was seen that cobalt was mostly forming non-reducible aluminates. Even though further investigation is still needed, the selective formation of oxidic species on aluminum hydroxide could be associated with its low surface area (~ 4 m^2/g) compared to γ-alumina (~ 250 m^2/g).

2.3- References

[1]- Alvarez W.E., Kitiyanan B, Borgna A., Resasco D.E. Synergism of Co and Mo in the catalytic production of SWNT by decomposition of CO, *Carbon*, **2001**, 39, 547.

[2]- Herrera J.E., Balzano L., Borgna A., Alvarez W.E., Resasco D.E. Relationship between the structure/composition of Co-Mo catalyst and their ability to produce SWNT by CO disproportionation, *J. Catal.*, **2001**, 204, 129.

[3]- Resasco D.E., Herrera J.E., Balzano L. Decomposition of carbon-containing compounds on solid catalysts for Single-Walled Nanotube production, *J. Nanosci. Nanotechol.*, **2004**, 4, 1.

[4]- Monzon A., Lolli G., Cosma S., Mohamed S.B., Resasco D.E., Kinetic Modeling of the SWNT Growth by CO Disproportionation on CoMo Catalysts, *J. Nanosci. Nanotechol.*, 2008, 8, 6141.

[5]- Brinker C.J., Sherer G.W., Sol-Gel science: The physics and chemistry of sol-gel processing, Academic press, **1989**.

[6]- Caruso R.A., Antonietti M., Sol-gel nanocoating: an approach to the preparation of structured materials, *Chem. Mater.*, **2001**, 13, 3272.

[7]- Mayerhöfer T.G.; Shen Zhijian, Leonova E.; Edén M.; Kritz A., Popp J.J., Consolidated silica glass from nanoparticles, *Solid State Chem.*, **2008**, 181, 2442.

[8]- Yuan P.; He H.P.; Wu D.Q.; Wang D.Q.; Chen L.J., Characterization of diatomaceous silica by Raman spectroscopy, *Spectrochim. Acta A*, **2006**, 60, 2941.

[9]- Maione A., Devillers M., Solid solutions of Ni and Co molybdates in silica dispersed and bulk catalysts prepared by sol-gel and citrate methods, *J. Sol. State Chem.*, **2004**, 177, 2339.

[10]- Resasco D.E., Herrera J.E., Balzano L., Decomposition of carbon-containing compounds on solid catalysts for single-walled nanotubes production, *J. Nanosci. Nanotechnol.*, **2004**, 4, 4, 398.

[11]- Pawelec B., Halachev T., Olivas A., Zepeda T.A., Impact of preparation method and support modification on the activity of mesoporous hydrotreating CoMo catalysts, *Appl. Catal. A*, **2008**, 30.

[12]- Ohler, N.; Bell, A.T., Selective oxidation of methane over MoO_x/SiO_2: isolation of the kinetics of reactions occurring in the gas phase and on the surfaces of SiO2 and MoO_x, *J. Catal.*,. **2005**, 231, 115.

[13]- Lim S., Wang C., Yang Y., Ciuparu D., Pfefferle L., Haller G.L., Evidence for anchoring and partial occlusion of metallic clusters on the pore walls of MCM-41 and effect on the stability of the metallic clusters, *Catal. Today*, **2007**, 123, 122.

---

[14]- Chen Y., Ciuparu D., Lim S., Haller G.L., Pfefferle L.D., The effect of the cobalt loading on the growth of single wall carbon nanotubes by CO disproportionation on Co-MCM-41 catalysts, *Carbon*, **2006**, 44, 67.

[15]- Chen Y., Ciuparu D., Lim S., Yang Y., Haller G.L., Pfefferle L., Synthesis of uniform diameter single-wall carbon nanotubes in Co-MCM-41: effects of the catalyst prereduction and nanotube growth temperatures, *J. Catal.*, **2004**, 225, 453.

[16]- Ciuparu D., Chen Y., Lim S., Haller G.L., Pfefferle L., Uniform-Diameter Single-Walled Carbon Nanotubes Catalytically Grown in Cobalt-Incorporated MCM-41, *J. Phys. Chem. B*, **2004**, 108, 2, 503.

[17]- Ciuparu D., Chen Y., Lim S., Yang Y., Haller G.L., Pfefferle L., Mechanism of Cobalt Cluster Size Control in Co-MCM-41 during Single-Wall Carbon Nanotubes Synthesis by CO Disproportionation, *J. Phys. Chem. B*, **2004**, 108, 15565.

[18]- Lim S., Li N., Fang F., Pinault M., Zoican C., Wang C., Fadel T., Pfefferle L.D., Haller G.L., High-Yield Single-Walled Carbon Nanotubes Synthesized on the Small-Pore (C10) Co-MCM-41 Catalyst, *J. Phys. Chem. C*, **2008**, 112, 12442.

[19]- Wang C., Lim S., Du G., Loebicki C.Z., Li N., Derrouiche S., Haller G.L., Synthesis, Characterization, and Catalytic Performance of Highly Dispersed Co-SBA-15, *J. Phys. Chem. C*, **2009**, 113, 14863.

[20]- Li N., Wang, Derrouiche S., Haller G.L., Pfefferle L.D., Role of Surface Cobalt Silicate in Single-Walled Carbon Nanotube Synthesis from Silica-Supported Cobalt Catalysts, *ACS Nano*, **2010**, 4, 3, 1759.

[21]- Ciuparu D., Haider P., Fernández-García M., Chen Y., Lim S., Haller G.L., Pfefferle L., X-ray Absorption Spectroscopic Investigation of Partially Reduced Cobalt Species in Co-MCM-41 Catalysts during Synthesis of Single-Wall Carbon Nanotubes, *J. Phys. Chem. B*, **2005**, 109, 16332.

[22]- Zygmunt, J.; Krumeich, F.; Nesper, R., Novel silica nanotubes with a high aspect ratio-synthesis and structural characterization, *Adv. Mater.*, **2003**, 15 1538.

[23]- Cheung, C.L.; Kurtz, A.; Park, H.; Lieber, C.M., Diameter-controlled synthesis of carbon nanotubes, *J. Phys. Chem. B*, **2002**, 106, 2429.

[24]- Henry M.; Jolivet J.P.; Livage J., Aqueous chemistry of metal cations: hydrolysis, condensation and complexation, *Struct. Bond.*, **1992**, 77, 153.

[25]- Herrera J.E.; Balzano L.; Borgna A.; Alvarez W.E.; Resasco D.E., Relationship between the structure/composition of Co-Mo catalysts and their ability to produce

single-walled carbon nanotubes by CO Disproportionation, *J. Catal.*, **2001**, 204, 129.

[26]- Alvarez W.; Kitiyanan B.; Borgna A.; Resasco D.E., Synergism of Co and Mo in the catalytic production of single-wall carbon nanotubes by decomposition of CO, *Carbon*, **2001**, 39, 547.

[27]- Herrera J.E.; Resasco D.E., Role of Co-W interaction in the selective growth of single-walled carbon nanotubes from CO disproportionation, *J Phys. Chem. B*, **2003**, 107, 3738.

[28]- Herrera, J., Resasco, D.E., Loss of single-walled carbon nanotubes selectivity by disruption of the Co–Mo interaction in the catalyst, *J. Catal.*, **2004**, 221, 354.

[29]- Herrera J.E.; Resasco D.E., In situ TPO/Raman to characterize single-walled carbon nanotubes, *Chem Phys Lett.*, **2003**, 376, 3-4, 302.

[30]- Chin R.L.,Hercule D.M., Surface spectroscopic characterlzatlon of cobalt-alumina catalysts, *J. Phys. Chem.*, **1982**, 86, 3079.

[31]- Declerk-Grimee R.I.,Canesson P., Friedman R.M., Friplat J.J., Influence of reducing and sulfiding treatments on Co/Al_2O_3 and Mo/$A1_20_3$ catalysts. An X-ray photoelectron spectroscopy study, *J. Phys. Chem-US*, **1978**, 82, 885.

[32]- Strydom C.A., Strydom H.J., X-ray photoelectron spectroscopy studies of some cobalt(II) nitrate complexes, *Inorg. Chim. Acta*, **1989**, 159, 191.

[33]- Finocchio E., Montanari T., Resini C., Busca G., Spectroscopic characterization of cobalt-containing solid catalysts, *J. Mol. Catal. A-Chem.*, 2003, 204, 535.

[34]- Wivel C., Clausen B.S., Candia R., Morup S., Topsoe H., Mössbauer emission studies of calcined Co-Mo/Al_2O_3 catalysts: catalytic significance of Co precursors, *J. Catal.*, **1984**, 87, 497.

[35]- Lim S., Ciuparu D., Chen Y., Pfefferle L., Haller G.L., Effect of Co-MCM-41 conversion to cobalt silicate for catalytic growth of single wall carbon nanotubes, *J. Phys. Chem. B*, **2004**, 108, 20095.

[36]- Jongsomjit B., Panpranot J., Goodwin J. G. Jr., Co-support compound formation in alumina-supported cobalt catalysts, *J. Catal.*, **2001**, 204, 98.

[37]- Stranick M.A , Houalla M., Hercules D.M., The influence of TiO_2 on the speciation and hydrogenation activity of Co/Al_20_3 catalysts, *J. Catal.*, **1990**, 125, 214.

CHAPTER 3

Acknowledgments:
J.Blackburn, National Renewable Energy Laboratory
R. Jentoft, The University of Oklahoma
M. Pilar Ruiz, The University of Oklahoma
Y. Tan, SouthWest Nanotechnologies
R. Prada Silvy, SouthWest Nanotechnologies

CHAPTER 3

3.1- Metrology

Assessment of purity and quantification of SWCNT in bulk samples is crucial in the production of nanotubes for commercial or scientific applications. Knowing with some degree of precision the SWCNT concentration in a given sample gives the application researchers the possibility of comparing the effects of adding varying amounts of SWCNT to the composite material [1-3] or devices [4-9] that they are developing. A good quantification of SWCNT concentration in a sample can also allow researchers to do proper comparison of SWCNT from different sources, or with varying structural characteristics. Raman spectroscopy has been widely used to assess SWCNT selectivity. For example, the full width at half maximum (FWHM) of the Raman D-band (~1350 cm^{-1}) has been used by several researchers [10-13]. The FWHM D-band of the non-SWCNT carbonaceous species is generally much broader than that of the SWCNT. Likewise, the absolute intensity of the G and D-bands (~1590 cm^{-1}, ~1350 cm^{-1}) [11,14,15] and, the G/D and D/G' ratios [11,16-20] have been used to measure the SWCNT selectivity. The G/D ratio is generally considered as a SWCNT selectivity parameter because the G-band, being a first-order Raman scattering process is not affected by defects. By contrast, the D-band is a second-order Raman scattering process that is enhanced by the presence of defects. The use of the G/D ratio as a quantification method for the density of defects has generated some controversy. For instance, Antunes et al. [12] have shown that the intensity of the D-band is affected by curvature effects. They have proposed that the product of the D/G intensity ratio and the FWHM of the D-band is a better indicator of CNT selectivity. A method that may simplify the problem was proposed by Nishide et al. [14]. This work has pointed out that the Raman intensity of SWCNT is highly enhanced by resonance effects, but these effects are much weaker in amorphous carbon. Therefore, these authors concluded that the absolute intensity of the G-band may be a more suitable SWCNT selectivity parameter than the D/G ratio. Different authors have measured the shift between the second and the first order transitions [21], and used these values to quantify the purity of SWCNT in a sample. Another approach for assessing SWCNT selectivity is a technique proposed by Liu et al. [22] in which Raman scattering is combined with photoluminescence. In general, these selectivity assessment methods have been conducted on solid samples, which have the serious drawback of composition heterogeneity and variations in texture. If not properly weighted, these variations may greatly affect the results and yield wrong estimates of the purity. In this contribution, we propose a modified Raman analysis method that results in a reliable quantitative assessment of SWCNT purity.

Characterization techniques

Nuclear magnetic resonance (NMR)

This is a non-destructive technique that is used to determine the structure of organic molecules. Briefly, a solution of a sample is set between magnets (Fig. 58(a)) while irradiating the sample with radio frequency energy (rf). The rf absorbed is monitored and registered while varying the external magnetic field.

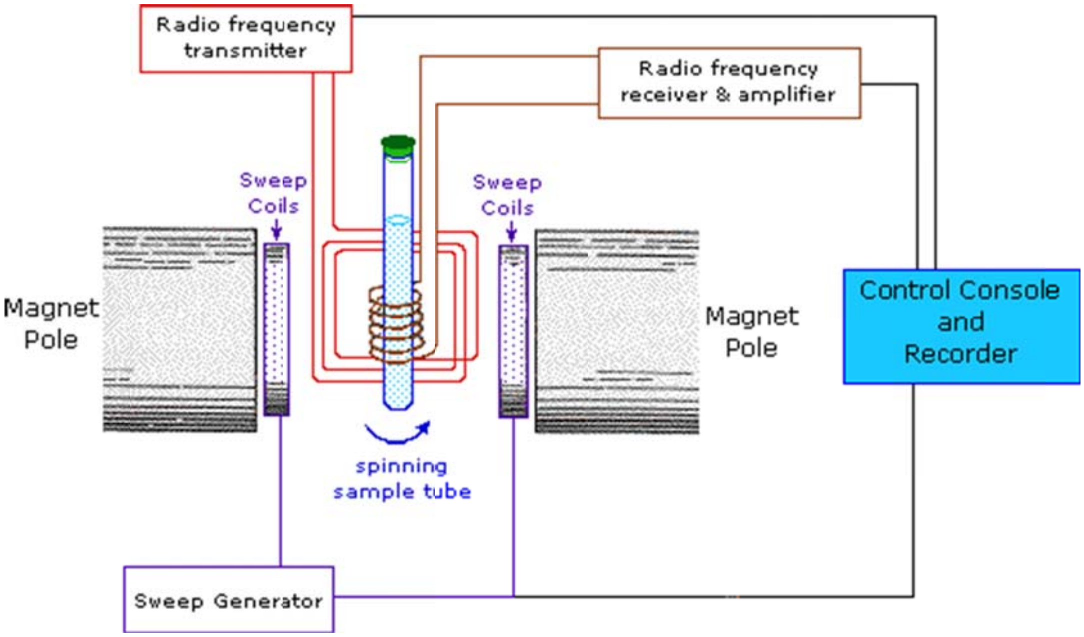

Figure 58(a): NMR equipment set up scheme.

Isotopes with fractional nuclei (proton) spin (1/2), such as ^{13}C, generate a magnetic field due to their spinning. When these isotopes are in the presence of an external magnetic field, there are two nuclei spin states, +1/2 and -1/2. The difference in energy (usually expressed in MHz) between the spin states depends on the external magnetic field (Fig. 58(b)). Radio frequency energy corresponding to the spin state separation causes the excitation from the +1/2 to the -1/2. The external magnetic field is varied in order to see the resonance (specific magnetic field value). The NMR for different compounds is different due to the surrounding electrons effect. They generate a secondary magnetic field opposed to the external and therefore in order to see the excitation +1/2 and -1/2 (resonance) different external field values are required.

The difference in energy spin states is named as chemical shift and consists of two contributions. The shielding tensor and the knight shift. The former one due to the electronic orbital magnetism and the latter one due to a Fermi contact effect of electron spin that appears only in metals. It is important to mention that the chemical shift is experimentally measured by comparison with a standard such as tetramethylsilane. The units of the chemical shift are parts-per-million (ppm). The NMR data is represented as the chemical shift (ppm) vs the signal strength that is proportional to the molar concentration of isotope in the sample.

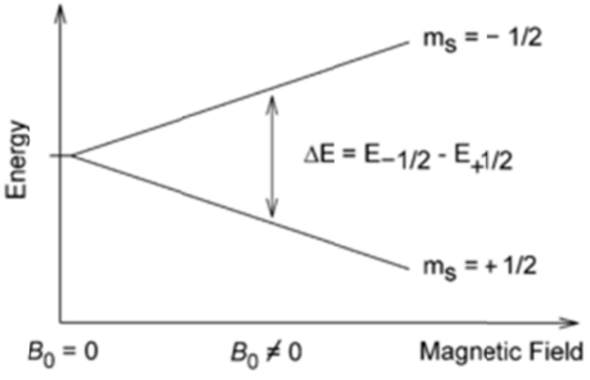

Figure 58(b): Spin states energy vs external magnetic field .

Photo luminescence (PL)

Photoluminescence is a process where photon excitation is followed by photon emission. Semiconductor materials present a gap between the valence band (electrons having energies below certain value) and the conduction band (electrons having energies above certain value). Loosely attached electrons can absorbed energy and be raised to excited electronic states when light (photon) with energy greater than the band gap interacts with them. The excited electron falls finally to the valence band emitting the excess of energy as a luminescent photon as shown in Fig. 59. The energy of the emitted photon is a direct measurement of the energy band gap.

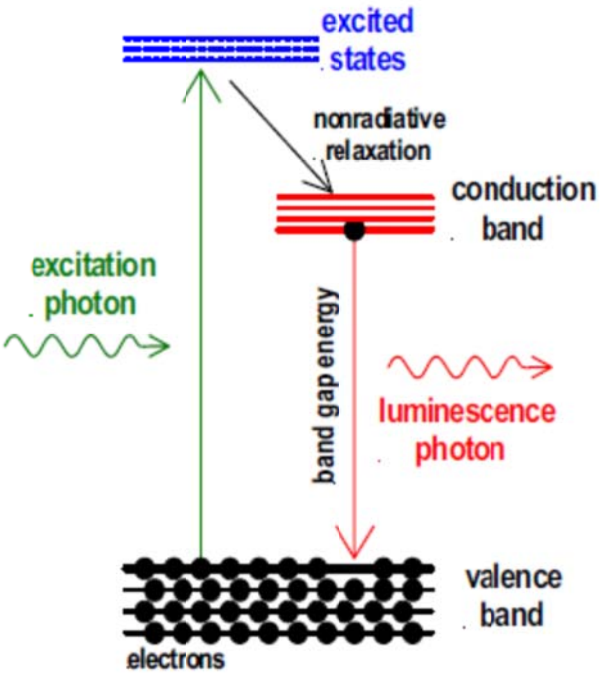

Figure 59: Photo luminescent phenomena.

Other characterization techniques such as Raman scattering, optical absorption, electron microscopy and thermal gravimetric analysis have been used for the data analysis of this chapter. The theoretical and equipment set up have been shown in previous chapters.

3.2- Raman scattering model

3.2.1- Experimental

The CoMoCAT® process, developed by our group in 1998 [23] and further improved during subsequent years [24-27], has been optimized for large-scale production and commercialization by SouthWest NanoTechnologies (SWeNT®). During this process, the influence of different operating parameters has been investigated. Among them, temperature of calcination, reduction, and growth, as well as space velocity (gas flow rate/catalyst volume ratio), reaction time, reactor design, operation, etc., have been found to have a strong influence on nanotube yield, nanotube type, and purity. From these optimization studies a range of SWCNT samples with varying degrees of SWCNT selectivity have been obtained. In the present study, a series of samples of varying SWCNT selectivity has been prepared to evaluate the assessment method. The growth of SWCNT for all samples was carried out on the same type of powder catalyst composed of Co–Mo particles supported on high-surface area silica, with a total metal loading of 2 wt % and a Co–Mo molar ratio of 1/2. Before starting the growth reaction, the catalyst was reduced in H_2 flow at 500 °C for 30 min. Then, H_2 was replaced by He, while increasing the temperature to 700 °C. At this temperature, the catalyst was placed in contact with carbon monoxide (CO) for 30 min. After the growth period, the system was cooled down under He flow. To separate the SWCNT product from the catalyst, the as-produced material was treated in 30 % HF solution, which completely dissolved the silica support. To eliminate the metal species (Co and Mo) the sample was further treated in an HCl solution. After these treatments the samples contained about 8 wt % Co and Mo, with no traces of Si or any other element. Two external samples of known SWCNT content were employed as reference points in the purity scale. A carbon black sample was used as the standard for zero SWCNT content. The sample to be considered as of maximum purity (100%) was provided by the National Institute of Standards and Technology (NIST), where it is identified as VAMAS TWA 34. The sample itself is a length-sorted SWCNT dispersion in an aqueous 1% (mass/vol) sodium deoxycholate solution. The estimated concentration of nanotubes in the original sample was about 50 mg/L. This sample was taken from the liquid that will become a NIST reference material for dispersed, length sorted, carbon nanotubes (RM 8281 ‘‘Long’’ fraction, estimated average length ~0.75 µm). The synthesized samples were purified again by using a method proposed by Miyata et al. [28], which includes sonication, suspension in sodium cholate, 1-h ultra-centrifugation at 207,000 g, and collection of the supernatant fractions. The intensity of the Raman G-band was measured for all the ultra-purified samples and correlated to the relative concentration of SWCNT in the sample. For comparison, seven as-produced solid SWCNT samples, still associated with the silica-supported catalyst, were analyzed by Raman scattering. Specifically, aqueous suspensions of the different SWCNT samples were prepared by placing 5 mg of purified SWCNT in 7 ml of 2 wt% solution of sodium cholate (SC) in DI water and ultra-sonicating with a Horn Sonic Dismembrator, Model 500, Fisher Scientific for 1 h at 7 mW of power. To compare these sonicated suspensions at the same total solid concentration, the following method was followed. First, the OA of the suspension was measured at a wavelength of 770 nm. Then, the concentration of all the suspensions, including the reference from NIST, was adjusted to obtain the same absorptivity for each one by diluting with DI water. A value of relative concentration equal to 1.0 was arbitrarily assigned to each suspension with an absorption coefficient of 0.85. To study the variation of Raman intensity with concentration, various dilutions were prepared for each sample.

Several methods were combined to assess the SWCNT selectivity of the samples in the series. Raman spectroscopy of the suspensions was conducted in a Jovin Yvon-Horiba Lab spectrometer, equipped with a CCD detector and with a laser excitation of 633 nm (He–Ne laser). Eight spectra were taken for each sample, varying the concentration by diluting with deionized water. In addition to the measurements on liquid suspensions, Raman spectra were obtained on solid samples. In this case, the collection time for each measurement was 10 s; to assure that the measurements provided an average that was representative of a given sample, 50 measurements on different spots were taken on each sample. The G/D ratio and the FWHM of the D-band were used as SWCNT selectivity indicators. The same SWCNT suspensions used in Raman characterization were characterized by OA in an UV–Vis (UV-2101PC, Shimadzu spectrophotometer). Images of the purified samples were obtained by Transmission (JEOL 2000-FX STEM), and Scanning Electron Microscopy (JEOL JSM-880 SEM). The samples analyzed by TEM were prepared by suspending the SWCNT by mild sonication in isopropanol and depositing a drop over the TEM grid. The samples analyzed by SEM were deposited onto copper strips and coated with gold and palladium. TGA of purified samples was conducted in a TGAQ500 (TA instruments Inc.) under flow of air at 200 °C for 15 min and heated to 750 °C at a rate of 5 °C/min. The as-produced solid SWCNT samples from the synthesis reactor were characterized using Raman spectroscopy. The collection time in each spot and number of spots probed for the as-produced solid sample were the same as those for the purified samples (10 s, 50 spots). As discussed below, these measurements allowed us to evaluate the level of heterogeneity in each sample and to obtain a representative average of the SWCNT selectivity parameters.

3.2.2- Results

3.2.2.1- Raman scattering of purified SWCNT samples

3.2.2.1.1- SWCNT suspensions

Nishide et al. [14] have proposed to use the G-band intensity of nanotube suspensions as an indication of the purity of a SWCNT sample. In this study we have found that this intensity is not only a function of the purity of the SWCNT sample but also of the overall solid concentration of the suspension. As shown in Fig. 60, the G-band intensity (I_G^{LIQ}) exhibits a characteristic profile as a function of relative concentration. As the concentration decreases from the initial value (1.0), the scattering intensity increases, reaching a maximum at about the same concentration for all the samples and then it decreases with further dilution. This ‘‘thickness effect’’ is typically observed when the light scattering initially increases with increasing concentration, but it is attenuated at higher concentrations by absorption. In this particular case, while the Raman scattered radiation is entirely due to the SWCNT scatterers present in the suspension, the absorption is caused by all the suspended species (attenuators). The fraction of incoming radiation scattered is proportional to the concentration of SWCNT since the scattering cross section of SWCNT is much larger than any other suspended species. But, at the same time, the absorption of both incoming and outgoing radiation is due to the relative concentration (C) of all the suspended species. Therefore, we can express the variation of the scattered radiation as a function of carbon concentration with the following equation:

$$\frac{I_S}{I_O} = PCe^{-SC} \quad (1)$$

where I_S and I_0 represent the effective scattered radiation and incoming radiation intensities, respectively. P is the fraction of SWCNT in each sample and S is a proportionality constant that is common for all samples. This equation has been used to fit the experimental data of intensity of the scattered G-band as a function of concentration of solids in the suspension. Using only P and S as adjustable parameters, the fitting for all the samples is very good and provides values of the fraction of SWCNT (P) for each sample (see solid lines in Fig. 60). By fixing the P factor obtained for the NIST reference sample as corresponding to 100% SWCNT we can obtain direct estimates of the fraction of SWCNT in each sample.

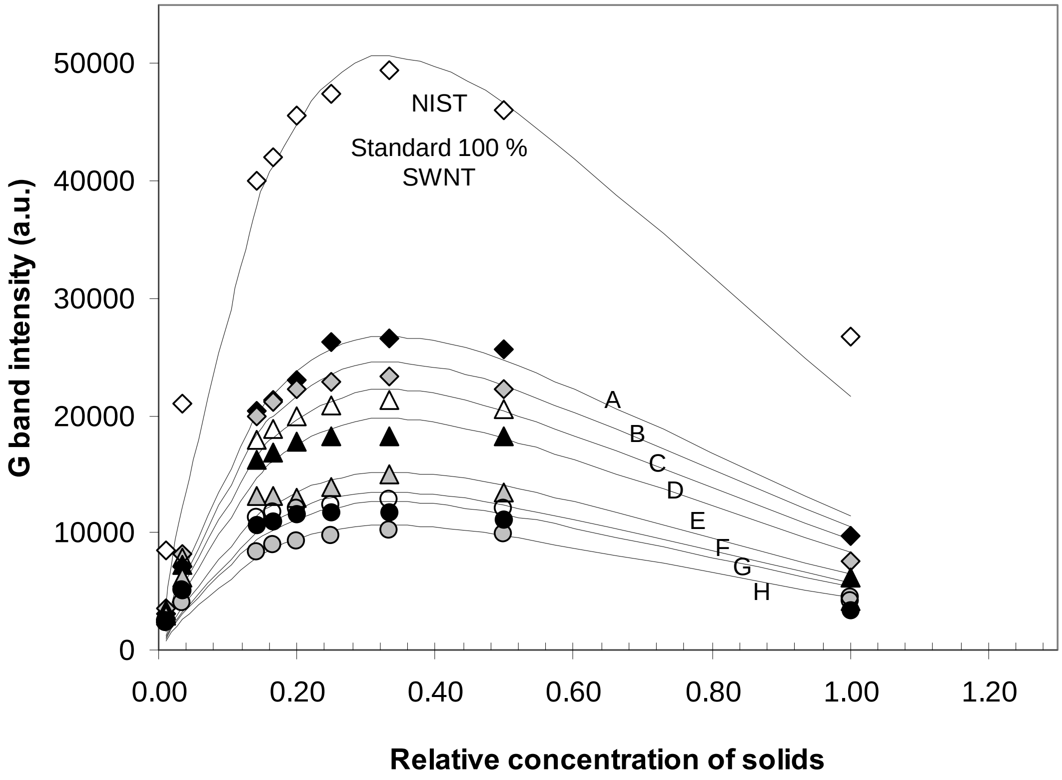

Figure 60: G band intensity of SWCNT suspensions of varying concentrations, relative to those showing the same absorption intensity.

The corresponding *P* factors for all the samples in the series are shown in Table 3. The samples are identified as A-to-H in order of decreasing SWCNT selectivity.

Table 3: P (%) values obtained from Raman of the liquid suspensions. SWCNT area/Total area obtained from TGA analysis. Resonance factor obtained from OA analysis. G/D (ap), G/D 3, G/D 50 and 1/FWHM D-band obtained from Raman of the solid samples.

	Raman suspensions	TGA	UV-Vis	Raman solids			
Sample	P (%)	SWCNT area/ Total area	Resonance factor (x100)	G/D (ap)	G/D 3	G/D 50	1/FWHM D-band (x100)
NIST ref	100.00	-	-	-	-	-	-
A	52.90	1.00	7.73	29.00	-	-	-
B	48.30	1.00	7.32	23.00	11.20	11.68	5.00
C	43.80	0.77	7.03	22.90	11.00	9.06	3.60
D	38.90	0.85	6.65	18.80	13.10	8.60	4.00
E	30.00	0.65	4.43	18.50	6.00	7.21	3.40
F	26.70	0.29	2.77	20.70	1.40	4.93	2.70
G	24.80	0.42	3.91	13.70	7.90	6.32	3.20
H	20.90	0.49	2.76	4.50	7.60	7.98	3.30

3.2.2.1.2- Solid samples

One of the most important aspects that need to be addressed when assessing the SWCNT selectivity of solid samples is heterogeneity. However, it has been common practice to assess SWCNT selectivity by doing the average of G/D ratios of only a few (e.g., one to three) Raman measurements [24,29-32]. Table 3 shows the average G/D Raman intensity ratios obtained on the samples in the series by using only three spots (G/D 3). As illustrated in Fig. 61, a poor correlation is obtained between the *P* factor obtained with the suspensions and the G/D 3 ratios obtained from averaging only three spots on the solid samples.

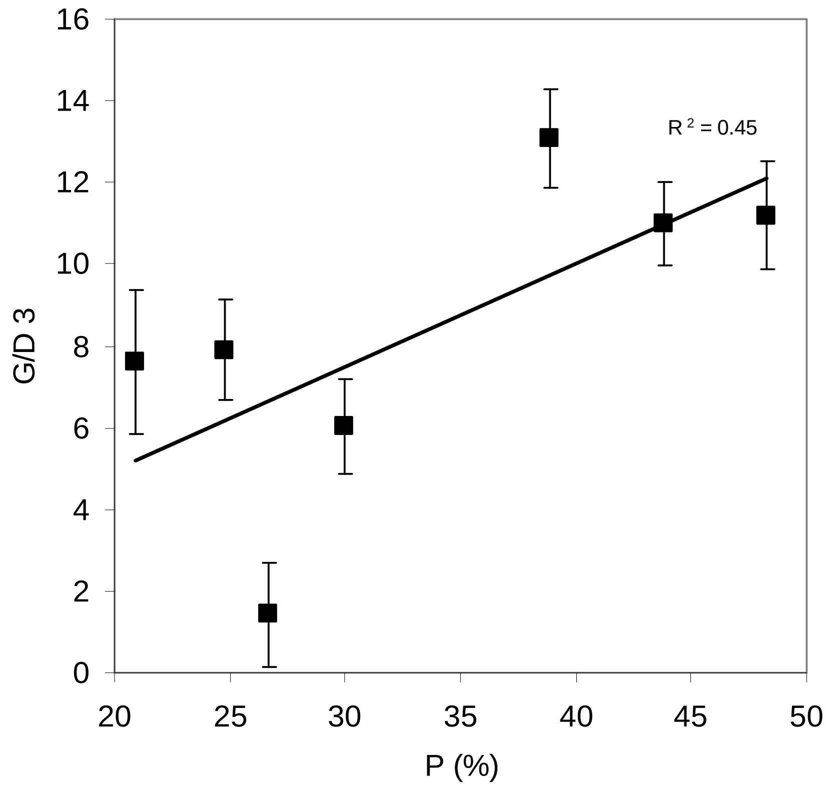

Figure 61: Comparison of the P (%)parameter values with the G/D ratios of the solid samples by averaging 3 spots (G/D 3).

A much more representative average can be obtained by increasing the number of measurements. For instance, Fig. 62 shows the rather high variability in the G/D ratios obtained on 50 different spots on a given sample together with the accumulated average, which as expected shows gradually lower variability as the number of measurements increases.

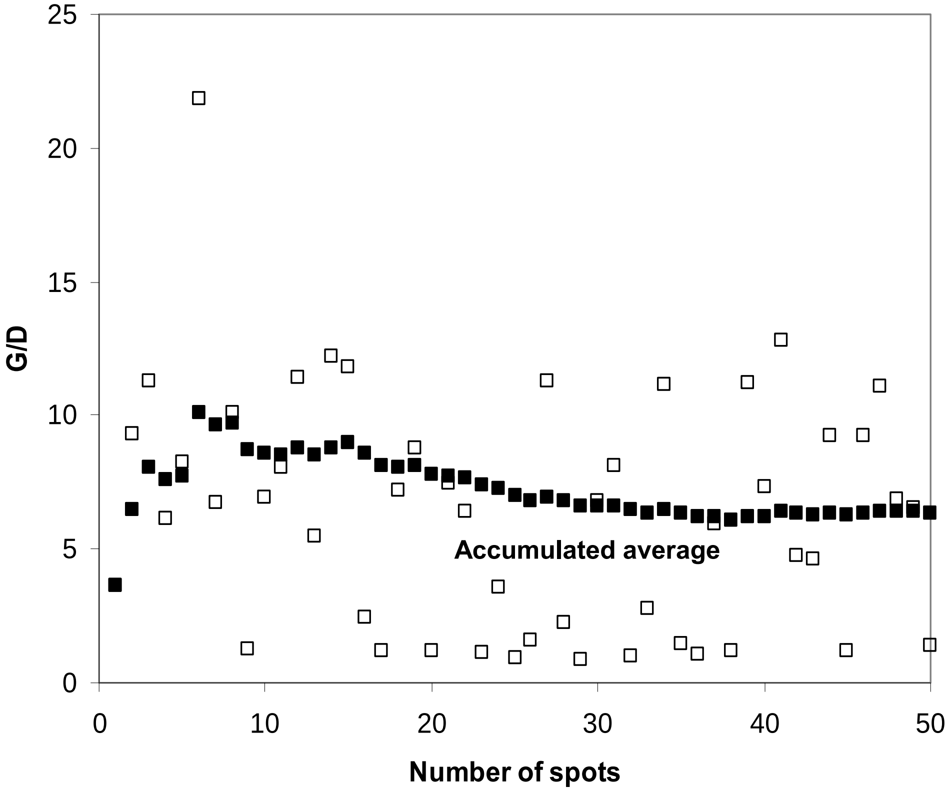

Figure 62: G/D accumulated average and the singular G/D ratios of solid samples for 50 different spots (Sample G).

Similar analysis was done for each solid sample in the series and the results of accumulated averages are compared in Fig. 63(a). It can be seen that depending on the variability of the specific sample one may need 30 or more spots to obtain a reliable average. We have used a common statistical method [33] to establish margins of error (E) in a number of measurements (n) with a given level of confidence, based on the following expression $E = z (\sigma/\sqrt{n})$, in which σ is the standard deviation and z is calculated from the desirable level of confidence. For example, for a level of confidence of 95% and assuming a standard normal distribution of the measurements, z becomes 1.96 [33]. Then for $n = 50$ measurements, the margins of error can be readily obtained for each sample (Margins of error for G/D 50 values – B: 1.33, C: 1.02, D: 1.2, E: 1.28, F: 1.76, G: 1.23, H: 1.15).

Figure 63(b) shows the accumulated average of the 1/FWHM of the D-band as a function of the number of measurements. The general trend shows that as the SWCNT selectivity of the sample increases, the D-band width decreases and therefore 1/FWHM D-band increases. Since the D-band is a convolution of different bands related to different defective carbon species, the more species there are in the sample, the broader will be the width. Table 3 shows the average for each sample. The margin of error for n = 50 measurements were obtained for each sample (Margins of error for 1/FWHM D-band (·103) – B: 0.34, C: 0.35, D: 0.37, E: 0.34, F: 0.39, G: 0.41, H: 0.51).

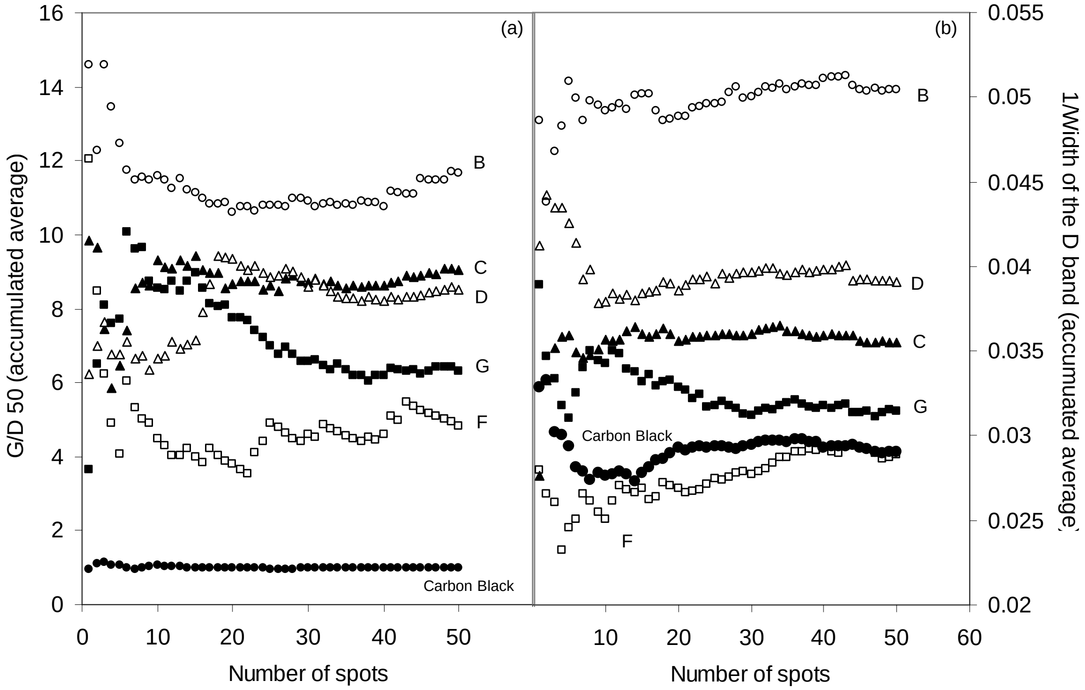

Figure 63: Accumulated average values (50 spots) of solid samples with different purities. (a) G/D ratios; (b) 1/FWHM of the D-band.

While the overall trend is that the G/D ratio increases and the width of the D-band decreases from the lowest-SWCNT selectivity sample to the highest-SWCNT selectivity sample, there are a few samples of intermediate values in which it is hard to make a decision about which one has a higher SWCNT content. Taking *P* of the suspensions as a measure of the fraction of SWCNT in the sample, we have plotted in Fig. 64 the variation of the G/D 50 average ratio and the 1/FWHM of the D-band in the purified solid samples with P in the suspensions to compare the goodness of each method. In this case, the correlation of *P* and G/D 50 is clearly much better than when few spots were used. The correlation factors for G/D 50 and 1/ FWHM of the D-band with *P* are 0.89 and 0.73, respectively, which are significantly higher than those obtained with three spots (0.45 and 0.41, respectively).

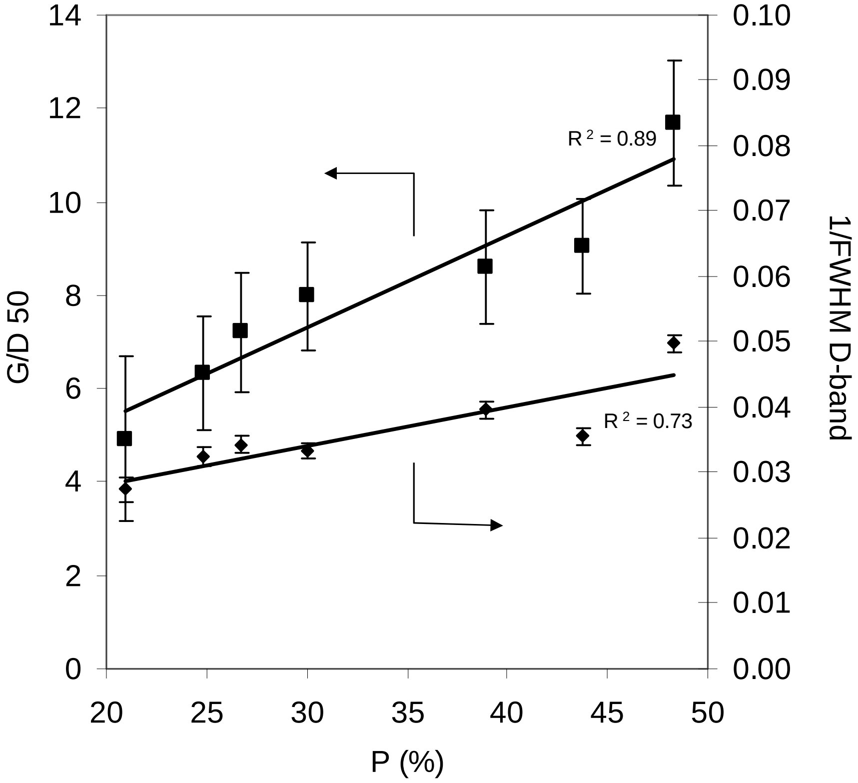

Figure 64: G/D 50 ratios-1/FWHM of the D-band vs the P (%) parameter values.

3.2.2.2- Scanning and transmission electron microscopy

Electron microscopy provides a visual assessment of the overall SWCNT selectivity of the sample, but assessment of the fraction of SWCNT by microscopy methods is at best semi-quantitative and in most cases, the imaged fraction of the sample may not be fully representative of the entire sample [34]. With these limitations in mind, a qualitative comparison of the various samples in the series has been attempted. Figure 65 shows the SEM images of all the samples in the series. To compare with the Raman results, the images were ordered by observation of SWCNT selectivity, starting with the one with the highest fraction of SWCNT present. The qualitative order obtained by SEM coincides very well with the quantitative *P* factor obtained from the Raman analysis of the suspensions. The samples with low *P* factor showed few SWCNT and larger quantities of non-SWCNT carbonaceous species and residual catalyst. Samples with intermediate values of *P* showed comparable amounts of SWCNT and impurities. Samples with the highest *P* factors exhibited only SWCNT in the SEM image. The TEM images for samples B and F compared in Fig. 66(a) and (b) clearly show the differences between high-SWCNT selectivity and low-SWCNT selectivity samples. The high-SWCNT selectivity sample B is mainly composed of SWCNT with small catalyst particles remaining. On the other hand, the low-SWCNT selectivity sample F exhibits other carbon structures like fibers and MWCNT as well as relatively large catalyst particles.

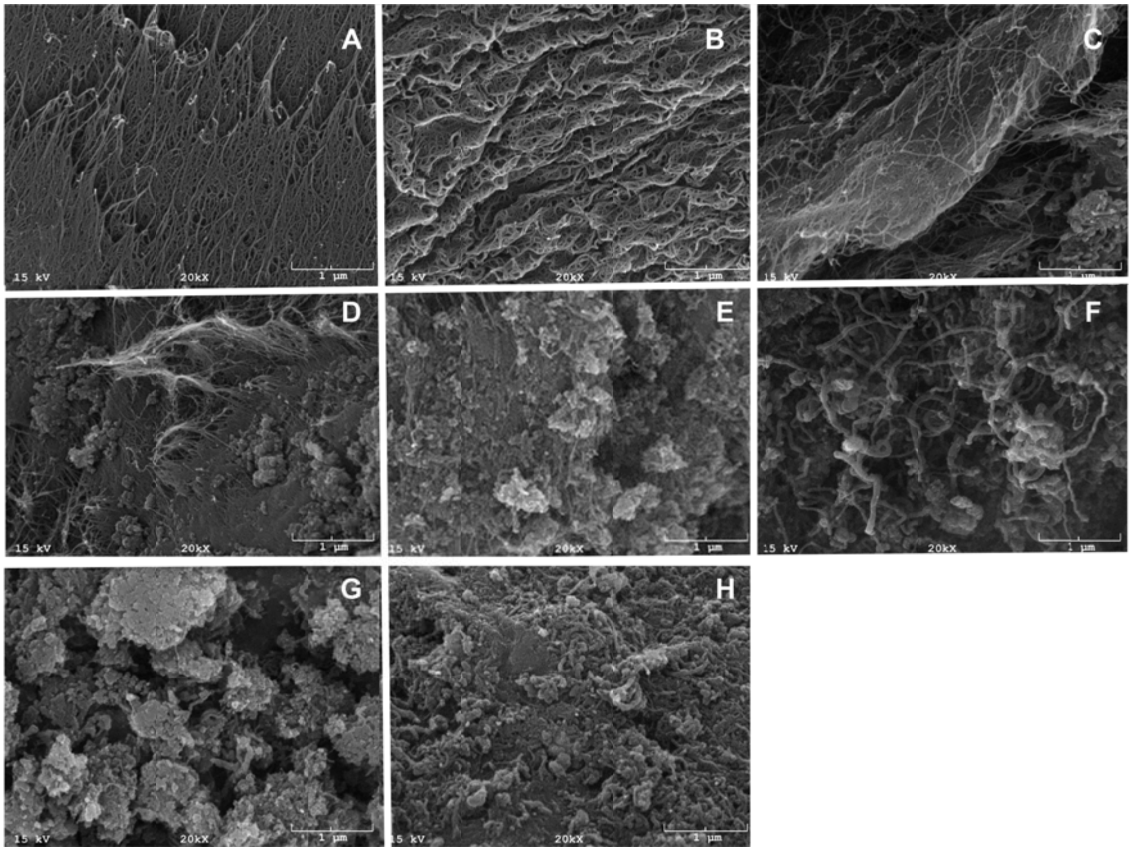

Figure 65: SEM images of the purified solid samples series. SWCNT selectivity decreases from A to H.

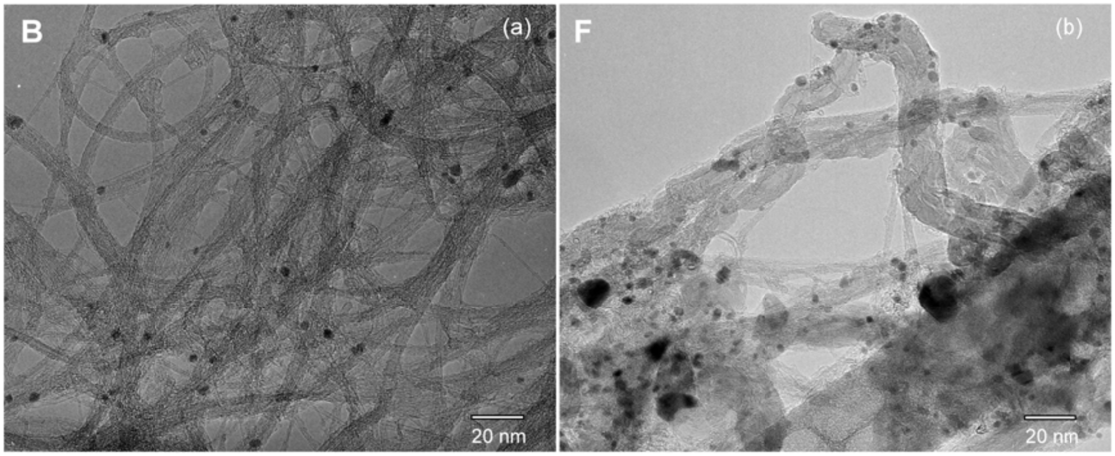

Figure 66: TEM images. (a) High SWCNT selectivity sample (Sample B); (b) Low SWCNT selectivity sample (Sample F).

3.2.2.3- Thermo gravimetric analysis

In TGA the weight change caused by oxidation of carbonaceous species is monitored in a microbalance [35]. This technique is typically used to obtain semi-quantitative estimates of the fraction of SWCNT in a sample but, as we discuss below, it is not a precise quantitative technique. Figure 67(a) shows the TGA profiles for two samples of the series, one with a high fraction of SWCNT (B, P = 48.3%) and one with low fraction (F, P = 26.7%). While the profile for the good sample B exhibits only one peak, the lower SWCNT selectivity sample F shows two. The peak appearing at the lower temperature is typically ascribed to the oxidation of SWCNT while the one at higher temperatures is related to other carbonaceous species, e.g. graphitic nano-fibers [35]. The TGA results, reported as the ratio of the area of low-temperature peak over the total area, are included in Table 3. At the same time, Fig. 67(b) compares the TGA data with the SWCNT fractions as estimated from the P factors. Again, while the general trend is in agreement, the correlation factor is relatively low, 0.68. It must be pointed out that the TGA method has some significant limitations that may affect the results. First, it must be noted that carbon oxidation reaction occurring in TGA can be significantly altered by the presence of metal impurities that can act as oxidation catalysts [36,37]. Second, the state of aggregation of the samples may significantly affect the rate of mass and heat transfer during the oxidation reaction and as a result can cause peak shifts in TGA. These two features are sometimes ignored but they may vary significantly from sample to sample causing significant differences in the estimated SWCNT purities. To illustrate these limitations of the technique, a clear example of the effects of aggregation on the TGA profile is shown in Fig. 68. In this case, both profiles correspond to exactly the same purified SWCNT sample, but one of the aliquots was oven-dried after purification while the other was freeze-dried. It is known that the former drying method results in higher extent of agglomeration than the latter. Clearly, the more highly agglomerated sample exhibited an enhanced fraction of carbon oxidizing at the high-temperature region compared to the freeze-dried sample, with a more open structure. This dramatic difference indicates that unless the level of impurities and state of agglomeration are kept constant, TGA can lead to erroneous measurements of SWCNT purity.

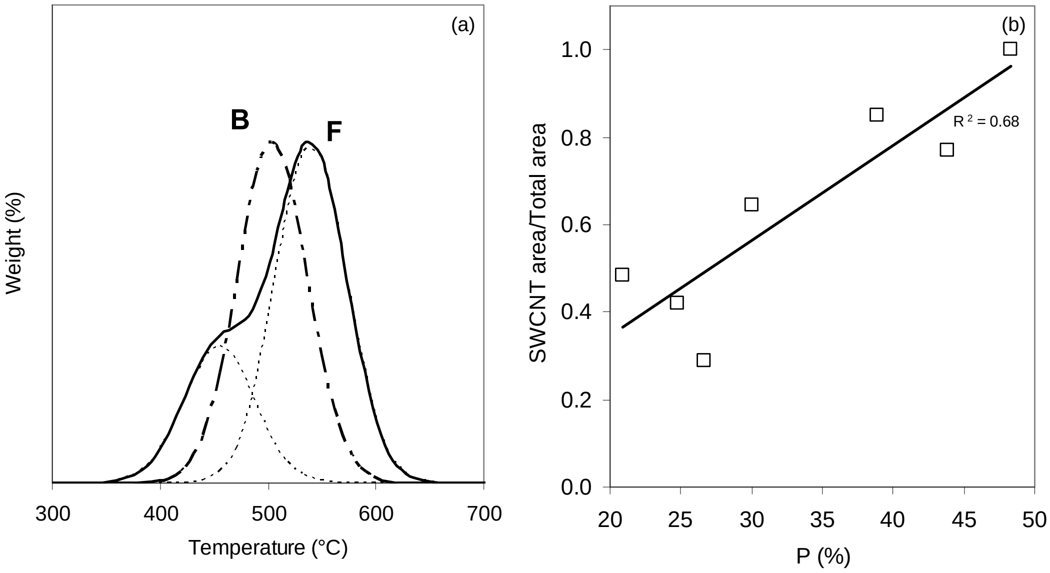

Figure 67: (a) TGA profiles of the purified solid samples B and F; (b) Comparison of the P (%) parameter values with the SWCNT slectivity values obtained from TGA.

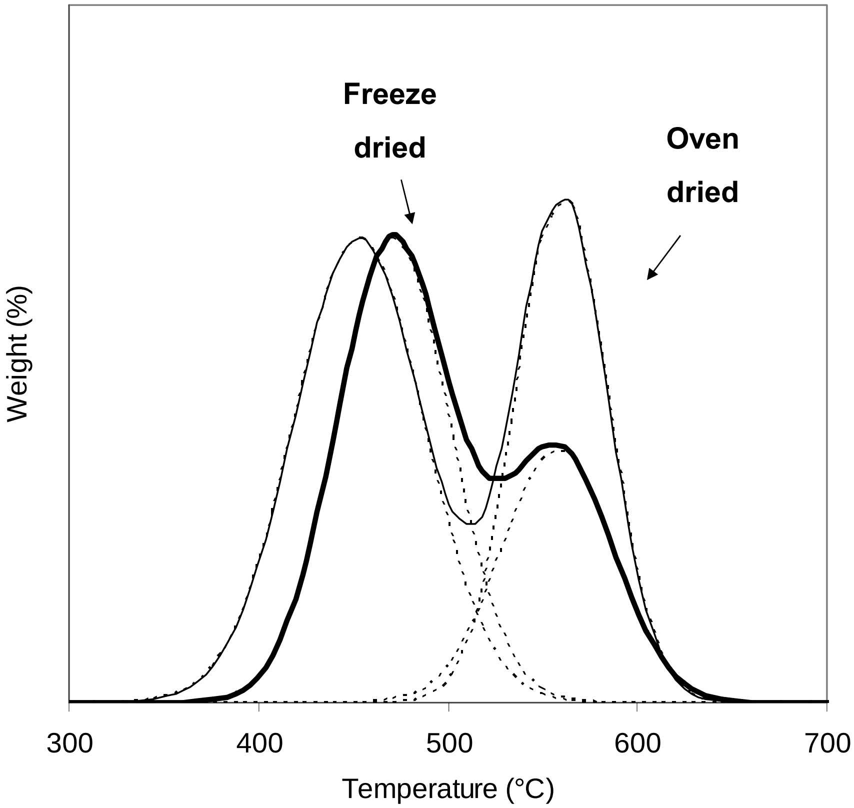

Figure 68: TGA profiles for the same sample with different states of aggregation.

3.2.2.4- Optical absorption

OA is a powerful technique that can be effectively employed to measure the (n,m) selectivity and SWCNT selectivity in a sample [38-41]. The absorption spectrum of SWCNT exhibits the characteristic bands of the 1-dimensional van Hove singularities. Semiconducting SWCNT give rise to transitions between mirror singularities in the electronic density of states termed S_{11}, S_{22}, etc. Integrating intensity of these bands and the spectral background provides a valuable parameter that can be used to estimate the purity of the sample. Itkis et al. [42] have developed a method that relates the area of the S_{22} transition and the total area under the spectra to the purity of the sample. A similar method was developed to evaluate the effectiveness of surfactants and dispersion methods on the same CoMoCAT® sample [43]. Some of the limitations of these methods are the uncertainty associated with the position of the spectral background and the variation of the absorption intensity with the state of dispersion [41]. More recently, Landi et al. [39] developed a modified version of this method that enhances its accuracy, as verified on a series of samples constructed with specific mass fractions of purified SWCNT and other carbonaceous species. This modified method is based on a non-linear plasmon model that includes the overlap of the transitions and peak broadening. To ensure accuracy of the fitting, it is important that the spectrum covers high enough energies as to reach the maximum plasmon intensity, occurring at about 4.5–5 eV. Fig. 69(a) shows the UV–Vis spectra of samples C and H, which according to the Raman *P* factors have fractions of SWCNT of about 43.8% and 20.9%, respectively. As mentioned above, the intensity of characteristic bands in the absorption spectrum intensity relative to the spectral background should correlate with the purity of the sample [42,43]. In good correlation with the prediction from the intensity of the Raman G band of the suspensions, it is seen that the ratio of areas under the resonance bands to the background drop by about a factor of two from sample C to sample H. The resonance factors calculated according to Tan et al. [43] are summarized in Table 3. To compare the correlation of these values with those from the Raman method, Fig. 69(b) shows the variation of the resonance factor with P for all the samples in the series. The correspondence between the two methods is very good, i.e., the correlation factor is 0.92.

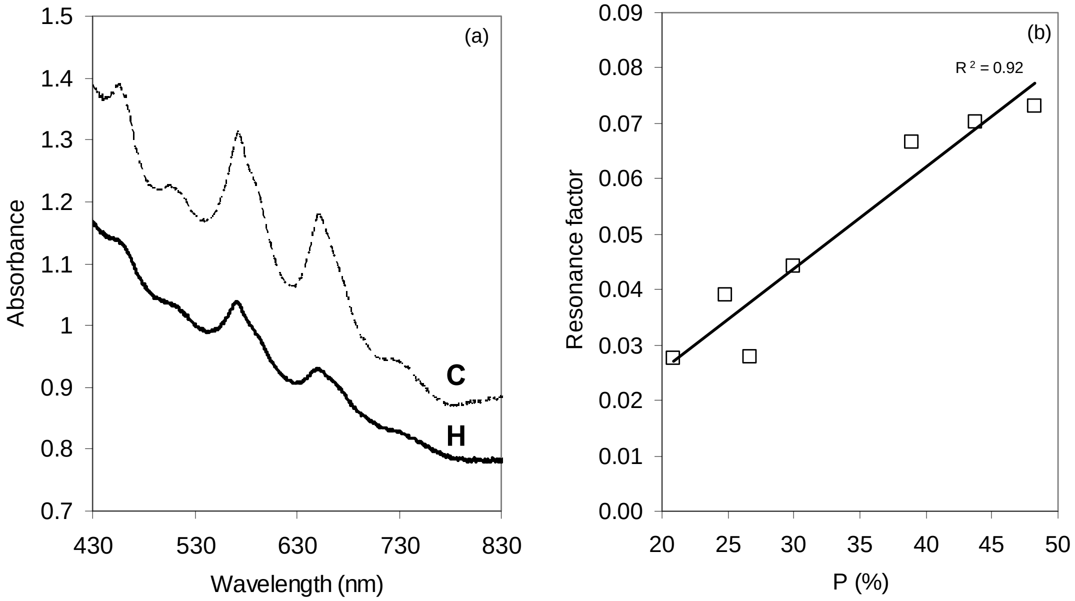

Figure 69: (a) UV-Vis spectra of suspensions prepared from the purified solid samples C and H; (b) Comparison of the P (%) parameter values with the resonance factors obtained from the OA analysis.

3.2.2.5- As-produced SWCNT samples

In most CVD methods used in the synthesis of SWCNT, the active metal catalysts are typically deposited on a high-surface area support in relatively low concentrations. As such, a large fraction of the as-produced material consists of the catalyst support, which needs to be separated from the SWCNT by chemical or mechanical means. In the particular case of the CoMoCAT® method employed in this study, the as-produced material contained 5–7 wt% C, 1–2 wt% Co–Mo, and the rest SiO_2. The as-produced solid material was analyzed by Raman scattering and the G/D ratios obtained are compared to those obtained on the purified samples. The G/D ratios obtained for the as-produced samples (G/D (ap)) are included in Table 3 together with those obtained for the purified samples. It can be seen that while the trend for the series is the same as that of the corresponding purified samples, the absolute G/D ratios for the as-produced samples were significantly larger than those for the purified samples. That is, while the

G/D ratios are still high in the purified samples, it is evident that the purification process enhances the intensity of the D-band, either by creating defects or by generating functionalized groups on the SWCNT walls. Similar reductions in G/D ratios after purification have been reported and ascribed to partial doping caused by the acid treatment, which may reduce the resonant Raman response [42,44].

3.3- Isotope doping (^{13}C)

The main goal of this project was to study the electronic environment of carbon nuclei on SWCNT. Blackburn et al [45] have reported the first solid-state ^{13}C NMR chemical shift assignment of carbon on metallic and semiconducting SWCNT varying the semiconducting content. This project has been done in collaboration with Jeffrey L. Blackburn from the National Renewable Energy Laboratory (NREL). Blackburn et al [45] have probed that ^{13}C NMR can be used to determine the surrounding environment of a nanotube in mixed SWCNT samples (metallic-semiconducting). They have used SWCNT produced by laser vaporization with a 20 % of isotope having an average diameter of 1.3 ± 0.1 nm. Metallic and semiconducting enriched samples were prepared by using the “Density Gradient Ultracentrifugation (DGU)” method. Absorbance spectroscopy was used to determine the metallic/semiconducting ratio. The ^{13}C NMR data has been fit with Gaussian peaks and they have probed, in agreement with Lai et al [57], that large diameter semiconducting and metallic tubes have similar chemical shifts. In the same publication they have suggested that NMR studies on SWCNT with smaller diameters (~1 nm) and narrow chirality distribution was interesting in order to probe the diameter dependence on the ^{13}C NMR resonance. Our group is well known for producing SWCNT with narrow distribution and diameters in the order of 1 nm. Therefore our material has the desirable characteristics for them to be studied.

Besides the NMR studies, doping SWCNT with ^{13}C is also interesting in order to understand different structural characteristics of the tubes. Figure 70(a) shows an in-situ experiment using Raman scattering while switching from ^{13}C to ^{12}C. If the defects on the tubes are present on their tips, the Raman scattering spectrum will show a higher intensity in the D band and the spectrum would present a redshift. This type of experiments will be useful to understand the nature of the defects on SWCNT. It is also of high importance to understand the burning kinetics of the SWCNT and the doping could also help to clarify this.

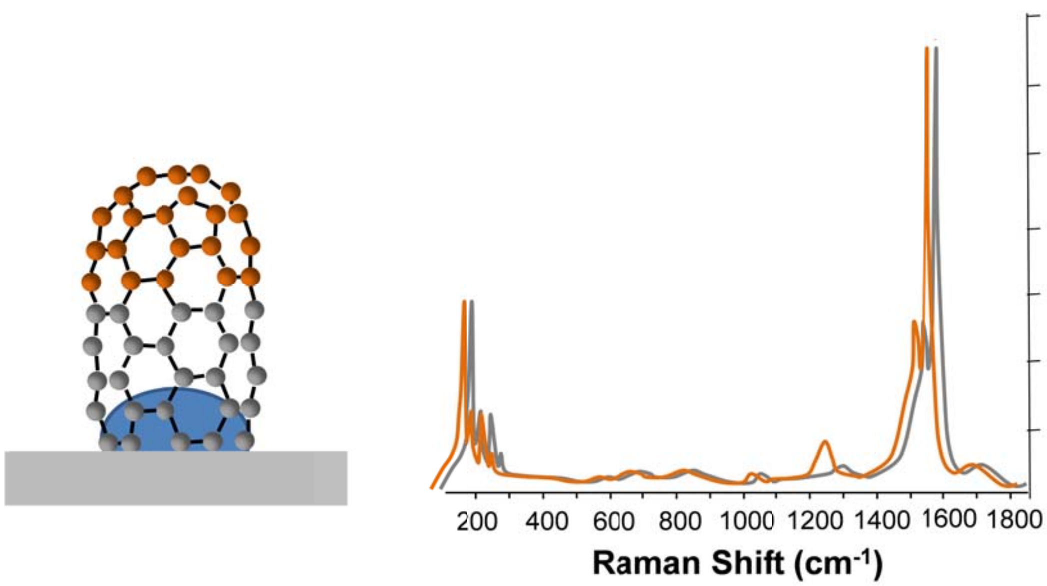

Figure 70(a): In-situ ^{13}C SWCNT growth Raman scattering experiment.

Figure 70(b) shows an interesting experiment where ^{12}C and ^{13}C were switched in order to have the latter one on the tips. By using a mass spectrometer and conducting a temperature programmed oxidation experiment, it could be possible to determine if the tubes start burning from the tips, from the sides or if everything happens at the same time.

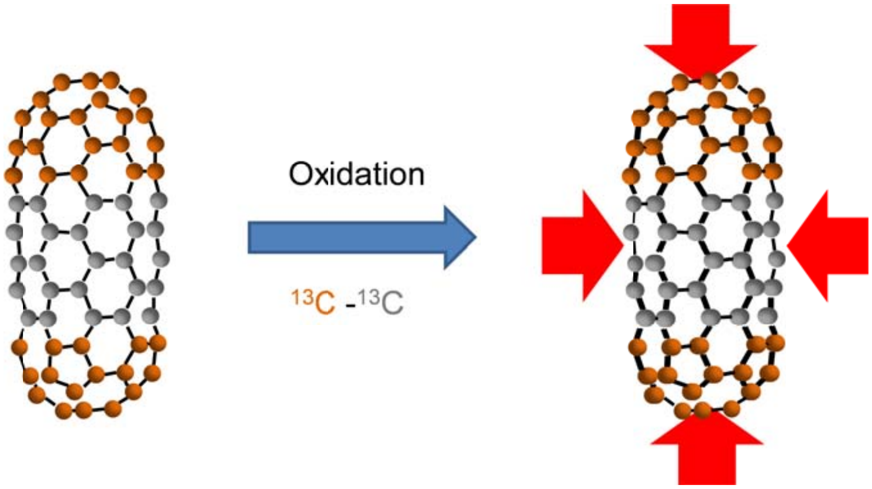

Figure 70(b): ^{13}C SWCNT's burning kinetics.

3.3.1- Experimental

SWCNT were produced by using a Co-Mo supported catalyst synthesized by SWeNT®. One gram of calcined catalyst was set into a vertical quartz reactor of ½ in diameter and pre-reduced under H_2 (300 sccm) for 30 min at 545 °C. Subsequently the temperature was raised to 680 °C under He (300 sccm). Carbon monoxide (300 sccm) was finally fed at 680 °C for 30 min. The production of ^{13}C doped SWCNT was done by mixing ^{12}CO and ^{13}CO (Cambridge Isotope Laboratories, Inc.). Pure ^{12}C and ^{13}C SWCNT were also synthesized for comparison. An scheme of the reactor is shown in Fig. 71. The as-produced samples were purified by acidic treatments and a series of oxidation steps. Both the as-produced and purified SWCNT were characterized by using different analytical techniques such as optical absorption, Raman scattering, TGA, PL and NMR.

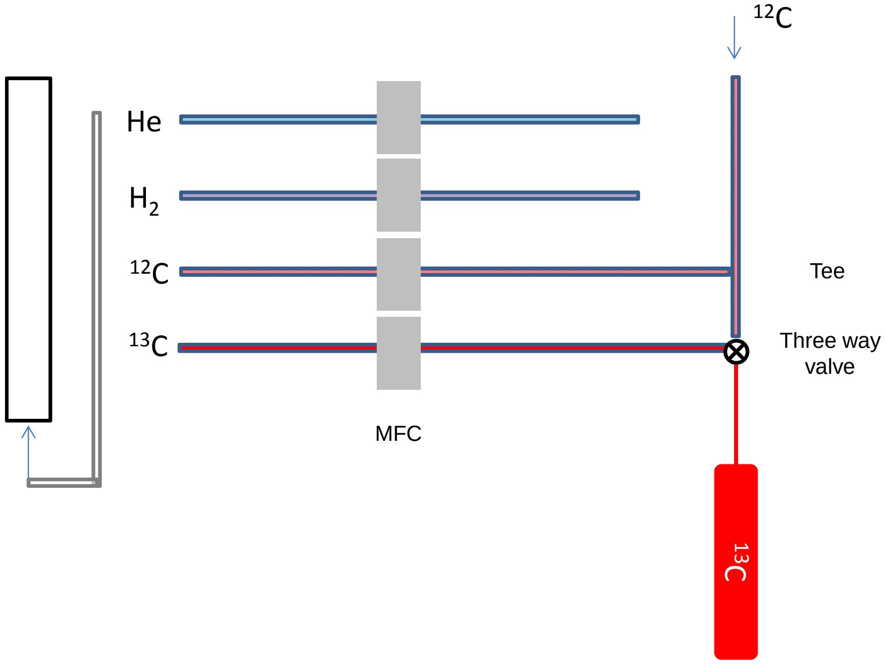

Figure 71: Reactor design scheme for SWCNT production.

3.3.2- Results

3.3.2.1- As-produced SWCNT

3.3.2.1.1- Optical Absorption

As it was explained before it was desirable to produce SWCNT with the narrowest chirality distribution favoring in particular the specie (6,5). Different catalysts and reaction conditions were used in order to optimize the final product. Figure 72 shows the OA spectrum of the as-produced SWCNT (^{12}C) with narrow distribution that was used for purification and later characterization. In particular, this sample was enriched in (6,5) and (7,6) being the former the predominant.

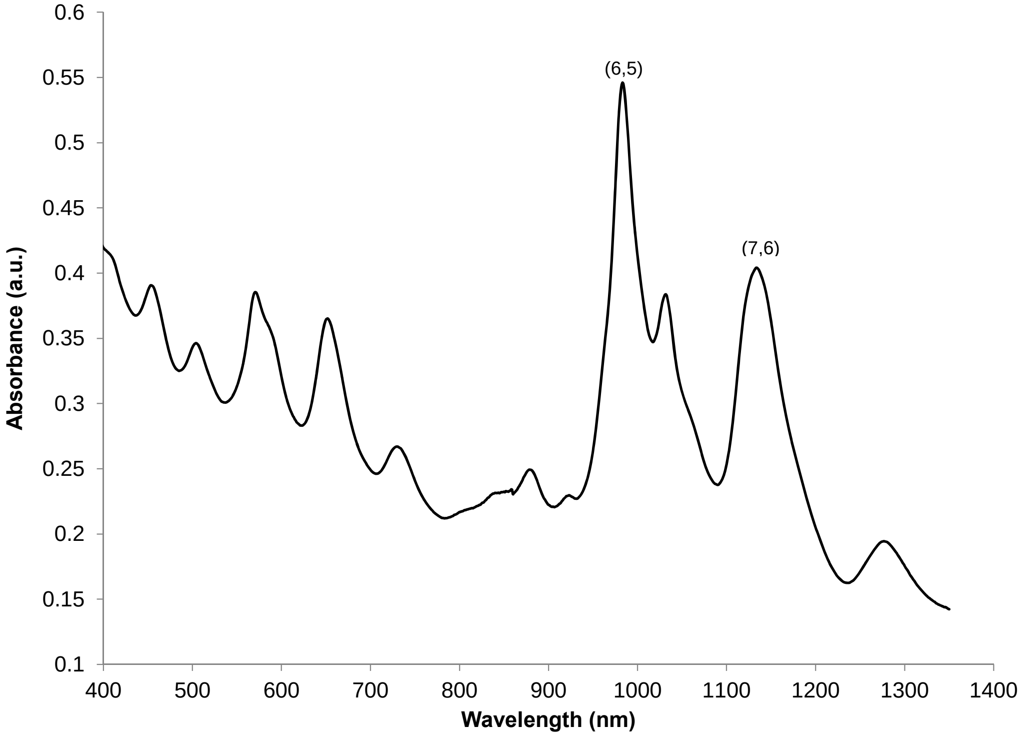

Figure 72: OA of SWCNT as-produced sample.

Once the desirable SWCNT product was synthesized, samples doped with ^{13}C were produced under those conditions and different analytical techniques were used to estimate the concentration of isotope.

3.3.2.1.2- Raman scattering

Raman scattering has been used not only to characterize the SWCNT selectivity of the samples but also to estimate the amount of ^{13}C present in them. As it has been seen in the literature [46-49] the presence of ^{13}C produces a redshift of the Raman scattering spectrum since the Raman mode frequencies are inversely proportional to the square root of the atomic mass ($w = 1/(2\pi)*(k*1/(m_1+m_2))^{1/2}$) [50]. This shift can be estimated by using the expression below.

$$\frac{w_1}{w_0} = \sqrt{\left[\frac{M^{12}C}{\left(x * M^{12}C + (1-x) * M^{13}C\right)}\right]} \qquad (1)$$

Being w_0 the Raman shift of the pure ^{12}C SWCNT, w_1 the Raman shift of the doped SWCNT, M^{12}C the mass of ^{12}C, M^{13}C the mass of ^{13}C and x the concentration of ^{12}C. By using 20 % of ^{13}C in the reaction, a ratio of 0.99176 is expected. For the as-produced samples, the D, G and G' band positions have been calculated for 15 different spots. The moving average was calculated as in previous publications [51] and is shown in Fig. 73(a) to (c). It can be seen that the average values variation have decreased as the number of spots increases. This analysis was conducted for as-produced SWCNT containing pure ^{12}C, 20 % ^{13}C and for a physical mixture of pure ^{12}C and 20 % ^{13}C. It can be seen that the average Raman shift for the doped sample has a red shift compared with the pure ^{12}C SWCNT sample as it was expected for having ^{13}C. The physical mixture has shown Raman shift values in between the doped and the pure ^{12}C SWCNT, being closer to the later one as it was expected.

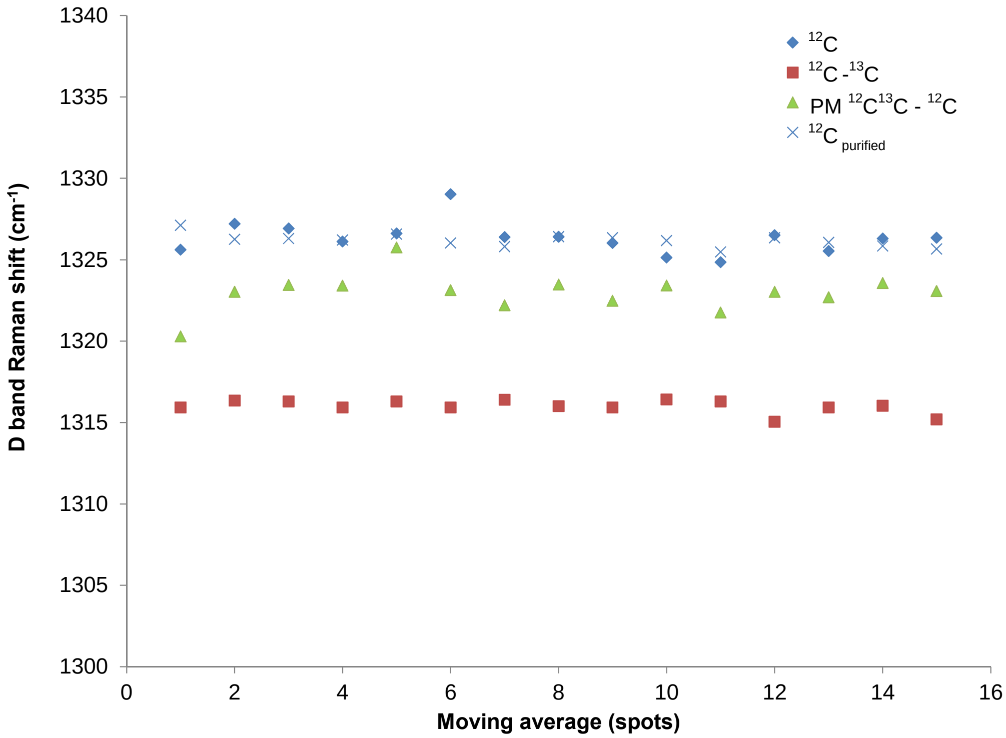

Figure 73(a): Moving average (15 spots) of the D band position.

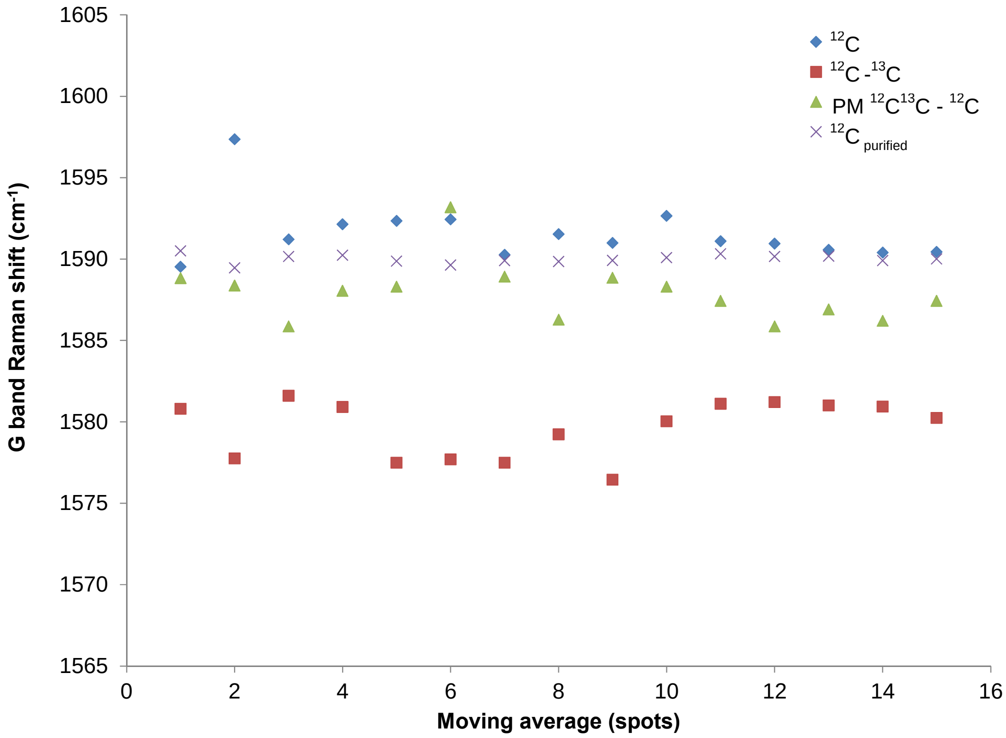

Figure 73(b): Moving average (15 spots) of the G band position.

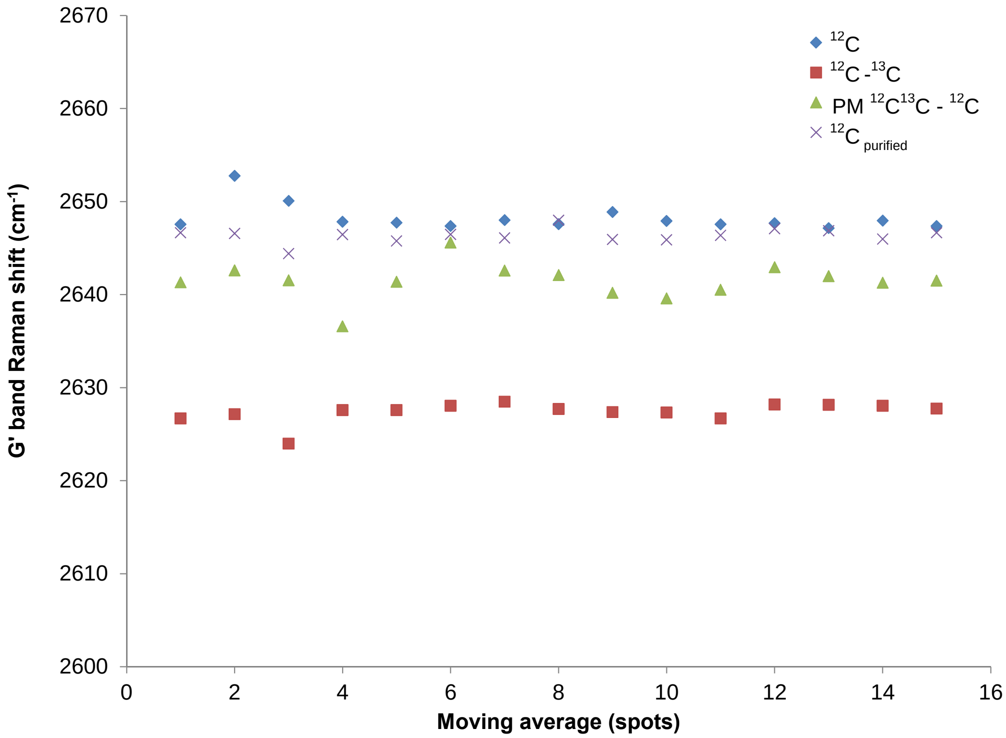

Figure 73(c): Moving average (15 spots) of the G’ band position.

By using the position value of the spot 15, the Raman shifts ratios and the concentration of ^{13}C using equation (1) were calculated and are shown in Table 4. As it can be seen, the values range from 15 %, obtained from the G band shift, to 22 % obtained from the D band shift. As it is explained in section 3.3.2.1.3, the amount of ^{13}C estimated by using TGA was 13.5 %, which is closer to the value obtained from the G band shift. The higher values obtained from both the D and G’ bands might be related to a wide distribution of diameters. It has been shown in the literature that these bands upshift when the diameter increases [52].

Table 4: Isotope concentration-Raman scattering as-produced material.

Band	^{12}C	^{12}C^{13}C	Δsh	ratio ^{12}C^{13}C/^{12}C	x	% ^{13}C
D	1326.340	1315.190	11.150	1.008478	0.796	20.433
G	1590.440	1580.230	10.210	1.006461	0.844	15.557
G'	2647.370	2627.750	19.620	1.007466	0.820	17.986

The Raman shift values variation might be related to either the heterogeneity of the solid samples, the presence of catalyst or an intrinsic shift due to the instrument. In order to analyze the effects of the catalyst, a purified SWCNT sample produced with pure ^{12}C was used and the distribution is shown in Fig. 73(a) to (c). It can be seen that the variation is significantly smaller than that for the as-produced samples. The remaining variation could be related to the heterogeneity of the solid sample.

Analysis of the intrinsic effects of the equipment has been also done and in this case the ratio between the G' Raman shift and the D Raman shift has been used. The G' band is the second harmonic of the D band. Therefore the ratio should be close to 2 as it has been shown in the literature [53,54].

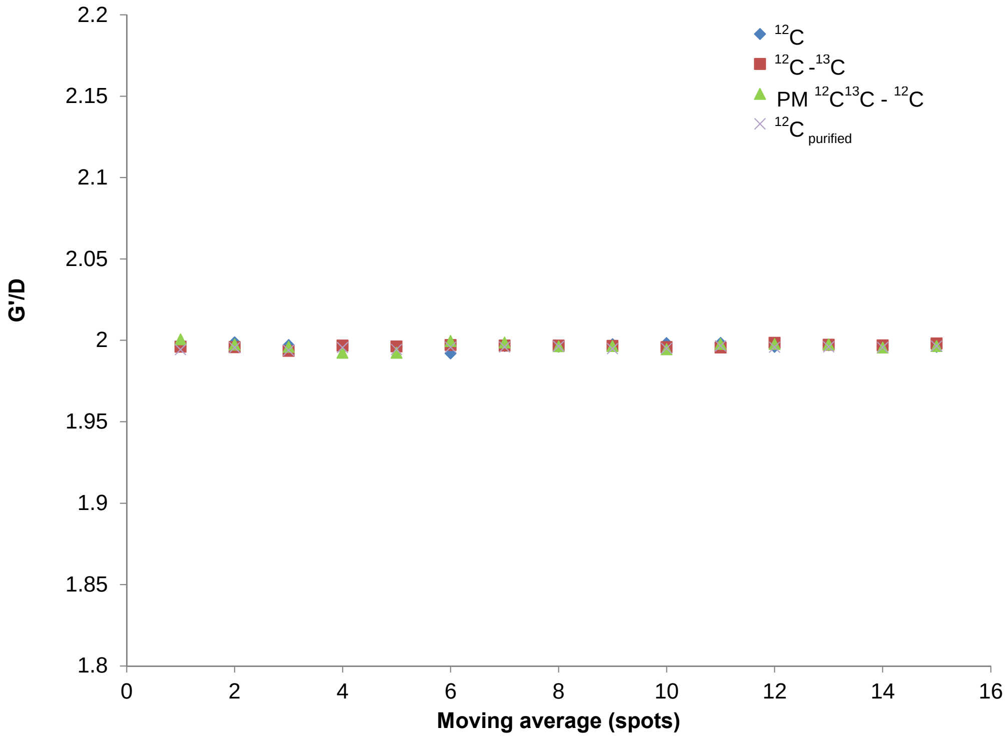

Figure 74: G'/D values.

As it can be seen in Fig. 74, the ratio is approximate to 2 for all the spots. Therefore it can be said that the variation is not related to the equipment.

3.3.2.1.3- Thermal gravimetric analysis

The amount of ^{13}C in the as-produced samples was estimated by conducting TGA-MS. The pure ^{12}C showed approximately 1 % of the isotope as it was expected because of the natural occurrence. The doped sample showed approximately 13.5 % of the isotope. The original partial pressure of ^{13}C to ^{12}C was 0.2, but the final concentration in the SWCNT is less than 20 %. This could be related to the consumption amount of the carbon source, the experiment set up, etc. The third sample analyzed was the one containing pure ^{13}C and the TGA-MS results confirmed the purity of this sample.

3.3.2.2- Purified SWCNT

The characterization of the purified samples has been done by Jeffrey L. Blackburn at the NREL as it was mentioned before. The purified SWCNT provided by our group were separated by using the "Density Gradient Ultracentrifugation" method described in a previous publication of Blackburn et al [45]. Hersam et al [55] have shown the goodness of this method to enrich SWCNT samples by diameter. They have used DNA wrapped SWCNT produced by either CoMoCAT® or HiPco® processes. The tubes were dispersed in aqueous dilutions of iodixanol with a linear density profile and the suspensions were centrifuged at 174000 g. After few hours of centrifugation, the tubes migrated to their isopycnic (same density) points. They have demonstrated that the DNA wrapped tubes were separated due to differences in the buoyant density having larger values the tubes with larger diameters until a critical diameter. Therefore the separation by DGU is governed by the diameter of the carbon nanotubes. Weisman et al [56] have shown recently that non-linear density profiles with mixed surfactants can separate species with tiny differences in diameter and buoyant densities. They have shown that this method can be used to accurately separate SWCNT with a large variety of species such as HiPco® as it can be seen in Fig. 75.

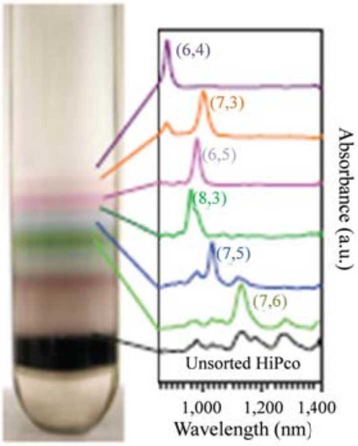

Figure 75: HiPco® sorting by non-linear DGU. [56]

Blackburn et al [45] have shown that the chemical shifts of metallic and semiconducting SWCNT with diameters ranging in 1.3 nm have similar values as it was predicted by Lai et al. In this publication Blackburn et al mentioned that conducting experiments with SWCNT that have a variety of diameters would allow them to understand the electronic structure effects with more detail.

After pure ^{12}C, pure ^{13}C and ^{13}C doped purified SWCNT were separated by DGU, an enriched (6,5) chirality fraction and a fraction of the bulk were characterized and compared.

3.3.2.2.1- Optical absorption

As an example of the spectra obtained after DGU for the two analyzed fractions, Fig. 76 shows the OA spectra for the (6,5) enriched and bulk fractions. The difference between both samples it can be seen in Fig. 76, while the bulk sample shows higher background intensity and larger diameter tubes, the enriched sample does not. This results confirms the narrow concentration of species in the enriched sample, being mostly (6,5). Figure 77 shows the OA spectra for the (6,5) enriched fractions of the samples with 100 % ^{12}C, 100 % ^{13}C and the doped ^{13}C sample. It can be seen that the spectra are very similar. Therefore, the analyzed enriched fractions have the same diameter composition (mostly (6,5)).

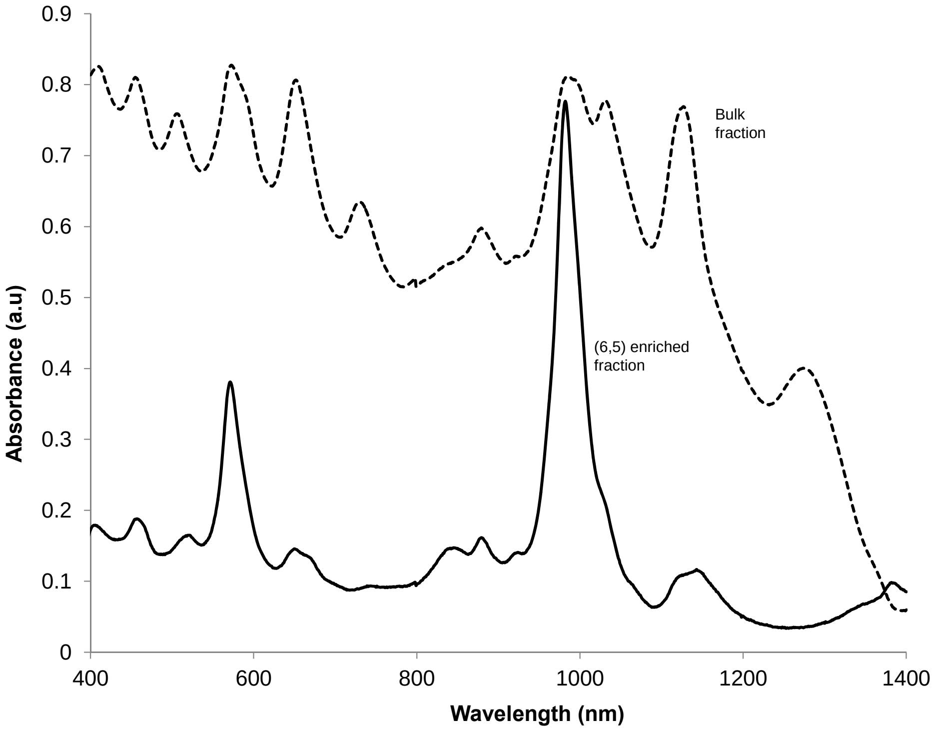

Figure 76: OA spectra of bulk and (6,5) enriched fractions.

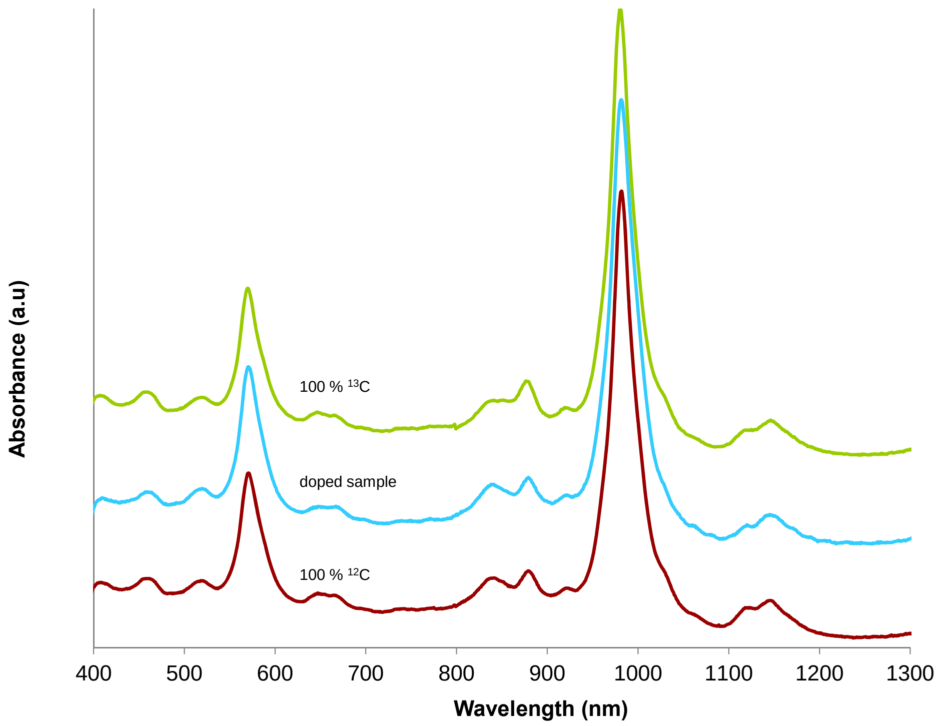

Figure 77: OA spectra of (6,5) enriched fractions with different isotope concentrations.

3.3.2.2.2- Photoluminescence

PL was used to confirm the enrichment of one of the fractions in small diameter tubes. As an example, Fig. 78(a) and (b) show a comparison in diameter distribution between the bulk and the (6,5) enriched fractions of a sample. It can be seen that the enriched fraction contains primarily (6,5) as it was imply by the results obtain using optical absorption. On the other hand, the bulk fraction shows a wider distribution of larger diameter tubes.

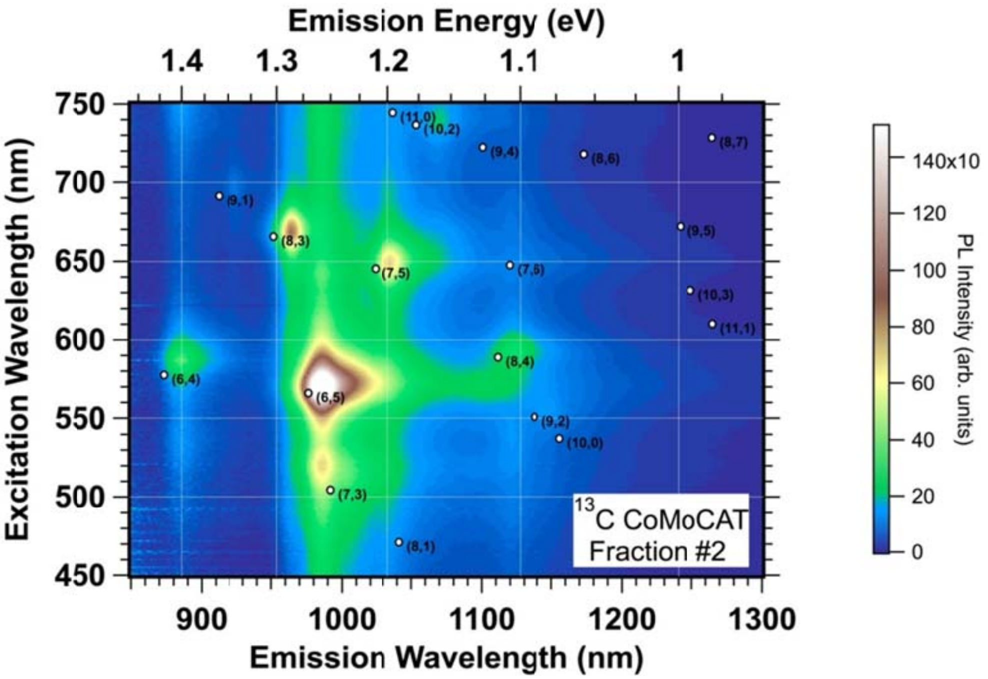

Figure 78 (a): PL of (6,5) enriched fraction.

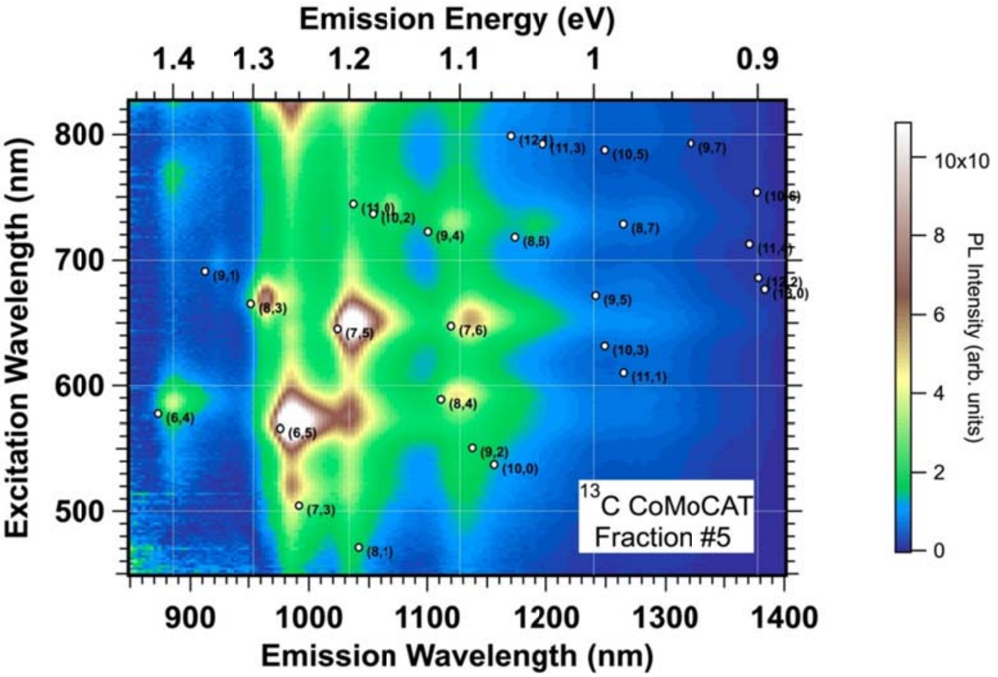

Figure 78 (b): PL of bulk fraction.

3.3.2.2.3- Raman scattering

Another characterization technique used to confirm the goodness of the DGU separation was Raman scattering. Figure 79 shows the comparison of the RBM vibrational modes of bulk and (6,5) enriched fractions. As mentioned before, the wavenumber of the RBM modes are inversionally proportional to the tube diameter. Therefore, the absence of peaks at low wavenumbers in the enriched sample implies the high concentration of small diameter tubes.

Figure 80 shows the G-band mode vibration of the 100 % ^{13}C, 100 % ^{12}C and doped samples. It can be seen that the larger the ^{13}C concentration, the larger is the red shift of the G-band. Even though the results corresponding to only one energy laser (532 nm) and one vibration mode are shown in Fig. 80, three different lasers and the G'-band have been used for this characterization (488 nm, 532 nm and 632.8 nm). The calculation of ^{13}C concentration on the doped sample was done by Blackburn's group and the values are shown in Table 5.

Table 5: ^{13}C concentration (%) by Raman scattering using three different laser excitations. Purified SWCNT.

	Exitation laser		
Band	**488 nm**	**532 nm**	**632.8 nm**
G	15.0	13.5	12.0
G'	19.0	18.0	20.0

In this case the concentration calculated from the G band is much closer to the value obtained by doing TGA (13.5%). This is also a confirmation that the presence of catalyst affects the results. When the concentration values were calculated from the G' band, they also were higher like in the as-produced samples.

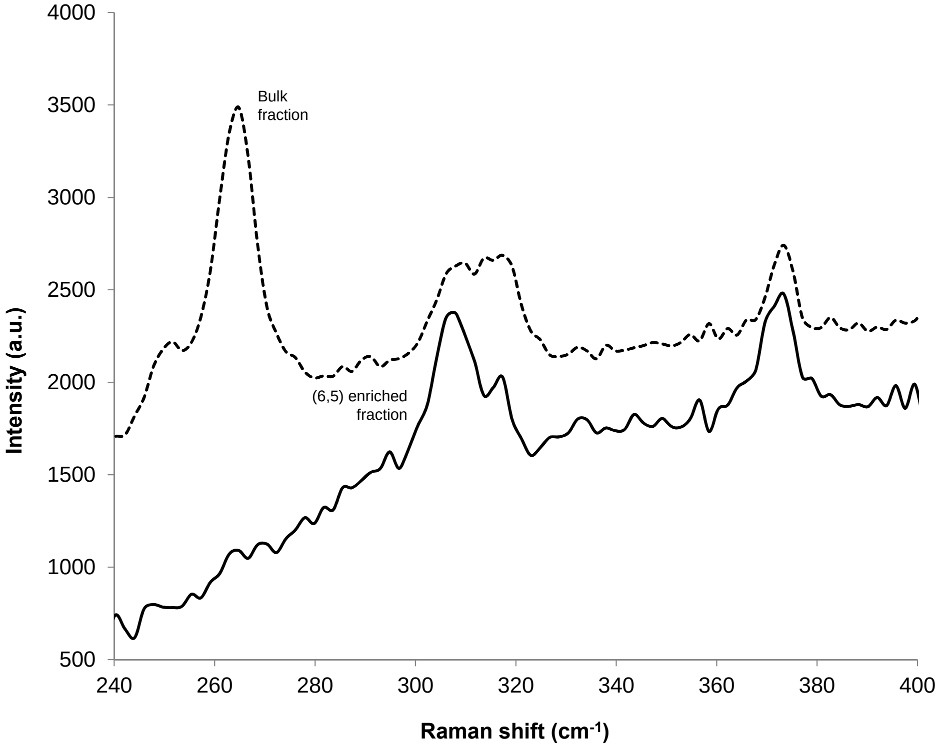

Figure 79: RBM Raman scattering of bulk and (6,5) enriched fractions.

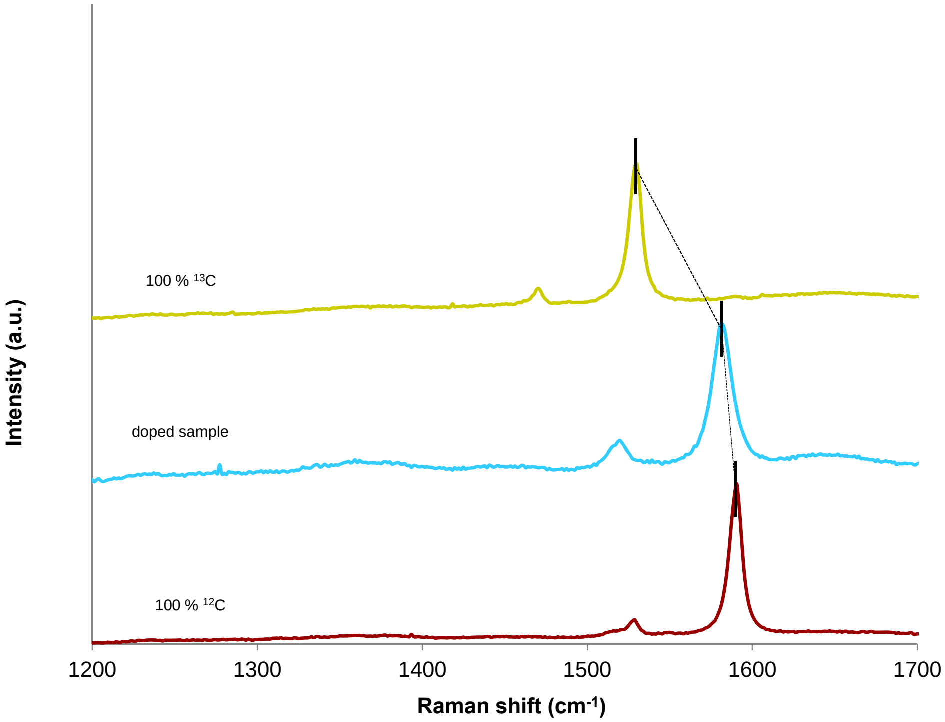

Figure 80:G-band Raman scattering of (6,5) enriched fractions with different isotope concentration.

3.3.2.2.4- Nuclear Magnetic Resonance

As it was explained, before the main goal of doping SWCNT was being able to identify the ^{13}C isotope by using NMR. While the nucleus of ^{12}C has no spin, making its identification by NMR impossible, ^{13}C has an identifiable spin of ½. As it was shown by Lai et al [57], the chemical shift of SWCNT is independent of chirality, having smaller values for metallic tubes when n< 18 and larger values when n>18, being 'n' a chiral number (n,0). Lai et al [57] demonstrated that the chemical shift of semiconducting zigzag tubes decreases when the diameter increases, while for metallic tubes the chemical shift goes through a minimum (Fig. 81).

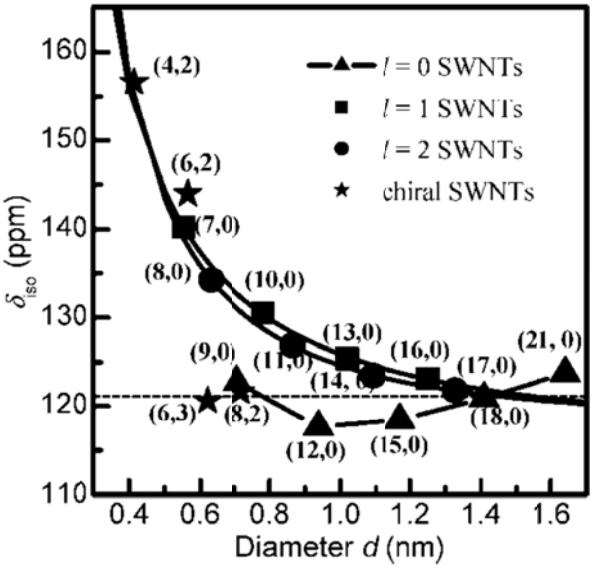

Figure 81: Chemical shift vs diameter. [57]

It has been also demonstrated by Lai et al that for diameters values around 0.7 nm the chemical shift of metallic tubes is 8 ppm smaller than for semiconducting what it would be the case for CoMoCAT® tubes. They concluded in their publication that the chemical shift seems to depend only on diameter and electronic structure. The reported chemical shifts for semiconducting tubes are between 122-129 ppm, centered at 126 ppm. In the case of metallic tubes, the chemical shift seems to be between 0-12 ppm smaller than for semiconducting tubes and it is centered at 120 ppm.

Figures 82(a) and (b) show the NMR results obtained of the (6,5) enriched and bulk fractions from the doped samples. It can be seen in Fig. 82(a) that the peak related to the enriched fraction seems narrower and centered at higher ppm (129 ppm). On the other hand, Fig. 82(b) shows a wider peak centered at lower ppm (127.3 ppm). As explained by Lai et al [57], semiconductor SWCNT with smaller diameter should have higher chemical shift. Therefore, the (6,5) enriched fraction is expected to show higher chemical shift as it can be seen comparing Fig. 82(a) and (b). The less symmetrical peak shown in Fig. 82(b) is due to the presences of metallic tubes centered at 123.6 ppm.

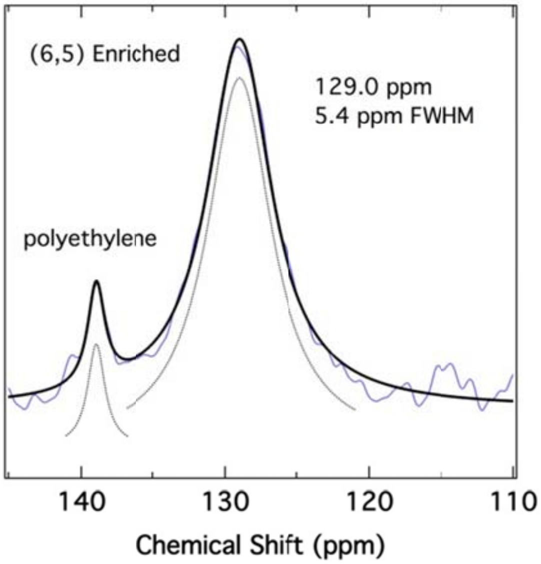

Figure 82(a): NMR of doped ^{13}C SWCNT (6,5) enriched fraction.

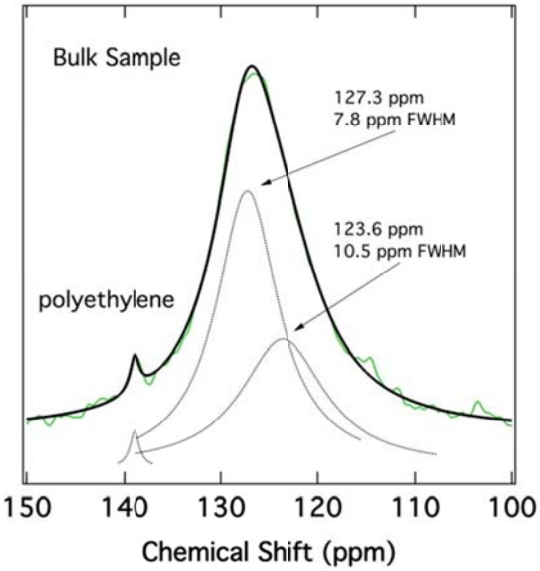

Figure 82(b): NMR of doped ^{13}C SWCNT bulk fraction.

Figure 83 shows that the experimental results obtained by Blackburn's group using purified CoMoCAT® correlate very well with the theoretical values predicted by Lai et al [57].

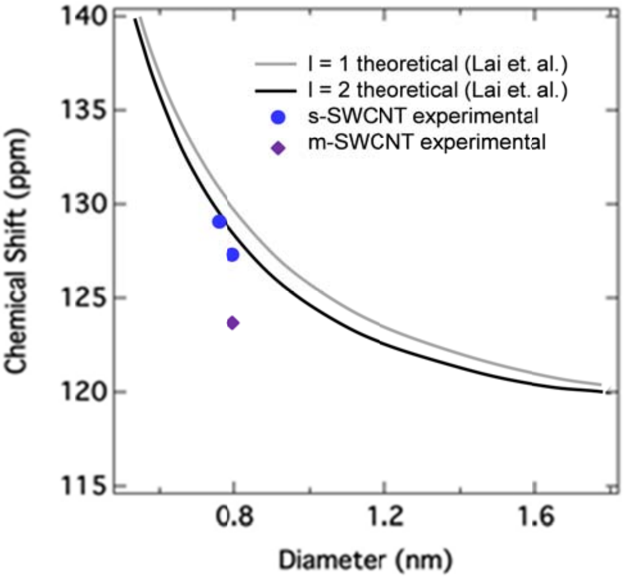

Figure 83: Comparison of experimental and theoretical chemical shifts values dependence with diameter. NMR of doped ^{13}C SWCNT.

3.4-Conclusions

The assessment of SWCNT selectivity of bulk samples has been complicated by the heterogeneity of solid samples. Most methods employed to date exhibit some limitations. The method most commonly used is Raman spectroscopy. However, to overcome the problem of sample heterogeneity and to obtain reliable and quantitative estimates of the percent of SWCNT in a sample it is needed a large number of measurements. By contrast, the measurement of the G/D ratio in liquid suspensions as a function of solid concentration has provided a more practical and reliable method than those previously used. A simple equation with two adjustable parameters can be used to directly extract the percent of SWCNT in the sample.

The effectiveness of using an isotope (^{13}C) to dope high SWCNT and (n,m) selectivity samples during the production process has been shown in this chapter. Comparisons between doped and un-doped tubes have been done by using different analytical techniques. DGU was used to separate the purified SWCNT samples by diameter. The different ^{13}C doped SWCNT fractions obtained after DGU were compared by using NMR. Through this study, the differences in chemical shifts for SWCNT within a diameter range of 0.8-1 nm and different metallicity have been seen for the first time.

3.5- References

---

[1]- Ramasubramaniam R., Chen J., Liu H., Homogeneous carbon nanotubes/polymer composites for electrical applications, *Appl. Phys. Lett.*, **2003**, 83, 14, 2928.

[2]- Shim B.S., Tang Z., Morabito M.P., Agarwal A., Hong H., Kotov N.A., Integration of conductivity, transparency, and mechanical strength into highly homegeneous layer-by-layer composites of single-walled carbon nanotubes for optoelectronics, *Chem. Mater.*, **2007**, 19, 5467.

[3]- Nepal D., Balasubramanian S., Simonian A.L., Davis V.A., Strong antimicrobial coatings: single-walled carbon nanotubes armored with biopolymers, *Nano Lett.*, **2008**, 8, 7, 1896.

[4]- Li Z., Biris A.S., Dervishi E., Saini V., Xu Y., Biris A.R., et al, Influence of impurities on the X-ray photoelectron spectroscopy and Raman spectra of single-wall carbon nanotubes, *J. Chem. Phys.*, **2007**, 127, 1546713, 1.

[5]- Kruusma J., Mould N., Jurkschat K., Crossley A., Banks C.E., Single walled carbon nanotubes contain residual iron oxide impurities which can dominate their electrochemical activity, *Electrochem. Commun.*, **2007**, 9, 2330.

[6]- Liu B., Ren W., Gao L., Li S., Pei S., Liu C., et al., Metal-catalyst-free growth of single-walled carbon nanotubes, *J. Am. Chem. Soc.*, **2009**, 131, 6, 2082.

[7]- Jones C.P., Jurkschat K., Crossley A., Compton R.G., Riehl B.L., Banks C.E., Use of high-purity metal-catalyst-free multiwalled carbon nanotubes to avoid potential experimental misinterpretations, *Langmuir*, **2007**, 23, 18, 9501.

[8]- Penza M., Tagliente M.A., Aversa P., Re M., Cassano G., The effect of purification of single-walled carbon nanotubes bundles on the alcohol sensitivity of nanocomposite, Langmuir-Blodgett films for saw sensing applications, *Nanotechnology*, **2007**, 18, 185502.

[9]- Johnston D.E., Islam M.F., Yodh A.G., Johnson A.T., Electronic devices based on purified carbon nanotubes grown by high-pressure decomposition of carbon monoxide, *Nature Mater.*, **2005,** 4, 589.

[10]- Dillon A.C., Yudasaka M., Dresselhaus M.S., Employing raman spectroscopy to qualitatively evaluate the purity of carbon single-wall nanotube materials, *J. J. Nanosci. Nanotechol.*, **2004,** 4, 7, 691.

[11]- Lee S., Peng J.W., Liu C.H., Probing plasma-induced defect formation and oxidation in carbon nanotubes by Raman dispersion spectroscopy, *Carbon*, **2009**, 47, 3488.

---

[12]- Antunes E.F., Lobo A.O., Corat E.J., Trava-Airoldi V.J., Influence of diameter in the Raman spectra of aligned multi-walled carbon nanotubes, *Carbon*, **2007**, 45, 913.

[13]- Jorio A., Fantini C., Dantas M.S.S., Pimenta M.A., Souza Filho A.G., Samsonidze Ge.G., et al., Linewidth of the Raman features of individual single-wall carbon nanotubes, *Phys. Rev. B*, **2002**, 66, 115411, 1.

[14]- Nishide D., Kataura H., Suzuki S., Tsukagoshi K., Aoyagi Y., Achiba Y., High-yield production of single-wall carbon nanotubes in nitrogen gas, *Chem. Phys. Lett.*, **2003**, 372, 45.

[15]- Musumeci A.W., Waclawik E.R., Frost R.L., A comparative study of single-walled carbon nanotube purification techniques using Raman spectroscopy, *Spectroquim. Acta A*, **2008**, 71, 140.

[16]- Simpson J.R., Fagan J.A., Becker M.L., Hobbie E.K., Hight Walker A.R., The effect of dispersant on defects in length-separated single-wall carbon nanotubes measured by Raman spectroscopy, *Carbon*, **2009**, 47, 3238.

[17]- Delhaes P., Couzi M., Trinquecoste M., Dentzer J., Hamidou H., Vix-Guterl C., A comparison between Raman spectroscopy and surface characterizations of multiwall carbon nanotubes, *Carbon*, **2006**, 44, 14, 3005.

[18]- Kobayashi Y., Takagi D., Ueno Y., Homma Y., Characterization of carbon nanotubes suspended between nanostructures using micro-Raman spectroscopy, *Physica E*, **2004**, 24, 1-2, 26.

[19]- Qian W., Liu T., Wei F., Yuan H., Quantitative Raman characterization of the mixed samples of the single and multi-wall carbon nanotubes, *Carbon*, **2003**, 41, 1851.

[20]- Heise H.M., Ruckuk R., Ojha A.K., Srivastava A., Srivastava V., Asthana B.P., Characterization of carbonaceous materials using Raman spectroscopy: a comparison of carbon nanotube filters, single- and multi-walled nanotubes, graphisited porous carbon and graphite, *J. Raman Spectrosc.*, **2009**, 40, 3, 344.

[21]- Thomsen C., Second-order Raman spectra of single and multiwalled carbon nanotubes, *Phys. Rev. B*, **2000**, 61, 7, 4542.

[22]- Liu T., Xiao Z., Wang B., The exfoliation of SWCNT bundles examined by simultaneous Raman scattering and photoluminescence spectroscopy, *Carbon*, **2009**, 47, 3529.

[23]- Resasco D.E., Kitiyanan B., Harwell J.H., Alvarez W., Method of producing carbon nanotubes, U.S. Patent No. 6333016, **2001**.

---

[24]- Lolli G., Zhang L.A., Balzano L., Sakulchaicharoen N., Tan Y., Resasco D.E., Tailoring (n,m) structure of single-walled carbon nanotubes by modifying reaction conditions and the nature of the support of CoMo catalysts, *J. Phys. Chem. B*, **2006**, 110, 5, 2108.

[25]- Alvarez W.E., Pompeo F., Herrera J.E., Balzano L., Resasco D.E., Characterization of single-walled carbon nanotubes (SWCNTs) produced by CO disproportionation on Co-Mo catalysts, *Chem. Mater.*, **2002**, 14, 4, 1853.

[26]- Resasco D.E., Alvarez W.E., Pompeo F., Balzano L., Herrera J.E., Kitiyanan B., et al., A scalable process for production of single-walled carbon nanotubes (SWCNT) by catalytic disproportionation of CO on a solid catalyst, *J. Nanopart. Res.*, **2002**, 4, 1-2, 131.

[27]- Resasco D.E., Herrera J.E., Balzano L., Decomposition of carbon-containing compounds on solid catalysts for single-walled nanotubes production, *J. Nanosci. Nanotechnol.*, **2004**, 4, 4, 398.

[28]- Miyata Y., Yanagi K., Maniwa Y., Tanaka T., Kataura H., Diameter analysis of rebundled single-wall carbon nanotubes using X-ray diffraction: verification if chirality assignment based on optical spectra, *J. Phys. Chem. C*, **2008**, 112, 15997.

[29]- Herrera J.E., Resasco D.E., In situ TPO/Raman to characterize single-walled carbon nanotubes, *Chem. Phys. Lett.*, **2003**, 376, 3-4, 302.

[30]- Strong K.L., Anderson D.P., Lafdi K., Kuhn J.N., Purification process for single-wall carbon nanotubes, *Carbon*, **2003**, 41, 1477.

[31]- Li Q., Yan H., Zhang J., Liu Z., Effect of hydrocarbons precursors on the formation of carbon nanotubes in chemical vapor deposition, *Carbon*, **2004**, 42, 4, 829.

[32]- Bartsch K., Arnold B., Kaltofen R., Täschner C., Thomas J., Leonhardt A., Effects of catalyst pre-treatment on the growth of single-walled carbon nanotubes by microwave CVD, *Carbon*, **2007**, 45, 543.

[33]- Lohr S.L., Sampling: Design and Analysis, Pacific Grove CA: Duxbury Press, **1999**.

[34]- Park T.J., Banerjee S., Hemraj-Benny T., Wong S.S., Purification strategies and purity visualization for single-walled carbon nanotubes, *J. Mater. Chem.*, **2006**, 16, 2, 141.

[35]- Zhang M., Yudasaka M., Koshio A., Iijima S., Thermogravimetric analysis of single-wall carbon nanotubes ultrasonicated in monochlorobenzene, *Chem. Phys. Lett.*, **2002**, 364, 420.

[36]- Stanmore B.R., Brilhac J.F., Gilot P., The oxidation of soot: a review of experiments, mechanisms and models, *Carbon*, **2001**, 39, 2247.

[37]- Arepalli S., Nikolaev P., Gorelik O., Hadjiev V.G., Holmes W., Files B., et al., Protocol for the characterization of single-wall carbon nanotubes material quality, *Carbon*, **2004**, 42, 1783.

[38]- Attal S., Thiruvengadathan R., Regev O., Determination of the concentration of single-walled carbon nanotubes in aqueous dispersions using UV-Visible absorption spectroscopy, *Anal. Chem.*, **2006**, 78, 23, 8098.

[39]- Landi B.J., Ruf H.J., Evans C.M., Cress C.D., Raffaelle R.P., Purity assessment of single-wall carbon nanotubes, using optical absorption spectroscopy, *J. Phys. Chem. B*, **2005**, 109, 20, 9952.

[40]- Landi B.J., Ruf H.J., Worman J.J., Raffaelle R.P., Effects of alkyl amide solvents on the dispersion of single-wall carbon nanotubes, *J. Phys. Chem. B*, **2004**, 108, 44, 17089.

[41]- Ryabenko A.G., Dorofeeva T.V., Zvereva G.I., UV-VIS-NIR spectroscopy study of sensitivity of single-wall carbon nanotubes to chemical processing and Van-der-Waals SWCNT/SWCNT interaction, Verification of the SWCNT content measurements by absorption spectroscopy, *Carbon*, **2004**, 42, 8-9, 1523.

[42]- Itkis M., Perea D.E., Jung R., Niyogi S., Haddon R.C., Comparison of analytical techniques for purity evaluation of single-walled carbon nanotubes, *J. Am. Chem. Soc.*, **2005**, 127, 10, 3439.

[43]- Tan Y., Resasco D.E., Dispersion of single-walled carbon nanotubes of narrow diameter distribution, *J. Phys. Chem. B*, **2005**, 109, 14454.

[44]- Itkis M.E., Niyogi S., Meng M., Hamon M., Hu H., Haddon R.C., Spectroscopic study of the Fermi level electronic structure of single-walled carbon nanotubes, *Nano Lett.*, **2002**, 2, 2, 155.

[45]- Engtrakul C., Davis M. F., Mistry K., Larsen B. A., Dillon A. C., Heben M. J., Blackburn J. L., Solid-state ^{13}C NMR assignment of carbon resonances on metallic and semiconducting single-walled carbon nanotubes, *J. Am. Chem. Soc.*, **2010**, 132, 9956.

[46]- Maruyama S., Miyauchi Y., Taniguchi Y., Effect of carbon isotope abundance on thermal conductivity and Raman scattering of single-walled carbon nanotubes, ISMME **2003**-109.

[47]- Kalbác M., Kavan L., Zukalova M., Dunsch L., In situ Raman spectroelectrochemical study of 13C-labeled fullerene peapods and carbon nanotubes, *Small*, **2007**, 3, 10, 1746.

[48]- Cheng Y., Zhou S., Isotope effect on phonon spectra in single-walled carbon nanotubes, *Phys. Rev. B*, **2005**, 72, 035410.

[49]- Fan S., Liu L., Liu M., Monitoring the growth of carbon nanotubes by carbon isotope labeling, *Nanotech.*, **2003**, 14, 1118.

[50]- Niemantsverdriet J.W., Spectroscopy in Catalysis, Wiley-VCH, **2007**.

[51]- Irurzun V., Ruiz M. P., Resasco D. E., Raman intensity measurements of single-walled carbon nanotubes suspensions as a quantitative technique to asses purity, *Carbon*, **2010**, 48, 2873.

[52]- Singh D.K., Iyer P.K., Giri P.K., Diameter dependence of interwall separation and strain in multiwalled carbon nanotubes probed by X-ray diffraction and Raman scattering studies, *Diam. Relat. Mater.*, **2010**, 19, 1281.

[53]- Dresselhaus M. S., Dresselhaus G., Saito R., Jorio A., Raman spectroscopy of carbon nanotubes, *Phys. Rep.*, **2005**, 409, 47.

[54]- Dresselhaus M. S., Eklund P. C., Phonons in carbon nanotubes, *Adv. Phys.*, **2000**, 49, 705.

[55]- Arnold M. S., Stupp S. L., Hersam M. C., *Nano Lett.*, **2005**, 5, 4.713.

[56]- Ghosh S., Bachilo S. M., Weisman R. B., Advanced sorting of single-walled carbon nanotubes by nonlinear density-gradient ultracentrifugation, *Nature Nanotech.*, **2010**, 5, 443.

[57]- Lai L., Lu J., Song W., Ni M., Wang L., Luo G., Zhou J., Mei W. N., Gao Z., Yu D., First principles calculations of C^{13} NMR chemical shifts of infinite single walled carbon nanotubes: New data for large diameter and four helical nanotubes, *J. Phys. Chem. C*, **2008**, 112, 16417.

CHAPTER 4

Acknowledgments:
A. Monzon, Universidad Tecnologica de Zaragoza, Spain
L. Zhang, The University of Oklahoma
S. Mrinal, The University of Oklahoma
D. Smith, The University of Oklahoma

CHAPTER 4

4.1- Non-conventional growth

CNT, as it has been mentioned before, can be used for different applications [1] due to their outstanding properties, such as high electrical and thermal conductivity, high Young's modulus, etc. Among these applications, Rogers et al. [2] have mentioned the goodness of SWCNT to synthesize or assemble stretchable electronics. Figure 84(a) shows a stretchable material composed of a rubber matrix loaded with SWCNT. Figure 84(b) shows a circuit made of organic transistors interconnected by the loaded matrix shown in Fig. 84(a) and supported onto poly(dimethylsiloxane).

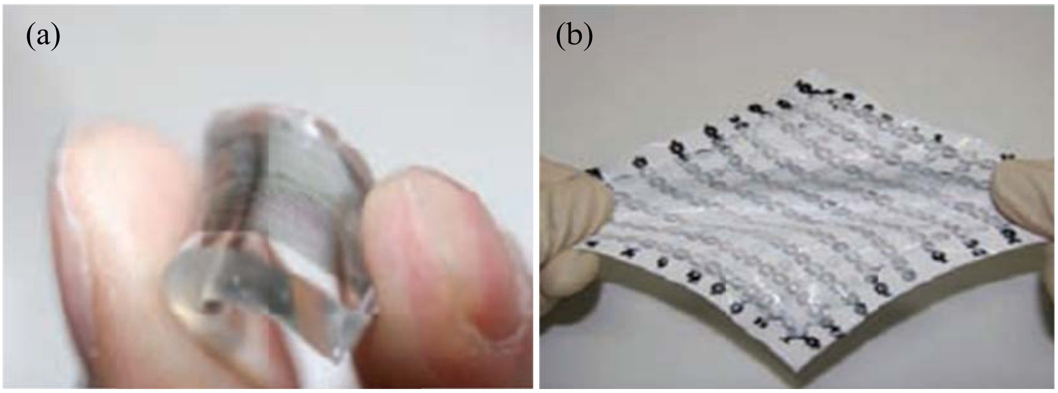

Figure 84: CNT to assemble stretchable electronics, [2].

Another property that makes CNT interesting is their capability to resist fatigue, super-compress and elastically compress. Xu et al. [3] have shown that special assembly of CNT would lead to viscoelastic CNT materials. They have synthesized CNT networks where each tube was in contact with several other tubes. Figure 85 shows the stress-strain analysis presented by Xu et al. [3]. This analysis showed that the CNT network had a stress-strain behavior similar to a viscoelastic rubber, showing 100

% strain and closed hysteresis. They emphasized the importance of tube-tube connection to improve cohesiveness and thermal stability.

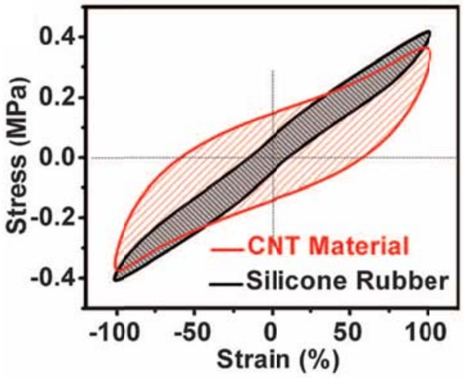

Figure 85: CNT hysteresis behavior. Xu et al. [3].

Gogotsi [4] has found that, while the viscoelasticity of most of the known materials is temperature dependent, it is not in the case of CNT due to their thermal stability. This property is related to the capacity to release energy through different mechanisms as mentioned by Gogotsi [4].

The zipping-unzipping (Fig. 86(a)) of tubes in contact and flattering-recover (Fig. 86(b)) behavior favor the energy dissipation, making them thermal stable at different temperatures.

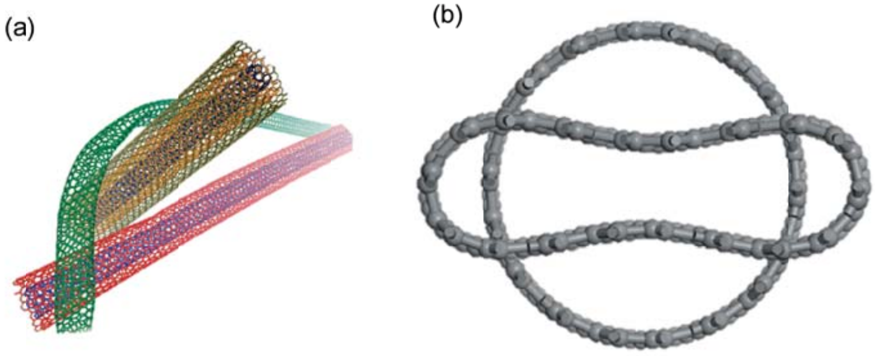

Figure 86: CNT arrangement leading to energy dissipation, [4].

The outstanding properties of CNT make them desirable materials for a wide range of uses as mentioned before. For this reason, not only traditional growth of CNT is an interesting field, but also non-traditional growth such as aligned CNT, hierarchical carbon structures and 3D carbon nano-structures.

Nano-carbon materials with high surface area, thin walls and mesoporous sizes are desirable for the synthesis of super capacitors with high performance, as it was shown by Li et al. [5]. They have shown that carbon materials can be used as electrodes due their high surface area, high electrical conductivity, high chemical stability and price. Li et al. [5] have also pointed out that the small micropores present a limitation for the accessibility of the ions during the charge/discharge process. They have shown that on the other hand, functionalized hierarchical mesoporous carbon structures (Fig. 87(a) and (b)) with high surface area and thin walls showed high charge/discharge performance.

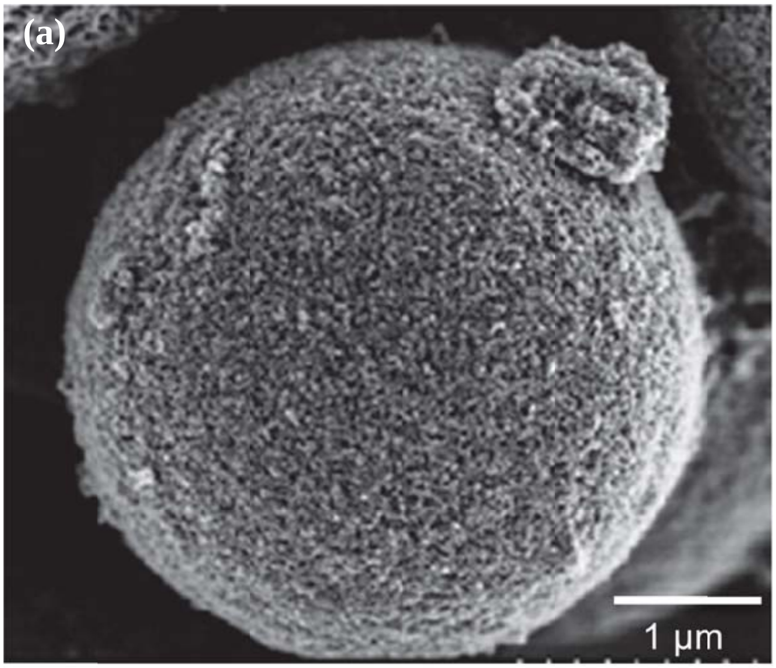

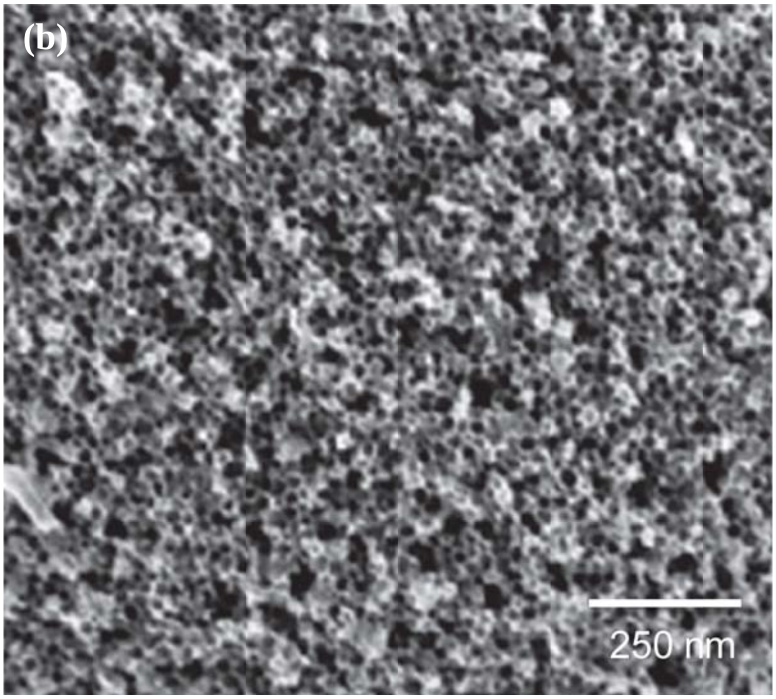

Figure 87: Hierarchical nano-carbon spheres, [5].

Baughman et al. [6] have also shown that SWCNT can be used as actuators by being used as electrolyte-filled electrodes of super capacitors. Briefly, an actuator is a mechanical device for moving or controlling a mechanism or system operated by a source of energy (usually electrical current). SWCNT are particularly interesting because, besides of the mechanical properties, electrical conductivity and charge transfer, they have high surface area compared to graphite. It was shown by Baughman et al. [6] that carbon sheets composed of bundles of SWCNT have the same good properties of natural muscle enhanced by the high surface area.

Jiang et al. [7] have also emphasized the goodness of hierarchical structures to be used as electrochemical capacitors. In this case, CNT were grown by CVD onto 3D niquel structures. This hybrid material has showed higher capacitance per surface area than other materials typically used, such as MWCNT. Figures 88(a) to (d) show the hierarchical structures obtained by Jiang et al. [7]. In Fig. 88(a) the macroscopic structure of the nickel covered by CNT can be observed. Figures. 88(b) to (d) are a close up showing the presence of CNT.

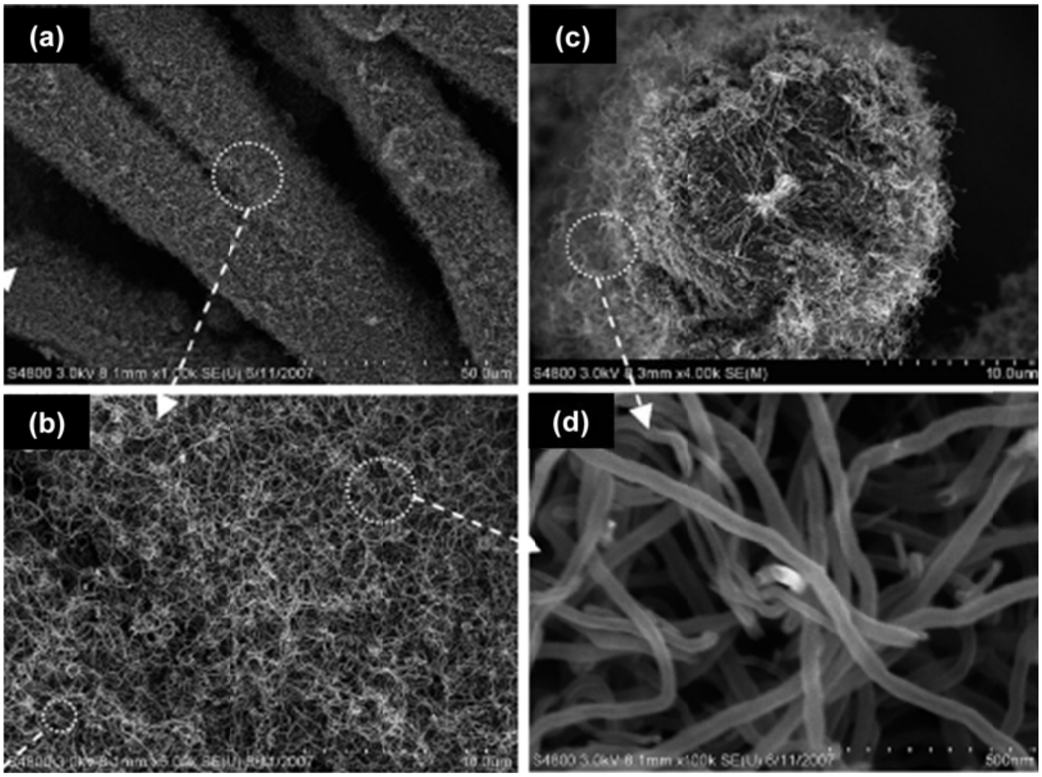

Figure 88: Hierarchical nano-carbon structure. CNT on 3D Ni structures, [7].

As mentioned by Zhang et al. [8], extensive efforts are being done to control the growing of SWCNT directly on different substrates [9-12]. Controlled arrangement of the CNT would make them more suitable to be used in devices such as nanosensors, microfluidic, etc. They have shown that physical properties such as hydrophobicity can be controlled, making this nano-arrangment suitable for different applications. Figures 89(a) to (d) show the difference in hydrophobicity between two different CNT arrangements. Figures 89(a) and (c) show a SWCNT crust on a flat surface and

SWCNT pillars. Comparing Fig. 89(b) and (d) it can be seen that when the surfaces are in contact with a drop of water, the crust shows lower hydrophobicity than the pillars. As explained by Zhang et al. [8], the roughness of the CNT surface determines the wettability.

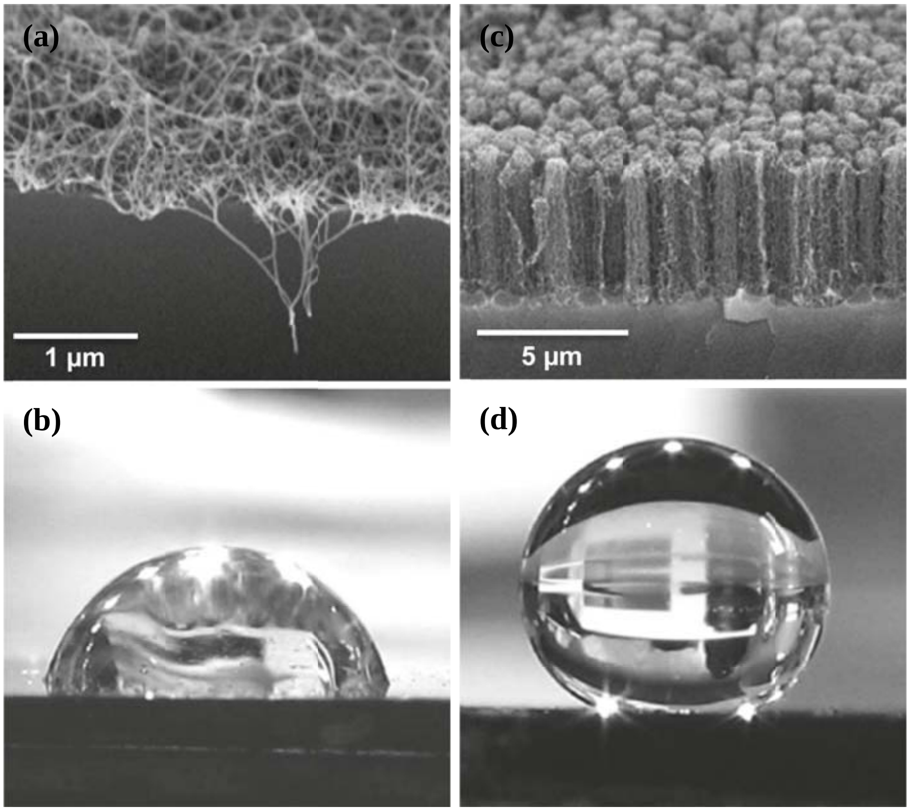

Figure 89: Super hydrophobic surfaces, [8].

As mentioned by Wu et al. [13], nowadays scientists are interested in the synthesis of 2D and 3D nano-structures to be used in electronic devices rather than well dispersed nano-materials. They have shown that 3D carbon nano-structures could be synthesized under controlled conditions. Figures 90(a) and (b) show the 3D carbon nanostructures synthesized by Wu et al. [13].

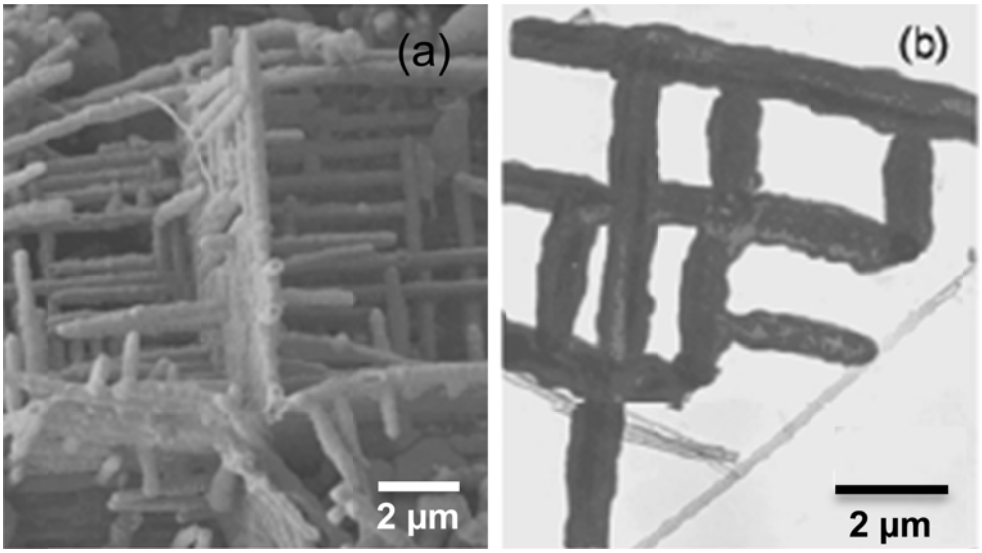

Figure 90: 3D carbon nano-structures, [13].

As it was explained before, CNT with special and controlled growth are being sought by most of the researchers nowadays. In this chapter two different approaches related to non-conventional growth are presented. The first case is related to the thermal conductivity properties of CNT. Hierarchical structures have been synthesized to improve the out-of-plane thermal conductivity of different composites. The second case is related to the growth of CNT onto flat surfaces in order to increase the carbon yield while decreasing the residue. It is important to mention that for most of the applications, low residue content is desirable.

4.1- Hierarchical structures: Interface connection enhancement

Carbon fabrics are widely use to synthesize composites because, not only improves the mechanical strength of the polymers, but also enhances the in plane thermal conductivity. However the out-of-plane thermal conductivity remains low because of the poor penetration of the fiber into the polymer layer. In this section it is shown how the hierarchical growth of different carbon species was tailored in order to enhance the out-of-plane thermal conductivity of carbon fabric composites (Fig. 91).

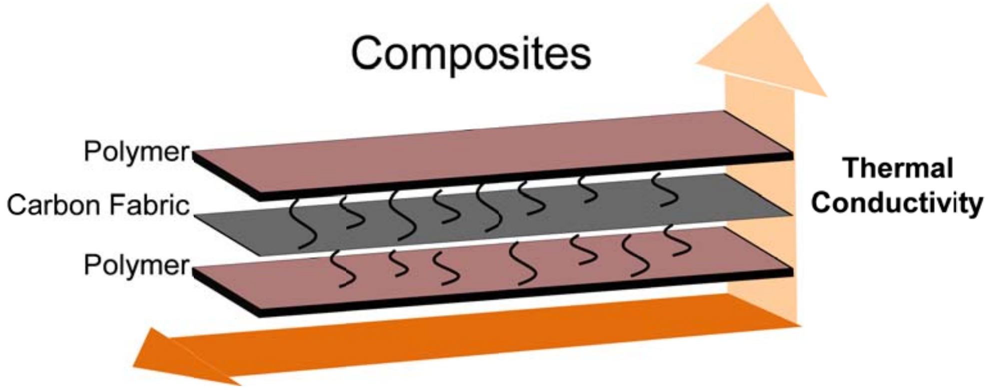

Figure 91: Scheme of carbon fabric composites.

4.1.1- Experimental

The hierarchical material was synthesized by successive metals depositions. The main structure was prepared by ionic exchange of $Cu(NO_3)_2{\cdot}3H_2O$ and $Ni(NO_3)_2{\cdot}6H_2O$ with a Cu/Ni molar ratio of 1/9 onto commercial carbon nano-fibers. This commercial material was pre-treated with nitric acid at 50-70 °C for 24 h in order to make the surface more suitable for metal anchoring. After washing the fibers with water, the treated fibers were introduced in a flask containing ammonium hydroxide and an aqueous solution of the precursors was finally added. The temperature of the system was increased to 70 °C while flowing N_2 and the reaction was conducted for 24 h. Finally the doped fibers were dried and calcined at 400 °C for 30 min and at 500 °C for 60 min. A mass of 60 mg of this calcined primary structure was set into a quartz reactor as it is shown in Fig. 92, and it was pre-reduced under 160 sccm of H_2 for 30 min at 500 °C. Then the temperature was increased to 650-750 °C under 160 sccm of He and, finally, a mixture of acetylene/H_2 with a partial pressure of 0.1 was fed for 30 min.

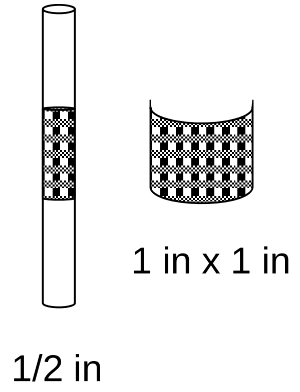

Figure 92: Carbon fabric arrangement in ½ in quartz reactor.

The secondary structure was pre-treated with hydrogen peroxide under the same conditions explained for the previous pre-treatment. A mass of 250 mg of the pre-treated secondary structure was set into a flask with ammonium hydroxide and an aqueous solution of the metal precursors was added. The reaction was conducted for 24 h at 70 °C under N_2. In this case the precursors were $Co(NO_3)_2 \cdot 6H_2O$ (Sigma Aldrich) and $(NH_4)_6Mo_7O_{24}.4H_2O$ (Sigma Aldrich) with a Co/Mo molar ratio of 3. The reaction was conducted for 24 h at 60 °C. Finally, the sample was dried and calcined at 300 °C for 30 min in an oven, and at 500 °C for 60 min under He. A mass of 100 mg was finally set in a quartz reactor and pre-reduced at 500 °C for 30 min under H_2. Then the temperature was increased to 750 °C under He and the carbon source (carbon monoxide) was fed for 30 min at 750 °C.

4.1.2- Results

The first attempt to increase the interconnection between layers was to grow CNT by depositing active metals onto the commercial fibers. This experiment was not successful and the reason was that the surface of the commercial fibers, as it can be seen in Fig. 93, is extremely smooth not having enough defects for the metal precursors to anchor.

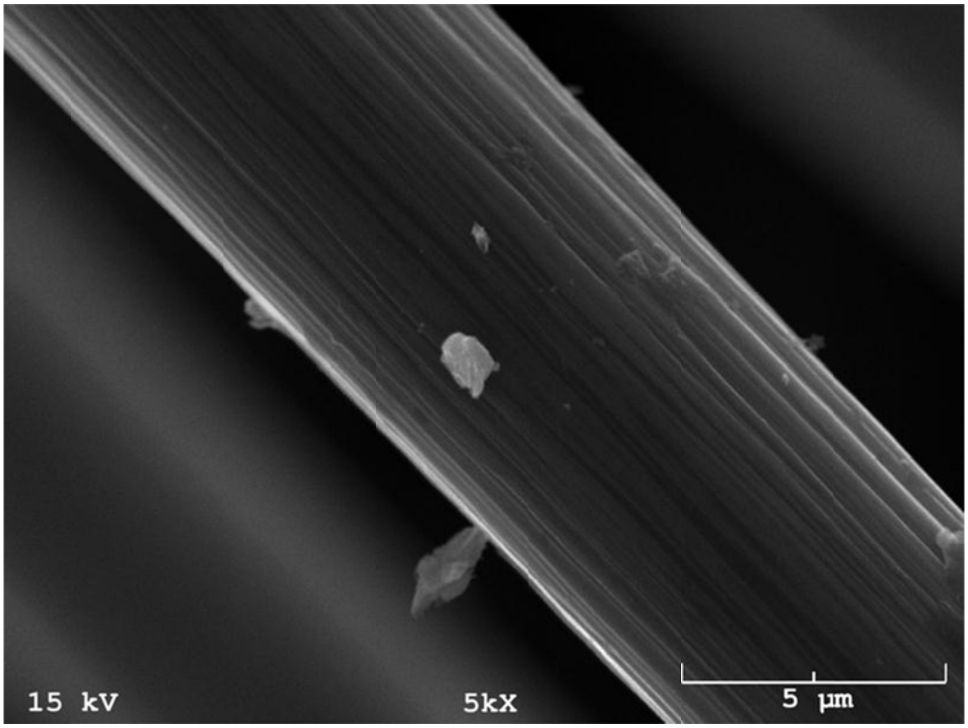

Figure 93: Scanning electron microscopy image of commercial carbon fibers.

The second attempt was to grow secondary carbon layers in order not only to increase the surface area, but also to generate defects to improve the metal anchoring and dispersion [14-18]. Electron microscopy techniques were used to characterize the growth of the different structures.

4.1.2.1- Scanning electron microscopy

4.1.2.1.1- Primary structure

Figure 94(a) shows the structure of the neat carbon fiber sample pre-treated with acid [19,20] before the impregnation with Cu/Ni. Figure 94(b) shows a scheme of the first metal deposition. The small pink dots represent the bimetallic alloy composed of Ni and Cu. This primary structure was calcined, pre-reduced under H_2 and finally exposed to acetylene/H_2 (10 %) to grow carbon nano-fibers.

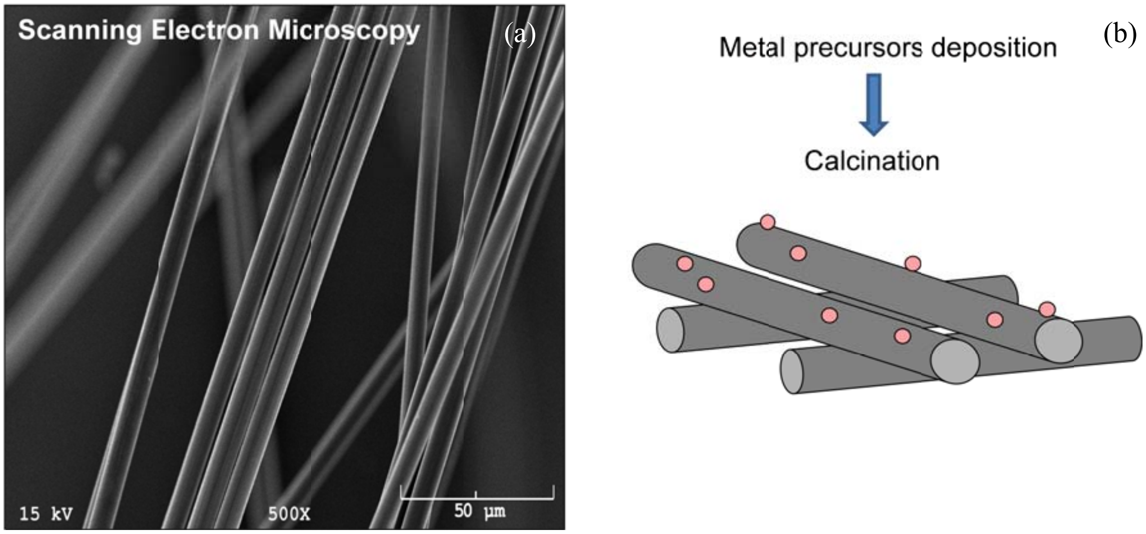

Figure 94: (a) SEM image of acid pre-treated commercial carbon fibers. (b) Scheme of the first metal deposition onto the commercial carbon fibers.

4.1.2.1.2- Secondary structure

Figure 95(a) shows the secondary structure conformed of carbon nanofibers (CNF) grown onto the commercial CF (fabric). As it can be seen in this SEM image, this surface seems to be more suitable for the anchoring and dispersion of the metals.

Figure 95(b) shows an scheme of the Co/Mo deposition onto the secondary structure. The blue dots represent the bimetallic alloy. This secondary structure was calcined and pre-reduced under H_2 leading to the formation of the tertiary structure after feeding the carbon source (carbon monoxide).

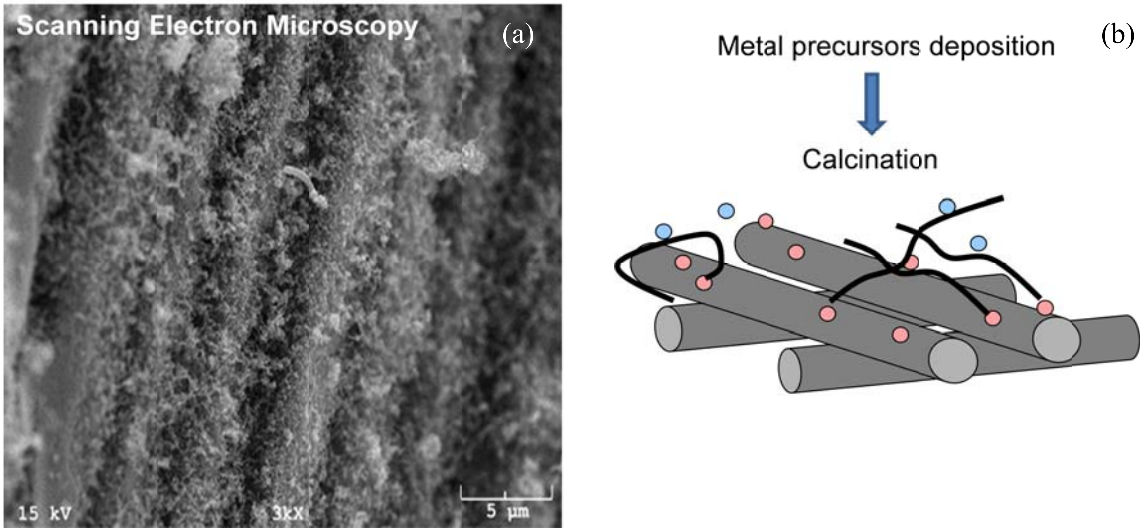

Figure 95: (a) SEM image of secondary structure (CNF-CF). (b) Scheme of the second metal deposition onto the secondary structure.

4.1.2.1.3- Tertiary structure

Figure 96(a) is a close up image of the CNT grown onto the CNF previously shown in Fig. 95(a). In this image, the CNF and the CNT can be clearly differentiated due to the differences in diameter. It is important to mention that the diameter of the CF was approximately between 10-15 µm, the diameter of the CNF was approximately 60-100 nm and the CNT diameter was between 10-20 nm. Figure 96(b) shows an scheme of the final hierarchical structure.

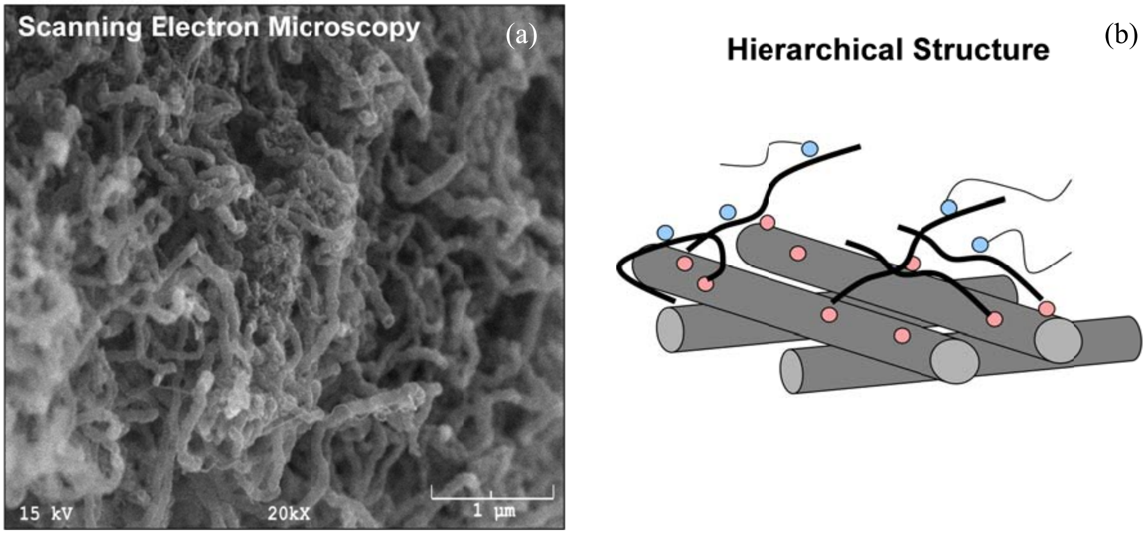

Figure 96: (a) SEM image of tertiary structure (CNT-CNF-CF). (b) Scheme of the final Hierarchical structure.

4.1.2.2- Transmission electron microscopy

Figure 97 shows a TEM image of the final structure.

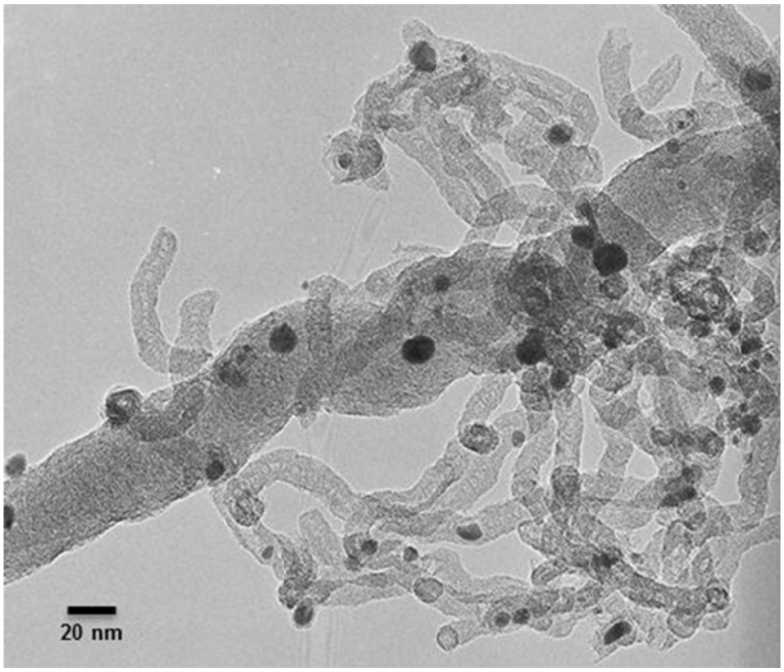

Figure 97: TEM image of carbon nanofibers and carbon nanotubes that composed the secondary and tertiary structure.

It is worth noting that, in this image, only the secondary (CNF) and tertiary (MWCNT) structures are observable because the size of the primary structure (CF) was out of scale for this characterization technique. The largest diameter structures in this image are CNF and the smaller diameter species are MWCNT.

4.1.2.3- Temperature programmed oxidation

TPO was conducted in order to characterize each intermediate structure. This technique was conducted by flowing 80 sccm of 5 % O_2 in He through a vertical quartz reactor of 1/8 in. The amount of CO_2 produced was detected and recorded by using flame ionization detector (FID).

It can be seen in Fig. 98 that the oxidation temperature is the highest for the neat commercial carbon fiber. After the first deposition of metal (Cu/Ni), the oxidation temperature shifts to lower values and the total area decreases slightly. The shifts to lower temperatures can be related to the synergetic effect of the metal catalyzing the oxidation and the presence of defects due to the acid pre-treatment. The third sample analyzed was the secondary structure conformed of CNF onto CF. As it can be seen in Fig. 98, the profile shifts also to lower temperatures and splits in two different regions. The lower temperature zone related to the oxidation of thin and defective CNF and the zone at higher temperature related to the CF. In this case the CF oxidation peak seems to appear at lower temperature. This could be an effect of the presence of thin CNF accelerating the burning process of the CF. The fourth sample analyzed was the tertiary structure. While the lowest oxidation temperature remains constant, the highest oxidation temperature shifts to higher temperatures. This could be due to the presence of less defective CNF burning at higher temperatures. In this case, the split between peaks, is not as clear as in the previous case due to the presence of MWCNT burning at temperatures between 600 °C and 750 °C.

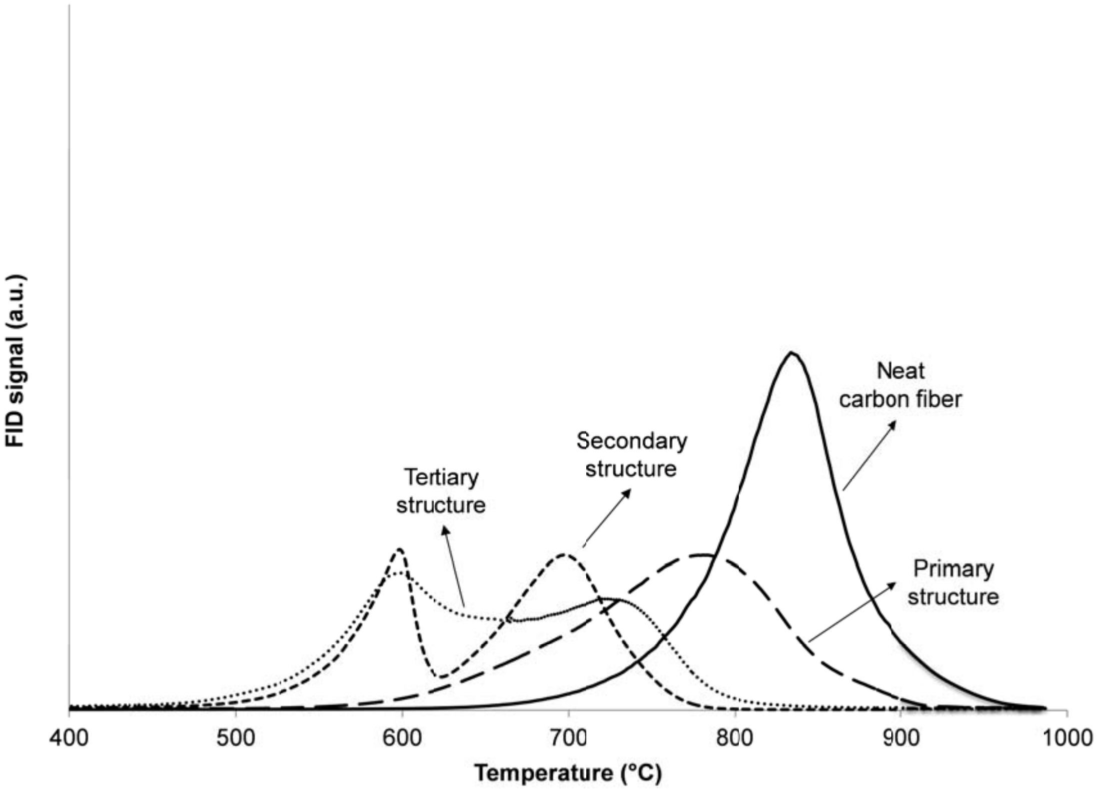

Figure 98: Temperature programmed oxidation of intermediate structures.

4.1.2.4- Raman scattering

Figure 99 shows the Raman scattering spectra of the different intermediate carbon species. From the bottom to the top, the lowest intensity spectrum is the one corresponding to the neat carbon fiber. It can be seen that not only has the lowest intensity but also the D and G bands are wide and have similar intensities. This spectrum is similar to the one expected for amorphous carbon. The spectrum with mid intensity corresponds to the secondary structure (CNF/CF). In this case the intensity is still low but the D band seems to be more defined than in the previous case. This could be related to a higher order structure. The spectrum of the tertiary structure presents, not only the highest intensity, but also the narrowest D and G bands. In all the cases the D band has larger intensity than the G band due to the defects in the material. In this case, the width of the D band shows that the tertiary structure is governed by species with higher order.

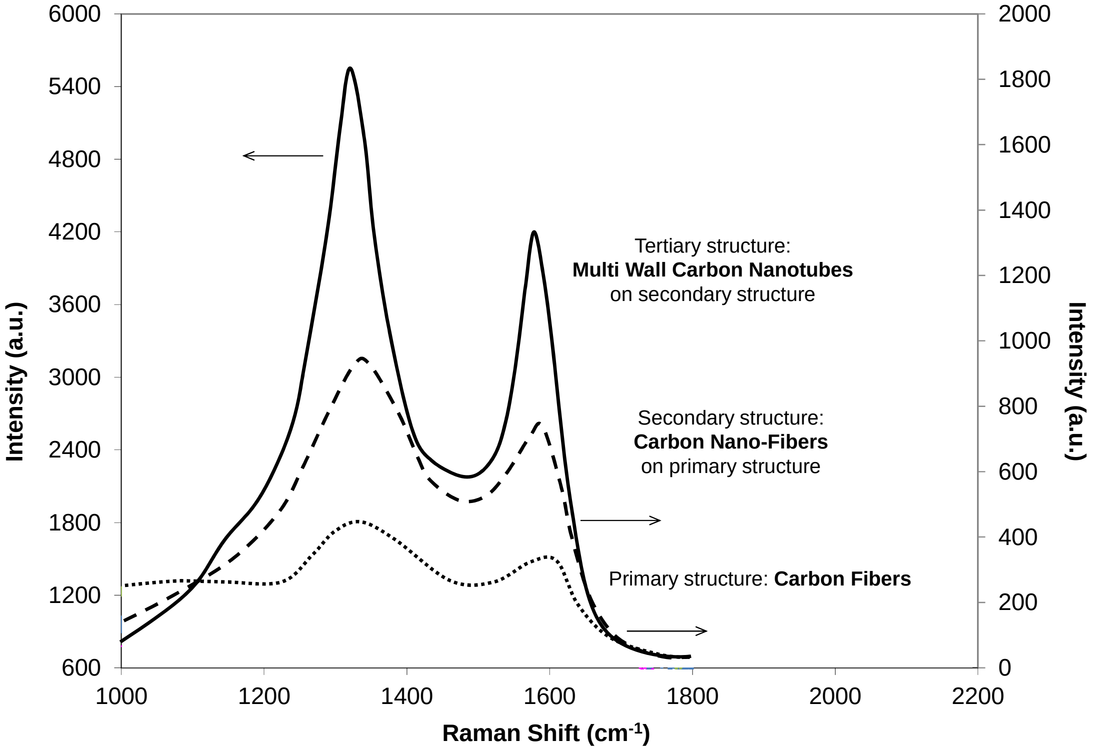

Figure 99: Raman scattering spectra of intermediate structures.

4.1.2.3- Scaling up and optimization

As it was mentioned before, the goal of this project was to increase the out-of-plane thermal conductivity of composites conformed of carbon fabric layers. After the synthesis method was developed, optimization and scaling up was necessary. The necessity of scaling this process up was because larger carbon fabric pieces were needed to measure thermo conductive and mechanical properties. The optimization was also needed because the yield of CNF-CNT has to be controlled for different applications. The scaling up and optimization were conducted by another graduate student (Daniel Smith). The characterization of the composites has been done in collaboration with the School of Aerospace and Mechanical Engineering at OU (Dr. Mrinal C. Saha). Some preliminary data for thermal conductivity was obtained for the neat commercial fiber and for the secondary nano-structure. The 3-omega method has been used to quantify the conductivity.

Figure 100 shows preliminary data related to the out-of-plane thermal conductivity measurements of secondary structures with different degrees of growth. The neat fabric shows the lowest conduction values at any of the temperatures. The samples with 80 and 250 % of CNF growth show higher conduction values than the neat sample. Even though at 25 and 50 °C there is no much improvement going from 80 % to 250 % growth. On the other hand, when the measurements were done at 75 °C, the sample with larger growth seems to show higher conductivity. It is important to mention that these are preliminary results done by Dr. Mrinal’s group and that the methodology is still being optimized. Even though, the general trend shows an improvement in the out-of-plane thermal conductivity of secondary structures.

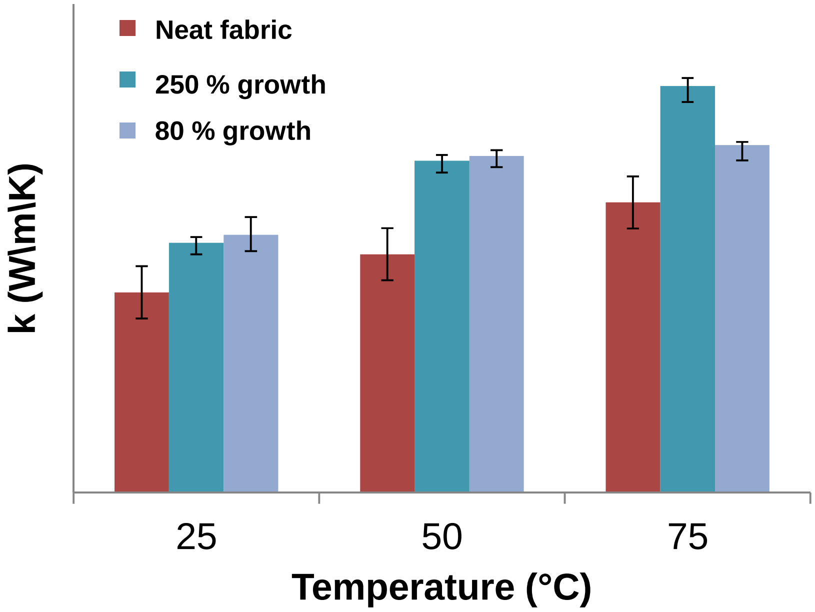

Figure 100: Out-of-plane thermal conductivity trend. Courtesy of D. Smith and S.C. Mrinal.

4.2- Flat surfaces

As it is clear from the name of this chapter, "Non-conventional growth", in this section, growth of SWCNT on different flat surfaces is shown. Our group is known for the development of SWCNT forest [8-912]. Other researchers [21-26] have also shown the importance and potential of growing CNT on flat surfaces.

The main goal of this project was to increase the carbon yield and decrease the amount of residue present in the as-produced sample, while keeping the SWCNT selectivity high. Two different surfaces and different deposition techniques were used to prepare these flat catalysts to grow SWCNT.

In this case, as in the previous section, SEM and TEM were used to visualize the samples, and Raman scattering was used to evaluate the SWCNT selectivity.

4.2.1- Experimental

These catalysts were prepared by using the sol gel method, as it was explained in section 1.1.1.1.2. Briefly, $Co(NO_3)_2{\cdot}6H_2O$ (Sigma Aldrich) dissolved in isopropanol and $MoCl_5$ (Sigma Aldrich) dissolved in water were mixed together and a silica precursor (tetraethoxysilicate) was added. Few drops of this dissolution were set on two different flat surfaces, an stainless steel sheet and a silicon wafer. Figure 101(a) shows an scheme of the catalyst preparation. The flat surface was then set in a filter connected to an Erlenmeyer containing NH_4OH. The system was heated up to 40-50 °C while stirring for 12 h. Figure 101(b) shows a scheme of the aging system. The samples were then dried and calcined at 450 °C for 2 h. The SWCNT growth was conducted by pre-reducing the samples at 500 °C for 30 min, then increasing the reaction temperature to 750 °C under He and finally feeding carbon monoxide for 30 min.

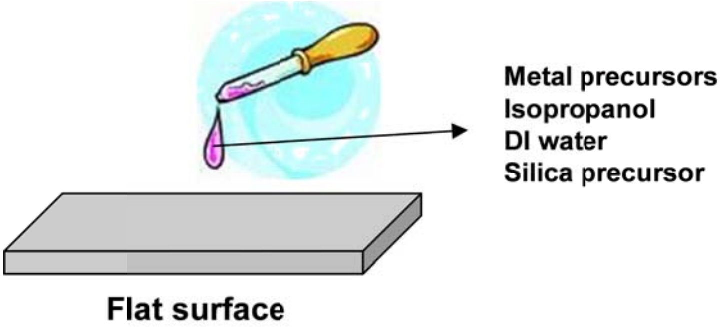

Figure 101(a): Flat surface catalyst preparation by using the sol gel method. Deposition of precursors.

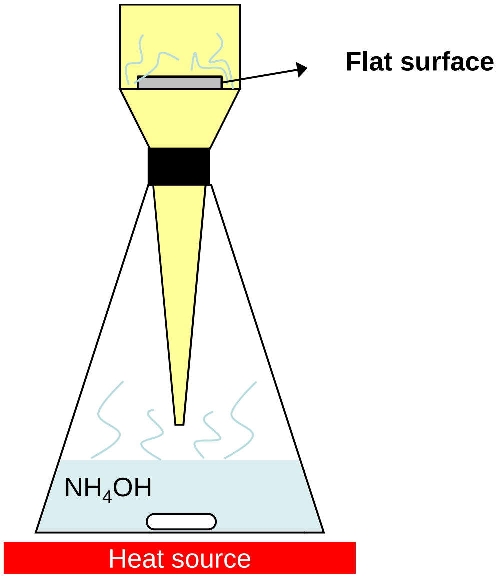

Figure 101(b): Flat surface catalyst preparation by using the sol gel method. Aging.

4.2.2- Results

Figures 102(a) to (d) show scanning electron microscopy images of the products after the reaction using the flat catalysts. As it can be seen in the images with high resolution, the carbon species grown seem to be mostly amorphous carbon rather than SWCNT when stainless steel was used as support.

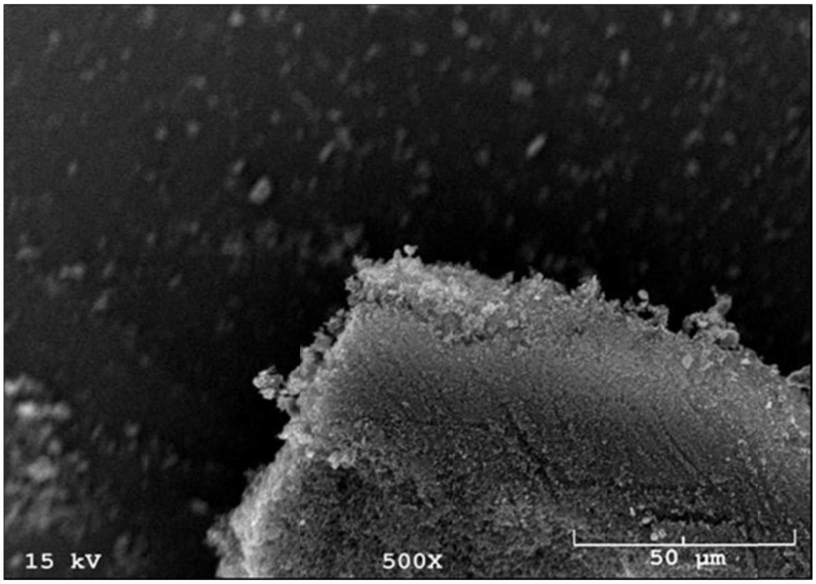

Figure 102(a): SEM image of Co/Mo supported on flat stainless steel by the sol gel method (50 µm scale).

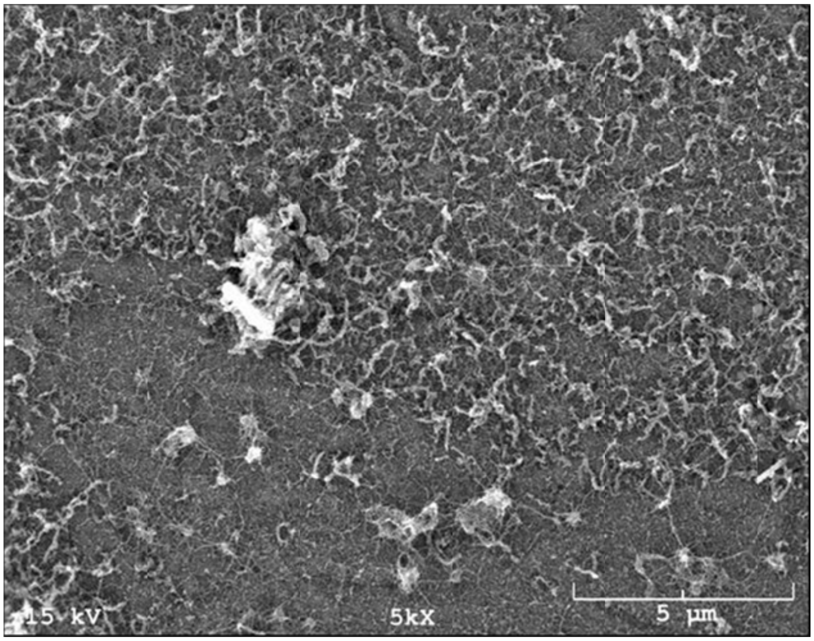

Figure 102(b): SEM image of Co/Mo supported on flat stainless steel by the sol gel method (5 µm scale).

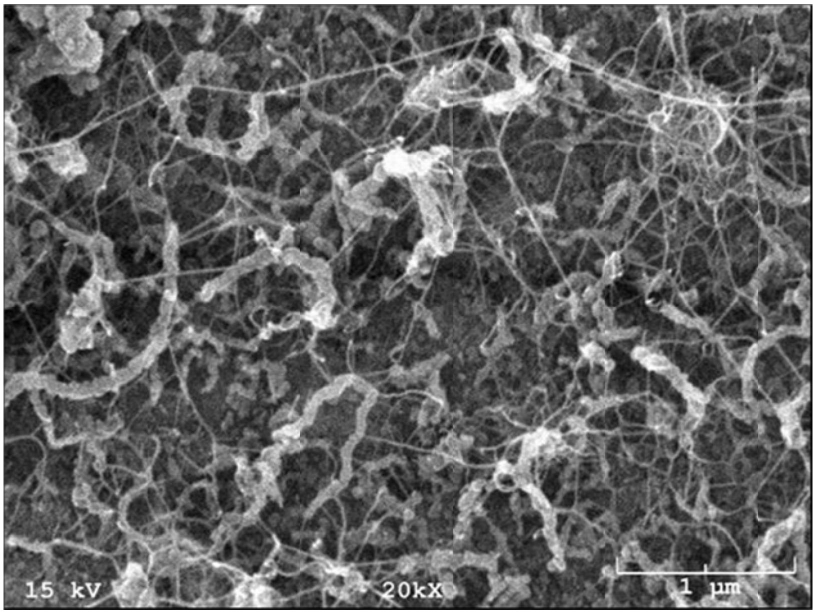

Figure 102(c): SEM image of Co/Mo supported on flat stainless steel by the sol gel method (1 µm scale).

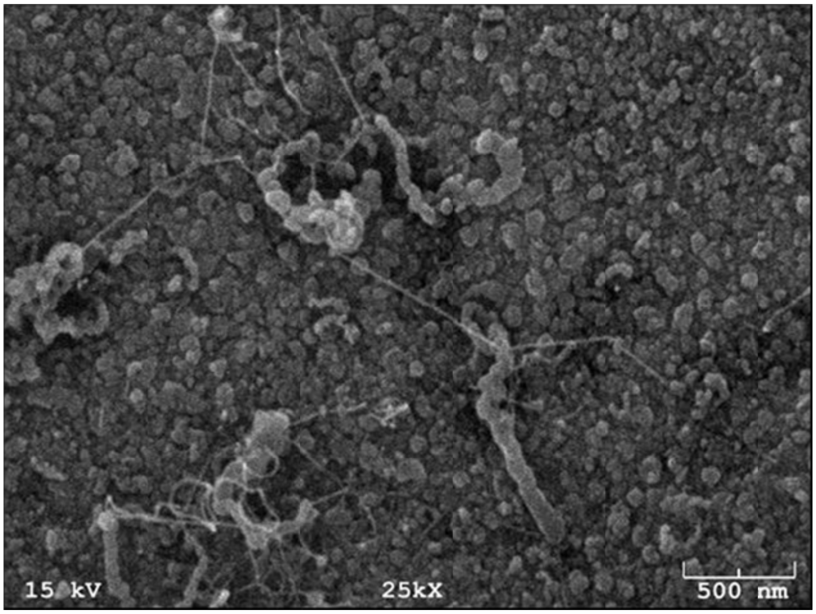

Figure 102(d): SEM image of Co/Mo supported on flat stainless steel by the sol gel method (500 nm scale).

On the other hand, when a silicon wafer was used as support it can be seen in Fig. 103(a) to (e) that SWCNT were selectively produced. In this case, not only high selectivity towards SWCNT was achieved, but also high carbon yield. Raman scattering has been also conducted for both samples grown onto both supports, stainless steel and silicon wafer (Fig. 104).

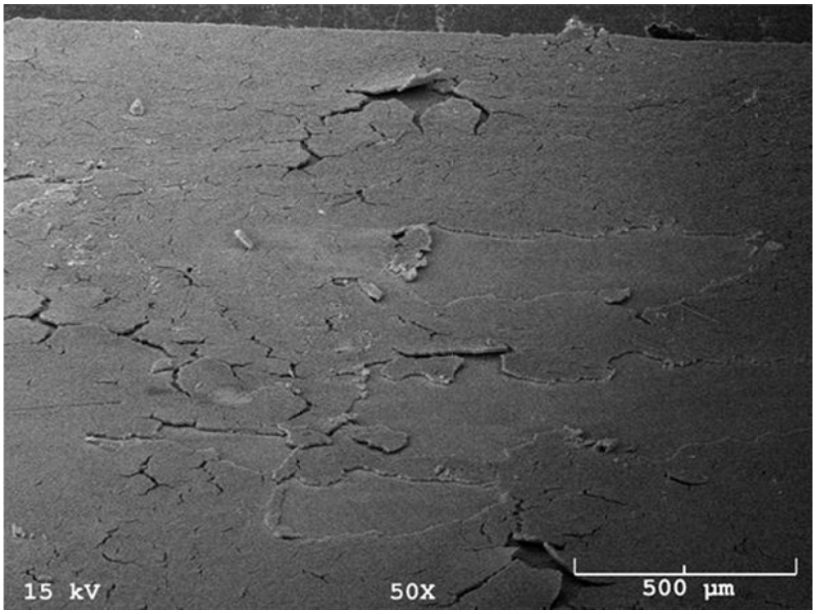

Figure 103(a): SEM image of Co/Mo supported on a flat silicon wafer by the sol gel method (500 µm scale).

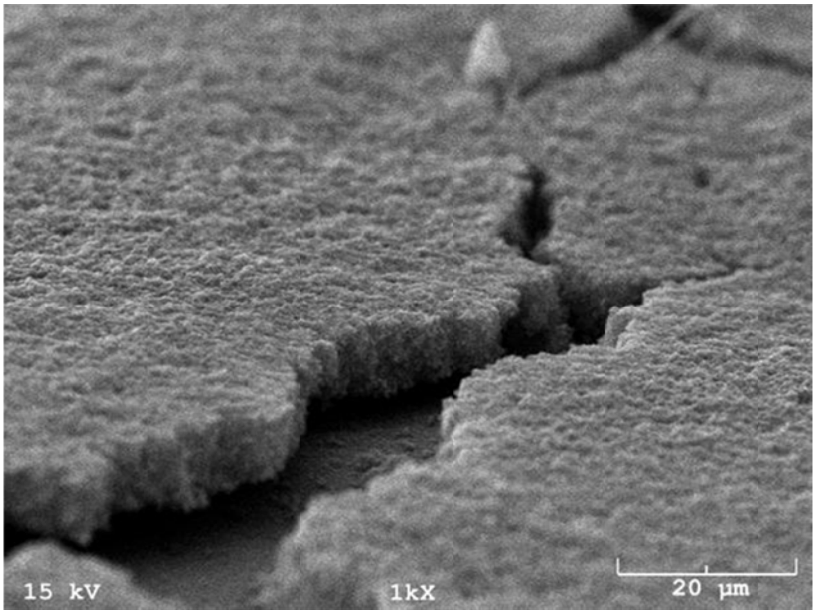

Figure 103(b): SEM image of Co/Mo supported on a flat silicon wafer by the sol gel method (20 µm scale).

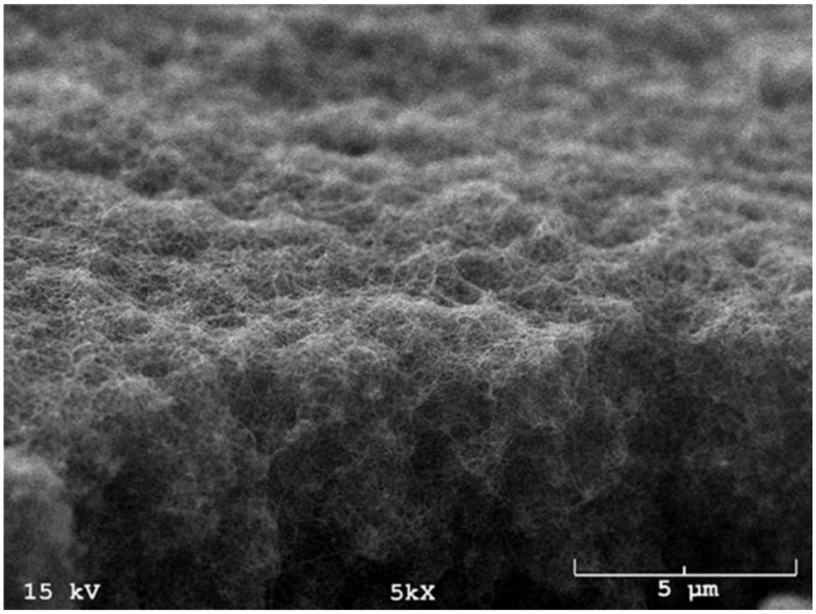

Figure 103(c): SEM image of Co/Mo supported on a flat silicon wafer by the sol gel method (5 µm scale).

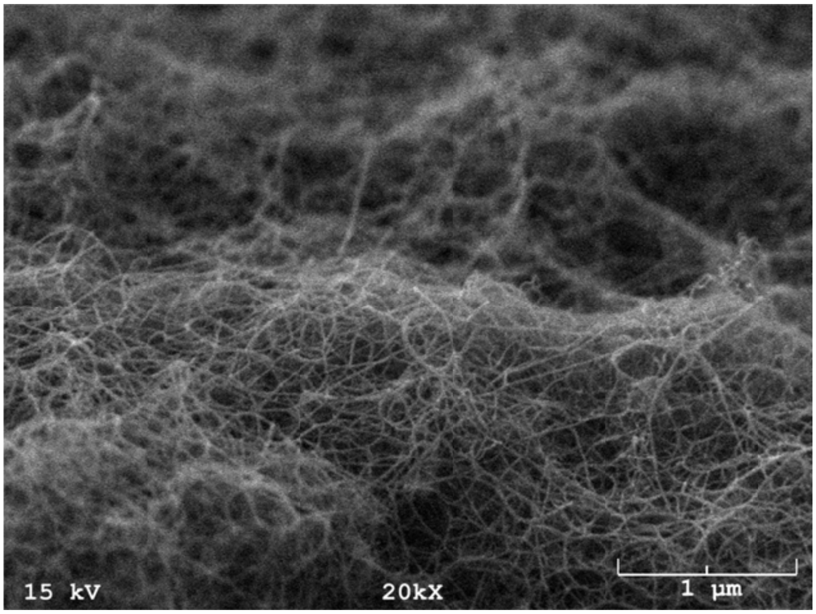

Figure 103(d): SEM image of Co/Mo supported on a flat silicon wafer by the sol gel method (1 µm scale).

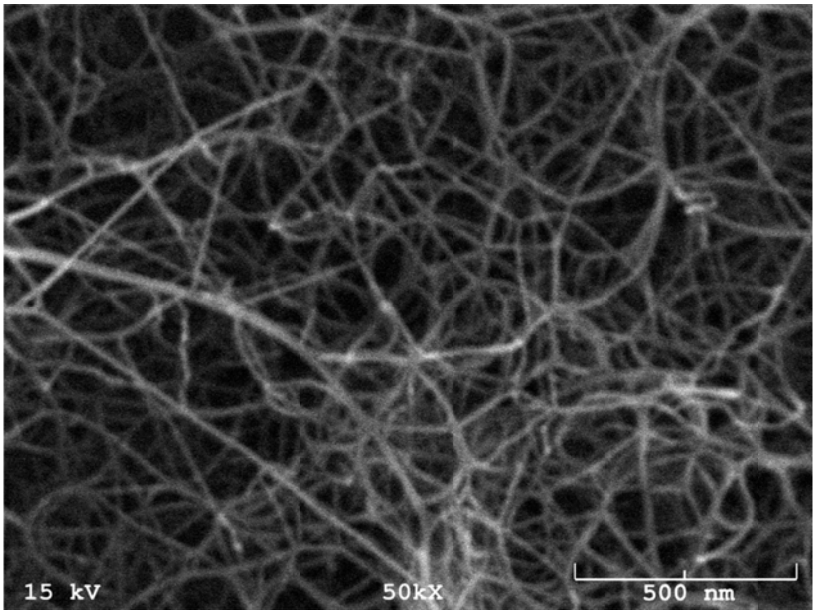

Figure 103(e): SEM image of Co/Mo supported on a flat silicon wafer by the sol gel method (500 nm scale).

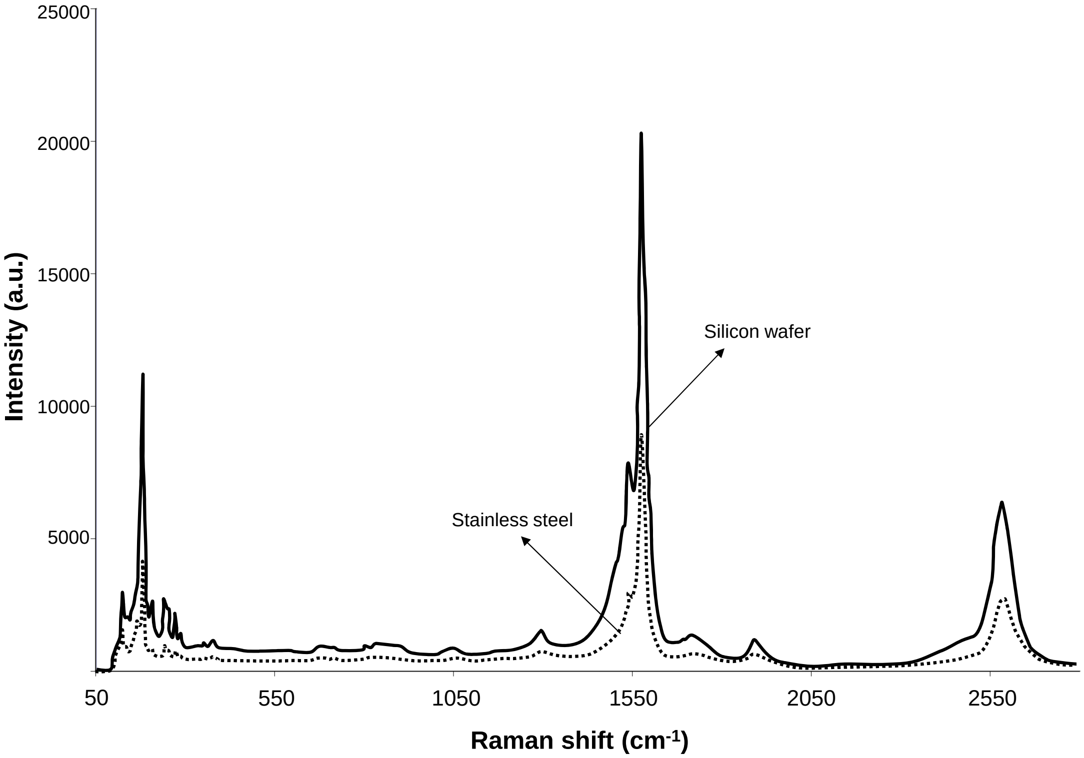

Figure 104: Raman scattering carbon species grown on flat surfaces by the sol gel method.

4.3- Conclusions

Non-conventional CNT growth has been shown in this chapter. Seeking improvement of the out-of-plane thermal conductivity of composites, the growth of carbon hierarchical structures has been conducted. It has been seen that the synthesis of carbon nano-species on top of commercial carbon fibers has led to a suitable surface for the non-conventional growth of CNT. Preliminary thermal conductivity measurements have shown improvements when comparing neat fibers and non-conventional growth hierarchical structures.

CNT synthesis on flat surfaces by using the sol-gel method has been shown to be successful. It was shown that different carbon yields and SWCNT selectivity were obtained when using different supports. While stainless steel wafers have shown to be detrimental to the SWCNT selectivity and carbon yield, catalysts prepared on silicon wafers seemed to show the best performance.

4.4- References

---

[1]- Baughman R.H., Zakhidov A.A., de Heer W.A., Carbon nanotubes-the route toward applications, *Science*, **2002**, 297, 787.

[2]- Rogers J.A., Someya T., Huang Y., Materials and mechanics for stretchable electronics, *Science*, **2010**, 327, 1603.

[3]- Xu M., Futaba D.N., Yamada T., Yumura M., Hata K., Carbon nanotubes with temperature-invariant viscoelasticity from -196 °C to 1000 °C, *Science*, **2010**, 330, 1364.

[4]- Gogotsi Y., High-temperature rubber made from carbon nanotubes, *Science*, **2010**, 330, 1332.

[5]- Li Q., Jiang R., Dou Y., Wu Z., Huang T., Feng D., Yang J., Yu A., Zhao D., Synthesis of mesoporous carbon spheres with a hierarchical pore structure for the electrochemical double-layer capacitor, *Carbon*, **2011**, 49, 1248.

[6]- Baughman R.H., Cui C., Zakhidov A.A., Iqbal Z., Barisci J.N., Spinks G.M., Wallace G.G., Mazzoldi A., De Rossi D., Rinzler A.G., Jaschinski O., Roth S., Kertesz M., Carbon nanotubes actuators, *Science*, **1999**, 284, 1340.

[7]- Jiang F., Fang Y., Liu Y., Chen L., Xue Q., Lu Y., Lu J., He M.Y.., Paper-like 3-dimensional carbon nanotubes (CNTs)–microfiber hybrid: a promising macroscopic structure of CNTs, *J. Mater. Chem.*, **2009**, 19, 3632.

[8]- Zhang L., Resasco D.E., Single-wall carbon nanotube pillars: a superhydrophobic surface, *Langmuir*, **2009**, 25, 8, 4792.

[9]- Zhang L., Li Z., Tan Y., Lolli G., Sakulchaicharoen N., Requejo F.G., Mun B.S., Resasco D.E., Influence of a top crust of entangled nanotubes on the structure of vertically aligned forests of single-walled carbon nanotubes, *Chem. Mater.*, **2006**, 18, 5624.

[10]- Zhang L., Tan Y., Resasco D.E., Oriented growth and subsequent handling of vertical single-walled carbon nanotube forest characterized by electron and probe microscopy, *Microsc. Microanal.*, **2007**, 13, 2.

[11]- Li Z., Zhang L., Mun B.S., Requejo F.G., Resasco D.E., Angle-resolved X-ray absorption near edge structure study of vertically aligned single-walled carbon nanotubes, *Appl. Phys. Lett.*, **2007**, 90, 103115.

[12]- Zhang L., Tan Y., Resasco D.E., Controlling the growth of vertically oriented single-walled carbon nanotubes by varying the density of Co-Mo catalyst particles, *Chem. Phys. Lett.*, **2006**, 422, 198.

[13]- Wu C.Z., Luo W., Ning B., Xie Y., A simple solution route to assemble three-dimensional (3D) carbon nanotube networks, *Chinese Sci. Bull.*, **2009**, 54, 11, 1894.

[14]- Jie C., Xiang X., Peng X., The effect of carbon nanotube growing on carbon fibers on the microstructure of the pyrolytic carbon and the thermal conductivity of carbon/carbon composites, *Mater. Chem. Phys.*, **2009**, 116, 57.

[15]- Alcañiz-Monge J., Lillo-Rodenas M.A., Bueno-López A., Illán-Gómez M.J., The influence of iron chloride addition to the precursor pitch on the formation of activated carbon fibers, *Micropor. Mesopor. Mater.*, **2007**, 100, 202.

[16]- Lee Y.S., Kim Y.H., Hong J.S., Suh J.K., Cho G.J., The adsorption properties of surface modified activated carbon fibers for hydrogen storages, *Catal. Today*, **2007**, 120, 420.

[17]- Smiljanic O., Dellero T., Serventi A., Lebrun G., Stansfield B.L., Dodelet J.P., Trudeau M., Désilets S., Growth of carbon nanotubes on ohmically heated carbon paper, *Chem. Phys. Lett.*, **2001**, 342, 503.

[18]- Lim S., Yoon S.H., Korai Y., Mochida I., Selective synthesis of thin carbon nanofibers: I. Over nickel-iron alloys supported on carbon black, *Carbon*, **2004**, 42, 1765.

[19]- Bulushev D.A., Yuranov I., Suvorova E.I., Buffat P.A., Kiwi-Minsker L., Highly dispersed gold on activated carbon fibers for low-temperature CO oxidation, *J. Catal.*, **2004**, 224, 8.

[20]- Maciá-Agulló J.A., Moore B.C., Cazorla-Amorós D., Linares-Solano A., Influence of carbon fibres crystallinities on their chemical activation by KOH and NaOH, *Micropor. Mesopor. Mater.*, **2007**, 101, 3, 397.

[21]- Edgeworth J.P., Wilson N.R., Macpherson J.V., Controlled Growth and Characterization of Two-Dimensional Single-Walled Carbon-Nanotube Networks for Electrical Applications, *Small*, **2007**, 3, 5, 860.

[22]- Ago H., Nishi T., Imamoto K., Ishigami N., Tsuji M., Ikuta T., Takahashi K., Orthogonal Growth of Horizontally Aligned Single-Walled Carbon Nanotube Arrays, *J. Phys. Chem. C*, **2010**, 114, 30, 12925.

[23]- Lu C., Liu J., Controlling the Diameter of Carbon Nanotubes in Chemical Vapor Deposition Method by Carbon Feeding, *J. Phys. Chem. B*, **2006**, 110.

[24]- Wen Q., Zhang R., Qian W., Wang Y., Tan P., Nie J., Wei F., Growing 20 cm Long DWNTs/TWNTs at a Rapid Growth Rate of 80-90 μm/s, *Chem. Mater.*, **2010**, 22, 4, 1294.

[25]- Kang S.J., Kocabas C., Ozel T., Shim M., Pimparkar N., Alam M.A., Rotkin S. V., Rogers J.A., High-performance electronics using dense, perfectly aligned arrays of single-walled carbon nanotubes, *Nat. Nanotechnol.*, **2007**, 2, 230.

[26]- Popp A., Yilmazoglu O., Kaldirim O., Schneider J.J., Pavlidis D., A self-supporting monolith of highly aligned carbon nanotubes as device structure for sensor applications, *Chem. Comm.*, **2009**, 3205.

APPENDIX

A-1: Definitions of terms

A. Selectivity

The term selectivity is used several times through this dissertation. It is important to mention that selectivity is a measure of how selective something is. In this particular case the terms SWCNT selectivity, MWCNT selectivity, CNT selectivity and (n,m) selectivity have being used. Their definitions are shown below.

SWCNT selectivity: quantity of SWCNT related to the total number of species.
MWCNT selectivity: quantity of MWCNT related to the total of species.
CNT selectivity: quantity of CNT related to the total amount of species.
(n,m) selectivity: quantity of specific (n,m) related to the total (n,m) area.

B. Carbon yield

Another term that has been used through this dissertation and it is important to define is carbon yield. This term is defined below.

Carbon yield (%): mass of carbon divided by the total initial amount of catalyst (metal-support) multiplied by 100.

A-2: Internship

The use of different analytical techniques (surface area analysis, temperature programmed analysis, etc.) learned during a summer internship at ConocoPhillips have been applied to the research topic concerning this doctoral dissertation.